ACCELERATING EDITED MAGNETIC RESONANCE SPECTROSCOPY AND SPECTROSCOPIC IMAGING OF THE HUMAN BRAIN AT 3T

by

Kimberly L. Chan

A dissertation submitted to Johns Hopkins University in conformity with the requirements for the degree of Doctor of Philosophy

Baltimore, MD

March, 2019

Abstract

Edited magnetic resonance spectroscopy is a method capable of probing biochemical processes non-invasively, but suffers from an inherently low signal-to-noise which results in long acquisition times. Increasing the efficiency of these scans would reduce these acquisition times and can increase the number of scans, and consequently the amount of information, that can be acquired within a time-limited scan session in clinical and research settings.

This thesis addresses this need with methods to increase the number of metabolites and regions that can be detected within a single scan as well as a method to reduce the duration of the preparation pulses. In particular, we demonstrate the ability of two techniques to detected glutathione and lactate simultaneously. We then move on to introduce 'Hadamard Encoding and Reconstruction of MEGA-Edited Spectroscopy' (HERMES) and demonstrate that it can detect two and three metabolites simultaneously. As an example of this method, a scheme for separately detecting N-acetylaspartate (NAA) and N-acetylaspartylglutamate (NAAG) is presented. This scheme is then extended to separately edit Aspartate in addition to NAA and NAAG. All multi-metabolite editing schemes are shown to be capable of optimally detecting each metabolite separately in simulations, phantom, and in vivo experiments. Relative to separate acquisitions of each metabolite separately, multi-metabolite editing results in a scan time reduction of two-fold and three-fold for editing two metabolites and three metabolites respectively.

This thesis then introduces and evaluates methods for multi-region editing. First, a new technique 'Spatial Hadamard Editing and Reconstruction for Parallel Acquisition' (SHERPA) is introduced and found to be capable of separating the GABA-edited spectra from two voxels. HERMES is then extended for use with magnetic resonance spectroscopic imaging (MRSI) and is found to be also introduced and is shown to decrease subtraction artifacts in GABA-edited spectra. Lastly, a short-duration water suppression technique compatible for use with fast edited

MRSI sequences is introduced and is shown to suppress water better than VAPOR.

Readers: Peter Barker, DPhil and Richard Edden, PhD

Acknowledgements

This thesis would not have been possible without the instrumental support of my advisors, friends, and family. First, I would like to thank my wonderful mentor, Richard Edden. When I first joined the lab, I felt overwhelmed and very much out of my element. You helped me get on my feet and took the time to sit by my side and teach me the theory and techniques necessary to proceed with my research. I greatly appreciate all the hours you spent on mentoring me and I hope I have made you proud. I would also like to thank my lovely advisor, Peter Barker for your support during all these years and for giving me the confidence to pursue my ideas. Your expertise and knowledge has been invaluable, and I feel honored to have you as a mentor. I know I will remain in touch with both of you and I hope that we will have the opportunity to collaborate in the future. Thank you very much for looking out for me all these years; I am truly indebted to both of you.

I also must absolutely acknowledge my amazing fiancé, Ben, whose support kept me sane during the latter half of my PhD. Thank you for giving me perspective and reminding me of the important things in life. You are my anchor and my home, and I feel fortunate that I could benefit from your delicious home cooked meals that fueled me the last few years. I love you!

I would also like to thank my mom and dad whose love and support kept me going all these years. It wasn’t easy being away from the Bay Area, especially in the first couple of years, but your support helped me keep going. I know you’re proud of me, and I hope I continue to make you proud.

I would also like to thank past and present members in my lab. Nick, I greatly appreciated your friendship all these years, especially during my first few years here in Baltimore. Being able to hang out and talk to you about video games and life made the homesickness much more tolerable. Thanks for looking out for me. Anouk, Subechhya, and Ashley: thank you for making me feel welcome when I first came to this lab. Mark, Muhammad, Georg, Adam, Michal and Anna: thank you for insightful input and for creating such a lovely lab environment for me to work in. Mike, your input on everything pulse programming related has been instrumental to the success of this thesis. You have been an invaluable resource!

I would also like to thank my future mother and father in-law, Theresa and Michael. You've treated me like a daughter and with so much kindness over the years. Thank you for coming out to support me during my thesis defense!

Last, but not least, I would like to thank my long-time friends from California. Kelsey, I feel blessed that we could maintain such a wonderful friendship for over 20 years. Thanks for your support during my PhD and for keeping touch in spite of the distance. Laura, thank you for always being there for me even in the hardest of times.

Table of Contents

Chapter 1 – Background and Introduction

1.1 General Introduction

In vivo ^{1}H MR spectroscopy (MRS) is capable of non-invasively detecting a large range of metabolites in the brain that are known to be involved in the pathophysiology of a large range of neurological diseases and psychiatric disorders such as autism (1, 2), brain tumors (3, 4) and schizophrenia (5, 6) as well as basic brain function (7). Despite its usefulness, some limiting issues have prevented the technique from becoming more widespread. In particular, in vivo MRS has an inherently low signal-to-noise ratio (SNR) as MR is an inherently insensitive technique and the molecules of interest often have a relatively low concentration. In addition, ^{1}H-MRS suffers from a lack of spectral dispersion which makes it especially difficult to detect lower-concentration metabolites. In order to detect these metabolites, specialized techniques such as J-difference editing are needed, and long scan times are needed to obtain sufficient SNR.

A limitation of J-difference editing, however, is that J-difference edited experiments are typically tailored to detect one metabolite in one region at a time. This limits the amount of information that can be collected at a time and can reduce the scope of a clinical or research study. The limited spatial coverage is particularly a disadvantage in instances where mapping the spatial distribution of metabolite concentrations is essential such as identifying a potential problem area. To address this issue, J-difference editing has been used in combination with multi-voxel localization and has shown to be capable of mapping low-concentration metabolites such as GABA (8, 9) and GSH (10). These scans are of particularly long duration and are more artifact-prone than single-voxel acquisitions as they are particularly sensitive to motion. Motion in J-difference acquisitions can result in subtraction artifacts that result from misalignment of the different sub-acquisitions. Thus, accessible motion correction methods for edited-MRSI acquisitions are important for improved reliability. These problems necessitate the development of techniques to improve the reliability and spatial coverage of in vivo MRS as well as ways to reduce the overall scan time.

1.2 Brain Metabolites

In vivo ^{1}H MR spectroscopy is capable of detecting a variety of biologically-relevant endogenous compounds. In order for compounds to be detected, they must be present in millimolar concentrations and be small, mobile molecules.

1.2.1 N-Acetyl Aspartate (NAA)

NAA is the largest signal in the in vivo brain spectrum. Although it's precise function is unknown, it has been speculated that it is needed for lipid synthesis, as a regulator of protein synthesis, and serves as a place of storage for aspartate. NAA is considered to be a marker of neuronal density due to several lines of evidence. Decrease in NAA intensity has been shown to be linked with disorders that have associated neuronal loss such as stroke and tumors (11). In addition, immunocytochemical staining has shown that NAA is primarily located in the axons and dendrites of neurons (12).

1.2.2 N-Acetyl Aspartate Glutamate (NAAG)

NAAG is a dipeptide of glutamate and N-substituted aspartate and consists of acetyl, aspartyl, and glutamate moieties. NAAG has been suggested to be involved in excitatory neurotransmission as a modulator of glutamatergic signaling and as a source of glutamate. Its signal is often indistinguishable from NAA. Because of that, the sum of the two singlet peaks are often measured in order to estimate the amount of NAA-containing molecules.

1.2.3 γ-Aminobutyric Acid (GABA)

GABA is an inhibitory neurotransmitter in the brain with a low concentration of ~1 mM (11, 13). Because of overlap from more intense resonances from compounds with higher concentrations, it is difficult to detect GABA using conventional methods so spectral editing is typically used for GABA detection (11, 13).

1.2.4 Aspartate (Asp)

Aspartate is a non-essential amino acid and is an excitatory neurotransmitter present in the brain at a low concentration of 1 – 2 mM (11, 13).

1.2.5 Choline (Cho)

The most prominent Cho signal in the spectrum is a singlet which includes contributions from glycerophosphorylcholine (GPC) and phosphorylcholine (PC) in addition to free choline (11-13). Because the signal does not consist purely of free choline, the signal is referred to as total choline. The concentration of total Cho ranges from 1 – 2.5 mM (11, 13). PC and GPC make up the rest of the choline signal at 0.6 mM and 1 mM respectively. Changes in Cho has been associated with in membrane turnover, and although free choline contributes little in the normal brain, the concentration of free choline can be significantly increased in tumors, Alzheimer's disease, and multiple sclerosis (11-13). Decreases in Cho have been associated with liver disease, and stroke (11).

1.2.6 Creatine (Cr)

Creatine and phosphocreatine (PCr) have resonances that originate from the methyl and methylene protons (13). Because Cr and PCr resonances are indistinguishable from one another, they are measured together and are often referred to as 'total creatine' (11). Both Cr and PCr are present in both neuronal and glial cells and have been shown to play a role in tissue energy metabolism (11). They are both present at high concentrations in vivo at 4 – 5.5 mM for PCr and 4.5 – 6 mM for Cr and have higher levels in gray matter than in white matter (11). Across age and a variety of diseases, total creatine is relatively constant, although decreased Cr levels have been observed in tumors and strokes (11).

1.2.7 Glutamate (Glu)

Glutamate is an amino acid present in vivo at concentrations ranging from 6 to 12.5 mM and acts as both an excitatory neurotransmitter in the brain and as a precursor for GABA (11). Glutamate has also been shown to be an important component in the synthesis of various other metabolites such as glutathione (11). It's present in all cell types, but is present in larger quantities in glutamatergic neurons than in astroglia and GABA-ergic neurons (11). At lower magnetic fields such as 1.5 T and 3.0 T, this spectrum overlaps substantially with glutamine (11, 13). However, at higher field strengths such as 7.0 T, their resonances at H4 protons become distinguishable (11).

1.2.8 Glutamine (Gln)

Glutamine is primarily involved in intermediary metabolism and is located in astroglia (11). In addition, Glutamine is closely in involved in the Glu–Gln neurotransmitter cycle with Gln being synthesized from Glu. Glutamine also has a similar structure to Glutamate and is difficult to distinguish from Glutamate, especially at lower magnetic field strengths.

1.2.9 Glutathione (GSH)

Glutathione is the dominant antioxidant in the brain primarily located in astrocytes (14, 15). and has been implicated in the pathophysiology of various psychiatric and neurological diseases such as schizophrenia (14, 15) and Parkinson's disease (11, 16). The structure of glutathione consists of a glycine, cysteine and glutamate. Like GABA, GSH is present in vivo at low concentrations of 1 – 3 mM and thus are typically detected using specialized techniques such as spectral editing (11, 17, 18).

1.2.10 Lactate (Lac)

Lactate is indicator of non-oxidative glycolysis and increases in Lac have been seen in conditions where blood flow is restricted (e.g. ischemic stroke) (11). With inadequate lipid suppression and/or localization, Lac can overlap with lipid resonances at 1.3 ppm in addition to macromolecules. Thus, Lac is best detected using spectral editing in such cases (11, 18).

1.2.11 Macromolecules

In addition to metabolites, macromolecules also contribute much to the baseline especially at low echo times (11, 19). It is estimated that there at least 10 macromolecule resonances.

1.3 Basic Principles

1.3.1 Nuclear Spins

The nuclear magnetic resonance phenomena arises from atoms with an odd number of protons which have a spin angular momentum (20). This vector quantity can be calculated as:

$$S = \hbar I$$

(1.1)

where ħ is Planck's constant divided by 2π and *I* is the spin operator in quantum mechanics. The magnetic dipole moment μ associated with *S* can be defined as (20):

$$\mu = \gamma S = \gamma \hbar I$$

(1.2)

where γ is a constant called the gyromagnetic ratio, a specific property of the nucleus under investigation. Several atoms can fit this category, however, the most commonly detected nucleus is the hydrogen proton due to the natural abundance of water (and other proton sources) in the body which gives rise to the largest signals (20).

1.3.2 Nuclear Spin Interaction with a Magnetic Field

The MR signal originates from the manipulation and detection of a bulk signal arising from the precession of an ensemble average of spins. In the absence of a magnetic field, the spin vectors are oriented in random directions. In the presence of a magnetic field, however, spins have a tendency to align in the direction of the external magnetic field to create a net magnetization moment M. This magnetization moment is oriented in the direction of B_0 and thus it can be inferred that the magnetic dipole moment μ also aligns the direction of the external magnetic field with $M = \sum \mu$ (20). Conventionally, the applied B_0 field is in the z-direction (also known as the longitudinal duration) which is perpendicular to the xy-plane (or the transverse direction). In the presence of a magnetic field, the energy E of a magnetic moment, μ can be described as (20):

$$E = -\mu_z B_0 = -\gamma S_z B_0$$

(1.3)

However, S_z is quantized to $\hbar I_z$ which for hydrogen, $I_z = \pm \frac{1}{2}$ which leads to two energy states that are separated by ΔE and can be defined as (20):

$$\Delta E = \gamma \hbar B_0 = \mathrm{h} \frac{\gamma}{2\pi} B_0$$

(1.4)

From the quantization of the spin angular momentum, two populations of nuclei in different energy states arise: one that is parallel to the external magnetic field (n_+) and one that is anti-parallel to the external magnetic field (n_-). Spins tend to populate the lower energy arrangement which is parallel to the external magnetic field (n_+). However, spins can populate the higher energy arrangement which is anti-parallel to the *B₀* field provided that the thermal energy available is sufficient to exceed this energy separation. Although the energy of the sample is minimized if all the magnetic moments are aligned with the field, the orientation of the spins within a sample are most often a mixture of states due to thermal molecular motion. Thus, the ratio of the two spin populations is dependent on the Boltzmann distribution can be expressed as (20):

$$\frac{n_-}{n_+} = e^{-\Delta \mathrm{E}/\mathrm{k}T}$$

(1.5)

where k is Boltzmann's constant and *T* is absolute temperature. Even with this thermal disruption, however, a slight preference still exists for the spins to populate the lower energy level with a ratio that is marginally less than 1. Over the entire sample, this population bias, in addition to the random distribution of the phases of individual spins, leads to a bulk longitudinal equilibrium magnetization vector parallel to B_0 which forms the basis for the MR signal. This magnetization at thermal equilibrium (or the magnetic moment per unit volume) can be calculated from the Boltzmann distribution which can be shown to be (20):

$$M_0 = \left(\frac{\rho_0 B_0 \gamma^2 \hbar^2}{4\mathrm{k}T}\right)$$

(1.6)

where B_0 is the strength of the external magnetic field in Tesla, n is the total number of nuclear spins within a sample, and, ρ_0 is the spin density defined as spins per unit volume. From this, it can be deduced that M_0 would scale linearly with the strength of the magnetic field, thus increasing the detection sensitivity.

If *M* is made to point away from the z-direction, it starts to precess about the B_0 field direction with an angular frequency of (20):

$$\omega_0 = \gamma B_0$$

(1.7)

For the hydrogen proton, the gyromagnetic ratio is 42.58 MHz/Tesla. Thus, for a 3 Tesla (3T) scanner, the nuclear spins precess at a rate of 127.74 MHz. This precession rate is referred to as the Larmor frequency.

1.4 Chemical Shift

In vivo, most volumes contain more than one nuclear spin other than those with a Larmor frequency as specified by equation 1.1. In addition to the gyromagnetic ratio γ and the external B_0 field, the resonant frequency also depends on the chemical environment which can cause a displacement in the resonant field. This effect is called chemical shift and is caused by shielding of the nuclei from the external magnetic field by the motion of surrounding electrons. This reduces the magnetic field experienced by the nucleus (11, 20):

$$B_{\mathrm{nuc}} = B_0(1 - \sigma)$$

(1.8)

where σ is the shielding constant which depends on the chemical environment. Plugging this into equation (xx), the resonant frequency of a chemical species can be rewritten as (20):

$$\omega_{nuc} = \omega_0(1 - \sigma)$$

(1.9)

Thus, the change of frequency due to the chemical environment is proportional to B_0. The chemical shift δ is specified relative to a chemically inert compound and can be defined as (11):

$$\delta = 10^6 \text{ x } \frac{\omega - \omega_{\mathrm{ref}}}{\omega_{ref}}$$

(1.10)

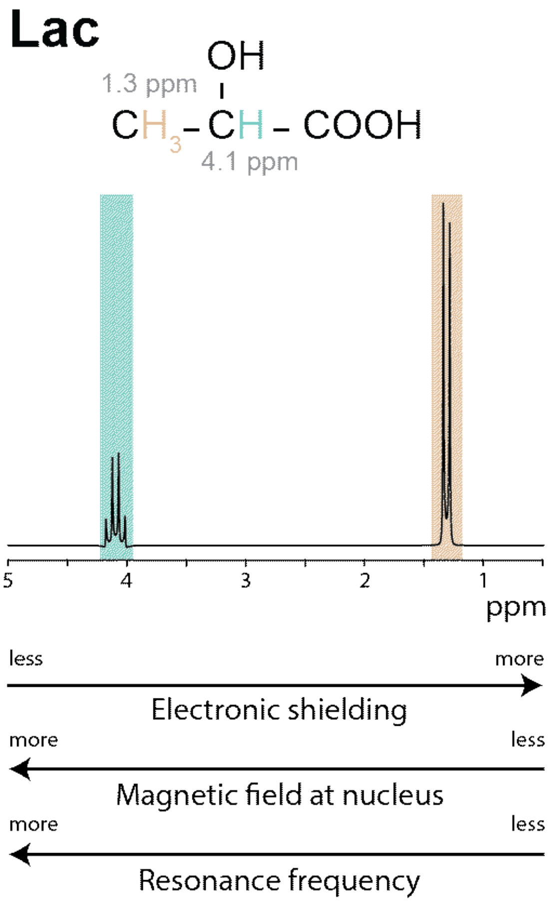

Figure 1.1. Origin of chemical shift demonstrated for the example of the lactate. The –CH group is adjacent to the electronegative oxygen atom which shifts electron density away from the –CH group. Thus, its feels a greater magnetic field at the nucleus and consequently, a higher resonant frequency and chemical shift at 4.1 ppm. The $-CH_3$ group, however, is two bonds away from the oxygen group and thus has a higher amount of electron shielding and consequently, experiences a reduced magnetic field at the nucleus. Consequently, it has a lower resonant frequency and chemical shift at 1.3 ppm. Figure based on reference 11.

where ω is the frequency of the compound and ω_{ref} is the frequency of the reference compound. The constant δ is typically expressed in terms of parts per million (ppm) instead of Hertz (Hz) so that the peaks are independent of the external magnetic field strength. This difference in resonant frequencies allows for detection of different compounds depending on their differing resonant frequency along the chemical shift axis. The exact position along the chemical shift axis depends on the degree of electron shielding which reduces the amount of the magnetic field felt by the nucleus (11). More electronegative atoms such as oxygen and nitrogen shift the electron density away from protons. Thus, protons that are located closer to electronegative atoms on the chemical structure will have a higher Larmor frequency. Figure 1.1 depicts this concept for the example of lactate. In figure 1.1, it can be seen that the –CH group is closer to electronegative oxygen than the $-CH_3$ group which results in a higher Larmor frequency. Chemical shifts for some compounds commonly detected in vivo can be seen in Table 1.1.

Compound	Chemical shift (ppm)
N-acetylaspartate (NAA)	Acetyl moiety: 2.0080; Aspartate moiety: 4.3817, 2.6727, 2.4863, 7.8205
N-acetylaspartylglutamate (NAAG)	Acetyl moiety: 2.042; Aspartyl moiety: 4.607, 2.721, 2.519, 8.26; Glutamate moiety: 4.128, 2.049, 1.881, 2.18, 2.19, 7.95
Alanine	3.7746 1.4667
Ascorbate	3.73, 4.01, 4.5
Gamma aminobutyric acid (GABA)	3.0128 1.8890 2.2840
Aspartate	3.8914, 2.8011, 2.6533
Choline	3.185, 4.054, 3.501
Creatine	3.027, 3.913, 6.649
Ethanolamine	3.8184, 3.1467
Glutamate	3.7433, 2.0375, 2.12, 2.3378, 2.3520
Glutamine	3.753, 2.129, 2.109, 2.432, 2.454, 6.816, 7.529
Glutathione	Glycine moiety: 3.769, 7.154; Cysteine moiety: 4.5608,

	2.9264, 2.9747, 8.1770; Glutamate moiety 3.769, 2.159, 2.146, 2.510, 2.560
Glycerophosphorylcholine	Glycerol moiety: 3.605, 3.672, 3.903, 3.871, 3.946; Choline moiety: 4.312, 3.659, 3.212
Glycine	3.5480
Homocarnosine	4.472, 3.185, 3.003; Imidazole ring: 7.075, 8.081; GABA moiety: 2.962, 1.891, 2.367, 7.899, 6.397
Myo-Inositol	3.5217, 4.0538, 3.5217, 3.6144, 3.269, 3.6144
Scyllo-Inositol	3.34
Lactate	4.0974, 1.3142
Phenylalanine	3.9753, 3.2734, 3.1049
Phosphocreatine	3.029, 3.93, 6.5810
Phosphoryl choline	4.2805, 3.641
Serine	3.8347, 3.9379, 3.9764
Taurine	3.4206, 3.2459
Threonine	3.5785, 4.2464, 1.3158
Tryptophan	4.0468, 3.4739, 3.2892; Indole ring: 7.3120 7.7260 7.2788 7.1970 7.5360
Tyrosine	3.9281 3.1908 3.0370; Phenyl ring: 7.1852 6.8895 6.8895 7.1852

Table 1.1. Commonly measured metabolites with in vivo ^{1}H MR spectroscopy and their chemical shifts. Values taken from references 13, 21, 22.

1.5 Magnetization Signal Detection

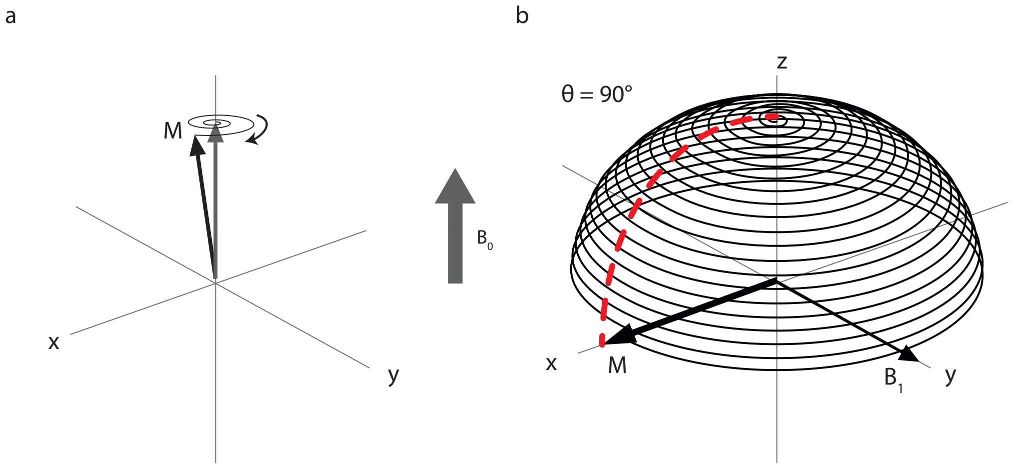

Figure 1.2. (a) Precession of the magnetization about the z-axis. (b) B$_1$ induces the magnetization to rotate onto the magnetization onto the transverse plane (xy) plane. Figure based on reference 20.

In order for a detectable MR signal to be generated, the magnetization vector ($\vec{M}$) must be disturbed from its initial position aligned with the longitudinal (z) axis parallel to the external magnetic field where it is referred to as longitudinal magnetization (21, 23). When the magnetization is no longer aligned with the B_0 field, a nutation of the magnetization vector is induced about *z*-axis as it's tipped away from the *z*-axis as shown in figure 1.2a (11, 23). This can be done by applying a radiofrequency (RF) pulse at the Larmor frequency to create a B$_1$ field in the transverse plane as shown in figure 1.2b (23). The RF pulse applies a torque which rotates the magnetization away from its alignment along the B_0 axis. It can be applied with a particular strength and duration to determine the flip angle of the pulse. RF pulses typically have strengths on the order of microteslas (μT) with durations on the order of milliseconds (ms). RF can rotate the equilibrium $\vec{M}$ 90° so that the magnetization vector is on the transverse field as shown in figure 2b or even 180° so that the magnetization vector is on the –*z*-axis. These pulses are referred to as excitation and inversion pulses respectively.

Once $\vec{M}$ is tipped completely onto the transverse axis plane, the resulting magnetization has a magnitude of M_0 and precesses about the *z*-axis. Its x and y (transverse) components can be summed up to form what is referred to as transverse magnetization which has sinusoidal time dependence at the Larmor frequency (23). The complex magnetization can be defined as (23):

$$M_{+}(t) = M_x(t) + iM_y(t) = M_0 e^{-i\omega_0 t + i\phi_0}$$

(1.11)

expressed in terms of magnitude and phase. The initial phase angle, ϕ_0, is determined by the axis the magnetization is rotated about (23).

1.6 Relaxation

After excitation, the transverse component of the magnetization vector decays over time while the longitudinal component returns to equilibrium. These two relaxation processes are known as transverse relaxation and longitudinal relaxation respectively, or T_2 and T_1 relaxation.

The change in the longitudinal component of the magnetization over time can be described by the following equation (20):

$$\frac{dM_z}{dt} = -\frac{M_z - M_0}{T_1}$$

(1.12)

Solving this equation (20):

$$M_z = M_0 + (M_z(0) - M_0)e^{\frac{-t}{T_1}}$$

(1.13)

Assuming $M_z(0) = 0$ after 90° excitation, this equation simplifies down to (21):

$$M_z = M_0(1 - e^{\frac{-t}{T_1}})$$

(1.14)

T_1 is the spin-lattice relaxation time constant characterizing the longitudinal relaxation time back to equilibrium when M_z is restored to M_0 (20, 23). This relaxation results from an energy exchange between the spins and the surrounding lattice (20). Once the magnetization is rotated into the transverse plane, it will regrow along the direction of the B_0 field, typically denoted as the z-direction which can be characterized by its T_1 relaxation constant. In human tissue, in B_0 field strengths of 0.1 T and more, T_1 values can range from tens to thousands of milliseconds (23). In general, T_1 has smaller values when there are larger molecules in the environment, and liquids tend to have longer T_1 values while fat tends to have short T_1 values. After an initial disturbance, the longitudinal magnetization starts to grow back exponentially as illustrated in figure 1.3 (24-

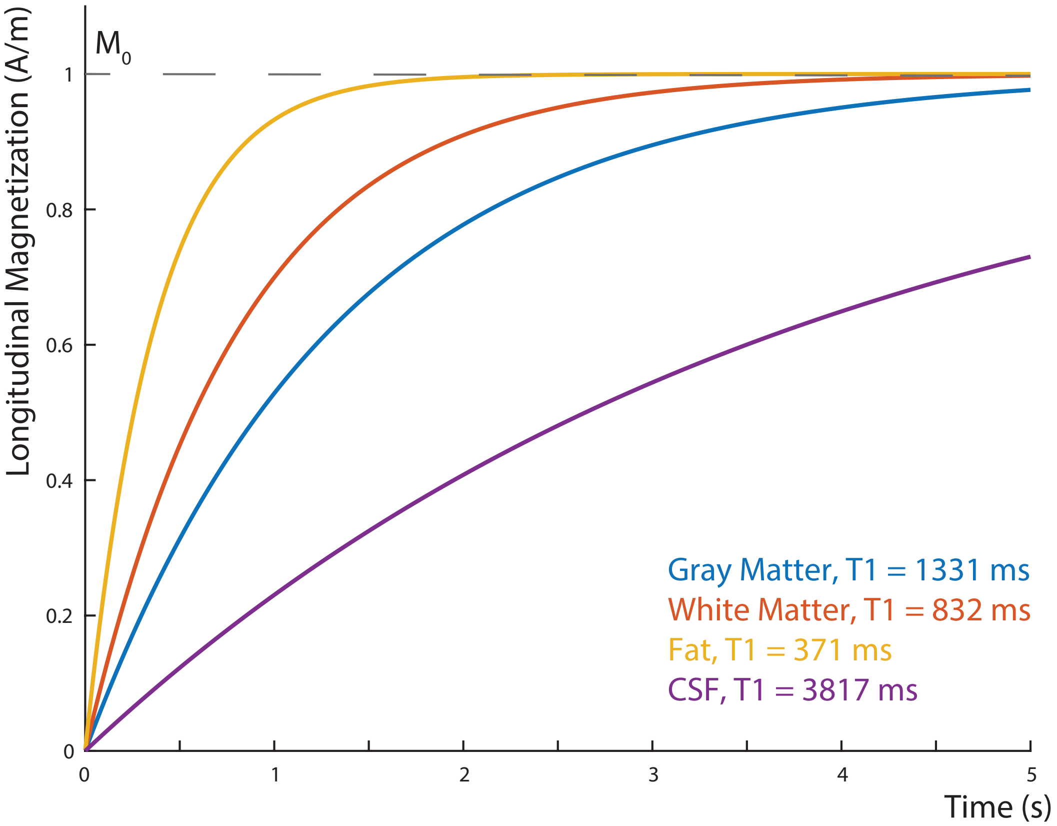

Figure 1.3. Recovery of longitudinal magnetization over time due to T1 relaxation in different tissues. M_z recovers more quickly in tissues with short T_1s such as fat and white matter than in tissues that have longer T_1s such as gray matter and cerebral spinal fluid (CSF).

26). Spins with shorter T_1 values have longitudinal magnetization that grows back faster while spins with longer T_1 values grow back slower (figure 1.3).

For the transverse component, the decay of the magnetization over time can be described by:

$$\frac{dM_{xy}}{dt} = -\frac{M_{xy}}{T_2}$$

(1.15)

After a 90° excitation, $M_{xy}(0) = M_0$ and the above equation becomes:

$$M_{xy} = M_0 e^{\frac{-t}{T_2}}$$

(1.16)

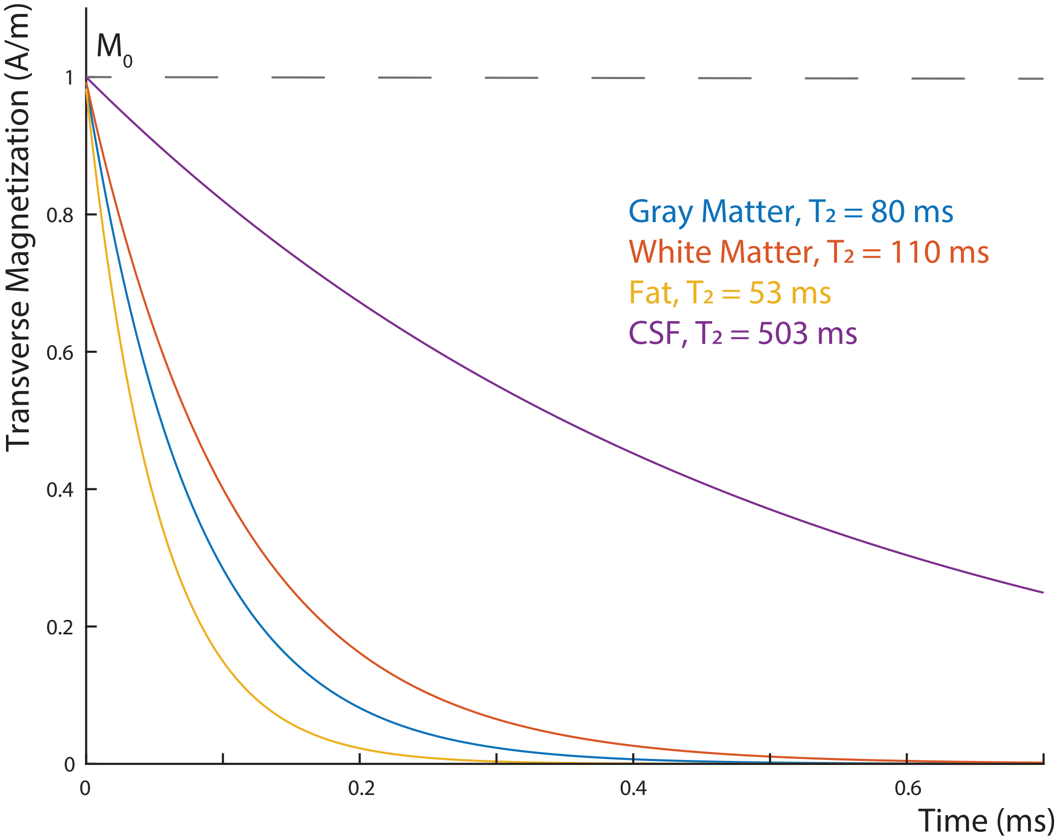

Figure 1.4. Recovery of transverse magnetization over time due to T_2 relaxation in different tissues. M_{xy} decays more quickly in tissues with short T_2s such as fat, white matter, and gray matter than in tissues that have longer T_2s such as cerebral spinal fluid (CSF).

T_2 is the spin-spin relaxation time constant describing the decay of transverse magnetization. This transverse relaxation arises from the dephasing of different spins due to location-dependent variations in precessional frequency. and with the T_2 decay term, this transverse magnetization vector decreases exponentially in magnitude over time as illustrated in Figure 1.4 due to dephasing of the spins. Spins with shorter T_2 values have transverse magnetization that decays faster while spins with longer T_2 values decay slower (Figure 1.4). (24, 27, 28).

In practice, however, there is additional T_2 decay component originating from B_0 field inhomogeneity which results in spins precessing at frequencies other than the Larmor frequency. This results in the transverse magnetization to decay more rapidly and consequently, further suppression of the signal. Denoting this additional decay component as T_2', the effective relaxation rate of $\frac{1}{T_2^*}$ becomes (23):

$$\frac{1}{T_2^*} = \frac{1}{T_2} + \frac{1}{T_2'}$$

(1.17)

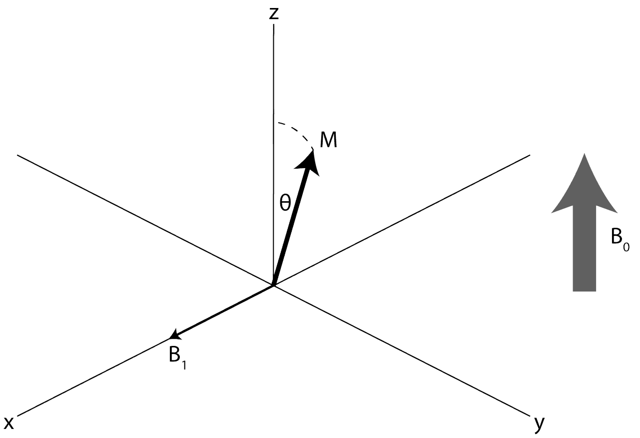

Figure 1.5. Magnetic field vector and magnetization vector in the rotating frame of reference. With the application of a RF pulse, a B_1 field vector is introduced in the transverse plane. This tips the magnetization a defined flip angle θ away from the longitudinal axis (z).

This loss in transverse magnetization due to T_2' relaxation is recoverable, however, which will be described in a later section.

1.7 Free Induction Decay

When in the transverse plane, the magnetization induces a time-varying electromotive force (EMF) which induces a voltage in the RF receiver coil (20, 23). The magnitude of the signal varies with the square of the main magnetic field, B_0 (23):

$$|signal| \propto \frac{\gamma^3 B_0^2 \rho_0}{T} \tag{1.18}$$

The generated signal over time is called the free induction decay which forms the basis for the MR signal.

1.8 Rotating Reference Frames

To aid in describing MRI/MRS experiments, a reference frame rotating at the Larmor frequency is often used and rotates clockwise about the z-axis (23). From our rotating perspective, however, the axis does not move at all. When a RF field ($\overrightarrow{B_1}$) with x and y components is applied, spins are tipped away from $\hat{z}$ and into the transverse plane (figure 1.5). If the transmit field matches the Larmor frequency, the magnetization vector appears to be stationary in space in the rotating reference frame (23).

1.9 Radiofrequency (RF) Pulses

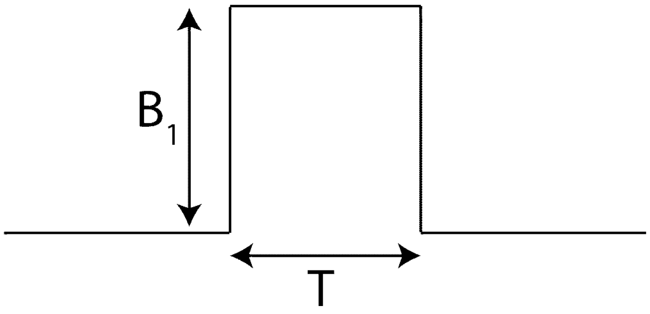

Figure 1.6. A rectangular (hard) pulse with an amplitude B_1 and a duration T.

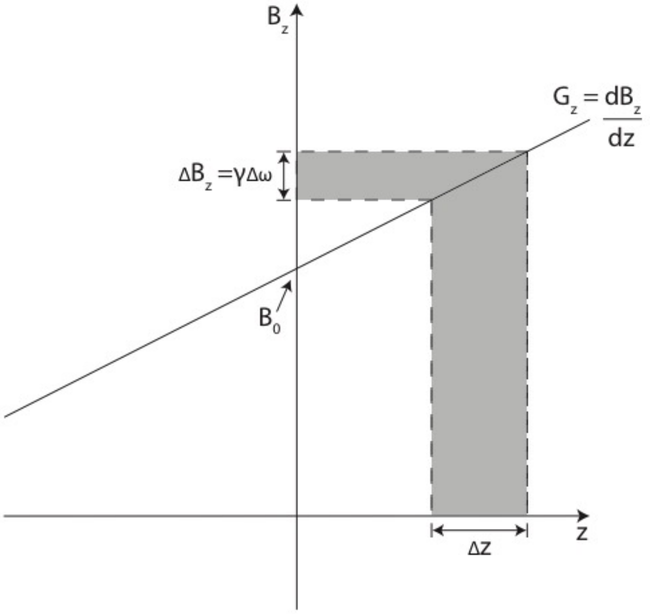

Figure 1.7. Schematic of slice selection with a gradient played out in a z-direction which results in a spatial variation of the magnetic field strength, and consequently, the resonant frequencies, over the z direction. A frequency-selective RF pulse can then be applied to select a range of frequencies and consequently, a range of locations. Figure based on reference 20.

RF pulses are one of the basic building blocks of all MRI/MR S sequences, the primary tools to perform essential manipulations of the magnetization such as excitation, refocusing, and inversion (11). These pulses act to tip the magnetization from its original direction by inducing B_1 magnetic field along some axis to add to the static magnetic field and create an effective B field (11). By applying a RF pulse with certain characteristics, the magnetization can be rotated a flip angle θ, relative to its original direction (figure 1.5) (11).

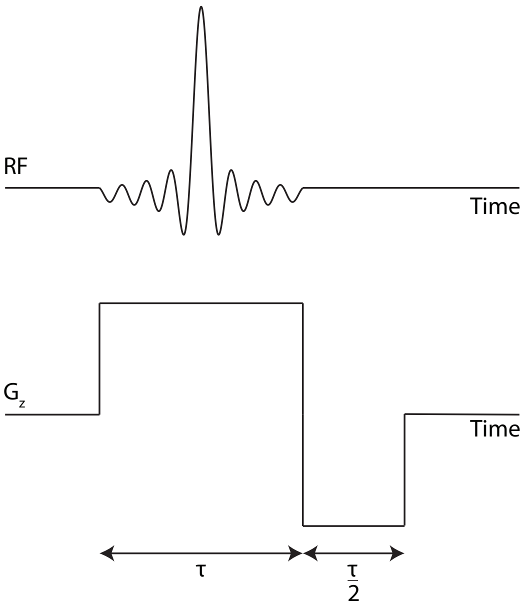

Figure 1.8. Excitation pulse played out with a slice selective gradient and followed by a rewind gradient to unwind the linear phase introduced over the slice width by the slice-selective gradient.

The most simplistic RF pulse is the “square” RF pulse with a constant amplitude B_1 amplitude played out over a given time as shown in figure 1.6 to target a specific set of spins by applying the pulse at its Larmor (resonant) frequency (29). However, it is often desirable to target a large range of spins in order to perform important functions such as spatial localization. In order to do so, RF pulses with more complicated B_1 amplitude waveforms are needed to allow for a selection of a spins with a range of resonant frequencies. The RF pulse waveform, which is denoted as $B_1(t)$ which has units of microteslas and varies with time, can be optimized to get a desired slice profile (or frequency response) which can be calculated using Bloch equations. The pulse duration can also be optimized to obtain a certain pulse bandwidth which is the range of frequencies affected. This pulse bandwidth is typically measured as the full width at half maximum (FWHM) of the frequency response profile (29). In addition to the bandwidth, the central frequency of the frequency response can be optimized by changing the carrier frequency of the RF pulse. Moreover the flip angle of a pulse can generally be determined by finding the integral of the RF pulse envelope (29).

1.9.1 Slice selection

RF pulses are often used in combination with a magnetic field gradient to make the resonant frequency of the spins vary linearly as a function of location along an axis (20). This allows for the selection of a slice of magnetization at a specific range of frequencies as shown in figure 1.7. This is often used for slice-selective excitation (in the z-direction) to rotate the magnetization completely into the transverse axis where a signal can be recorded. To excite a certain slice along this axis, the RF pulse applied is tuned to a certain transmitter frequency along the z-axis. That is, the B_1 frequency envelope should be equal to that of the spins within a slice of interest. The slice thickness depends on both the magnetic field gradient strength and the bandwidth of the RF pulse. Stronger magnetic field gradients result in a larger range of Larmor frequencies across the slice axis and consequently, a thinner slice is excited, provided that the RF pulse bandwidth stays the same. The same can be achieved if the magnetic field gradient was kept the same and the bandwidth of the RF pulse was reduced. The relationship between slice thickness (Δz), the magnetic field gradient ($G_z = \frac{dB_z}{dz}$), and bandwidth of the RF pulse (BW) can be described as (20):

$$BW = \gamma G_z \Delta z$$

(1.19)

Rearranging this equation, it can be seen that the slice thickness is inversely related to the gradient strength but directly related to the bandwidth of the RF pulse:

$$\Delta z = \frac{BW}{\gamma G_z}$$

(1.20)

Although all spins encompassed by the bandwidth of the RF pulse are excited, the magnetization at different spatial locations across the slice precess at different frequencies due to the applied field gradient while the spins are in the transverse plane. Because of this, the magnetization vector at different points across the slice acquire phase relative to one another, and consequently a loss of signal. To reverse this phase dispersion, a linear ‘rephase’ z-gradient with opposite polarity can be applied to undo the position-dependent phase accrual (20). For this to happen, the reversal gradient must have the same area as the gradient played out while the spins are in the transverse plane accruing phase. For a symmetrical sinc excitation pulse, this is about half the total area of the slice-selective gradient as shown in Figure 1.8.

The excitation pulse forms the basis for the simplest sequence known as the FID sequence shown in figure 1.9 (23). An excitation pulse is applied which rotates the longitudinal magnetization into the transverse plane where the spins start to precess. This induces an EMF in the RF coils to generate a free induction decay (FID) which is sampled over time to generate a signal (23). This sequence is repeated with a repetition time (TR).

1.9.2 Refocusing pulses

Once the magnetization vector is in the transverse plane following the excitation pulse, the transverse component of the magnetization vector starts to decay over time due to T_2^* relaxation as described previously. Decay due to T_2’ relaxation, however, can be reversed with the addition of an RF pulse with a 180° flip angle which is referred to as a refocusing pulse. An excitation pulse followed by a refocusing pulse as shown in figure 1.10 forms the basis for the spin-echo pulse_ sequence. After the 90° excitation pulse, the signal starts to decay with a time constant proportional to T_2^*. After the application of the 180° refocusing pulse, however, the spins in the transverse plane are flipped over the transverse axis. This inverts the phase that the spins accumulated and since the rate and direction of phase accrual remains the same, the signal starts to recover, but only up to the envelope defined by T_2 decay. While the spin-echo sequence allows for recovery of signal due to T_2’ decay, it does not reduce the effect of T_2 decay. However, T_2 loss is not especially severe for liquids and data can be collected over a time interval

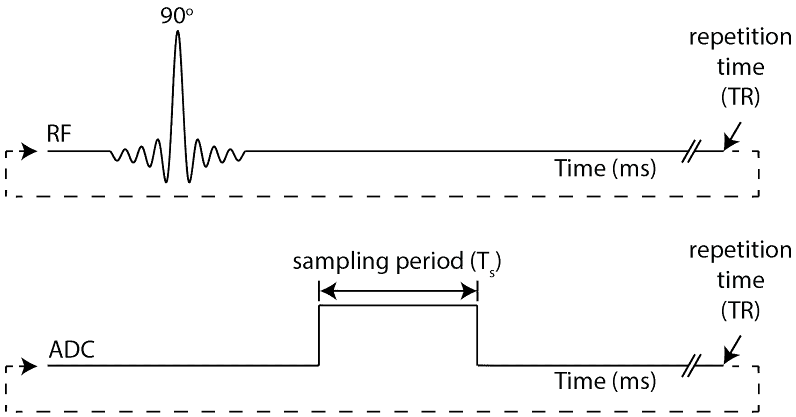

Figure 1.9. Pulse sequence diagram for a FID sequence. After an excitation pulse is played out, the FID is sampled with an analog-to-digital converter (ADC) during a sampling time period (T_s). After a period of time, T_R, has elapsed, the sequence is repeated for a specified number of times. Figure based off reference 23.

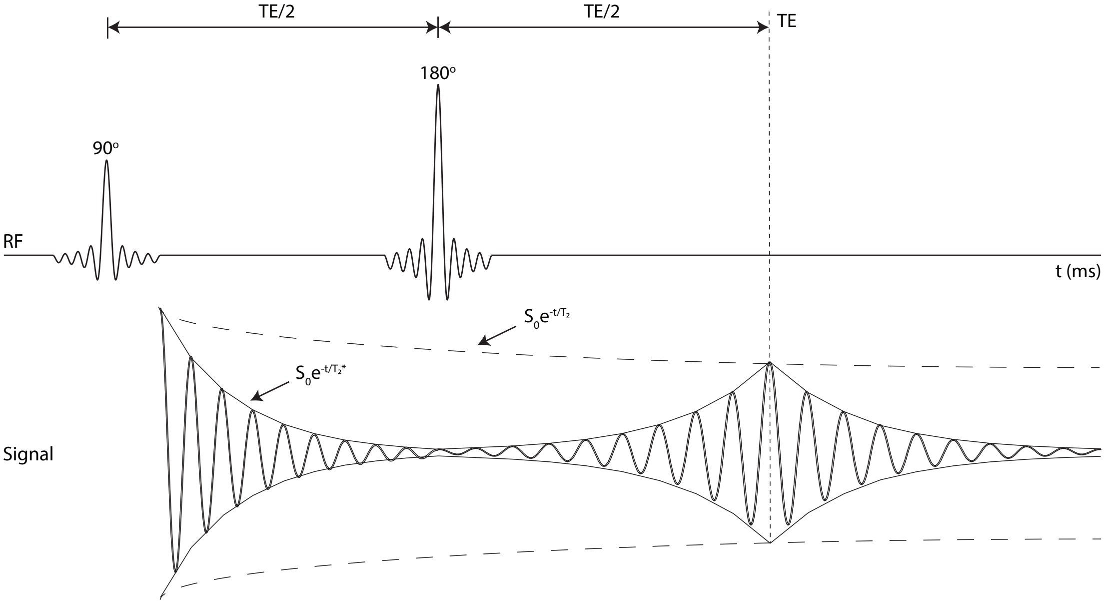

Figure 1.10. RF pulses and timing in the spin-echo sequence and corresponding signal response over time. After the excitation pulse, the signal decays exponentially with a T_2* constant due to field inhomogeneity. After the 180° refocusing pulse played out at TE/2, however, signal recovery occurs as the spins are rephased at the echo time (TE). The signal is still limited, however, by the envelope of the inherent T_2 decay. Figure based off reference 23.

that is short relative to T_2. The signal becomes rephrased when the spins become aligned at the same time after the refocusing pulse, called the echo time (TE). Like excitation pulses, refocusing pulses can be paired with a gradient so that only spins within a particular region are targeted by the refocusing pulses.

Prior to the application of the refocusing pulse, compounds resonating at different Larmor frequencies acquire phase relative to on another. However, the refocusing pulse reverses the phase accrual and chemical shift is refocused.

1.9.3 Inversion pulses

The function of these pulses is to rotate the magnetization vector away from its alignment with the main magnetic field to antiparallel to the B_0 field. These inversion pulses typically have a flip angle of 180° and rotates the magnetization about the transverse axis. Like refocusing pulses, inversion pulses also have a flip angle of 180°. However, unlike refocusing pulses whose magnetization are aligned with the transverse plane prior to the pulse, inversion pulses invert magnetization that is aligned with the $\vec{z}$ axis. Although both inversion and excitation pulses share the same initial magnetization condition, the result of an excitation pulse is substantial transverse magnetization while ideal inversion pulses result in no transverse magnetization.

1.9.4 Specific Absorption Rate (SAR)

One downside to these RF pulses is that they deposit unwanted energy that can heat up the patient and is typically expressed as the specific absorption rate (SAR). As such, regulatory guidelines exist for the maximal amount of SAR deposited in each part of the body. However, SAR is calculated differently on the field strength of the MR scanner. For low field MR scanners (0.2 – 0.3 T), SAR scales with the square of B_0 (29) however, SAR is also dependent on the square of the flip angle as well as the pulse bandwidth (holding flip angle and pulse width fixed). Thus, the relationship with these parameters with SAR can be summarized as (29):

$$SAR \propto B_0^2\theta^2\Delta\mathrm{f}$$

(1.21)

1.10 Field Gradients

In the static B_0 field, all the spins with the same chemical shift precess at the same resonant frequency. Thus, if an excitation pulse is applied, all spins within the RF coil will be affected. Linear gradient fields (in addition to B_0) can be used to differentiate between spins in different regions. These gradients make the external magnetic field position-dependent, so that spins in different locations precess at a different resonant frequency. For example, during a linear magnetic field gradient pulse G_x applied in the x-direction, the field strength varies with x-position (20):

$$G_x = \left(\frac{\mathrm{d}B_x}{\mathrm{d}x}\right)$$

(1.22)

Thus, the magnetic field experienced by spins at position *x* will be (20):

$$B_0 + G_x x$$

(1.23)

and the frequency of the spins becomes a function of the *x*-location (20):

$$\omega = \gamma B_0 + \gamma \mathrm{Gx}$$

(1.24)

Gradient pulses can also be used for spatial encoding of the spins in both the *y*- and *z*-directions.

1.10.1 Crusher gradients

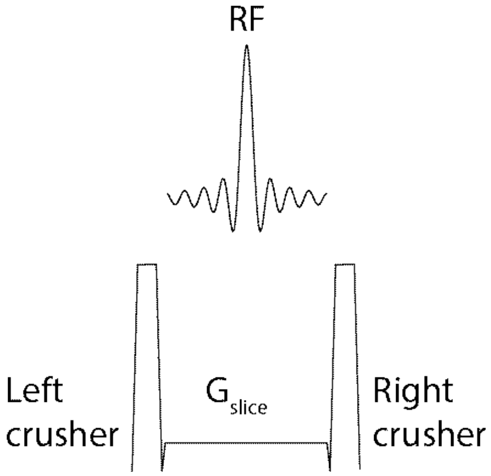

Figure 1.11. A crusher gradient pair (left and right crushers) alongside a slice-selective gradient played at the same time as an RF pulse. Figure based on reference 29.

When a pulse sequence contain non-ideal refocusing RF pulses, areas outside the targeted region can be affected by the RF pulses (29). This can be accounted for, however, by applying a pair of field gradients about the refocusing pulses as shown in figure 1.11 to act as a correction gradient pair crush any unwanted signals. This is known as a crusher pair while each of the individual field gradients are known as crusher gradients (29). Each gradient often has the same polarity and area as shown in figure 1.11. While in the transverse plane. the first crusher gradient lobe introduces a spatially dependent phase to the magnetization. After the refocusing pulse, the phase of the spins affected by the RF pulse are inverted. The second crusher gradient lobe introduces a spatially dependent phase of the same magnitude as the first lobe which “undoes” the phase introduced by the first crusher gradient in the spins affected by the refocusing pulse. Any transverse components outside of the bandwidth of the refocusing pulse are instead dephased by the second crusher gradient (29). By not allowing the contribution of signals outside of the region of interest, the introduction of crusher gradients makes the refocusing pulses slice-selective.

An ideal slice profile has uniform signal within the slice, no signal outside of the slice, and a very narrow transition band. Realistically however, most pulses have a transition band that cover at least 10% of the slice (11). This results in uneven signal across the slice with some signal outside of the slice being included. Thus, when a slice-selective pulse is placed too close to the scalp, some lipid can still contaminate the voxel due to imperfect slice profiles.

1.11 Basic Spectroscopy Pulse Sequences

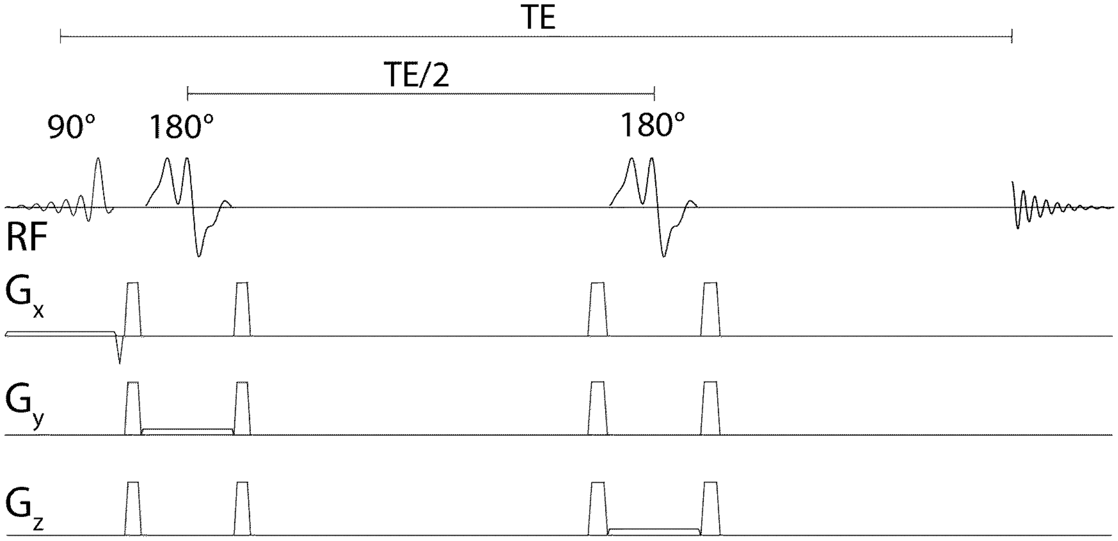

Figure 1.12. PRESS pulse sequence consisting of a slice selective excitation pulse followed by two slice selective refocusing pulses at a time of TE/2 apart from one another. The FID is then acquired after an echo time (TE).

The basic pulse sequences for detecting spectra can be divided into two types of localization: single voxel and multivoxel with MR spectroscopic imaging (MRSI) also known as chemical shift imaging (CSI). Of these two types of localization, single voxel is more widely used as it is considered less artifact prone than spectroscopic imaging. However, MRSI has been of great interest for mapping the distribution of important metabolites.

1.11.1 Point RESolved Spectroscopy (PRESS)

At 3T, the most common pulse sequence used is the PRESS sequence as shown in Figure 1.12. This pulse sequence consists three RF pulses: a 90° excitation pulse followed by two 180° degree refocusing pulses. Each RF pulse is slice-selective along a different orthogonal axis to localize signal to a volume of interest; signals outside of the volume are either not excited or eliminated (30). Data are then acquired at the top of the echo.

Once data are acquired, the resulting FID can be Fourier transformed to form a frequency-domain signal or spectrum. The properties of this spectrum can vary significantly depending on the properties of the compounds, and acquisition and sampling parameters. Figure 1.13 shows an example spectrum using a conventional PRESS sequence similar to the one shown in Figure 1.12. In the spectrum shown, it can be seen that several different compounds can be detected in vivo including myo-Inositol (mI), choline (Cho), creatine (Cr), and N-acetylaspartate (NAA).

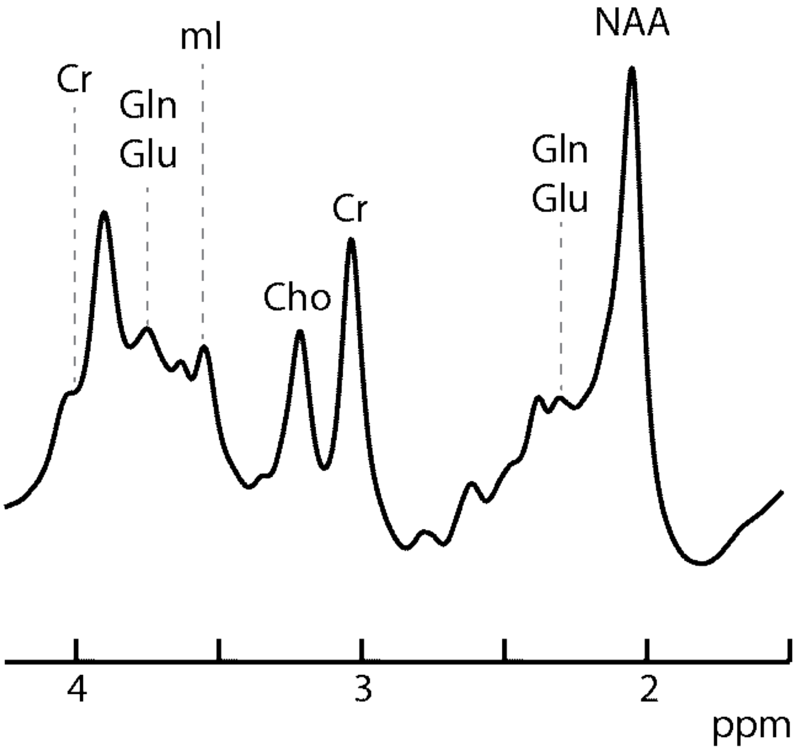

Figure 1.13. A spectrum resulting from a PRESS acquisition acquired from a 3 x 3 x 3 cm^3 voxel in the insula region at an echo time of 35 ms.

1.12 Chemical shift displacement

With the application of an RF pulse in the presence of a spatially-varying gradient, a slice of spins resonating at a frequency covered by the bandwidth of the pulse can be affected. Since the resonant frequency differs between chemical species, the spatial position of this excited slice differs as well and is proportional to the difference in the Larmor frequency between compounds and the applied gradient (11). This results in the volume of interest for different metabolites to be shifted an amount Δd relative to one another due to their different resonant frequencies (11) which can be calculated as:

$$\Delta d = \frac{\Delta \omega}{\gamma G_x}$$

(1.25)

where $\Delta \omega$ is the difference in Larmor frequency and G_x is the gradient strength needed to achieve a certain voxel size in the x-direction and is proportional to the bandwidth of the RF pulse. Thus, the chemical shift displacement amount can also be summarized as:

$$\Delta d = d_x * \frac{\Delta \omega}{BW_x}$$

(1.26)

where d_x is the voxel length in the x-direction and BW_x is the bandwidth of the RF pulse in the x-direction. For example, applying an RF pulse to target the water spins at 4.68 ppm in a specific slice also excites neighboring 2.0 ppm NAA spins. Because of the frequency difference between the water and NAA (~343 Hz at 3T), the excited slices for each compound are offset from one another as shown in Figure 1.14. For a slice 3 cm in length and a RF pulse bandwidth of 1250 Hz, this amounts to a shift of 0.82 cm between the NAA and water box. The spatial displacement of the volumes results in the edges of the volume having different ratios of metabolites relative to

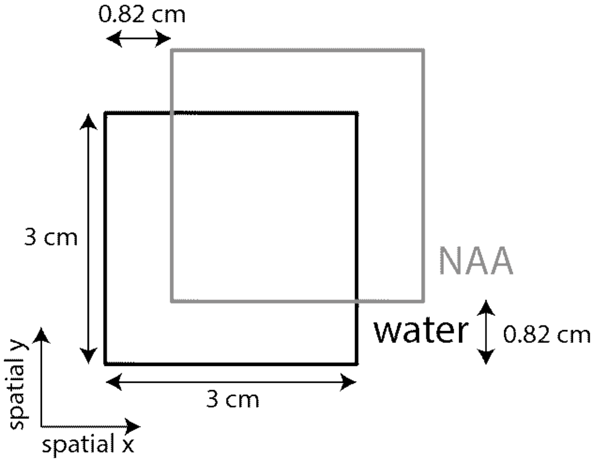

Figure 1.14. Spatial displacement of the NAA and water volume in the x and y refocusing pulse directions due to chemical shift. This effect is demonstrated for a voxel length of 3 cm in the x and y directions and a refocusing pulse bandwidth of 1250 Hz. The displacement of the NAA box relative to the water due to chemical shift amounts to about 0.82 cm in both directions.

the very center of the volume which has an overlap between all the excited metabolites. This can be a problem for quantitation rising from tissue differences between the excited slices and B_0 and B_1 inhomogeneity over the different slices (11). This can also be an issue for volume pre-localization as volumes based on the water resonance can have contamination from adjacent lipids due to placing the volume too close to the scalp (11). This can be remedied, however, by placing the volume based on a resonance closer to the frequency of lipid such as the NAA singlet at 2.0 ppm (11).

1.13 Zero Filling

The spectral width (SW) of the spectrum is determined by the sampling rate of the signal digitization, and is equal to $1/\Delta t$ where Δt is the time between consecutive sample points (11). After Fourier transform, the spectrum also contains N points, and the spectral resolution Δv can be defined as SW/N. The spectral resolution Δv is also equal to $1/T_{acq}$ where T_{acq} is the total

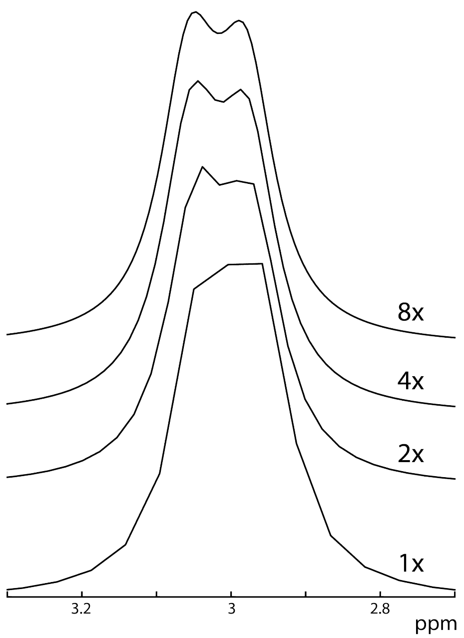

Figure 1.15. Simulated difference lactate 1.3 ppm doublet line-broadened to in vivo linewidths as a function of different zero-filling factors. As the zero-filling factor increases, the lactate resonance becomes increasingly more well resolved.

acquisition time (11). Since the total acquisition time is also equal to the number of sampling points times the duration of the sampling periods (Δt), the spectral resolution Δv can also be defined as (11):

$$\Delta v = \frac{1}{T_{acq}} = \frac{1}{N\Delta t}$$

(1.27)

The spectral resolution (in combination with the decay rate of signals) determines the ability to resolve resonances so that the amplitudes of each resonance can be discerned. According to the above equation, an increase in the effective acquisition time, T_{acq}, results in the frequency difference between points Δv decrease and a subsequent increase in the apparent spectral resolution. This can be increased during acquisition by either decreasing the spectral width or increasing the acquisition time. There is a limit, however, to the increase in spectral resolution achieved by decreasing the spectral width. In addition, increasing the acquisition time will increase the amount of noise present as the signal intensity decreases with acquisition time. In post-processing, however, the effects of increasing the acquisition time can be simulated through the process of zero-filling (11). This process artificially extends the acquisition time by adding zeros onto the end of the FID before Fourier transformation. In general, zero-filling can improve spectral appearance, but cannot add information to the spectral content (11). The effects of zero-filling on the spectral appearance can be seen in Figure 1.15 where the spectral appearance of the lactate doublet. In addition, zero-filling by one-fold results in an increase in the signal-to-noise ratio. Beyond one-fold, however, leads to only an improvement in the spectral appearance and not the SNR.

1.14 Linewidths

Peaks in the spectrum that arise from Fourier transformation of an exponentially decaying signal can be described by a Lorentzian lineshape. This complex lineshape has both absorptive and dispersive components to it, which are shown in Figure 1.16a. The dispersive component is the broader of the two and has a net integral of zero. Thus, the absorptive lineshape is preferred for resolving peaks in a spectrum.

In general, the phase of the acquired signal (and thus the spectrum) varies due to scanner hardware, and a mixture of absorptive and dispersive lineshapes are present. Taking the Fourier transform of the time-domain signal results in both real and complex signals which can be described as (11):

$$R(\omega) = A(\omega)\cos(\phi) - D(\omega)\sin(\phi)$$

$$I(\omega) = A(\omega)\sin(\phi) + D(\omega)\cos(\phi)$$

(1.28)

where A(ω) and D(ω) are the absorption and dispersion components of a Lorentzian lineshape respectively. This mixure of absorptive and dispersive lineshapes can be addressed by 'phasing the spectrum', that is calculating a complex mixture of R(w) and I(w), such that the real spectrum only contains absorptive lineshapes and the imaginary dispersion (11):

$$A(\omega) = R(\omega)\cos(\phi) + I(\omega)\sin(\phi)$$

$$D(\omega) = I(\omega)\cos(\phi) - R(\omega)\sin(\phi)$$

(1.29)

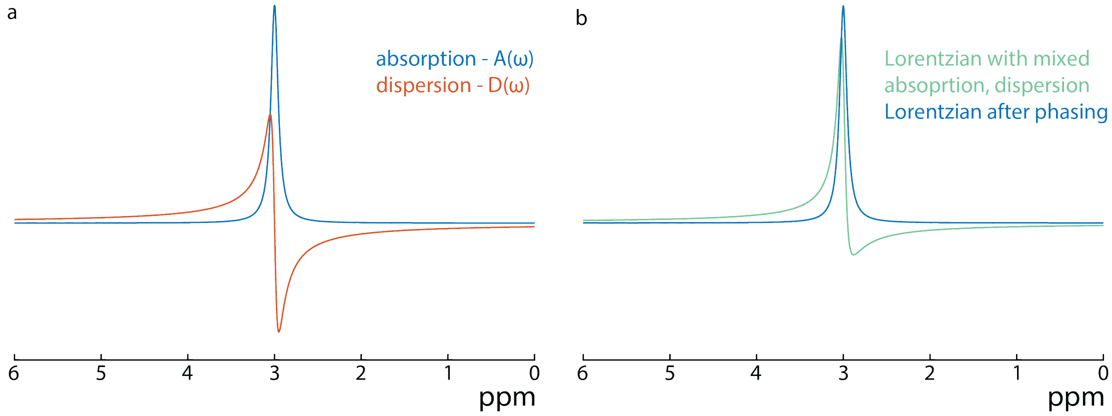

Figure 1.16. Fourier transform of an exponentially decaying FID results in a Lorentzian lineshape. (a) Absorption and dispersion components of the Lorentzian lineshape. (b) The phase of the FID is typically non-zero and thus the Lorentzian lineshape has both absorption and dispersion components. After phasing, the Lorentzian takes on a pure absorption lineshape. Figure based on reference 11.

This is called a zero-order phase correction. When there are hardware imperfections or timing errors, however, the phase can depend on the resonance frequency. To correct this, first-order phase correction is needed. This can be done by setting the corrected phase ϕ_c to be (11):

$$\phi_c = \phi_0 + (\omega_0 - \omega)\phi_0$$

(1.30)

The absorptive and dispersion components of the Lorentzian lineshape and the peak before and after phase correction are shown in Figure 1.16b.

In the phased (absorptive) lineshape, the peak is centered at some frequency while the width of the peak can be determined by calculating the width at half max (31). Because of the linewidth of the peaks, the closer the peaks get to each other, the more they overlap and at some point, they will merge until they're indistinguishable from one another figure 1.17. However, at what point they overlap does depend on the lineshape of the resonance as well as the linewidth (31). For example, lines with a width of 1 Hz become indistinguishable at lower frequency separations than lines with a width of 2 Hz (figure 1.17).

1.15 Time Doman Filtering

Apodization (or time-domain filtering) is often applied to the MR time domain signal. This is done by multiplying the signal by a filter function such as an exponential-weighted filter (11):

$$f_{filter}(t) = e^{-t/T_w}$$

(1.31)

This function improves the SNR of the frequency-domain signal by attenuating the low-SNR data points at the end of the FID and making the FID envelope decay more rapidly. Since the effective acquisition time is reduced, however, the effective spectral resolution is reduced as well and the lines in the spectrum are broader than the unweighted FID.

1.16 Scalar Coupling

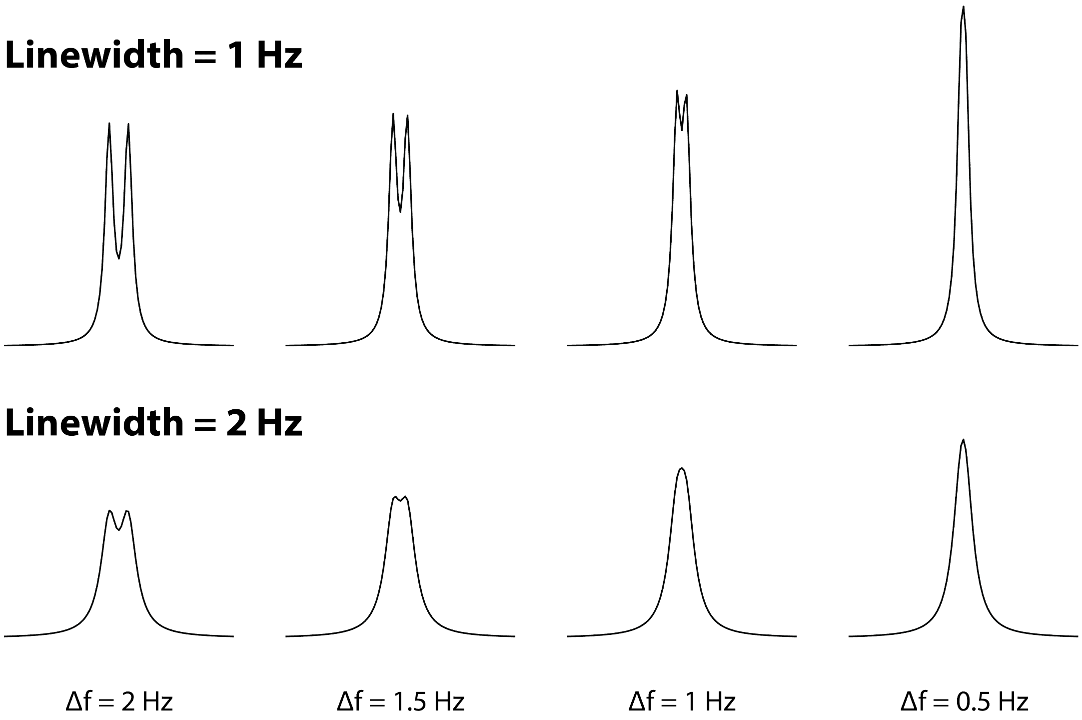

Figure 1.17. The effect of linewidth on the ability to resolve lines in a spectrum with decreasing frequency separation between the two lines. Lines with a linewidth of 2 Hz become more difficult to resolve at a larger frequency separation than lines with a smaller linewidth of 1 Hz. Figure based on reference 31.

In addition to the dispersion of resonances along the frequency axis due to chemical shift, resonances can also appear as multiplets, split into several lines, due to scalar coupling (also known as J-coupling or spin-spin coupling). The splitting due to coupling results from interactions between neighboring spins mediated through chemical bonds. The coupling magnitude J is independent of the magnetic field strength and is expressed in Hertz (Hz). A two-spin AX spin system, in which the frequency difference between the two spins $|\omega_A-\omega_X|$ is much bigger than the coupling constant between them (J_{AX}), is considered to be weakly coupled (11). If two nuclei are coupled, the signals in the spectrum will split into two lines (figure 1.18). Each line represents a different state of the coupled spin which adds or subtracts from the existing external magnetic field. This pattern of splitting is called a doublet. For a doublet, one line is associated

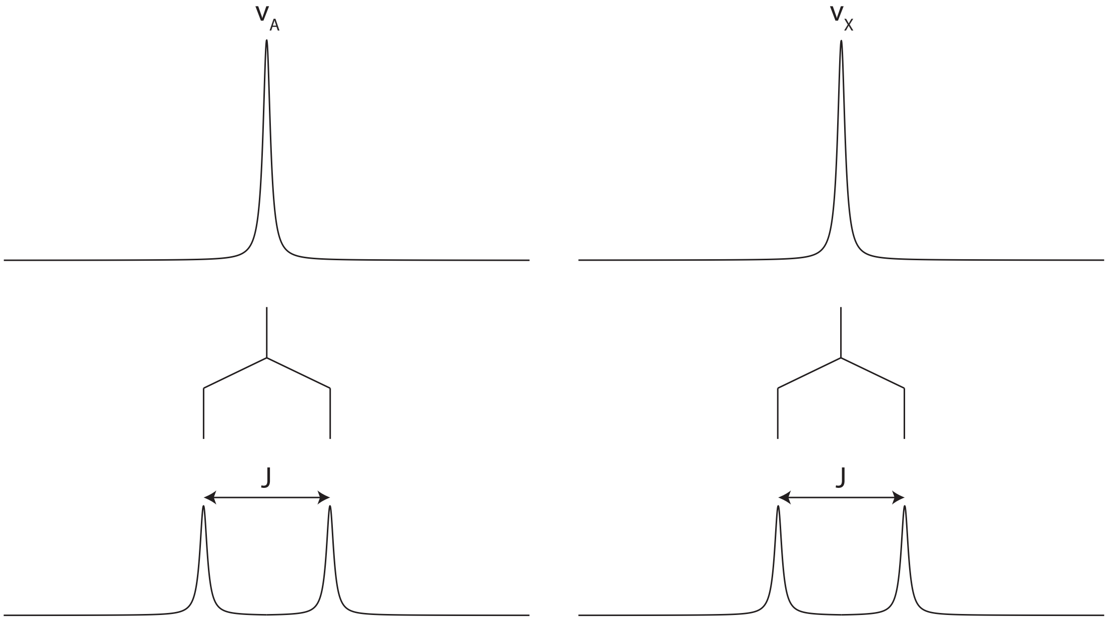

Figure 1.18. Scalar coupling between nuclei leads to singlet resonances splitting into doublets. Figure based on reference 11.

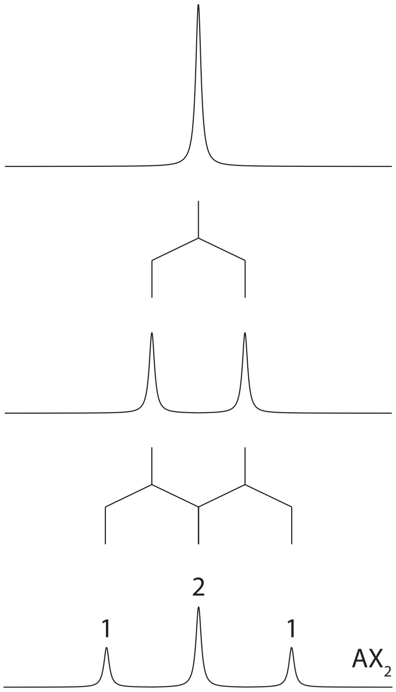

Figure 1.19. Successive splitting of an AX_2 spin system to form a triplet with a 1:2:1 ratio between its lines. Figure based on reference 11.

with the spin being in the up state while the other line is associated with the spin being in the down state.

The splitting characteristics in the spectrum are often times much more complicated than a doublet pattern, however. The splitting pattern can be predicted, though, based on the discrimination between chemically equivalent and magnetically equivalent nuclei. If two nuclei are magnetically equivalent, they have the same chemical shift and are coupled with the same constant to a third nuclei with a different chemical shift. However, if they are magnetically nonequivalent, they have differing scalar coupling constants to this third nuclei, they are considered magnetically nonequivalent. Complex splitting will occur if scalar coupling exists between nuclei pairs at the same chemical shift. If nuclei are magnetically equivalent, however, their spectral pattern can be predicted according to a binomial pattern where the lines of the multiplet are split according to their scalar coupling constant (11). For example, given an AX_n spin system, if $n = 2$, the spectral pattern can be predicted as a doublet splitting into three lines (triplet) that has an amplitude with a 1:2:1 ratio as shown in Figure 1.19. If $n = 3$, the spectral pattern will have amplitudes with a 1:2:2:1 and the triplet pattern will additionally split into four lines (quartet).

While it is convenient to estimate spin systems as being weakly coupled, many spin systems have a frequency difference that is on the same order of magnitude as the coupling constant and the system is considered to be strongly coupled. These strong coupling effects result in second-order spectra that need quantum mechanical density matrix calculations for simulation of the spectral multiplet as strong coupling changes the relative intensity of the peaks and frequency of resonances (11).

1.17 Spectral Editing

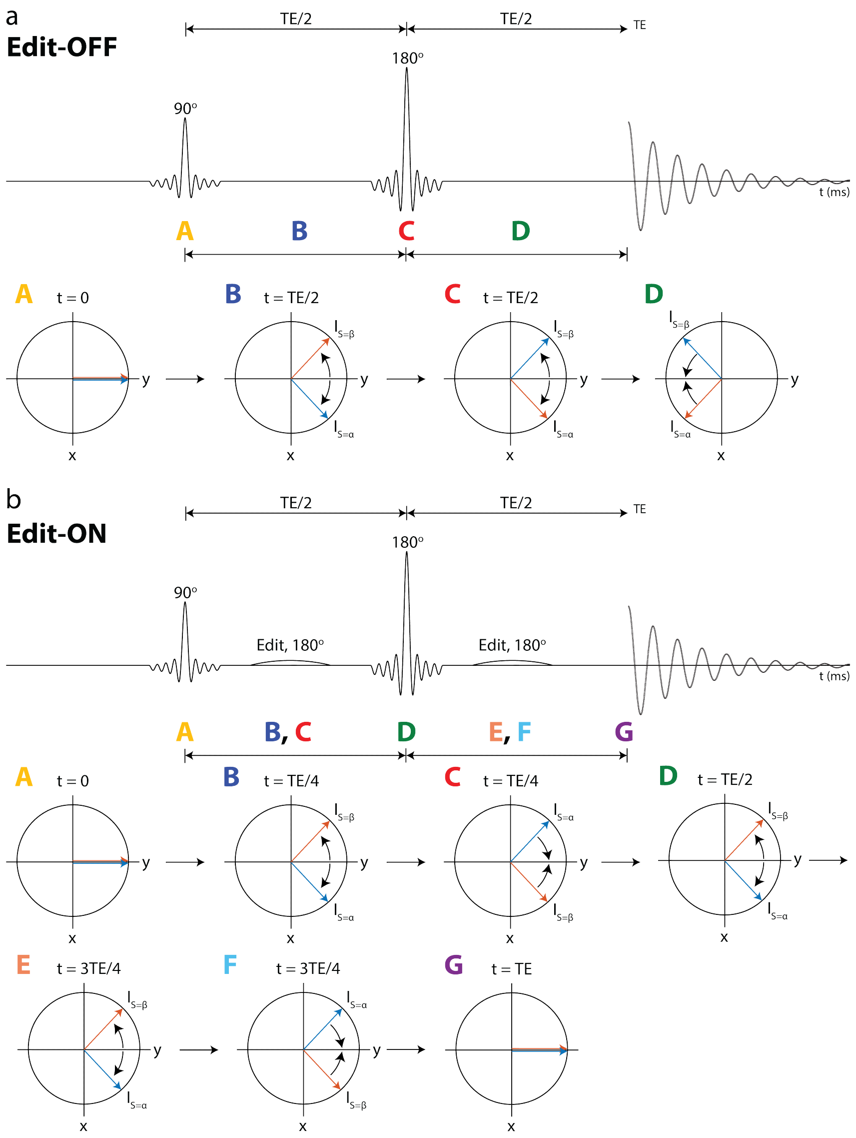

Figure 1.20. (a) Evolution of the scalar coupling for two spins: I and S during a spin-echo sequence (edit-OFF acquisition). After excitation, the I spin populations acquire phase relative to one another depending on the echo time specified. After the refocusing pulse, the phase of the I spin populations is inverted. However, the S-spin populations are inverted as well, leading to the I spins acquiring additional phase relative to one another. (b) Evolution of the scalar coupling for two spins: I and S during a spin-echo sequence with added frequency-selective editing pulses with a 180° flip angle (edit-ON acquisition). As in the edit-OFF case in (a), I spin populations acquire phase relative to one another after excitation depending on the echo time specified. However, after the editing and refocusing pulse, the phase of the I spin populations is inverted but the S-spin population stays the same. This leads to the I spins being refocused along the y-axis. Figure based on reference 11.

Not all metabolites can be detected reliably using conventional means due to spectral overlap from more concentrated metabolites with larger signals. Important metabolites for which this issue arises include GABA and GSH whose 3.0 ppm peaks are overlapped by the more concentrated Cr peak. To detect lower concentration metabolites, spectral editing is needed to simplify the spectrum by removing any overlapping signals. This is done by using the scalar coupling between adjacent protons within a chemical structure to distinguish between compounds. For example, GABA has spins that resonate at 1.9 ppm and 3.0 ppm as previously described in Table 1 that are coupled to one another. In a conventional spectrum, GABA is difficult to distinguish as it is obscured by the significantly larger Cr peak. However, GABA can be separated from the rest of the spectrum by differentially affecting it's 3.0 ppm spins by playing an editing pulse at its coupled 1.9 ppm spins.

1.17.1 J-difference Editing

The most commonly used spectral editing method is J-difference editing. Figure 1.20 shows a diagram of a typical J-difference editing pulse sequence with spin-echo localization. It can be seen that after the 90° excitation pulse and before and after the 180° refocusing pulses of spin-echo pulse sequence, frequency-selective editing pulses are used. A typical J-difference editing experiment has 2 sub-acquisitions: an edit-OFF and an edit-ON acquisition. In the edit-ON acquisition, these editing pulses are applied to one of the spins of a metabolite of interest to affect its coupled spin. In the edit-OFF acquisition, these editing pulses are placed OFF resonance with respect to the metabolite of interest. When the spectra from the two sub-acquisitions are subtracted from one another, overlying signals are subtracted away revealing a reduced spectrum containing your metabolite of interest.

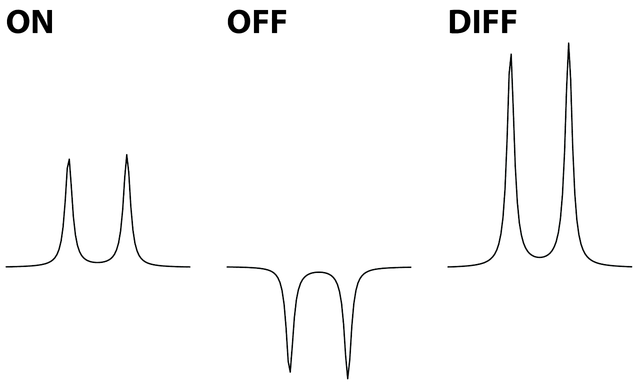

Figure 1.21. The lactate resonance at 1.3 ppm and an echo time of 144 ms. In the edit-ON case, coupling is completely refocused and the lactate resonance appears as a doublet. In the edit-OFF case, coupling is allowed to evolve and the lactate resonance appears as an inverted doublet. Subtracting the two sub-acquisitions from one another results in a difference multiplet (DIFF) with twice the area as either the doublet in the ON or the OFF.

Figure 1.21 depicts the evolution of a two-spin system during a J-difference editing sequence where the observed (I) and remote (S) spins have a lower (α) and higher (β) energy state respectively. In the edit-OFF case (Figure 1.20a), spins in the transverse plane are initially in phase with one another after excitation (11). With time, the $I_{s=\alpha}$ and $I_{s=\beta}$ spin populations acquire phases in directions opposite to one another as the I spins attached to the S spins in the α state resonate at a lower frequency than I spins attached to the S spins in the α state resonate at a lower frequency than I spins attached to the S spins in the β state (11). This phase difference is proportional to the J-coupling constant. Once the 180-degree refocusing pulse is applied, both I and S spins are inverted, and the acquired phase is inverted. Consequently, evolution of coupling continues during the second half of the spin echo and the two I-spin populations obtain a net phase difference at the top of the echo (11).

In the edit-ON case, spins in the transverse plane start out in phase with each other as in the edit-OFF case. The I spins then acquire an echo time dependent phase until TE/4 when a selective 180° editing pulse is applied (Figure 1.20b). Since the editing pulse only affects the observed I spin but not the remote spin so the I spins are completely refocused along the y-axis (11). When the spins then experience the refocusing pulse at TE/2, both I and S spins are inverted and the phase of the I spins is reversed. Evolution of coupling continues for another TE/4 until another selective editing pulse is applied which results in the I spins being refocused at the top of the echo (11).

The echo time at which the multiplet is completely refocused depends on scalar coupling constant (J) between the observed and remote spins. For a 3-bond chemical structure, this is at 1/2J while doublet-like signals edited at 1/J. This estimation becomes uncertain, however, in the presence of strong coupling effects and require quantum mechanical density matrix simulations.

Subtracting the two sub-acquisitions from each other results in a reduced spectrum containing only those signals impacted by the editing pulses. This technique has been used to detect several important metabolites such GABA, GSH, and Lac and can be seen illustratively for the example of editing Lac shown in figure 1.21. Lactate has two resonances that are coupled to one another: a doublet at 1.3 ppm and a quartet at 4.1 ppm. J-difference editing is commonly used to detect Lac as due to its low concentration by placing an editing pulse at its 4.1 ppm in the edit-ON acquisitions to affect its coupled spins at 1.3 ppm. Figure 1.21 depicts the 1.3 ppm Lac multiplet in the edit-ON case and in the edit-OFF case at an echo time of 144 ms (≈1/J where J = 6.93 Hz). In the edit-ON case, coupling is refocusing at the top of the echo and thus the 1.3 ppm Lac resonance takes on doublet lineshape. In the edit-OFF case, however, coupling evolves in the second half of the echo. Subtracting the two sub-acquisitions results in a DIFF in which the 1.3 ppm peak appears as a doublet.

Similar principles can also be applied to editing other metabolites with more complicated structures. in example GABA-edited data in one subject as shown in Figure 1.22. In a typical

GABA-editing experiment, an edit-ON pulse is placed at 1.9 ppm which modulates the shape of the signal at 3.0 ppm, while in the edit-OFF acquisition, the editing pulse is placed OFF resonance for GABA (figure 1.22a). Uncoupled resonances, like creatine, do not have scalar coupling and are unaffected by the editing pulses. Thus, the Cr peak is the same in the ON and the OFF acquisition and is thus subtracted out when the OFF is subtracted from the ON and a GABA peak is unveiled at 3.0 ppm in the DIFF spectrum (figure 1.22b). Thus, J-difference editing allows for a select observation of a few metabolites without minimal impediment from nearby resonances.

1.18 Editing design considerations

Although the principle of J-difference editing has been introduced, actual implementation of J-difference editing has many practical considerations such as the choice of which resonance to edit and which to observe, co-editing of adjacent resonances, and pulse sequence timings. Some considerations of acquisition parameters will be discussed here using editing GABA as an example.

1.18.1 Selection of edited and observed resonances

Since J-differencing editing is an inherently low SNR technique, the number of protons in the detected resonance must be taken into consideration as it is directly related to the signal intensity of the resonance. As it turns out, each of the individual GABA resonances as shown in figure 1.23 have the same number of protons, and thus, the same signal integral. However, editing the H2-methylene protons ~2.28 ppm by targeting its coupled H3 multiplet at ~1.9 ppm (figure 1.23) is difficult since the editing pulse bandwidth often includes glutamate and glutamine resonances at ~2.1 ppm whose coupled resonances at ~2.4 ppm overlap with the GABA ~2.28 ppm resonances. In addition, it is undesirable to detect the 1.9 ppm resonance due to its decreased intensity originating from its multiple coupling partners. Since at a glance, the H4 GABA resonance at 3.01 ppm only overlaps with the Cr singlet resonance, it can be considered a good candidate for editing and is the most commonly edited GABA resonance (11, 32, 33). However, the 3.0 ppm GABA peak also overlaps with a macromolecule peak whose coupled resonance at 1.72 ppm is included in the envelope of the 1.9 ppm editing pulse (19, 33-35) and is thus co-edited in the edited spectrum. In many studies, this macromolecule contamination is accepted and the edited 3.01 ppm peak is referred to as GABA+MM or GABA+. Although it has been

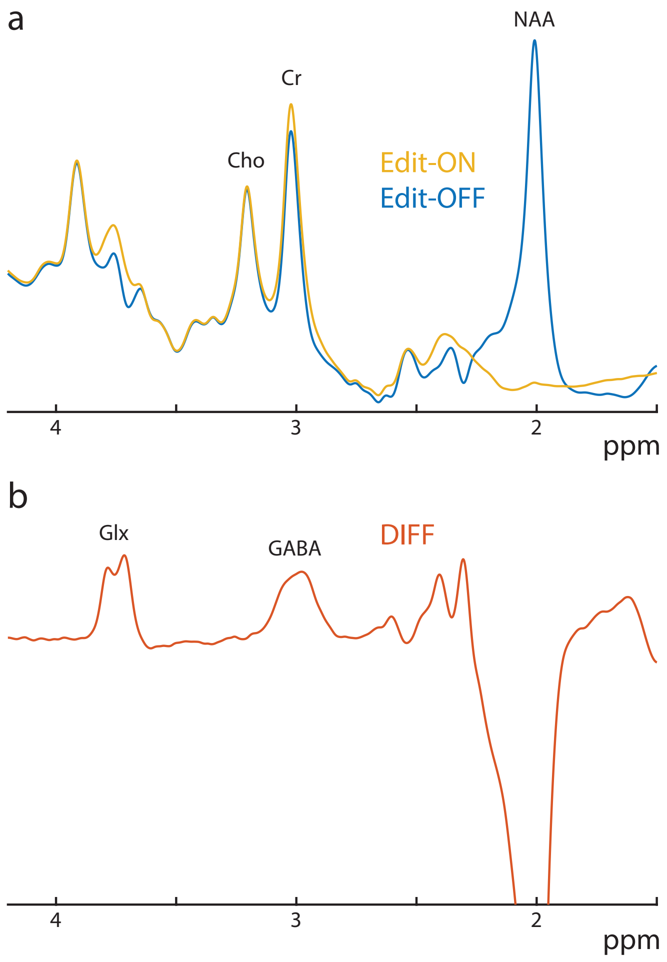

Figure 1.22. (a) Example ON and OFF spectra taken from an in vivo GABA-edited acquisition. The ON and OFF spectra look similar to one another except at frequencies of coupled spins affected by the edit-ON pulse such as GABA at 3.0 ppm. Subtracting the two sub-acquisitions from one another results in an DIFF spectrum with a clear GABA peak at 3.0 ppm.

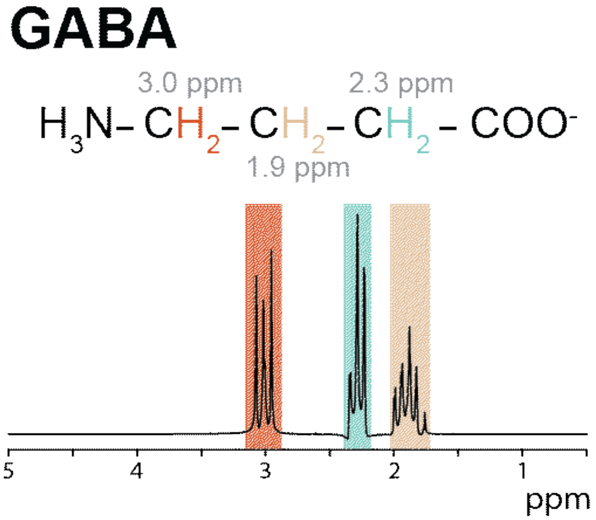

Figure 1.23. The GABA molecule and corresponding resonances along the ppm axis. GABA has protons that resonate at 3.0 ppm. 2.3 ppm, and 1.9 ppm. Typically editing of GABA is performed by placing an editing pulse at 1.9 ppm to affect its coupled spins at 3.0 ppm.

shown that this macromolecule content does not change between tissue type, it is uncertain as to whether these measurements are correlated especially in aging or disease states (36-38).

1.18.2 Editing pulses

Since selective targeting of a metabolite resonance is necessary in order to isolate its spectrum, sinc-Gaussian pulses. These pulses are typically placed TE/2 apart from one another in the sequence so that coupling evolution is fully refocused at the top of the echo in order to maximize editing efficiency. In addition, these pulses often have bandwidths on the order of tens of hertz so to target a small range of resonances. For the example of GABA-editing, an editing pulse of a duration of 14 – 20 ms and a bandwidth ~60 Hz, is often used. This allows for a select range of spins from 1.66 ppm to 2.13 ppm incorporating the 1.9 ppm GABA spins to be affected by the editing pulse. For more selective editing of a particular metabolite, more selective editing pulses are desired. However, there are a couple of downsides to this increase of selectivity. In order to obtain more selective editing pulses, longer-duration editing pulses are needed. This may not be feasible if the optimal echo time for maximal signal intensity is too short to incorporate these long-duration editing pulses. In addition, the resonant frequency can change significantly over time due to gradient heating/cooling over the course. This is often referred to as "frequency drift" or "B_0 drift" and can lead to loss of editing efficiency due to the editing pulse being played off resonance relative to the actual frequency of the spins.

1.18.3 Frequency drift

In addition to decreasing the editing efficiency frequency drift can result in subtraction artifacts as illustrated for GABA-editing in figure 1.24. This originates from the fact that the frequency offset of the peaks in the spectrum changes from average to average in the presence of frequency drift. Thus, when the OFFs are subtracted from the ONs, resonances that should be subtracted away from the spectrum instead leave a residual peak in the spectrum which is a problem for

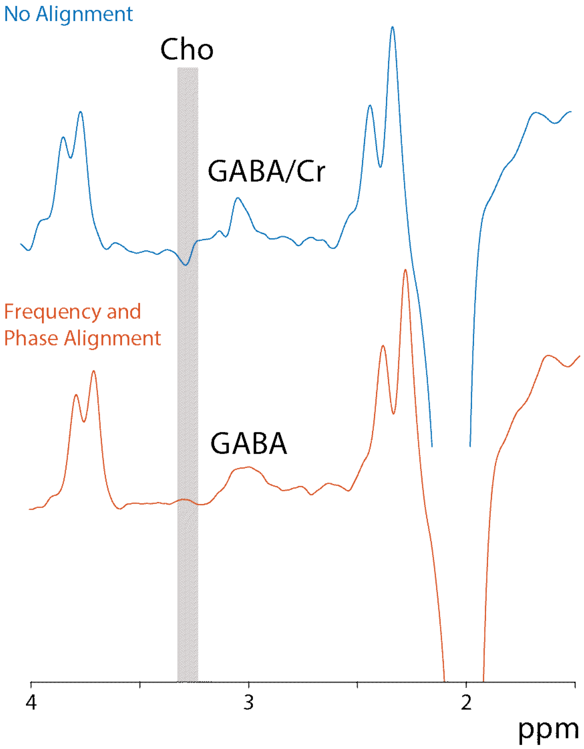

Figure 1.24. MM-suppressed GABA-edited spectra before and after frequency and phase alignment. With no alignment, a Cho subtraction artifact can be seen ~3.2 ppm which is largely removed after performing frequency and phase alignment.

quantification when the subtraction artifacts overlap with the edited peak of interest. For example, frequency offsets between the Cr singlet in the ON and the OFF subspectra result in a subtraction artifact at 3.0 ppm where the edited GABA peak is at. Since NAA is suppressed in the GABA-ON spectrum, the subtraction artifacts can be assessed by the appearance of a residual Cho peak at 3.2 ppm.

Frequency drift can be reduced prospectively by interleaving unsuppressed water acquisitions, measuring the center frequency of the water peak, and correcting the resonant frequency to the measured water frequency after each water-unsuppressed average (39, 40). This can also be corrected for in post-processing as well using phase- and frequency- correction techniques to align subspectra to one another (41-44). Although these post-processing techniques cannot make up for the loss in editing efficiency due to frequency drift during the scan, these techniques can reduce the appearance of subtraction artifacts in the difference spectrum. This is demonstrated for the example of MM-suppressed GABA editing as shown in figure 1.24. With no frequency

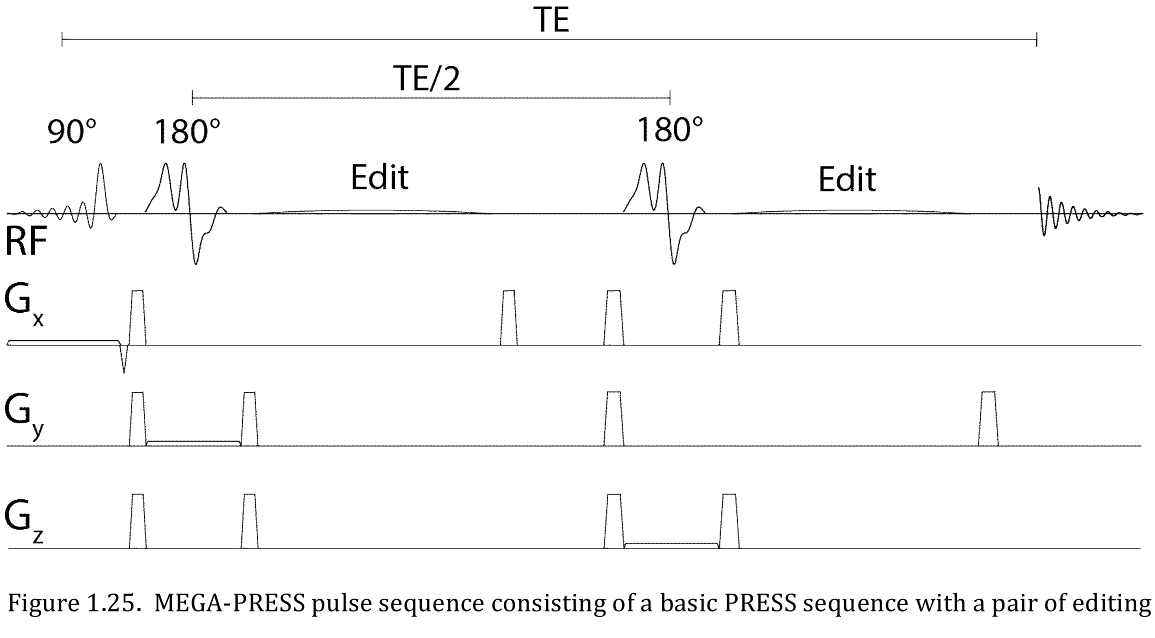

Figure 1.25. MEGA-PRESS pulse sequence consisting of a basic PRESS sequence with a pair of editing pulses straddling the second 180° refocusing pulse.

alignment, a Cho subtraction artifact can be seen about 3.2 ppm. This is largely removed, however, with frequency and phase alignment (44).

1.18.4 PRESS sequence

Although J-difference editing was discussed earlier in terms of the spin-echo pulse sequence, J-difference editing with single-voxel localization is typically done in conjunction with a PRESS pulse sequence. The resulting pulse sequence is referred to as MEGA-PRESS and is shown in figure 1.25.

In MEGA-PRESS the timings of the slice-selective RF pulses are fundamental for successful implementation of J-difference editing. The echo time of a PRESS sequence can be broken down into two subecho times: TE1, the duration of the first spin echo, and TE2, the duration of the second spin echo. Typically, TE1 is kept short so minimize excitation of multiple-quantum coherence pathways. The duration of TE1, however, can vary depending on a number of factors including the maximum B1 strength, gradient strength, and slice-selective RF pulse duration. Appearance of J-couple metabolites can change significantly depending on the relative values of TE1 and TE2 (45).

Another important element is the choice of slice-selective RF pulses. One important property of RF pulses to consider is its slice profile or how rectangular of a slice can be generated by the RF pulses. This affects both the signal intensity of final spectrum as well as the appearance of the spectral multiplet (46), a difference that is most apparent in phantom acquisitions which have more narrow linewidths due to longer T2 values. Another important property is the bandwidth of the PRESS volume selection pulses. Due to the frequency difference between J-coupled spin partners, the edited and observed spins are not affected equally by the slice-selective RF pulses (46). Since the slice-selective excitation pulse generally has a large bandwidth, chemical shift effects can be largely ignored in the slice-selective excitation direction. However, refocusing pulses typically have lower bandwidths which affects the edit-OFF scan and leads to a loss in edited signal intensity known as a the “4-compartment artifact” (46). The severity of this signal loss depends on the frequency difference between coupling partners relative to the bandwidth of the refocusing pulses. Thus, signal loss due to the 4-compartment artifact can be minimized, with the use of high bandwidth pulses to reduce the portion of the localized volume consisting of unwanted signal modulations (47).

1.18.5 SNR considerations

Ideally, an arbitrary sized and shaped voxel can be used to target any region of interest with single-voxel spectroscopy. In general, however, the shape of the voxel is limited to a rectangular box due to the slice-selective RF pulses used in the MEGA-PRESS sequence. Due to the inherently low SNR of the metabolites measured with J-difference editing, the voxel must be big enough to obtain a reliable measure. In general, voxels on the order of 3 x 3 x 3 cm^3 are sufficient to obtain adequate signal quality (42). For edited spectroscopic imaging, however, smaller voxels are often prescribed to increase the k-space sampling rate and reduce bleeding from adjacent voxels.

In addition to acquiring data from a relatively large voxel, hundreds of averages are typically acquired to obtain sufficient SNR. For maximal SNR gains, however, it is better to increase the voxel size than to increase the number of averages as SNR only increases with the square root of the number of averages.

1.18.6 Referencing

Since the amplitude of the MR signal can depend on various factors such as acquisition-specific parameters such as the type of RF pulses use and loading on the RF coil, results are typically reported relative to an internal concentration reference (48). This enables the comparison of data between sites with different hardware and acquisition parameters and facilitates biological interpretations (48). A common internal reference compound is water as it is relatively uniformly distributed throughout the brain and changes little in pathological conditions (48). Because of this, several water-unsuppressed averages are often acquired to aid with quantitation of the edited signal.

1.19 Lipid and Water Suppression

In vivo, metabolites of interest are present at relatively low concentrations and thus have significantly lower signal intensities relative to water and lipids originating from the scalp. Without proper suppression of these contaminating signals, accurate detection of endogenous metabolites is difficult. Thus, multiple ways of suppressing these compounds have been developed.

1.19.1 Volume Localization

One of the most common methods of performing lipid suppression is through volume localization which takes advantage of the spatial distribution of the lipids relative to the rest of the brain where the metabolites are measured. This method can be divided into two different types of techniques: outer volume suppression, and one that affects the magnetization so that any unwanted magnetization outside of the VOI would be removed, also known as single volume localization.

Single volume localization is typically performed using the slice-selective RF pulses such as the ones from the basic PRESS sequence described previously. These pulses are made slice-selective by the pair of crusher gradients on either side of the RF pulses which refocuses any signal

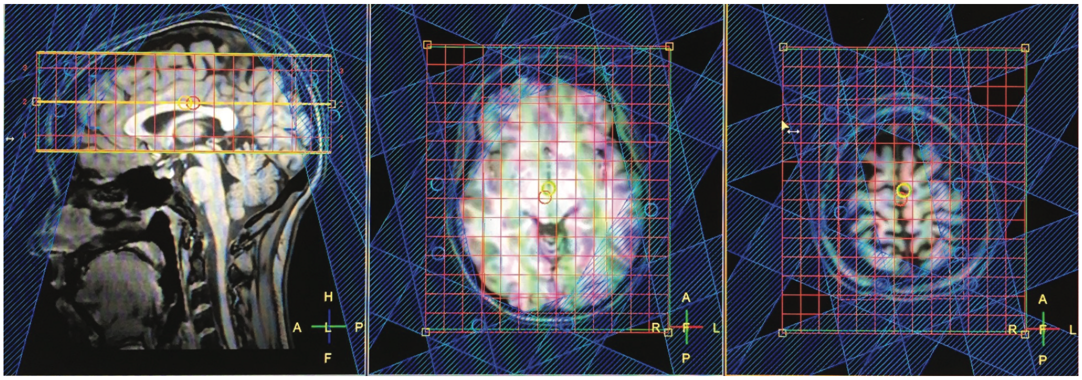

Figure 1.26. Placement of a multi-slice MRSI acquisition field-of-view (red) on a sagittal slice (left) and axial slices (right two) from a T1-weighted image and 8 OVS pulses (blue) placed elliptically at the scalp to suppress unwanted lipid resonances.

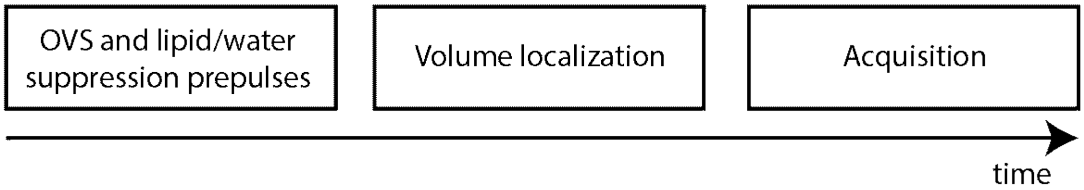

Figure 1.27. Timing of each of the individual pulse sequence modules. Any OVS and lipid/water suppression prepulses is then followed by volume localization and data acquisition.

affected by RF pulse and dephases signals that aren't. Volumes can be placed so that lipids located at the scalp are dephased by the crusher gradients (11). As a consequence of volume-localization, however, imperfect slice profiles and chemical shift displacement effects are emphasized (11).

Outer volume suppression (OVS) also uses a principle similar to volume localization. However, instead of localizing a volume from which a metabolite signal is detected, slices at the lipid-rich edges of the brain are excited and transverse magnetization is dephased by crusher gradients. Example placement of these OVS pulses can be seen in figure 1.26. Once OVS is performed, metabolite and water spins within the brain can be excited with minimal lipid contamination. Imperfect OVS suppression of lipids can occur, however, due to B_1 field inhomogeneity and lipid

T_1 relaxation times. With B1 field inhomogeneity, the OVS pulses fail to achieve a perfect 90 degree pulse needed to excite all the lipids to the transverse plane. And because of lipid T1 relaxation, some of the longitudinal lipid magnetization can recover prior to slice-selective excitation (11).

1.19.2 Saturation/inversion prepulses

Additional lipid suppression can be achieved with chemical-shift-selective prepulses played out prior to signal acquisition (49, 50). These lipid suppression sequences consist of frequency-selective saturation and/or inversion prepulses at the 1.3 ppm lipid peak prior to signal acquisition. The large water peak at 4.68 ppm can be suppressed using a similar fashion with frequency-selective presaturation and/or inversion prepulses. Some commonly used sequences include inversion recovery sequences (51), CHESS (52) which relies on pre-saturation pulses to dephase the transverse signal, and WET (53) which also relies on pre-saturation, but compensates for B1 variations by choosing prepulses with optimized flip angles. The most commonly used sequence is VAPOR (54) which is a combination of both inversion recovery and pre-saturation and consists of 7-8 optimized flip angles and delays to compensate for a large range of B1 variations and water T1 relaxation times. Figure 1.27 shows the relative timings of the difference sequence modules with OVS and suppression prepulses followed by volume localization and data acquisition.

1.19.3 Removal of Residual Water

With good shimming, most of the large water resonance can be reduced to 1% or less of the unsuppressed water peak (55). However, for MRSI scans and for single voxel cases in certain regions of the brain, the magnetic field can be quite inhomogeneous which can result in a large residual water peak. Much of this signal can be removed in post-processing, and while there are many post-acquisition methods that can remove this water peak, the most reliable method is single value decomposition (SVD) of the FID. This is made possible by the fact that the largest singular value is the largest resonance in the spectrum. When SVD is performed and the singular values corresponding to the water region are selected and reconstructed, a spectrum resembling the isolated water resonance can be reconstructed. Subtracting the reconstructed water peak from the spectrum results in a spectrum with a reduced residual water peak.

1.20 Imaging

Single-voxel pulse sequences are useful if it is desirable to probe a specific region of interest. Multi-voxel or imaging techniques are needed in situations where the affected area is unknown or if several areas are of interest.

1.20.1 Frequency and Phase Encoding

Once a slice is selected, spatial location in the other two directions still needs to be encoded with gradient fields. In a typical imaging acquisition, a gradient can be applied in one of the other two axes for frequency encoding after excitation. Typically, this is performed during the acquisition period. A gradient is switched on during the sampling period so that spins along a particular axis resonate at different frequencies. If the gradient is in the x-direction, the frequency of the spins as a function of x is (20):

$$\omega = \gamma(B_0 + xG_x)$$

(1.32)

Although the signal received is the sum of the signals coming from all the x-coordinates, the signal from each spatial location can be demodulated by taking the Fourier transform of the signal.

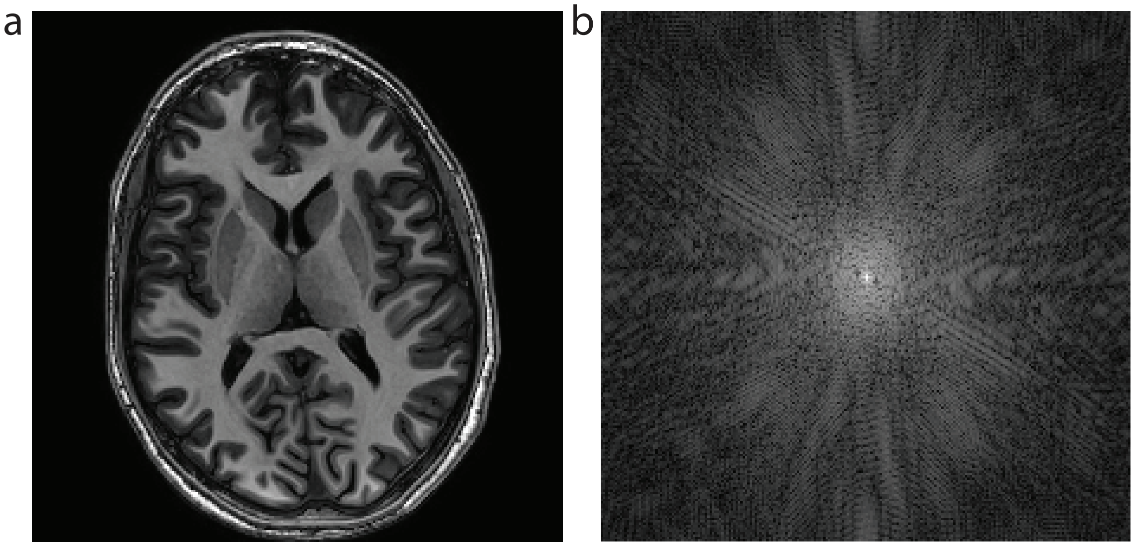

Figure 1.28. Example T1-weighted image of a slice across the brain (a) and its representation in k-space (b) before 2D Fourier transformation.

To obtain spatial information from the second dimension (for example, y-coordinate), phase encoding with a magnetic field gradient is used. Phase encoding is similar to frequency encoding, however, instead of using a gradient to encode the frequency of the spins, the phase of the magnetization is encoded as a function of position (11). Typically, a phase encoding gradient is turned on for a given amount of time after slice excitation and before signal readout and phase. Since phase is the integral of frequency over time, different amounts of phase are accrued as a function of the y-coordinate. In order to differentiate between signals at different y-coordinates, however, additional acquisitions with different phase encoding gradients are needed so that different amounts of phase accrued at each y-position. By repeating the acquisition N_{PE} times, spins in N_{PE} locations can be differentiated with a Fourier transform over all the acquisitions with different phase encoding gradients.

Both frequency and phase encoding are often used in non-spectroscopic imaging sequences. Since the compounds measured with spectroscopy are detected along the frequency axis, however, MR spectroscopic imaging sequences typically use phase encoding in both spatial dimensions.

1.21 K-space

K-space is a representation of the spatial frequency transform of an object (figure 1.28). In a typical MR imaging sequence, the vectors all point in the same direction. Since all the vectors have the same phase, they sum up coherently and their value is equal to that of the magnetization in the volume. Spatial dependence can be induced, however, by imposing an additional linear field gradient. Once all of k-space is covered, the distribution of the spins can then be determined from the frequency content of the MR signal by taking the Fourier transform.

With no gradients, the magnetization vector has a phase of 0 in both the x and y directions. After turning on a y-gradient, the spins further away from the center of the gradient precess at higher frequencies. After the gradient is left on for a given amount of time, increasing amounts of phase are accrued with y-position. This gradient can be described according to the following equation (23):

$$G_y = \frac{\partial B_z}{\partial y}$$

(1.33)

When this linearly varying field is added to a static field, the y-component of the field can be defined as (23):

$$B_y(y, t) = B_0 + zG(t)$$

(1.34)

Plugging this into equation 1.1, we get the following equation (23):

$$\omega(y,t) = \omega_0 + \omega_G(y,t)$$

(1.35)

where $\omega_y(y,t) = \gamma y G(t)$. The accumulated phase over a time interval t can be defined as (23):

$$\begin{aligned}\phi_G(y,t) &= \int_0^t \omega_G(y,t')\,dt' \\ &= -\gamma y \int_0^t G(t')\,dt'\end{aligned}$$

(1.36)

From this, the signal at the end of the interval can be calculated to be (23):

$$s(t) = \int_0^t \rho(y) e^{i\phi_G(y,t)}\,dy$$

(1.37)

This signal equation can expressed in terms of its spatial frequency (k) with $k_y = -\gamma \int_0^t G(t')\,dt'$ and rewritten as (23):

$$s(k) = \int_0^t \rho(y) e^{-i2\pi k_y y}\,dy$$

(1.38)

In the case where a gradient is applied with a constant amplitude over a given time interval, the k-value would be equal to (23):

$$k_y = \gamma G t$$

(1.39)

If G_y is left on for a longer period, the signal in the y-direction accumulates more phase of a higher spatial frequency k_y. Data are acquired at different points in k-space in two or three directions to cover a large enough range so that position in image space is encoded.

1.21.1 2D Gradient Echo Example

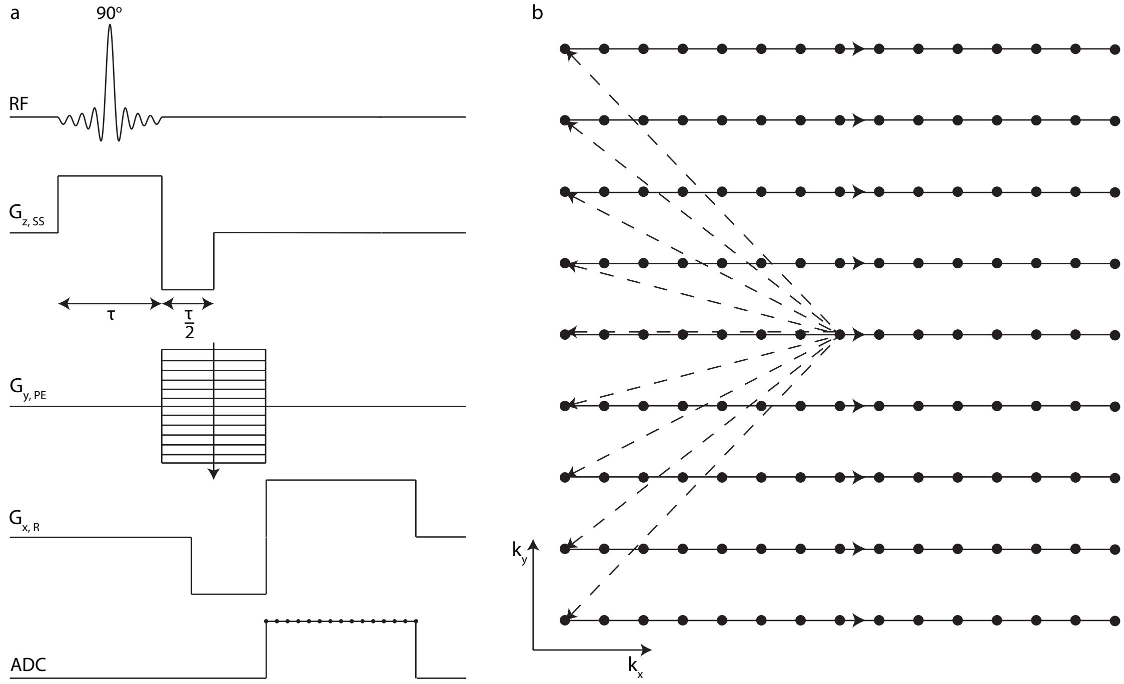

Figure 1.29. (a) Example 2D gradient echo pulse sequence. An excitation pulse is followed by a rephrase gradient in the z-direction played at the same time as the phase encoding gradient and prewind gradient in the y and x directions respectively. After that, a gradient in the readout direction (x) is played out and data is sampled (represented by the black dots in the ADC). (b) Corresponding k-space sampling scheme in the phase encoding (k_y) and refocusing (k_x) directions. While the phase encoding gradient and readout prewinder are being played out, k-space moves to the k_x, k_y point determined by the gradients. Data is then sampled in the x-direction during readout. Figure based on reference 23.

K-space sampling and coverage can be illustrated using a gradient echo sequence Figure 1.29a as shown in Figure 1.29b. In this example, the slice select gradient is in the z-direction while the two imaging directions are in the x and y directions. Thus, the phase encode and frequency encoding gradients are in the y-axis and x-axis respectively.

During the excitation pulse, a z-gradient with a constant amplitude is played out for a time τ_{rf} and then another gradient on the same axis is played out with opposite polarity to rephase the spins from the slice. In order to ensure the spins are rephased, the area under the second gradient must be half of that of the first gradient. Thus, in this case, $G_{rephase}$ must be equal to $-G_{SS}$ and must be on for a time $\tau_{rf}/2$. The signal from the entire slice at the end of the rephase gradient can be calculated as (23):

$$s(\tau_{rf}) = \int\int dxdy \left[\int_{z_0-\frac{\Delta z}{2}}^{z_0+\frac{\Delta z}{2}} p(x,y,z)\,dz\right]$$

(1.40)

The spin density can then be probed in the x and y direction with the application of a series of gradients in each direction. Once the slice select gradients are turned off, a boxcar phase encoding gradients can then be applied, labeled $G_{y,PE}$ in the y-axis as shown in Figure 1.10a. After the gradient is played for a given time, τ_{PE} and the signal can be defined as (23):

$$s(\tau_{rf} + \tau_y) = \int \left[\int \left[\int_{z_0-\frac{\Delta z}{2}}^{z_0+\frac{\Delta z}{2}} p(x,y,z)\,dz\right] e^{-i2\pi\bar{\gamma}G_y\tau_y y}\,dy\right] dx$$

(1.41)

In subsequent acquisitions of the sequence the amplitude of G_y can be varied in a stepwise fashion with increments of ΔG_{PE} so that over the acquisitions, information about the y-dependence of the spin density can be obtained. A read gradient can then be applied afterwards in the x-direction during data acquisition for frequency encoding. This gradient, G_x, consists of a negative dephasing lobe followed by a positive read rephrasing lobe during which the signal is measured. With $t' = t - T_E$, the signal can be calculated as (23):

$$s(t', G_y) = \int \left[\int \left[\int_{z_0-\frac{\Delta z}{2}}^{z_0+\frac{\Delta z}{2}} p(x,y,z)\,dz\right] e^{-i2\pi\bar{\gamma}G_y\tau_y y}\,dy\right] e^{-i2\pi\bar{\gamma}G_x t' x}\,dx$$

(1.42)

with $-T_S/2 < t' < T_S/2$. Putting the signal equation in terms of k-space values: k_x and k_y, we can rewrite the equation as (23):

$$s(k_x, k_y) = \int \int \left[\int_{z_0 - \frac{\Delta z}{2}}^{z_0 + \frac{\Delta z}{2}} p(x, y, z)\, dz \right] e^{-i2\pi(k_x x + k_y y)} dx dy$$

(1.43)

Suppressing the z-dependence with a slice centered z_0, this equation can be simplified to (23):

$$s(k_x, k_y) = \int \int p(x, y, z_0) e^{-i2\pi(k_x x + k_y y)} dx dy$$

(1.44)

Thus, at each average, data is acquired at a different k_y point and a line of k_x points during the read gradient, and stepped changes in G_y in subsequent acquisitions allow for different lines of k-space to be sampled. This is illustrated in Figure 1.28b (23).

1.21.2 Basic MRSI sequences

PRESS-MRSI

Spectroscopic imaging with PRESS localization is performed similarly to single-voxel PRESS acquisition except with added phase encoding gradients in two of the localizing directions. These are incremented with each average so that all of k-space is sampled over all the acquisitions. Taking the 2D Fourier Transform over each time point results in a FID point at each spatial location. A spectrum can then be formed by taking the Fourier Transform over time.

One limitation of PRESS-MRSI, however, is that signal detection is limited to the cuboid defined by the slice-selective RF pulses. This places a limitation on the areas of the brain one is able to detect signals from; for example, with PRESS-MRSI, regions located at the edge of the brain would not be included in the PRESS volume of interest (VOI) which limits its ability to acquire data from important cortical brain regions (8).

Spin-Echo MRSI

The limitation of the PRESS VOI can be mitigated using different localization techniques such as the spin-echo pulse sequence which consists of a 90° excitation pulse followed by 180° refocusing pulse. Neither of these pulses are slice selective and thus allows for the detection of signals coming from the edge of the brain in addition to those coming from the center of the brain.

1.21.3 Spatial Resolution

The nominal voxel size in a MR spectroscopic imaging acquisition can defined as the field-of-view divided by the number of phase encoding gradient increments in that direction. However, the true voxel size is often larger than this calculated size due to characteristics of the Fourier Transform.

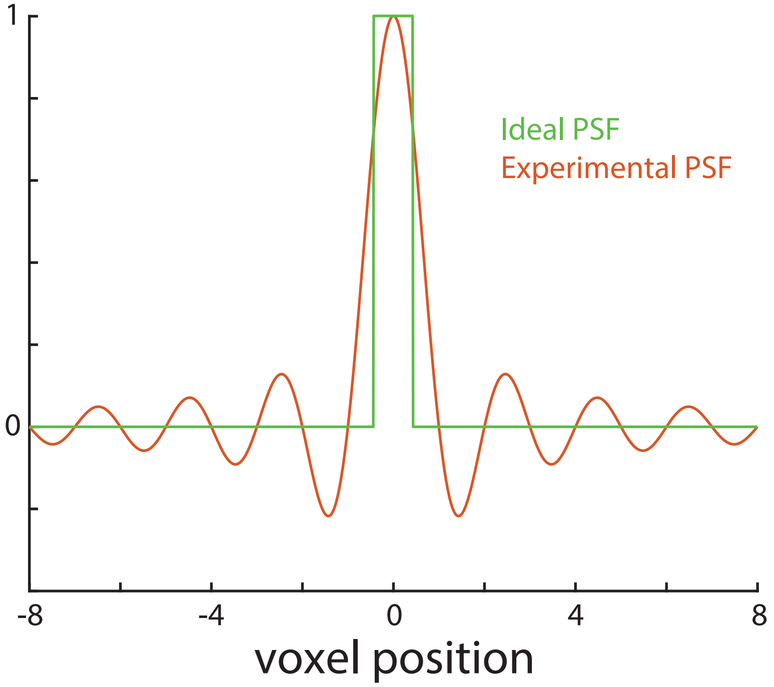

Figure 1.30. PSF of a voxel in a MRSI experiment acquired with 32 phase encoding gradients compared to the ideal PSF. The experimental PSF deviates significantly from the ideal PSF with a larger central lobe width and sinc ripples impinging on other voxel positions. Figure based on reference 11.

A signal sampled in k-space over an infinitely long time will result in a single frequency once the Fourier Transform of that signal is taken. However, in a typical MRI/MRSI scan, this signal is only sampled a finite amount of times and taking the Fourier Transform over the sampling points results in a frequency with some width also known as the point-spread-function (PSF). While this affects the single-voxel acquisitions, it is less of an issue as the signal has decayed to zero by the end of the acquisition period and the PSF is not a large issue (11). The PSF becomes more of a dominating factor for MR spectroscopic imaging, however, due to the limited number of phase encoding gradients (and hence k-space samples) and lack of T2 relaxation in the spatial domain (11). Figure 1.30 shows the PSF resulting from a nominal resolution compared the PSF from the actual resolution resulting from a region being sampled in k-space by 32 points. As a result of the larger central lobe and the sinc lobes propagating out from central lobe in the actual PSF, some signals from outside of the nominal voxel contaminate the voxel and some of the signal within the nominal voxel is spread out to adjacent voxels. This is a problem with MRSI acquisitions as residual lipid coming from voxels located at the scalp can propagate into voxels located in central locations of the brain.

Apodization functions can be applied in k-space in order to improve the PSF. Some commonly used are Gaussian functions, and are typically symmetrical about the origin of k-space and work by preferentially weighting the signals at the center of k-space over those at the edges of k-space. The effect of these an apodization function on the PSF can be seen in Figure 1.31. These functions increase the full-width at half max (FWHM) of the central lobe while reducing the side ripples which consequently leads to reduced spatial resolution. However, of these functions, the Hanning function is found to the most optimal filter by maximizing ripple reduction and minimizing FWHM increase (11).

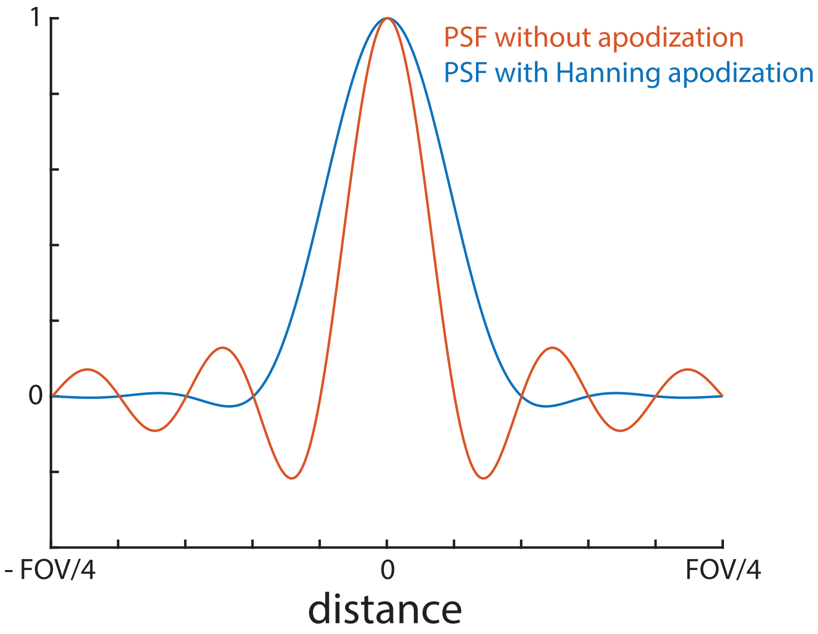

Figure 31. Point spread function (PSF) of a MRSI sequence before apodization and after apodization by a Hanning k-space filter. With apodization, the PSF is improved with fewer sinc ripples emanating from the central lobe. The FWHM of the central lobe, however, is broader.

1.21.4 Circular K-Space Sampling

The bulk of the observed signal o riginates from data collected at lower frequency k-space points. The higher spatial frequencies contains information about the details of objects and contributes little to the overall bulk signal. Because of the inherently low SNR, MRSI has a relatively low resolution due to the relatively large voxels needed and circular k-space sampling is often used to emphasize low k-space acquisitions to favor sensitivity over detail. This reduction in the number of acquisitions results in substantial reduction in scan time of up to 22% for 2D k-space sampling (11). However, this sampling scheme also has the consequence of increasing the width of the central lobe of the PSF by 29% compared to a volume acquired with standard sampling, but also reduces the contamination to/from other voxels (11).

1.21.5 Processing and Display

After sorting the MRSI data by its k-space location, an apodization filter is typically applied over the k-space points prior to taking the 2D Fourier Transform. The k-space data can also be zero-filled upon Fourier Transform to improve the appearance of the processed MRSI data. Although this does not affect the PSF or add any additional information to the processed dataset, this does allow for the calculation of spectra at intermediate spatial locations. The FID data is now spatially resolved after taking the 2D Fourier Transform and taking the 1D Fourier Transform over the FID time points produces spectra at each spatial location. Once this is done, the data can be visualized by displaying the spectra from each spatial location. However, this way of displaying may be too complex to analyze and interpret. Thus, MRSI data is often summarized by fitting the metabolic peaks in each voxel, extracting their areas, and displaying a map of their signal intensities over the spatial locations measured.

Scope of the Dissertation

This dissertation describes work aiming to improve the reliability, accuracy and time-efficiency of J-difference edited single voxel and multi-voxel experiments. Improvements in the reliability of J-difference edited scans by finding optimal parameters to maximize SNR for editing various metabolites, improve water suppression, and reduce artifacts caused by motion are investigated. Methods to decrease the overall scan time by multiplexing J-difference editing experiments by first extending the MEGA-PRESS pulse sequence to acquire the spectra from more than one metabolite simultaneously then extending the sequence to acquire edited spectra from more than one region at the same time are introduced and evaluated. Chapters 2 and 3 focus on developing optimal parameters for measuring various coupled metabolites as well as schemes to edit multiple metabolites simultaneously: GSH and Lac, NAA and NAAG, and NAA, NAAG, and Asp. Chapter 4 focuses on extending J-difference editing to multiple regions simultaneously. In Chapter 5, multi-metabolite editing is extended to many regions simultaneously for mapping the distribution of multiple metabolites simultaneously with MRSI acquisitions, and Chapter 6 focuses on improving the reliability of edited MRSI experiments with post-acquisition phase correction and removal of motion-corrupted averages. In the Chapter 7, the final chapter, a novel water suppression method with improved suppression factors and reduced sequence duration is described and evaluated. Chapters 2 – 4 and Chapter 7 are modifications to already published manuscripts (17, 18, 55-58). Chapter 5 has been accepted for publication in a peer-reviewed journal (59). Chapter 6 is being prepared for submission to a peer-reviewed journal.

Chapter 2 - Simultaneous detection of glutathione and lactate using spectral editing at 3T

2.1 Introduction

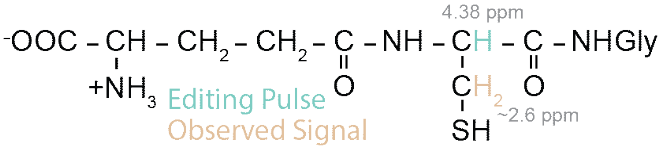

Figure 2.1. Structure of glutathione (GSH). GSH is a tripeptide of glycine (Gly), cysteine and glutamate (Glu). The glutamate moiety is attached through its side-chain carboxylate (denoted Glu'). Editing pulses are applied to the cysteine alpha proton at 4.56 ppm. The observed signal originates from the beta protons at 2.93 ppm and 2.97 ppm.

Glutathione (GSH) is the brain's main antioxidant and is primarily located in astrocytes (60, 61). Lactate (Lac) is an indicator of non-oxidative glycolysis, elevation of which is considered an indicator of metabolic abnormalities or oxygen deficiency (3, 47, 62). Both metabolites are present in healthy brain tissue at approximately millimolar levels (13) and can therefore be detected non-invasively in vivo by proton magnetic resonance spectroscopy ^{1}H-MRS. Lac and GSH are also of interest in the pathophysiology of various brain pathologies such as schizophrenia (14, 63-65), bipolar disorder (66-69), obsessive-compulsive disorder (70), and chronic fatigue syndrome (71). Detection of either metabolite using MR spectroscopy, however, is not trivial due to their relatively low *in vivo* concentrations under normal conditions. Like other metabolites with coupled spin systems, the spectrum of GSH and Lac has several broad low-amplitude signals, none of which is fully resolved from other compounds in the in vivo spectrum. Quantification of both metabolites is therefore challenging, and while it can be estimated from 'LCModel fitting' of conventional high field MRS (72), more frequently spectral-editing approaches are used, either based on multiple-quantum filtering (73, 74) or J-difference editing (47, 63, 75). In recent times, the J-difference method has become the more commonly used editing approach for GSH and Lac.

J-difference editing using the MEGA-PRESS sequence (76) is currently the most widely used spectral editing technique in vivo. J-difference editing sequences are usually designed to detect one molecule at a time. However, if different molecules have coupled spins that have similar chemical shifts and which lie within the bandwidth of the editing pulse, it is possible to simultaneously edit more than one molecule. A well-known example of this is the co-editing of glutamate and glutamine (Glx') in experiments designed to primarily edit GABA, since the coupled Glx resonances at ~2 ppm are usually also affected by the GABA editing pulse applied at 1.9 ppm (77). Another approach for editing two compounds, dubbed 'Double Editing With (DEW) MEGA-PRESS' (78), alternates editing pulse frequencies between the targeted resonances of two molecules in the acquisitions traditionally considered as 'ON' and 'OFF', resulting in signals from both molecules being present in the difference spectrum, but with opposite polarity. DEW was originally demonstrated for glutathione and ascorbate (the 'antioxidant profile') but can also be adopted for other combinations of compounds, such as glutathione and lactate. To maximize sensitivity, however, an echo time that allows for high-SNR detection of both metabolites must be chosen. Lac has a simple and well-defined spin system and has been shown to have a maximal edited signal at 144 ms (79). For GSH, however, an echo time for optimal editing has yet been reported.

As shown in Figure 2.1, glutathione is a tripeptide of glutamate, cysteine, and glycine. The cysteine moiety forms an ABX spin system, with signals at 2.93, 2.97, and 4.56 ppm (21). In J-difference editing of GSH, the editing pulse is applied at 4.56 ppm, and an edited signal is observed at ~2.95 ppm. The optimal echo time (TE) used for editing depends on the target molecule. In theory, ignoring relaxation, triplet-like signals should be edited at a TE of 1/2J (where J is the scalar coupling constant; for a typical 3-bond proton-proton coupling constant of 7Hz, 1/2J ≈70 ms), while doublet-like signals should be edited at 1/J (~140 ms) to maximize the edited signal. Approximating GSH as a simple A_2X spin system suggests the longer TE (140 ms) would be optimal. However, strong coupling effects (and the impact of transverse relaxation in vivo) make this prediction uncertain.

As a result, a large range of echo times (from 68 ms to 131 ms) has been reported as 'optimal' for in vivo J-difference editing of GSH. Terpstra *et al.*, who pioneered the measurement, reported that TE 68 ms is optimal based on phantom measurements made at 4T; this echo time continues to be used in vivo at 4T and 3T (80-84). Echo times of 80 ms and 94 ms have also been used at 3T (63, 85). One study proposed a TE of 131 ms based on phantom data and density operator simulations at 3T to maximize the edited GSH signal and minimize spectral interference from the co-edited N-acetyl-aspartate (NAA) signal (86); this echo time has been used in vivo at 3T (87).

This wide range of echo times is perhaps surprising, in contrast to GABA, for example, for which an echo time of 68 ms has been consistently used since editing was first reported (32). Thus, the aim of the first part of this study was to systematically investigate the TE-dependence of the edited GSH signal, taking into account both the effects of scalar couplings and T_2 relaxation, using a combination of density-matrix simulations, and phantom and in vivo experiments, and to choose an optimal echo time to edit GSH and Lac simultaneously. Two approaches are then developed and compared for the simultaneous detection of the two metabolites: MEGA-PRESS with less selective sinc pulses referred to as sinc-MEGA (sMEGA) and DEW with more selective editing pulses. In addition to optimizing editing pulse characteristics, it is important to consider how unwanted co-edited molecules may vary with TE. The two methods are compared in terms of sensitivity, co-editing of overlapping compounds, as well as to conventional single-metabolite MEGA-PRESS acquisitions in vivo.

2.2 Methods

2.2.1 GSH Echo Time Determination

Simulations

To determine the optimal echo time to edit GSH using MEGA-PRESS, density-matrix simulations were performed for a B_0 field strength of 3T using in-house MATLAB-based software and literature values (13) for GSH chemical shifts and coupling constants. Excitation pulses were assumed to be an ideal rotation around the x-axis with a flip angle of 90°. Note that there was no need to perform a full spatial simulation of the excitation pulse, since this does not effect the evolution of spin-spin couplings, and would only serve to make the simulations more time-consuming. The MEGA-PRESS pulse sequence (76) was simulated using 20 ms sinc-Gaussian editing pulses with a bandwidth of 75 Hz and slice-selective refocusing pulses with a bandwidth of 1300 Hz and a duration of 6.91 ms ('GTST' pulses) (88, 89) for a nominal voxel size of 3 cm x 3 cm, in the dimensions defined by these pulses. The spin-system evolution was simulated for all positions on a 19x19 two-dimensional array spanning 3.6 cm x 3.6 cm to examine spatial effects across a range that extends beyond the limits of the 3 cm x 3 cm nominally excited region. The simulations are performed over a larger dimension than the nominal voxel size in order to capture the actual slice selection profile of the refocusing pulses used, and the effects of chemical shift displacement. This spatial simulation approach has been described in detail previously (45). Such spatially resolved simulations are important, as the time-evolution of coupled spin systems is spatially inhomogeneous (45, 90-94). The signal that is acquired experimentally is the sum over the whole voxel and representative simulations must therefore capture this spatial inhomogeneity. At each position, a 2048-point free induction decay was simulated with 2 kHz spectral width, apodized with a 2.5-Hertz exponential filter, zero-filled to 8192 datapoints, and Fourier transformed.

Simulations were performed at TEs from 70 ms to 240 ms in 10 ms increments. The duration of the first slice-selective spin echo (TE1) was 13.4 ms, with the second spin echo adjusted to make up the remainder of TE. For each TE, spatially resolved spectra were integrated between 2.71 ppm and 3.19 ppm and summed to represent the signal from the whole (simulated) voxel.

Phantom experiments

A one-liter phantom of 50 mM GSH in phosphate-buffered saline with a pH of 7.0 was prepared. A Philips Achieva 3T scanner was used, with body coil transmit and an 8-channel head coil for receive.

J-difference editing experiments were performed at TEs from 70 ms to 240 ms in 10 ms increments using the MEGA-PRESS pulse sequence. TE1 was fixed at 13.4 ms and TE2 was changed to vary the total TE, as in the simulations. 2048 datapoints were acquired at a spectral width of 2000 Hz and a TR of 2s. The slice-selective refocusing bandwidth was 1300 Hz (GTST pulses; limiting B_1 field 13.5 μT; duration 6.91 ms) (88, 89). A 20 ms editing pulse with a bandwidth of 75 Hz was applied at 4.56 ppm in editing-ON acquisitions, and at 8 ppm in the OFF acquisitions. Spectra were processed with 3 Hz exponential line broadening and zero-filling to 8192 datapoints. A linear baseline correction was applied to the resulting spectra and the edited GSH peak at 2.95 ppm was integrated.

When inferring optimal in vivo acquisition parameters from phantom data, one major issue is estimating the effects of transverse (T_2) relaxation. The function $S_p(\mathrm{TE})$ that describes the signal intensity of phantom experiments is T_2-weighted according to a time constant $T_{2,\mathrm{phantom}}$ that will be substantially longer than (but not negligible with respect to) the time constant in vivo $T_{2,\mathrm{iv}}$. Thus the in vivo response function $S_{\mathrm{iv}}(\mathrm{TE})$ can be predicted according to:

$$S_{iv}(\mathrm{TE}) = e^{-\mathrm{TE}/\,T_{2,iv}} e^{-\mathrm{TE}/\,T_{2,\mathrm{phantom}}}.$$

(2.1)

Although the $T_{2,\mathrm{iv}}$ of GSH at 3T has not been reported to date as far as we are aware, it has been measured as 67 ms at 4T (95). T_2 is expected to be approximately inversely proportional to B_0, giving an estimated value of 89 ms at 3T. The in vivo T_2 of GABA at 3T has previously been measured as 88 ms (96), in good agreement with that estimate. GABA has a coupled spin system similar to GSH, but is a somewhat smaller molecule, so it might be expected that the T_2 of GSH would be slightly shorter than that of GABA. Therefore, using Equation 1, the predicted in vivo GSH signal as a function of TE was calculated for these upper and lower limits for $T_{2,iv}$, 89 and 67 ms. The phantom T_2 estimated as 260 ms, based upon previous measurements for a similar GABA phantom at 3T (96).

In Vivo experiments

Five healthy volunteers (two female, age 31 ± 8 years) gave informed written consent with local Institutional Review Board approval. For each subject, edited measurements were performed at TEs of 68 ms and 120 ms. For the shorter TE measurement, slice-selective refocusing was

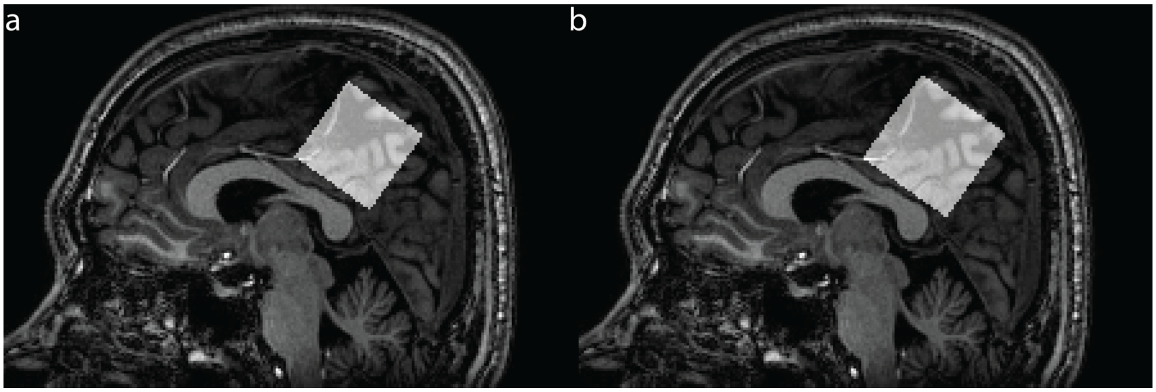

Figure 2.2. Example voxel placement in a 3.6 cm × 3.6 cm × 3.6 cm (a) and a 4 cm × 4 cm × 4 cm midline parietal region overlaid on sagittal T1-weighted images in one subject.

achieved using the same "GTST" pulses (88, 89) also used for the phantom TE series (bandwidth 1300 Hz). For the longer TE, two measurements were made either using GTST refocusing pulses or the longer-duration frequency-modulated refocusing pulses "fmref07" (bandwidth 2200 Hz; (32, 42)). Measurements were made in a (3.6 cm)^3 midline parietal region using VAPOR water suppression as shown in Figure 2.2a (97). Other parameters matched the phantom experiments with the exception that TE1 was increased to 26.6 ms in measurements using fmref07 refocusing pulses. For the in vivo data, the Gannet program (44, 98) was used to frequency-and-phase-correction individual transients based on frequency-domain modeling of the NAA methyl signal. Time-averaged time-domain data were then loaded into the program csx3 (99), and the signal at ~2.95 ppm in the difference spectrum was integrated after a linear baseline correction with 3 Hz line broadening.

2.2.2 GSH Lac Dual Editing

Pulse Sequences

The MEGA-PRESS sequence was used as the starting point for sequence development. The basic concept for dual- (or multi-) metabolite editing is that the editing pulses should invert the target coupled resonances of each molecule to be detected. In the case of the sMEGA this was achieved by using a relatively non-selective sinc-derived editing pulse (25 ms duration and a bandwidth 160 Hz and applied at 4.35 ppm in the ON case and at 10 ppm in the OFF case) with a rectangular inversion envelope to invert both GSH (4.56 ppm) and Lac (4.1 ppm) spins (Figure 2.3a and b). To adapt the DEW method (78) for simultaneous GSH and Lac detection, Bloch-equation simulations were performed to determine the editing-pulse frequency selectivity needed so that the 4.56 ppm ON pulse doesn't significantly invert the 4.1 ppm Lac peak and vice versa. Thus, in the case of the DEW method, selective sinc-Gaussian editing pulses (30 ms duration with a bandwidth of 40 Hz) were applied alternatively on Lac (4.1 ppm) and GSH (4.56 ppm) in the 'ON' and 'OFF' acquisitions respectively (Figure 2.3a and b). As can be seen from the

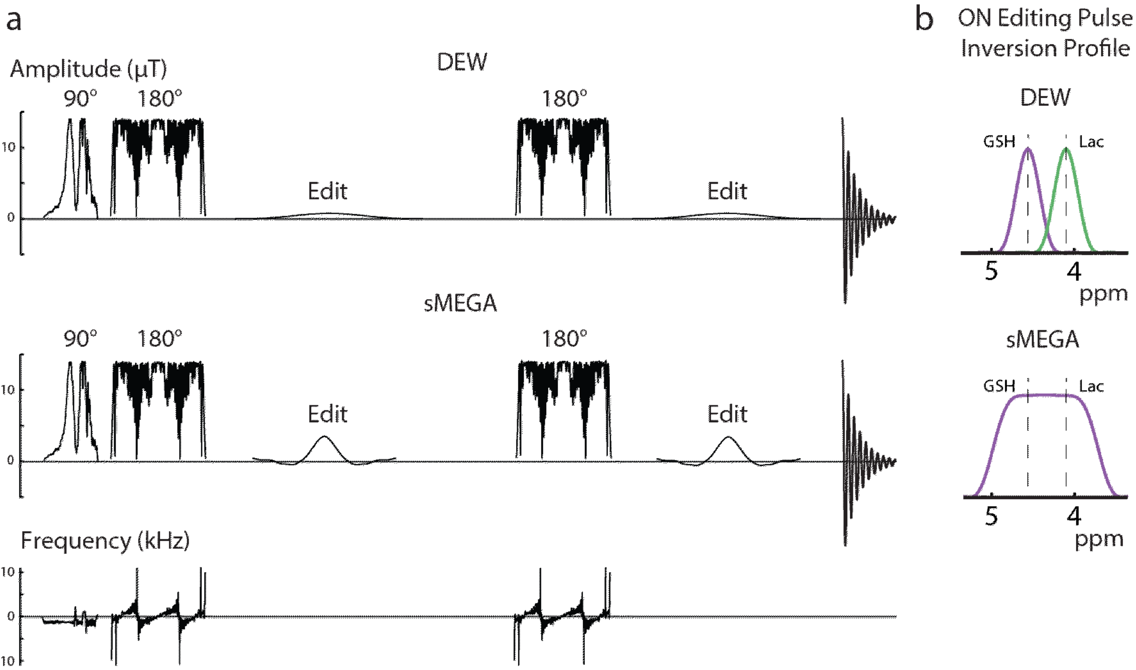

Figure 2.3. Schematic diagram of the two different GSH-Lac editing schemes. (A) the radiofrequency (RF) pulse sequence of both the DEW method and the sMEGA method. Both methods use high-bandwidth, frequency-modulated, refocusing pulses but different editing pulses. (B) the sMEGA method uses an editing pulse with a more rectangular profile to invert both the GSH and lac spins in the ON subacquisition. In the DEW method, more selective editing pulses alternate between ON-GSH and ON-Lac in the subacquisitions.

inversion profiles of the editing pulses shown in Figure 2.3b, the editing pulses are selective enough to avoid the nearby resonance of the other edited metabolite even in the presence of minor B_0 drift. Considering the low bandwidth of these editing pulses, it is estimated that the maximal tolerable B_0 drift to maintain at least 90% editing efficiency is 10 Hz. For the conventional MEGA-PRESS acquisitions, 20-ms sinc-Gaussian editing pulses with a bandwidth of 60 Hz were applied at 10 ppm in the OFF acquisition and at 4.1 ppm in the ON acquisition for Lac MEGA-PRESS or at 4.56 ppm in the ON acquisition for GSH MEGA-PRESS.

For spectral editing of lactate, echo times of 135-144 ms are most commonly used (47, 79, 100) corresponding to TE ~ 1/J, where J = 6.93 Hz (13). In the current study, experiments were performed at TE 140 ms which was determined to be a good intermediate echo time to edit both lactate and GSH with near maximal sensitivity without complication from the NAAG and NAA signals adjacent to GSH (at ~2.6 ppm).

Simulations

Density-matrix simulations were performed as in the GSH echo time determination except 'FID-A', a MATLAB-based spectral simulation package (21), was used and only at the center of the voxel. Both methods were simulated for both the GSH and Lac spin systems and compared to conventional MEGA-PRESS acquisitions of the same metabolites.

To assess the degree to which other brain metabolites may co-edit with Lac and GSH, simulations of metabolites with coupled spins that occur within the bandwidth of the editing pulse were also performed. These metabolites included phosphoethanolamine (PE), N-acetyl-aspartate (NAA), N-acetyl aspartyl glutamate (NAAG), creatine (Cr) and aspartate (Asp). Particular attention was paid to NAA and NAAG (including modeling their TE-dependence, ranging from 110 to 160 ms) since these compounds are known to prominently co-edit with GSH, and have the potential to overlap with the detected GSH resonance at 2.95 ppm. Although traditionally Cr is not thought to edit in J-difference spectra, in fact a small coupling ($J \approx 0.3$ Hz) does exist between the Cr CH2 and CH3 groups (101, 102), so a 3.0 ppm Cr peak will appear in the difference spectrum since the editing pulse partially inverts the coupled 3.9 ppm Cr CH2 protons (see below). Simulations for each compound were weighted according to their concentration values in literature (13).

Phantom experiments

sMEGA, DEW, and MEGA-PRESS experiments were performed in two 1-liter phantoms with 26 mM Lac (pH 7) and 14 mM GSH (pH 7.1). Scans were performed with TR/TE = 2s/140 ms; GSH and Lac phantom data were acquired in a $(3.5\text{ cm})^3$ voxel with 128 averages. Prospective frequency correction for B_0 field drift during the scan was performed based on the frequency of a non-suppressed water reference scan collected once every 8 averages. (39). GSH and Lac editing efficiencies for both sMEGA and DEW were also calculated as a percentage of separate MEGA-PRESS acquisitions for the two metabolites.

In Vivo experiments

Seven healthy volunteers (three female, age 29 ± 10 years) gave informed written consent after local Institutional Review Board approval. Dual-edited data was collected from 5 subjects, and conventional GSH MEGA-PRESS data and Lac MEGA-PRESS data were also acquired in 5 subjects, (three of which overlapped between the two acquisitions). All were acquired with 320 signal averages using VAPOR water suppression (54). MEGA-PRESS and sMEGA data were acquired in a $(4\text{ cm})^3$ midline posterior frontoparietal region (Figure 2.2b) while DEW data were acquired in a $(3\text{ cm})^3$ in the same region. Other parameters were the same as in the phantom experiments. As in the phantom experiments, frequency correction for B_0 field drift during the scan was performed based on the frequency of the water-unsuppressed scan acquired every 16 averages (39).

The 'Gannet' program (44, 98) was used to frequency-and-phase-correct individual transients, based on the 2-ppm N-acetyl peak of NAA, before the difference spectra were calculated. In the dual-edited spectra, a Cr peak at 3.03 ppm was fit with a Lorentzian function since the lineshape of Cr was expected to be singlet-like due the coupling between the Cr CH_2 and CH_3 groups being relatively small and the GSH peak was fit with a Gaussian at 2.95 ppm due to its doublet-like signals

and hence, broader lineshape. In the GSH MEGA-PRESS acquisitions, only a Gaussian was fit to the peak at 2.95 ppm. For fitting of lactate, the region of the spectrum around 1.3 ppm was fit with two Gaussian functions for the macromolecule (MM) resonances at 1.24 and 1.43 ppm (coupled to the 4.23 and 4.30 ppm resonances respectively (19)), and two Lorentzians to fit a doublet for the Lac peak at 1.33 ppm with a 7-Hz splitting. The GSH and Lac integrals were then normalized by an internal water reference signal obtained from the same localized voxel. To test for differences in GSH and Lac editing between the three different methods, two-tailed paired t-tests were performed with statistical significance defined as $p < 0.05$.

2.3 Results

Two-dimensional spatial simulations at TE 120 ms are shown in Figure 2.4a for the GTST refocusing pulses with a bandwidth of 1300 Hz. In the vertical dimension, corresponding to the direction of the first refocusing pulse (shorter TE1 duration), no significant spatial dependency of the multiplet signal is seen. However, in the horizontal dimension corresponding to the second refocusing pulse, there are two distinct regions, which have been color-coded green and red. In the green areas, the OFF multiplets are negative as desired, whereas they are positive in the red areas. ON multiplets are positive, as expected, in all regions. The difference between these two,

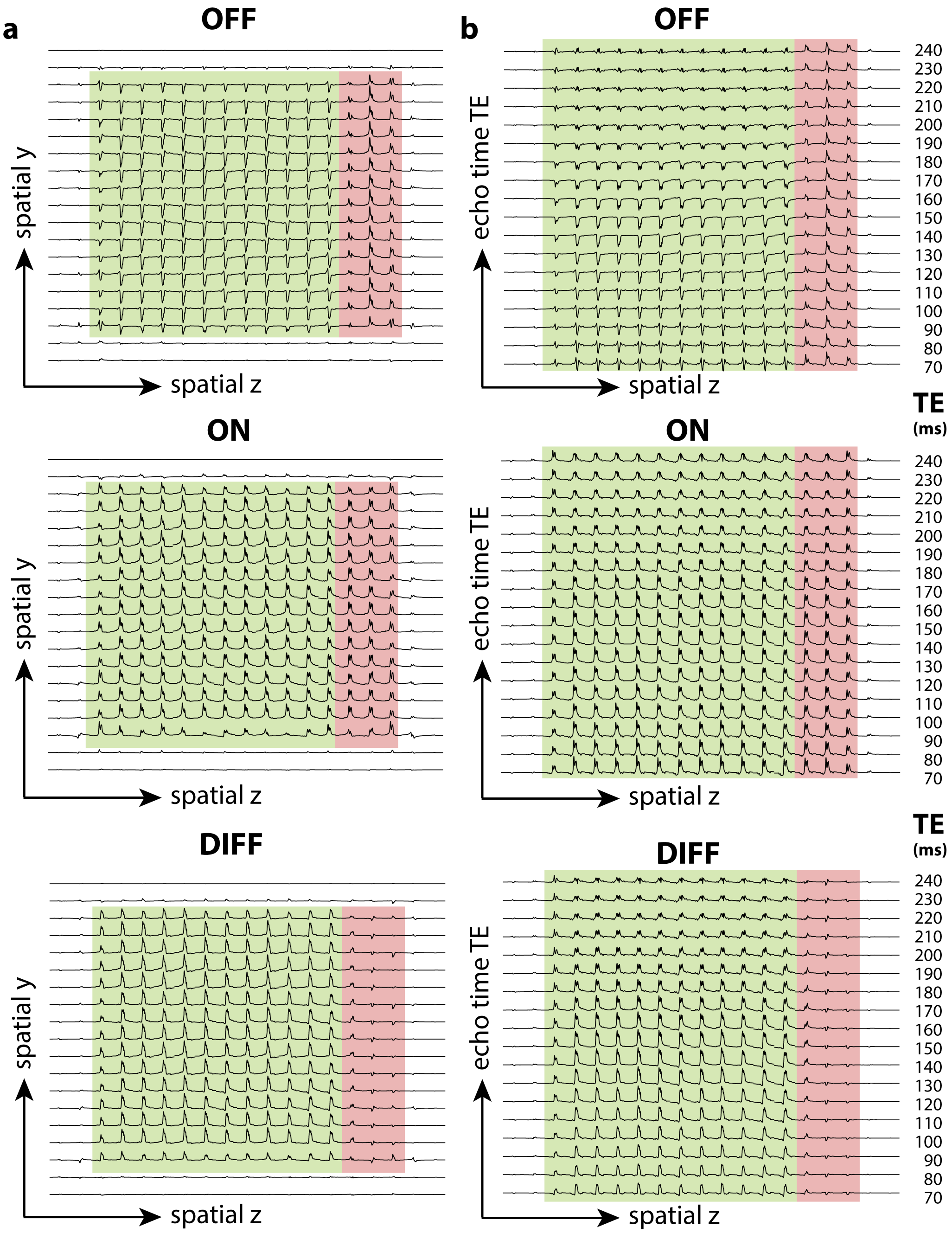

Figure 2.4. Spatial simulations of the GSH multiplet at 2.95 ppm using GTST slice-selective refocusing pulses for the MEGA-PRESS sequence with (ON) and without (OFF) editing pulses applied at 4.65ppm; the difference spectrum (DIFF = ON – OFF) is also shown. Regions in which coupling evolves as desired and produces a negative signal in the OFF spectrum are colored green, while regions where couplings are refocused in the OFF spectrum are colored red. (a) Two-dimensional spatial simulations for a TE of 120 ms. (b) One-dimensional spatial simulations at a range of TEs of 70–240 ms.

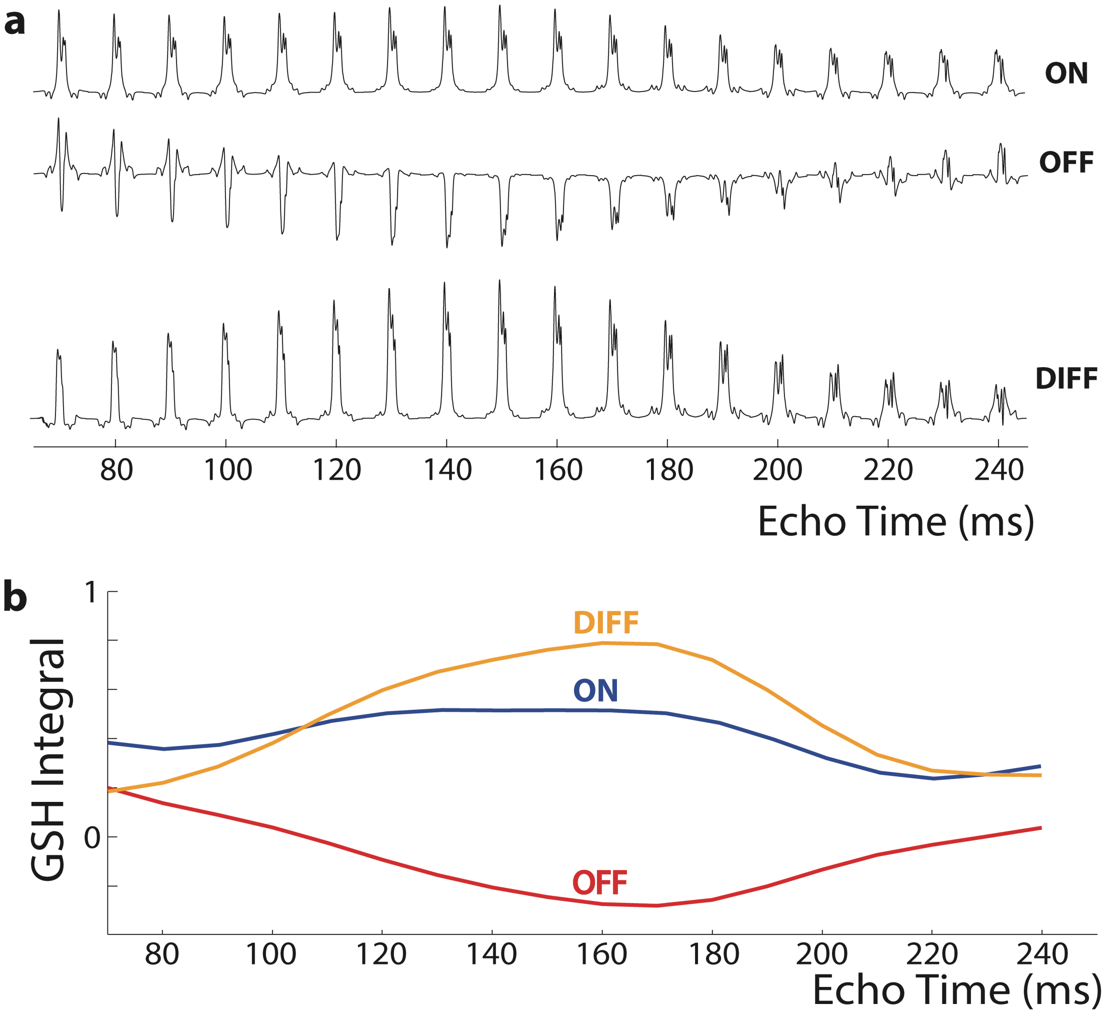

Figure 2.5. Simulations of GSH as a function of TE. The spatial simulations from Figure 2.4 were summed over the whole voxel at a range of TEs. (a) GSH multiplets plotted between 2.71ppm and 3.19ppm. (b) GSH integral curves. Note that in panel a, the ON multiplet varies subtly with TE, which is reflected in its corre- sponding integral in panel b. The DIFF line shape obtains its peak integral at a TE of 160–170 ms and has negative outer lobes at lower TEs (as seen in panel a).

labeled DIFF, gives positive signal in the green region and no signal in the red region. This spatial heterogeneity in editing sensitivity has previously been described for GABA (45). Red regions are those where the GSH cysteine-beta spins (~2.95 ppm) undergo the second slice-selective refocusing pulse, but the cysteine-alpha spins (4.56 ppm) do not. At a slice-selective

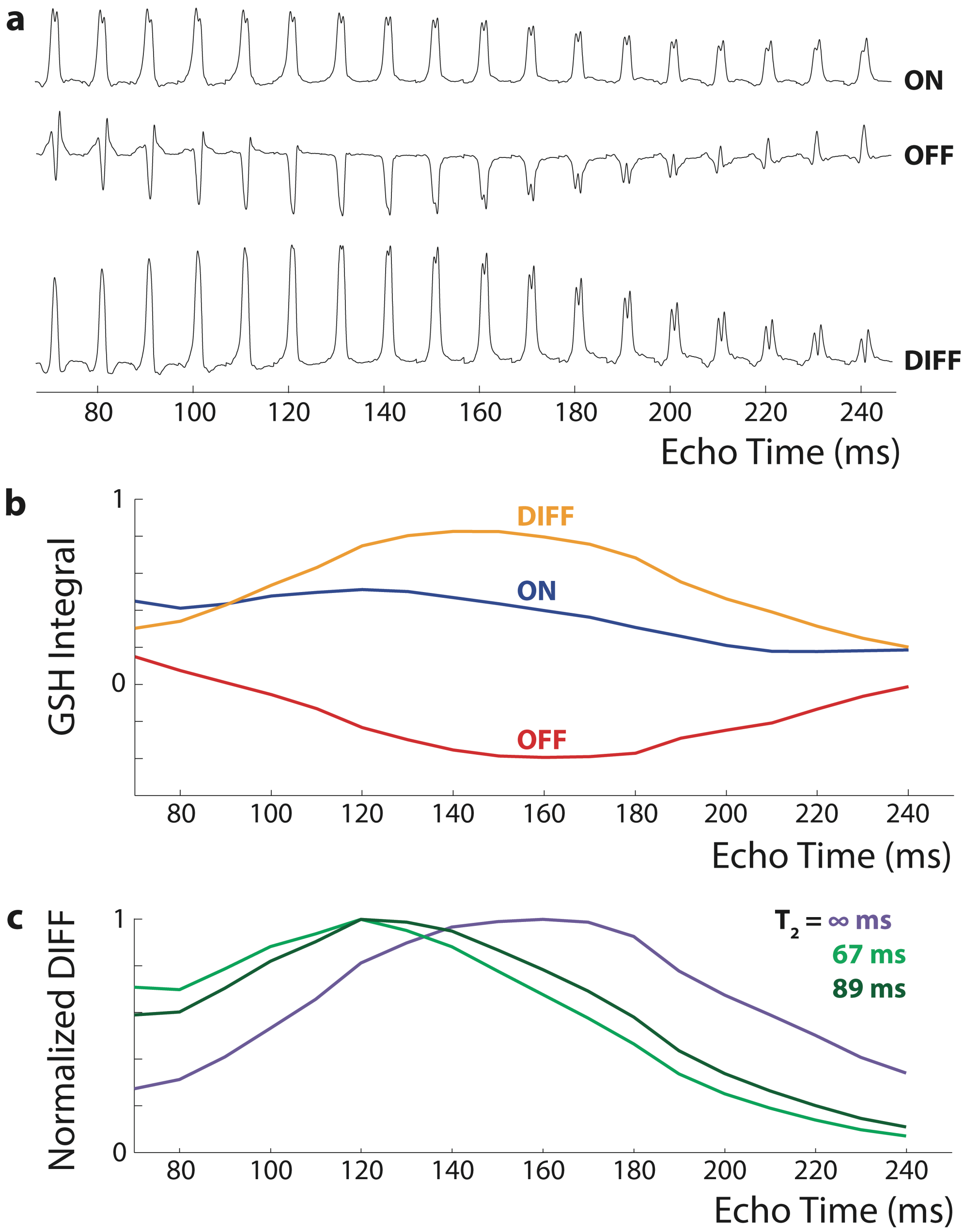

Figure 2.6. Phantom experiments at a range of echo times. (a) GSH multiplets plotted between 2.71 ppm and 3.19 ppm. (b) GSH integral curves. (c) normalized integral curves removing phantom T_2 effects ('$T_2=\infty$'), and simulating in vivo relaxation with T_2 values of 67 ms and 89 ms respectively (estimated to be the likely lower and upper limits of the in vivo GSH T_2 relaxation time at 3T, respectively). Note that the experiments were performed in increments of 10 ms; if TE was sampled more finely, it's likely that the optimum TE would be slightly different for TE 67 and 89 ms.

bandwidth of 1300 Hz, this accounts for 16% of the voxel, reducing to 9% for a slice-selective bandwidth of 2200 Hz.

Figure 2.4b shows the variation in the 2.95 ppm GSH multiplet as a function of TE. Since the spectra are homogeneous across the spatial dimension defined by the first refocusing pulse, this Figure only shows the spatial z-dimension. While the OFF spectra across most of the voxel (green) modulate with TE, as a result of coupling evolution, multiplets in the red region do not. In the ON spectra, evolution of the alpha-beta couplings is refocused throughout the voxel, giving a similar multiplet form at all TEs. However, there is some modulation due to evolution of the geminal (beta-beta) strong coupling (Figure 2.1). The difference spectra show TE-dependence of the size and shape of the positive signal in green regions, and a uniform loss of signal in red regions.

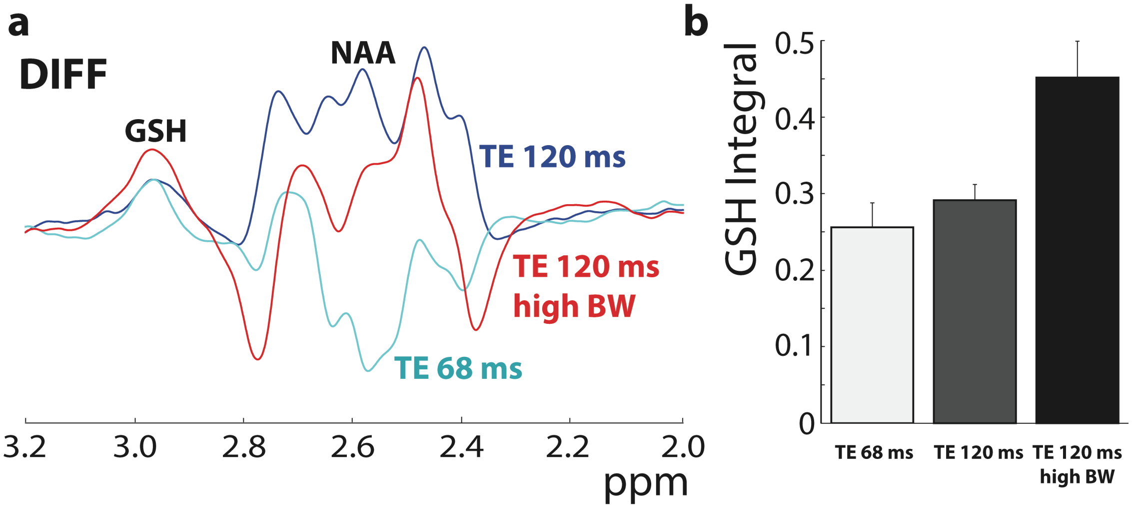

Figure 2.7. In vivo experiments using three different sets of parameters: an echo time of 68 ms with 1300 Hz refocusing bandwidth (green); an echo time of 120 ms with 1300 hz refocusing bandwidth (blue); and an echo time of 120 ms with 2200 Hz refocusing bandwidth (red). Representative spectra from one subject are shown in (a) for each of the different parameter sets. GSH integrals (2.95 ppm) normalized by the sum of the integrals from each subject averaged across all five subjects are shown in (b). Note that the aspartyl resonance of NAA (2.4-2.8 ppm) also varies strongly as a function of TE and slice-selective refocusing pulse bandwidth.

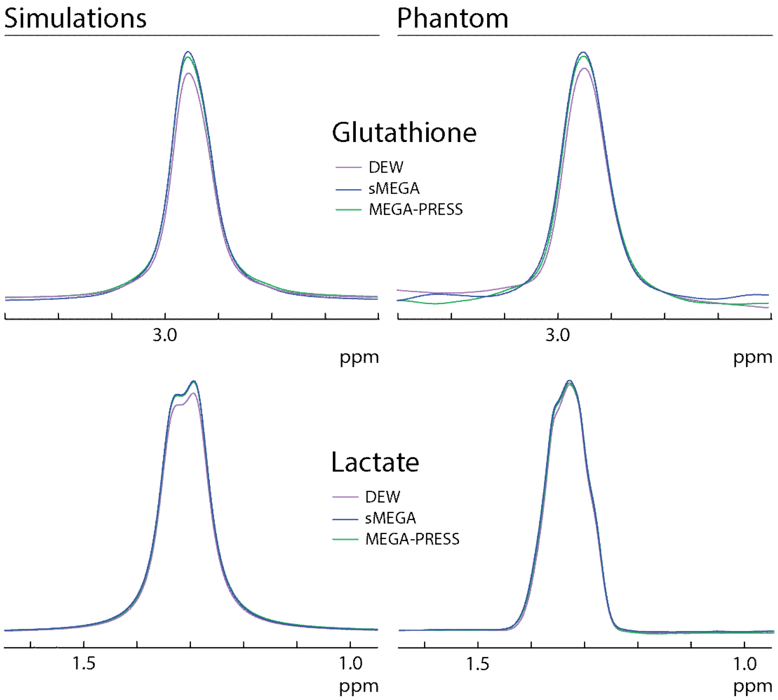

Figure 2.8. Comparison of the edited GSH and Lac signals in the three methods in both simulations and phantom experiments. For both GSH and lac, the sMEGA method (blue) performs better than the DEW method (purple). However, both methods maintain a high editing efficiency comparable with that of separate MEGA-PRESS acquisitions of the same metabolites.

Figure 2.5a shows simulations of the TE-modulation of the 2.95 ppm multiplet after integration over the whole voxel, and Figure 2.5b shows the integral of those spectra. The ON multiplets are positive with subtle TE-modulation (blue). The OFF multiplets vary more strongly with TE (red). The difference between the two results in spectra with net positive signal, that peaks at TE 160-170 ms. Figure 2.6 shows the same information (the TE-dependence of the spectra) for the phantom. Figure 2.6a shows multiplets that are in good qualitative agreement with the simulations of Figure 2.5a. Figure 2.6b shows the TE-dependence of the integrals, which again agree well with the simulations. The difference curve from Figure 2.6b can be corrected to remove the moderate T_2-weighting that occurs in a phantom, assuming a phantom T_2 of 260 ms. This curve is shown in Figure 2.6c as $T_2=\infty$, and is maximal at TE 160 ms. Reintroducing T_2

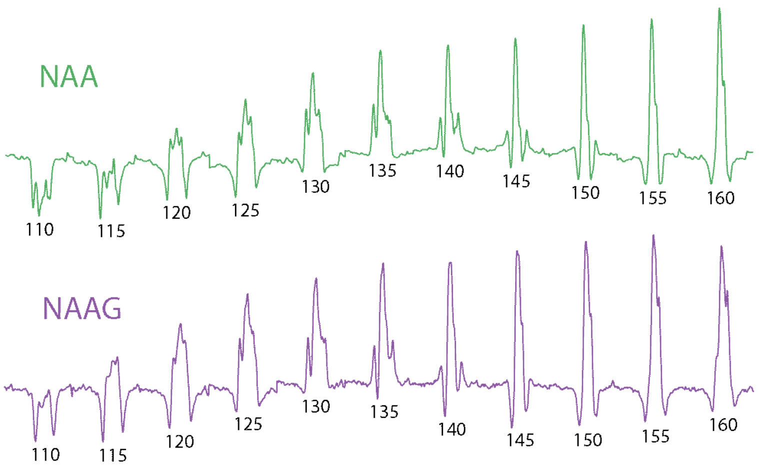

Figure 2.9. Edited NAA (green) and NAAG (purple) spectra in a phantom as a function of echo time. The NAA and NAAG resonances have the least negative/dispersion components present at TE 130-140 ms.

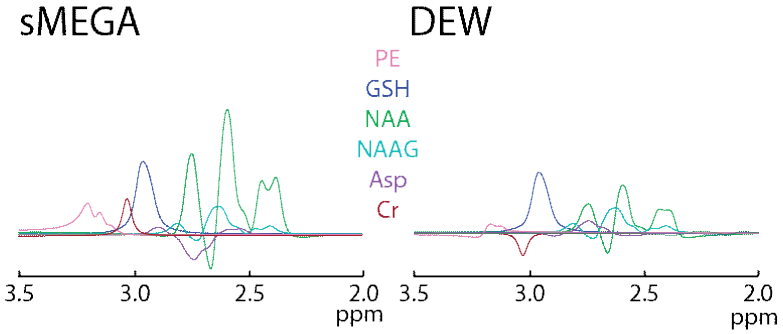

Figure 2.10. Simulations of co-edited metabolites for the GSH region of the spectrum for sMEGA and DEW methods: PE, NAA, NAAG, Asp, and Cr are plotted for both methods. sMEGA and DEW co-edit the same metabolites, but with greater intensity in sMEGA because of its less selective editing pulses. The co-edited Cr peak has the same sign as the GSH peak in sMEGA, but the opposite polarity in DEW

relaxation to simulate the in vivo case (and normalizing each curve to a maximum value of 1), the maximum signal intensity shifts to TE 120 ms for T_2 values of 67 ms and 89 ms.

Figure 2.7a shows representative DIFF spectra from one subject in vivo. It can be seen that the signal amplitude at TE 120 ms with higher-bandwidth refocusing pulses is significantly larger than the signal at a TE of 120 ms and 68 ms with lower-bandwidth refocusing pulses. Figure 2.5b shows the average GSH integral from all five subjects for each scan normalized by the total of each subject. The average DIFF GSH signal is 15% larger at TE 120 ms than at TE 68 ms. The integral is 57% larger at TE 120 ms using high-bandwidth refocusing pulses than using amplitude-modulated pulses. As such, an echo time of 140 ms was determined to be optimal for editing GSH and dual GSH and Lac editing is possible with near maximal sensitivity with a longer echo time. In addition, further SNR gains can be made by using higher-bandwidth frequency modulated refocusing pulses.

Simulations and phantom experiments of the dual-editing sequences acquired at a long echo time with frequency-modulated refocusing pulses confirm that both the sMEGA and DEW methods successfully edit both GSH and Lac with similar sensitivity (Figure 2.8). In addition, both simulations and phantom experiments show that both methods edit GSH and Lac with a high editing efficiency of at least 88% for GSH and at least 95% for Lac relative to conventional MEGA-PRESS acquisitions, which is also reflected in the ON and OFF subspectra of all three methods (Figure 2.9). In addition, these methods can be performed without any increases in specific absorption rate values which was 1.32 W/kg for all three methods. While both methods co-edit the same metabolites: PE, Cr, NAA, NAAG, and aspartate, sMEGA co-edits most of these metabolites to a significantly greater degree than the DEW method because of its less-selective editing pulse profiles. Of these co-edited metabolites, only the Cr peak overlaps with that of the

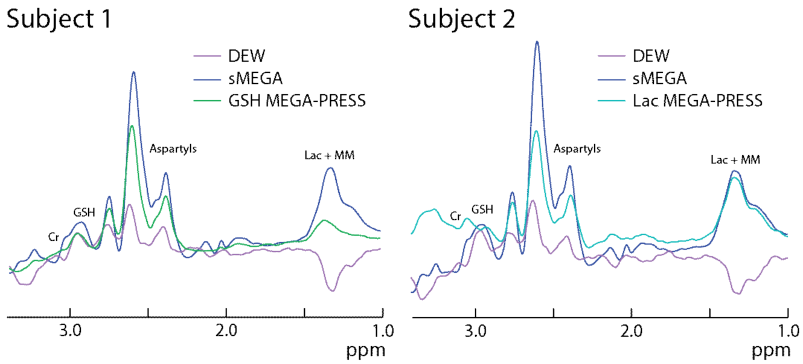

Figure 2.11. Representative GSH and Lac spectra in two subjects. It should be noted that the GSH peak has the opposite polarity relative to the Lac + MM peak in the DEW spectra, and there is a co-edited Cr peak at 3.02 ppm adjacent to the GSH peak which is inverted relative to GSH in the DEW spectra.

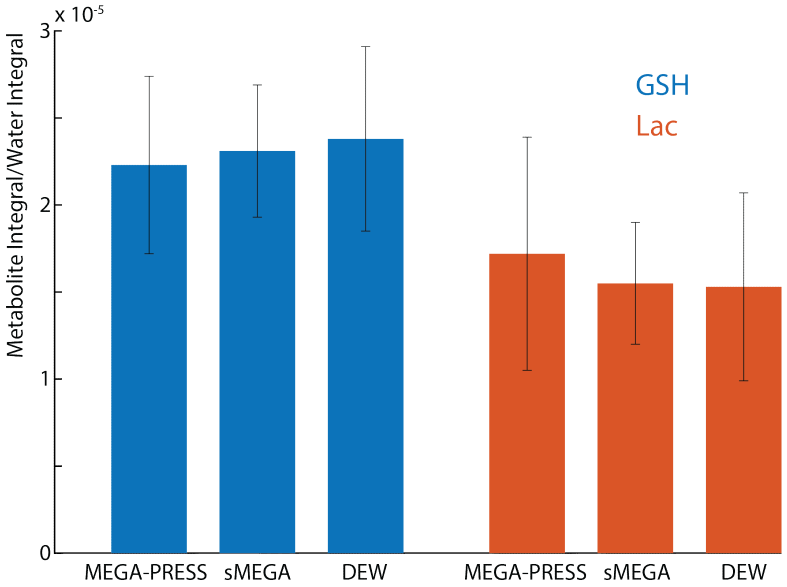

Figure 2.12. Fitted GSH and Lac integrals for all five subjects and all three overlapping subjects for both the sMEGA and DEW methods, as well as separate MEGA-PRESS acquisitions of the same metabolites. Both methods maintain a high GSH and Lac editing efficiency, comparable with that of conventional MEGA-PRESS acquisitions.

edited GSH signal (as shown in Figure 2.10). In sMEGA, this co-edited Cr peak has the same polarity as GSH, but in DEW it has the opposite polarity due to it being co-edited by the Lac editing pulse but not by the GSH editing pulse.

In vivo spectra (as shown in Figure 2.11) also confirm that the sMEGA sequence edits appreciably more NAA (and NAAG) than DEW. There is also co-editing of Cr at 3.02 ppm in the spectra in both methods (as seen in Figure 2.10). As in the simulations, sMEGA has a co-edited Cr peak that is the same polarity as GSH, but opposite polarity in the DEW method. In addition, there is co-editing of MM2 at 1.24 ppm and MM3 at 1.43 ppm in all three methods that overlaps the Lac peak at 1.31 ppm. After fitting out the co-edited Cr peak and macromolecules, it can be seen in Figure 2.12 that sMEGA and DEW have about equal GSH and Lac values indicating equivalent editing efficiency. In addition, both methods edit GSH and Lac to a similar degree as the conventional MEGA-PRESS acquisition in all subjects. Differences in measured metabolite integrals between the three methods were found to be not statistically significant, whether comparing only overlapping subjects or all subjects. In addition, the frequency of the water peak was 4.7 ppm (mean) ± 0.007 ppm (standard deviation) over the different in vivo acquisitions and the total B_0 drift over the different in vivo acquisitions was 0.9 Hz (mean) ± 0.4 Hz (standard deviation). Thus, minimal B_0 drift was present in the scans and thus did not affect the editing efficiency of the DEW acquisition.

2.4 Discussion

In vivo detection of glutathione is challenging, owing to the low concentration of GSH, its coupled spin system, and heavily overlapped spectrum. The determination of optimal acquisition parameters for GSH editing is important for multiple reasons: improved SNR can deliver better measurement reproducibility, shorter scan times, or reduced measurement volumes; additionally, establishing standardized acquisition parameters makes comparisons between different studies more meaningful. In this work, simulations and phantom experiments were used to establish the TE-dependence of GSH editing efficiency and predict that in vivo measurements at TE 120 ms should give improved SNR values over that at TE 68 ms. In vivo measurements supported this, and demonstrated a further benefit of the longer TE, namely that it allows the use of improved slice-selective refocusing pulses.

The glutathione cysteine spin system in the editing experiment can be treated as an ABX system, with signals at 4.56 ppm, 2.97 ppm and 2.93 pm corresponding to the cysteine alpha and beta protons respectively (Figure 2.1). Spatially resolved simulations of the spin system reveal substantial spatial heterogeneity in the coupling evolution, as a result of the chemical shift displacement between slice-selective refocusing bands for the alpha and beta spins. Integrating across the voxel, coupling evolution is represented in the OFF integrals by an approximately cosinusoidal function with a period of ~330 ms, reflecting the two alpha-beta couplings of 5 and 7 Hz. These couplings are refocused in the ON experiment, whose curve shows some residual modulation due to evolution of the 14-Hz beta-beta strong coupling, which is not refocused by the editing pulses.

Spatial inhomogeneity of coupling evolution during PRESS acquisitions have been widely discussed in the literature, with regard to lactate (88, 90, 91), and glutamate (91, 92). The OFF scan of MEGA-PRESS is essentially a PRESS acquisition, and inherits these issues, while they impact the ON scans much less strongly, as has been discussed for GABA (93, 94). To our knowledge, there has been little prior work investigating spatial effects in the detection of GSH, by editing or otherwise.

There is good qualitative agreement between the simulations and the phantom experiments in both the form of multiplets and the envelope of TE-modulation. The major discrepancy between the simulations and the phantom acquisitions is the omission of T_2 relaxation from the simulations. T_2 relaxation biases the signal curves towards shorter TEs. When this T_2 bias is removed from the phantom data (T_2=∞ curve), the TE-dependence of editing substantially agrees with the simulations. Applying estimated in vivo T_2 biases, the optimal TE shifts to 120 ms. Compared to the commonly used value of 68 ms, these phantom data suggest that 120 ms has a significant theoretical advantage (of 55% if T_2 is 89 ms, or 42% if T_2 is 67 ms).

The in vivo data also show that the TE of 120 ms gives more signal than 68 ms. However, this increase is much less than the phantom data suggested. One possible explanation is that the in vivo T_2 is shorter than 67 ms. An alternative explanation arises from the different lineshapes of the edited signal at the two TEs. At the shorter TE, the multiplet has negative outer lobes, as shown in Figures 2.3a and 2.4a; this might lead to misidentification of the baseline when quantifying in vivo data, considering the signal as a positive signal within a baseline well. Indeed, when phantom data are integrated incorrectly in this way, the shorter TE appears less disadvantageous; the marginal benefit of 120 ms is 0-20% as opposed to 42-55%. The in vivo benefit of a TE of 120 ms over 68 ms, measured to be 15%, lies within this range.

The in vivo data show that the clearest benefit of the longer TE is that it can accommodate better slice-selective RF pulses. The frequency-modulated refocusing pulses give more signal due both to the higher bandwidth and the more rectangular slice profile. Considering the simplistic two-compartment (red-green) model, increasing the refocusing bandwidth from 1.3 kHz to 2.2 kHz is expected to deliver 8% more signal due to reduced size of the red compartment. A secondary benefit of using higher-bandwidth pulses is reduction of the chemical shift displacement artifact, leading to improved localization of the full spectrum. The majority of the 57% signal increase arises due to the improved slice profile with flatter passband response within the slice and improved excitation of signal up to the edges of the voxel (calculated as 45.5% from the water reference integral ratios). These benefits occur twice over as two dimensions of the voxel are defined by slice-selective refocusing pulses.

GSH phantom TE series have been presented previously in the literature, with conflicting reports. Our findings are in agreement with one of those two reports (96) which shows that a TE of 130 ms gives more phantom signal than 110 ms or 150 ms. Other papers reported a maximum edited signal at TE 68 ms in phantoms (78, 103). While it is difficult to reconcile this finding with the data and simulations reported here, it should be remembered that the response of the GSH spin system depends on a number of factors, including the transmitter B_1 level, slice-selective pulse waveforms, bandwidth, and timing of the editing pulses. Some implementations of the MEGA-

PRESS sequence do not maintain the temporal spacing of the editing pulses at TE/2, which is the optimum setting required to remove J-modulation from the ON spectra. One further point raised in reference 25 is that it is appropriate to consider not just the optimal GSH signal but also the baseline impact of the co-edited NAA signal at 2.7 ppm. As seen in Figure 2.9, this NAA spectral shape also changes strongly as a function of both TE and the bandwidth of the slice-selective refocusing pulses used.

In addition to examining the echo time dependence of GSH, this chapter presents two methods to simultaneously editing GSH and Lac compares the data acquired with each method. Both the sMEGA method and DEW method perform well with a high overall editing efficiency of GSH and Lac comparable to separate acquisitions of each metabolite using conventional MEGA-PRESS. Although both sMEGA and DEW have high editing efficiencies, DEW needs highly selective editing pulses at frequency offsets close to one another (0.46 ppm separation) which makes the robustness of the measurements unlikely to hold in the presence of B_0 frequency drift. In this case, the editing pulse for the spins of one metabolite may start to impinge on that of the other resulting in losses of editing efficiency for both metabolites in addition to the usual subtraction artifact issues (39, 104). On the other hand, sMEGA uses less selective editing pulses than DEW, which would make the sequence more robust to B_0 field instability. However, the DEW method has less co-edited signals than the sMEGA method. The edited 3.02 ppm Cr signal that partially overlaps with the 2.95 ppm GSH peak is also co-edited to a greater degree in the sMEGA method, but does not appear to impact the quantification of the GSH peak if appropriate spectral fitting is used. The DEW method also has the added benefit of co-editing MM2 to a lesser degree due to partial symmetrical suppression of the 4.3 ppm MM2 resonance from the ON GSH editing pulse placed at 4.56 ppm and the ON Lac editing pulse placed at 4.1 ppm. In the DEW acquisition, the NAA and NAAG aspartyl resonances adjacent to the GSH peak are also co-edited to a lesser degree, thus aiding quantification by reducing spectral overlap between the GSH and aspartyl resonances.

Simultaneous editing of GSH and Lac is possible at 3T due to their similar echo time dependence and editing target frequencies. Compared to separate measurements of each compound individually, simultaneous editing results in a 50% reduction in scan time with essentially the same sensitivity. An echo time of 140 ms results in a high editing efficiency (~95%) of both GSH and Lac. This relatively long TE also allows sufficient time for the very selective editing pulses used in DEW and sinc editing pulses used in sMEGA to be played out. Also at this TE, the neighboring NAA and NAAG resonances are well resolved (and in-phase) from the GSH peak, thus facilitating quantification of the GSH peak (Figure 2.9).

One of the relatively surprising results of this study was the identification of a co-edited peak of the Cr CH_3 signal at 3.02 ppm, which is traditionally thought be to a singlet, and therefore not to contribute signal intensity to edited spectra. However, recent work has shown that there is a small (~0.3 Hz) long-range J-coupling between the Cr CH_2 protons at 3.9 ppm and the CH_3 protons, thus giving some co-editing of this signal at long TE. Fortunately it only partially overlaps the edited GSH signal at 2.95 ppm, allowing the two to be separated by appropriate spectral fitting routines.

In conclusion, a comprehensive study of J-difference editing of glutathione at a range of echo times has been presented and two methods were developed and compared for the simultaneous editing of GSH and Lac, compounds that have both been implicated in the pathophysiology of a variety of brain pathologies. Approximating the in vivo T_2 of GSH, simulations and phantom experiments suggest an optimal in vivo echo time of 120 ms. This longer echo time is shown in vivo to be an improvement over the commonly used TE of 68 ms. Although the margin of improvement is less than expected based on phantom experiments, the further benefit of using improved refocusing pulses of longer duration is substantial. In addition, the methods developed here allow for a 50% reduction in scan time compared to sequential measures of the two metabolites. In healthy subjects, the methods are shown to reliably edit both GSH and Lac with no loss in editing efficiency in comparison to conventional MEGA-PRESS acquisitions of the same metabolites. While the DEW method gives less co-editing of other compounds, the co-edited signals in sMEGA do not hinder quantification of either GSH or Lac in the sMEGA acquisition. Thus, the sMEGA sequence may be preferable especially when B_0 field drift is problematic.

Chapter 3 - HERMES: Hadamard Encoding and Reconstruction of MEGA-Edited Spectroscopy

3.1 Introduction

As discussed previously, *in vivo* proton (^{1}H) magnetic resonance spectroscopy suffers from limited dispersion of signals along the chemical shift dimension (30). 'J-difference' editing allows for the quantification of several low-concentration molecules, including N-acetylaspartylglutamate (NAAG) (105), gamma-aminobutyric acid (GABA) (32), lactate (106), glutathione (103) and 2-hydroxyglutarate (107). One disadvantage of this tailored approach is that, in general, only one molecule can be targeted per scan with optimal sensitivity. Since editing is used for low-concentration metabolites, long acquisitions are needed in order to obtain sufficient signal-to-noise ratio (SNR), making the detection of multiple metabolites from multiple brain regions very time consuming. This limits the amount of information that can be collected in clinical or research studies. However, some combinations of molecules can be edited simultaneously in a J-difference experiment. For example, experiments designed to edit GABA whose detected signals appears at 3.0 ppm usually also co-edit glutamate and glutamine whose detected signals appear at 3.75 ppm. This occurs because, in all three molecules, the detected multiplets are coupled to 'target' resonances that lie within the bandwidth of the editing pulses. Another approach to detect two different molecules, termed "Double Editing With MEscher-GArwood" (DEW-MEGA) (78), can be applied when the two molecules to be detected have both the target and detected signals resolved. In this case, editing pulses can be alternately applied to each target in the 'on' and 'off' scans, with the result that the two detected signals are edited with opposite phases in the difference spectrum.

In this chapter, a new method is presented for acquiring multiple edited signals simultaneously, that does not require the detected signals to be resolved from each other (unlike DEW-MEGA). The method, 'Hadamard Encoding and Reconstruction of MEGA-edited Spectroscopy' (HERMES) is demonstrated first for dual editing, but is scalable to acquire more than two molecules simultaneously, provided that the resonances targeted by the editing pulses are resolved from each other. The main novel aspects of HERMES are: Hadamard-encoded combinations of editing pulse frequencies, which give a multiplexed experiment that simultaneously edits more than one molecule; and Hadamard reconstructions of the sub-spectra to give separate difference spectra for each molecule. Compared to sequential acquisitions of individual molecules, temporal signal-to-noise ratio (SNR) is improved since the full acquisition duration is used to detect every molecule. As an example of the method, a scheme for separately detecting N-acetylaspartate (NAA, which reflects neuronal mitochondrial metabolism (108)), and its derivative N-acetylaspartylglutamate (NAAG, a moderator of glutamatergic neurotransmission (109)), is presented. This method can be also extended to edit a third target spin system simultaneously, demonstrated for aspartate (Asp).

As shown in Figure 3.1, NAA, NAAG and free aspartate (Asp) share the same aspartyl moiety, making it difficult to distinguish between their spectra using conventional localized spectroscopy. However, the **α** -aspartyl protons of each molecule have substantially different

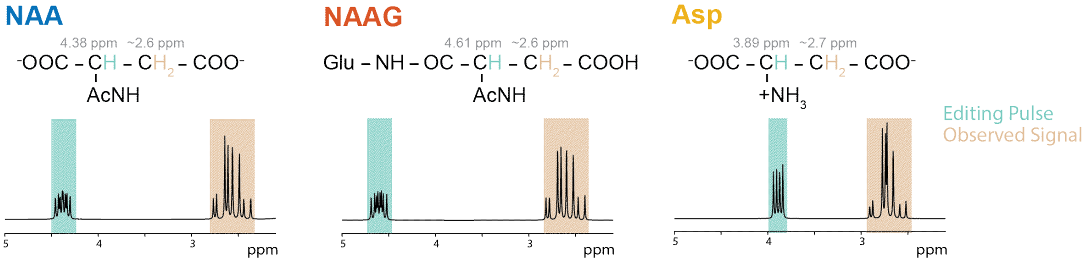

Figure 3.1. Chemical structures of Asp, NAA, and NAAG including chemical shifts for the α- and β-aspartyl resonances and corresponding spectra. The α-protons targeted by the editing pulses are highlighted in green while the observed β-aspartyl protons are highlighted in tan.

chemical shifts (NAA 4.38 ppm; NAAG 4.61 ppm; Asp 3.89 ppm), so that selective editing pulses can be applied to each of these separately, while their overlapping coupled **β** -aspartyl resonances are observed at ~2.6 ppm. Thus, it should be possible to simultaneously edit NAA, NAAG and Asp using HERMES.

HERMES was optimized for the simultaneous detection of NAA and NAAG and extended to edit Asp using density-matrix simulations. The echo-time modulation of the aspartyl spin system was also investigated using simulations and phantom experiments to determine the optimal echo time to edit NAA, NAAG, and Asp. Feasibility of these approaches were demonstrated in phantoms and *in vivo* in the human brain at a magnetic field strength of 3 Tesla. By simultaneously recording data from more than one metabolite, HERMES has the potential to substantially increase the scope of clinical and research studies while maintaining tolerable scan times.

3.2 Theory

Consider two metabolites, with coupled spin systems described as AX and BY, where the X and Y spins give overlapping signals in the spectrum and the A and B spins are resolved. Each can be separately detected using a J-difference-edited experiment, applying frequency-selective pulses to the A or B spin, respectively, in the ON condition and not in the OFF condition. HERMES allows us to detect both spin systems at the same time, by acquiring four scans with different combinations of editing pulses: (ON, ON); (ON, OFF); (OFF, ON); and (OFF, OFF). Thus, for each of the two spin systems, two scans are editing-ON, and two editing-OFF. By mapping ON to +1 and OFF to -1, this editing scheme can be represented as a Hadamard encoding matrix H (110), as shown in Figure 3.2a.

The matrix **M** of the reconstructed spectra of each molecule is calculated from the matrix **N** of the recorded spectra using the transpose of the encoding matrix, **H**:

$$\mathbf{M} = \mathbf{H}^{\mathbf{T}} \times \mathbf{N}$$

(3.1)

where, in this example, M is of dimension $2xn_{points}$, H is of dimension 4x2, and N is of dimension $4\ xn_{points}$, where n_{points} is the number of points in the spectra.

In order to reconstruct the edited spectrum of each molecule, the ON scans (with respect to that molecule) are summed and the OFF scans (with respect to that molecule) are subtracted from them. Since the columns of the Hadamard matrix are orthogonal, each combination contains no edited signal from the other molecule.

Figure 3.2b also demonstrates that the ‘fourth’ Hadamard combination of the four-step scheme can be used to edit a third molecule, without increasing the scan time. For 4-to-7 molecules, a total of 8 scans are required with different combinations of editing pulses as shown in Figure 3.2c. In general, for Hadamard matrices with 4n columns, up to (4n-1) molecules can in principle be edited. In these ideal cases, it is assumed that the target resonances are separated by more than the bandwidth of the editing pulses, so that selective excitation of each is possible. By acquiring signals from multiple compounds simultaneously, HERMES of n species potentially gives a theoretical $\sqrt{n}$ benefit in temporal SNR compared to sequentially acquiring spectra from each compound.

3.2.1 Theory: Example for editing and separation of NAA and NAAG

As shown in Figure 3.1, the aspartyl moiety of NAA makes an ABX spin system with three doublets of doublets at ~2.6 ppm, and 4.38 ppm (13). NAAG has a similar structure, consisting of NAA bonded to glutamate, with aspartyl multiplets at ~2.6 ppm, and 4.61 ppm. Because of the similarity between the structures of NAA and NAAG, it is difficult to distinguish between the spectra of the two molecules, particularly at lower field strengths (e.g. 1.5 or 3.0T). Previous efforts to differentiate them have either used model-based fitting of conventional, non-edited spectra using the slight difference in chemical shift of the N-acetyl resonances (2.01 vs. 2.04

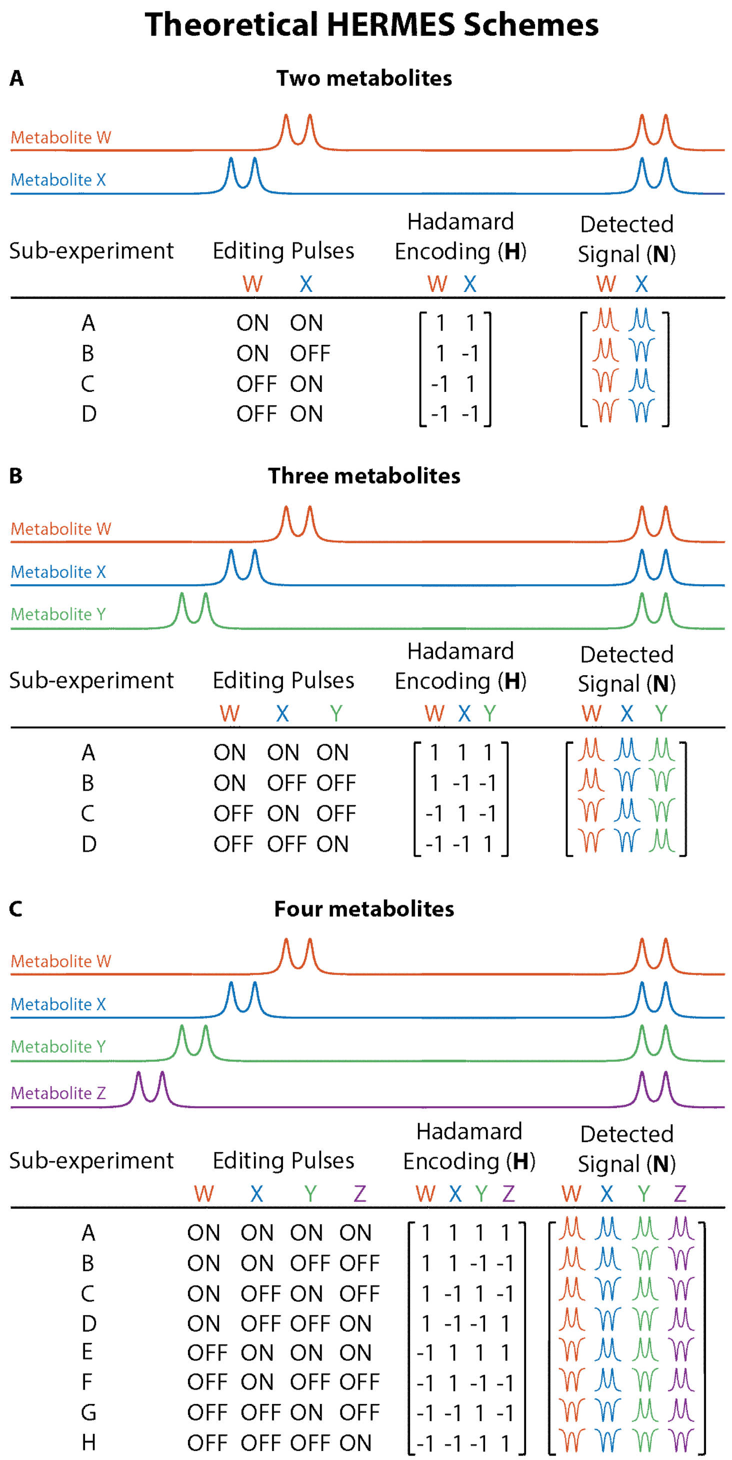

Sub-experiment	Editing Pulses W	Editing Pulses X	Hadamard Encoding (**H**) W	Hadamard Encoding (**H**) X
A	ON	ON	1	1
B	ON	OFF	1	-1
C	OFF	ON	-1	1
D	OFF	ON	-1	-1

Sub-experiment	Editing Pulses W	Editing Pulses X	Editing Pulses Y	Hadamard Encoding (**H**) W	Hadamard Encoding (**H**) X	Hadamard Encoding (**H**) Y
A	ON	ON	ON	1	1	1
B	ON	OFF	OFF	1	-1	-1
C	OFF	ON	OFF	-1	1	-1
D	OFF	OFF	ON	-1	-1	1

Sub-experiment	Editing Pulses W	Editing Pulses X	Editing Pulses Y	Editing Pulses Z	Hadamard Encoding (**H**) W	Hadamard Encoding (**H**) X	Hadamard Encoding (**H**) Y	Hadamard Encoding (**H**) Z
A	ON	ON	ON	ON	1	1	1	1
B	ON	ON	OFF	OFF	1	1	-1	-1
C	ON	OFF	ON	OFF	1	-1	1	-1
D	ON	OFF	OFF	ON	1	-1	-1	1
E	OFF	ON	ON	ON	-1	1	1	1
F	OFF	ON	OFF	OFF	-1	1	-1	-1
G	OFF	OFF	ON	OFF	-1	-1	1	-1
H	OFF	OFF	OFF	ON	-1	-1	-1	1

Figure 3.2. Schematic illustration of Hadamard-encoded editing. A) Four-step HERMES scheme for two molecules. B) The HERMES scheme for three molecules can also be achieved in four steps. C) The HERMES scheme for four molecules requires eight steps. In theory, up to seven molecules could be incorporated into an eight-step scheme.

ppm), which is difficult unless extremely good field homogeneity/stability is achieved (111, 112), or require two separate J-difference editing acquisitions, each optimized to detect one of the molecules at a time (105, 113). The editing approach takes advantage of the chemical shift difference between their aspartyl-alpha spins at 4.38 ppm (NAA) and 4.61 ppm (NAAG) in order to detect the aspartyl-beta resonances between 2.5-2.7 ppm. This approach requires two separate scans (i.e. double the scan time) in order to measure both NAA and NAAG, whereas it is possible to edit (and distinguish between) the two molecules (NAA and NAAG) simultaneously within a single acquisition using the HERMES scheme.

As discussed above, four HERMES experiments are needed: A (NAA ON, NAAG ON); B (NAA ON, NAAG OFF); C (NAA OFF, NAAG ON); and D (NAA OFF, NAAG OFF) (Figure 3.3a) . In order to generate the difference spectrum for NAA, the NAA-OFF scans are subtracted from the NAA-ON scans, i.e. A+B-C-D. Similarly, subtracting the NAAG-OFF scans from the NAAG-ON scans gives the difference spectrum for NAAG, i.e. A-B+C-D. Note that each subtraction is balanced with respect to the treatment of the 'other' target - from the point-of-view of NAA, the NAAG difference combination is ON-ON+OFF-OFF. Therefore, no NAA signal is expected in the NAAG difference spectrum and vice versa.

3.2.2 Theory: Example for editing and separation of NAA, NAAG, and Asp

Aspartate shares the same aspartyl moiety with NAA and NAAG. However, the α -aspartyl protons of Asp have a substantially different chemical shift from NAA and NAAG at 3.89 ppm. Thus, a selective editing pulse can be applied separately to all three metabolites to simultaneously edit them using HERMES.

As discussed before for dual editing of NAA and NAAG, four HERMES experiments are needed: A (NAA ON, NAAG ON, Asp ON); B (NAA ON, NAAG OFF, Asp OFF); C (NAA OFF, NAAG ON, Asp OFF); and D (NAA OFF, NAAG OFF, Asp ON) (Figure 3.3b). As described above, the difference spectrum for NAA and NAAG can be calculated by subtracting

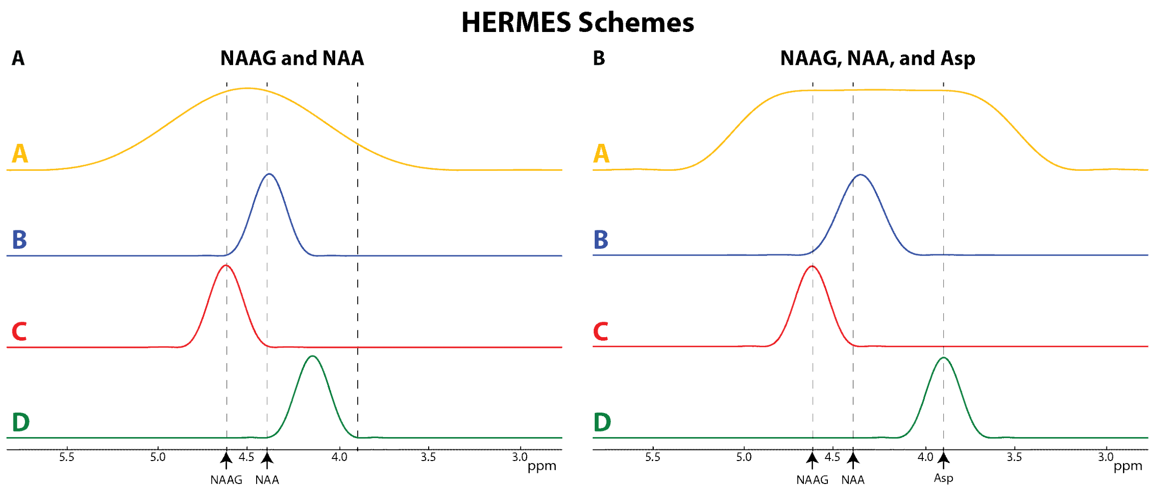

Sub-experiment	A	B	C	D
Edit Offset	4.50	4.38	4.62	4.14
Duration	10 ms	45 ms	45 ms	45 ms
NAA	ON	ON	OFF	OFF
NAAG	ON	OFF	ON	OFF

Hadamard Reconstructions

NAA	A + B – C – D
NAAG	A – B + C – D

Sub-experiment	A	B	C	D
Edit Offset	4.27	4.35	4.62	3.89
Duration	20 ms	35 ms	45 ms	45 ms
NAA	ON	ON	OFF	OFF
NAAG	ON	OFF	ON	OFF

Hadamard Reconstructions

NAA	A + B – C – D
NAAG	A – B + C – D
Asp	A – B – C + D

Figure 3.3. Editing pulse schematic for two HERMES editing schemes: one for editing both NAA and NAAG simultaneously (a) and one for editing Asp, NAA, and NAAG simultaneously (b). In the top panel, the inversion profile of the editing pulses are plotted, and color-coded by experiment. The middle table shows the four experiments acquired with the listed editing pulse offsets and durations, while the amplitude modulation functions of the four pulses are shown overlaid in the bottom left panel. The bottom table shows the Hadamard combinations of the different experiments that give the edited spectra of NAA, NAAG and Asp respectively.

the OFF scans from the ON scans for each metabolite: A+B-C-D and A-B+C-D for NAA and NAAG respectively. To reconstruct the difference spectrum for Asp, the Asp-OFFs are subtracted from the Asp-ONs with the combination A-B-C+D. As with HERMES editing of NAA and NAAG simultaneously, the encoding pattern of each metabolite is orthogonal to one another and thus separation between NAA, NAAG, and Asp spectra is expected. It is interesting to note that the encoding matrix –H is also valid, giving four experiments: A (NAA OFF, NAAG OFF, Asp OFF); B (NAA OFF, NAAG ON, Asp ON); C (NAA ON, NAAG OFF, Asp ON); and

D (NAA ON, NAAG ON, Asp OFF).

3.3 Methods

3.3.1 Simulations

Density-matrix simulations were performed for a B_0 field strength of 3T using FID-A, a MATLAB-based software package (21), with NAA, NAAG, and Asp chemical shifts and coupling constants taken from reference (13), as shown in Figure 3.2. A 2048-point free induction decay was simulated with 2 kHz spectral width, zero-filled to 8192 datapoints, and Fourier transformed. The excitation pulse was assumed to be an ideal 90° rotation around the x-axis. All simulations and experiments used single-lobe sinc-Gaussian editing pulses (35) and conventional amplitude-modulated slice-selective refocusing pulses (88, 89); only the center of the voxel was simulated.

Echo Time

To determine the optimal echo time (TE) for the edited signal for NAA, NAAG, and Asp, separate MEGA-PRESS pulse sequences were simulated from TE 70 ms to TE 210 ms at 5 ms increments (76). This was done with 20 ms editing pulses placed at 10 ppm in the OFF acquisition, and at 4.38 ppm, 4.61 ppm, and 3.89 ppm to invert the NAA, NAAG, and Asp alpha-aspartyl spins respectively in the ON acquisitions). The area of the detected β-aspartyl ~2.6 ppm peak was compared between that of NAA, NAAG, and Asp (up to TE = 260 ms). Bloch equation simulations of the inversion efficiency of the editing pulses as a function of frequency offset for different pulse durations were also performed, in order to determine what editing pulse selectivity is required to ensure selective editing of NAA and NAAG in the HERMES acquisition.

HERMES of NAA and NAAG

HERMES NAA/NAAG editing was simulated based on the implementation shown in Figure 3.3a. Experiment A (ON, ON) was performed with 10 ms editing pulses, applied at 4.5 ppm, to invert both the NAA spins at 4.38 ppm and the NAAG spins at 4.61 ppm. Experiments B (ON, OFF) and C (OFF, ON) were performed with more selective, 45 ms editing pulses applied at 4.38 ppm to invert the NAA spins and 4.62 ppm to invert the NAAG spins, respectively. The editing pulse to invert the NAAG spins were placed slightly off resonance at 4.62 ppm as opposed to 4.61 ppm to reduce the inversion of the nearby NAA spins at 4.38 ppm. To further suppress residual NAA signal in the NAAG spectrum (since NAA is several times more abundant than NAAG), experiment D was performed with 45 ms editing pulses placed at 4.14 ppm, so pulses in C and D are symmetrical about NAA at 4.38 ppm (34, 105). From these simulations, the NAA-edited spectrum was generated from the combination (A+B-C-D) and the NAAG-edited spectrum from the (A-B+C-D). Experiments were simulated for the NAA and NAAG spin systems independently, and NAA-edited and NAAG-edited combination spectra were calculated for each (according to the table in Figure 3.3); only peaks at ~2.6 ppm were plotted.

Non-ideal editing (here termed ‘crosstalk’), i.e. the presence of unwanted aspartyl signals in the different Hadamard reconstructions such as NAA signal in the NAAG spectrum, was quantified using a root-mean-squared (RMS) approach as the phase of such signals is variable. Crosstalk RMS values are expressed as a percentage of the signal in the intended reconstructed spectra for the same molecule. NAA crosstalk into the NAAG spectrum was also calculated for an acquisition with the editing pulse in experiment D placed at 10 ppm (the “OFF-OFF” case).

To determine the possibility of co-editing other molecules in the NAA- and NAAG-edited spectra, other brain metabolites with target spins in the range 5.5 ppm to 3.5 ppm, the full inversion range of the least selective editing pulse, and with coupled spins in proximity of the detected NAA and NAAG peaks at 2.6 ppm, were simulated in the same way. The NAA and NAAG reconstructed spectra for these metabolites (glutamate, glutamine, glutathione, and aspartate) were then plotted assuming equimolar concentrations. The fractional editing of the most highly co-edited metabolites in the HERMES experiment were calculated relative to the edited signal achieved in a MEGA-PRESS experiment with ON pulses applied on-resonance for each particular metabolite

HERMES of NAA, NAAG, and Asp

A four-step HERMES scheme was developed to edit NAA, NAAG, and Asp, consisting of four MEGA-PRESS sub-experiments A, B, C, and D as shown in Figure 3.3b with conventional amplitude-modulated slice-selective refocusing pulses (bandwidth 1200 Hz). In the first sub-acquisition A (ON_{NAA}, ON_{NAAG}, ON_{Asp}), a broader editing pulse with a rectangular inversion profile was optimized to invert the Asp spins at 3.89 ppm, NAAG spins at 4.61 ppm, and NAA spins at 4.38 ppm. This 20-ms sinc-Gaussian editing pulse was applied at 4.27 ppm (bandwidth 200 Hz). The other three sub-experiments (B, C, and D) applied narrowband editing pulses selective for one of the three metabolites (NAA, NAAG, Asp): Experiment B at 4.35 ppm with a duration of 35 ms and bandwidth of 35 Hz (ON_{NAA}, OFF_{NAAG}, OFF_{Asp}); Experiment C at 4.62 ppm with a duration of 45 ms and a bandwidth of 28 Hz (OFF_{NAA}, ON_{NAAG}, OFF_{Asp}); and Experiment D at 3.89 ppm with a duration of 45 ms and a bandwidth of 28 Hz (OFF_{NAA}, OFF_{NAAG}, ON_{Asp}). These editing pulse offsets and durations were chosen as a result of preliminary exploratory investigations aimed at minimizing editing crosstalk. Combining the sub-spectra as in the bottom table of Figure 3.2 leads to separate J-difference-edited spectra for NAA, NAAG, and Asp. As in HERMES dual editing of NAA and NAAG, crosstalk between the different Hadamard reconstructions was calculated between 2.3 ppm and 3.0 ppm.

In addition, other potentially co-edited metabolites, i.e. those with spins coupled to spins with chemical shifts that occur within the bandwidth of the editing pulses (taurine, tyrosine, the glutamate and cysteine moieties of glutathione (GSH), glutamate, and glutamine), were also simulated with the same HERMES scheme. Chemical shifts and coupling constants were taken from reference 13 and simulated spectra were evaluated both with equimolar concentrations and in vivo concentrations taken from the same reference.

3.3.2 Phantom experiments

All experiments were performed on a Philips Achieva 3T scanner using a body coil (maximum $B_1 = 13.5\ \mu T$) for transmitting RF pulses. HERMES NAA/NAAG experiments were performed using two separate 100 mL spherical phantoms, one containing NAA (10 mM, pH 7.2) and one containing NAAG (10 mM, pH 7.2) using an 8-channel phased-array knee coil for receive. Scan parameters were the same as the simulations above, with TR 2.2 s and TE of 150 ms, CHESS water suppression (114) with a 2.4x2.4x2.4 cm^3 voxel and 16 averages. Spectra were line-broadened using a 6.5-Hz exponential filter and reconstructed to generate NAA- and NAAG-edited spectra for each phantom (equation 1).

HERMES NAA/NAAG/Asp experiments were also performed in a 25 mM Asp phantom and in a 10 mM NAA phantom with a 32-channel head coil for receive. Scan parameters were: (3 $cm)^3$ voxel size; CHESS water suppression; TR = 2 s; and 64 averages. MEGA-PRESS acquisitions were also performed in the same phantoms with the same scan parameters. The TE was varied from 70 ms to 210 ms, with the 20 ms sinc-Gaussian editing pulses applied at 3.89 ppm (ON) and 10 ppm (OFF) for Asp; for NAA, the editing pulses were applied at 4.38 ppm (ON) and 10 ppm (OFF).

Percentage crosstalk values were also calculated for both HERMES NAA/NAAG and HERMES NAA/NAAG/Asp experiments as in the simulations.

3.3.3 In vivo experiments

All in vivo experiments were done in a 5x3x3 cm^3 voxel in the right centrum semiovale of healthy adults on a Philips Achieva 3T scanner, using the body coil for transmit and a 32-channel phased-array head coil for receive. Data were acquired with 384 averages and VAPOR water suppression (54). Prospective frequency correction for field drift during the scan was performed based on the water frequency of water-unsuppressed scans from the localized voxel, that were acquired every 24 averages (i.e. every ~53 seconds) (39). Post-processing included phase-and-frequency correction of individual transients prior to HERMES reconstruction, based on the NAA acetyl peak using the 'Gannet' program (98). Frequency correction based on the NAA acetyl peak was preferred over use of the residual water peak, because the editing pulses applied at 4.5 ppm (Experiment A in Figure 3.3) and 4.62 ppm (Experiment C in Figure 3.3) partially invert the water peak at 4.68 ppm.

HERMES NAA/NAAG

In vivo experiments were performed as in the simulations in 12 healthy adults (3 male, 9 female; age 28 ± 6 years) with a TR of 2.2 s, TE of 150 ms, and a total scan time of 15 minutes. HERMES reconstruction to give separate NAA- and NAAG-edited spectra was performed according to Equation 1.

A non-linear least-squares fitting algorithm (using nlinfit in MATLAB) was implemented to model the in vivo spectra. The model was based on simulated NAA- and NAAG-edited spectra, line-broadened by a 3.5 Hz exponential filter to match the linewidths of in vivo data, was used to fit the in vivo spectra. For NAA fitting, the model included the simulated NAA lineshape and a linear baseline, with three fitted parameters: NAA amplitude, slope and offset. For NAAG fitting, the model included the simulated NAAG lineshape, a Gaussian to model GSH and a linear baseline, with six fitted parameters: NAAG amplitude, GSH amplitude, offset and width, and baseline slope and offset. Both in vivo and simulated NAA and NAAG-edited spectra were zero-filled to 4096 data points. In vivo data were not line-broadened prior to fitting. The glutathione resonance that co-edits in the NAAG reconstruction was also included in the model as a Gaussian peak centered at 2.95 ppm. The percentage standard error in the amplitude coefficient of the fits was calculated to determine the uncertainty in the fits. After fitting, in vivo spectra were line-broadened using a 5 Hz exponential filter and zero-filled to 32k points for display purposes.

The 2-ppm N-acetyl singlet in the HERMES sum (A+B+C+D) spectrum was modeled as a Lorentzian lineshape in Gannet, to determine the peak integral A_{NA} while the 4.68-ppm water peak was modeled as a Lorentzian-Gaussian model. The total N-acetyl concentration was estimated relative to the unsuppressed water signal from the same volume (modeled as a Lorentz-Gaussian to determine A_W) , according to the following equation:

$$c_{\mathrm{NA}} = c_{\mathrm{W}} \frac{A_{\mathrm{NA}} n_{\mathrm{W}} (1 - \exp{(-\mathrm{TR}/T_{1\mathrm{W}})}) \exp{(-\mathrm{TE}/T_{2\mathrm{W}})}}{A_{\mathrm{W}} n_{\mathrm{NA}} (1 - \exp{(-\mathrm{TR}/T_{1\mathrm{NA}})}) \exp{(-\mathrm{TE}/T_{2\mathrm{NA}})}} \tag{3.2}$$

where c_W is the MR-visible water concentration in white matter (115), T_{1W} and T_{2W} are the longitudinal and transverse relaxation times of water in white matter, T_{1NA} and T_{2NA} are the longitudinal and transverse relaxation times of the N-acetyl methyl signal, and n_W and n_{NA} are 2 and 3 respectively, the numbers of protons contributing to each signal. Relaxation correction was performed using T_1/T_2 values for NA/water of: $T_{1NA} = 1.36$ s; $T_{1W} = 0.832$ s; $T_{2NA} = 0.277$ s; $T_{2W} = 0.0792$ s. MR-visible water concentration was assumed to be 35750 mM (115, 116). For each subject, separate concentrations of NAA and NAAG were determined by dividing c_{NA} according to the calculated NAA:NAAG ratio.

HERMES NAA/NAAG/Asp

Experiments were performed in 9 healthy adults (5 female; age 29 ± 5 years). Based on the simulations and phantom experiments, a TE of 150 ms was used for the *in vivo* scans. Reconstruction of the sub-acquisitions was then performed according to the bottom panel of Figure 3.2 to give separate NAA, NAAG, and Asp spectra.

NAA and NAAG were modeled as in the HERMES NAA/NAAG in vivo experiments. For Asp fitting, the model included the simulated Asp lineshape, as well as the NAA and NAAG

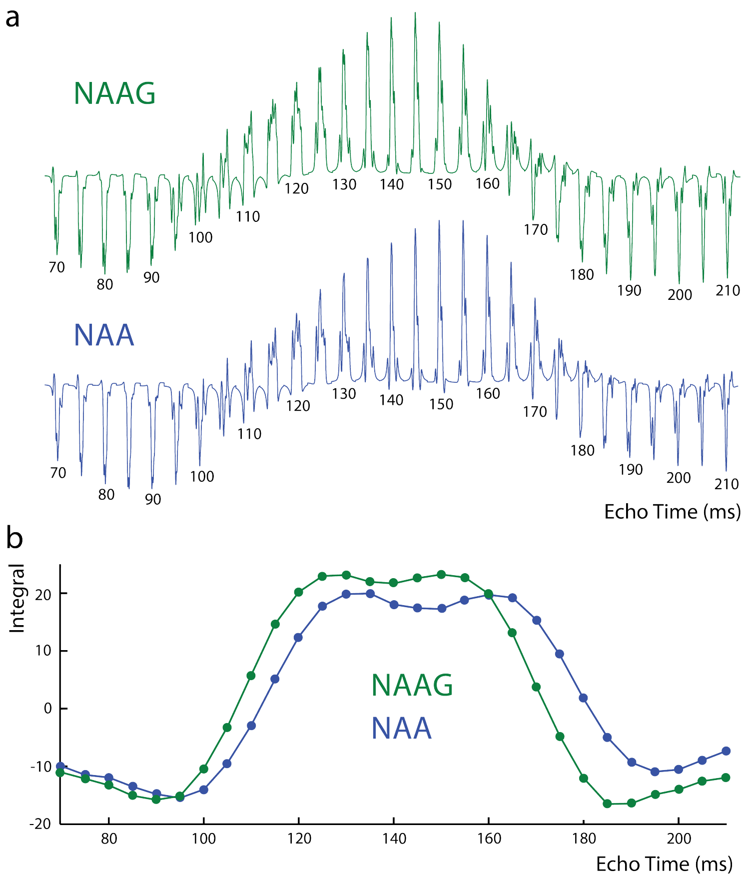

Figure 3.4. Simulations of MEGA-PRESS editing of NAA and NAAG at a range of echo times. Spectra (~2.6 ppm resonance) are shown in (a) and the corresponding integral (peak area) in (b). An echo time of 150 ms was selected for subsequent experiments, based on high editing efficiency for NAAG and to allow sufficient time for long, highly selective editing pulses to be used.

cross-term lineshapes (with fixed relative amplitudes set by the outcomes of NAA and NAAG modeling), and a linear baseline, i.e. four fitted parameters: Asp amplitude, the crossterm amplitude, and baseline slope and offset.

Scaling factors from the fitting routine indicate the relative concentrations of NAA, NAAG and Asp. The total [NAA+NAAG] concentration was estimated from the 2-ppm methyl signal and internal water reference as in the HERMES NAA/NAAG experiments. Based on the

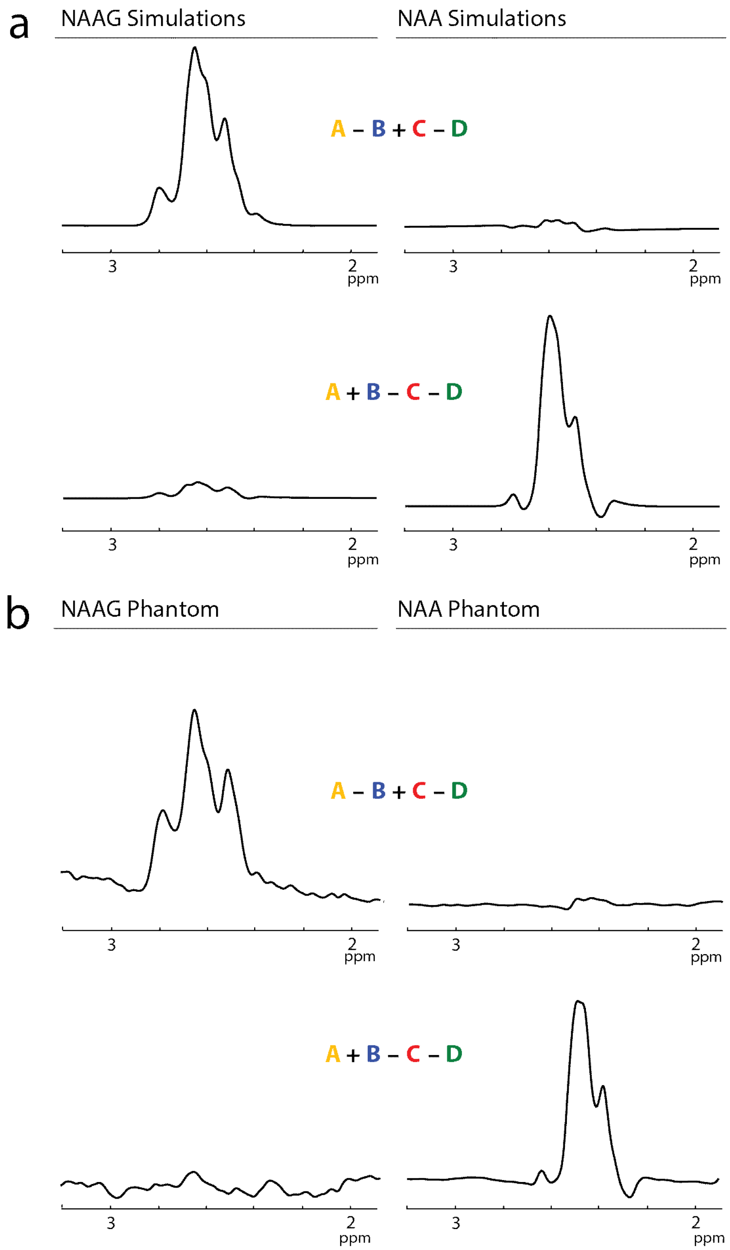

Figure 3.5. Simulations (a) and phantom data (b) demonstrate the excellent separation of NAA and NAAG signals into the desired HERMES recombination spectra with minimal metabolite crossover. The multiplet patterns of both NAA and NAAG are consistent between the simulated and reconstructed spectra.

calculated N-acetyl concentration, concentrations of NAA, NAAG and Asp were inferred (105) assuming that the aspartyl resonances of all 3 compounds have similar T_1 and T_2 relaxation times.

3.4 Results

3.4.1 HERMES NAA/NAAG

Figure 3.4a shows the simulation TE-modulation of the edited NAA and NAAG multiplets. Both have similar modulation as a function of TE, with maximal peak intensities at TEs between 130 ms to 160 ms, but are slightly offset from one another with the NAA maxima occurring ~10 ms after the NAAG (as the couplings are slightly different). This becomes more apparent from the integrals in Figure 3.4b, which show that the maximal difference signal intensities of the detected NAA spectra are shifted towards longer TEs relative to the detected NAAG spectra. Based on these data, a TE of 150 ms was chosen for HERMES NAA/NAAG detection to maximize the signal intensity of NAAG, which has substantially lower in vivo concentration, while still maintaining a high NAA signal. The longer TE also allows the use of the highly selective (45 ms) editing pulses necessary for HERMES NAA/NAAG experiments B, C and D (as in Figure 3.3).

Spectra from the HERMES simulations and phantom experiments demonstrate excellent agreement, in both the multiplet patterns of NAA and NAAG in their respective reconstructions, and the degree of residual cross-talk (Figure 3.5). RMS crosstalk of NAA into the NAAG reconstruction with the editing pulse in experiment D placed at 10 ppm was 3.7%. This was reduced to 2.8% by placing that editing pulse at 4.14 ppm. This low crossover was preserved in the NAA phantom experiments where the %RMSE was 4.1%. The RMS crosstalk of NAAG into the NAA reconstruction in the simulations was 9.4%, which is consistent with the crosstalk in NAAG-phantom experiments of 9.0%. These multiplet patterns were conserved in the *in vivo* spectra, as shown in Figure 3.6a. Both the *in vivo* NAA and NAAG multiplet patterns and relative signal intensities were consistent between subjects, as shown in Figure 3.6b. Representative fits to the in vivo data (Figure 3.6c) show that the simulated spectra fit the in vivo data well. This is reflected in the standard errors of the fitted amplitude coefficients, which were 1.36 ± 0.06% for NAA and 2.76 ± 0.5% for NAAG. Quantifying the NAA:NAAG concentration

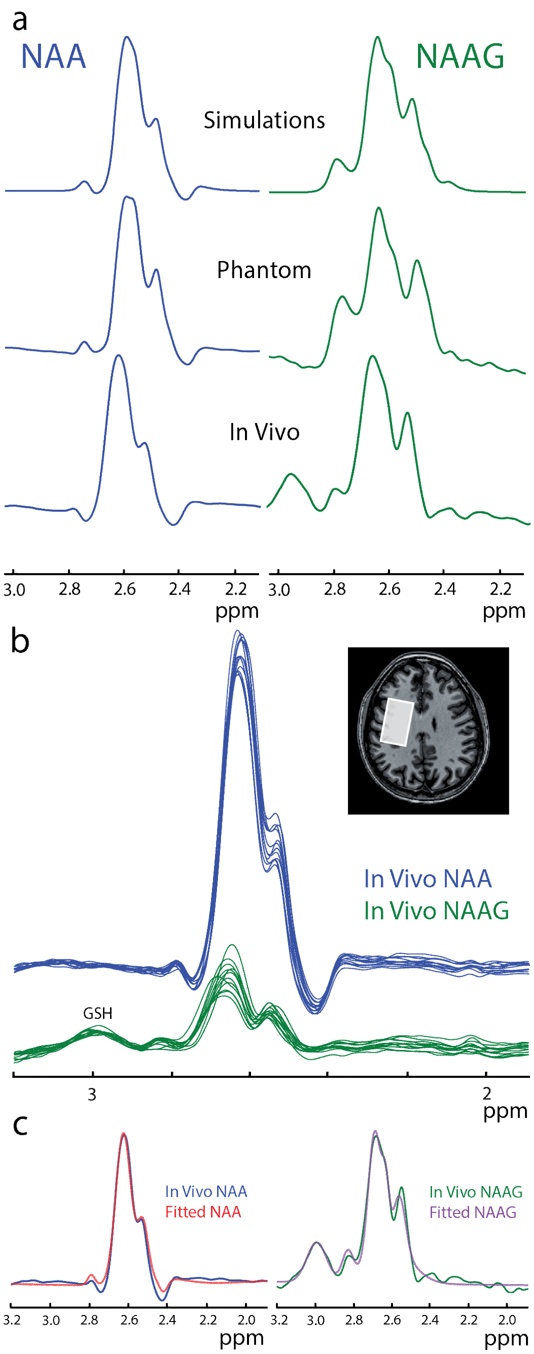

Figure 3.6. In vivo HERMES editing of NAA and NAAG. a) In vivo multiplet patterns show good visual agreement between simulations, phantom experiments and in vivo experiments (shown here for representative NAA and NAAG spectra), indicating good separation of NAA and NAAG in vivo. b) In vivo multiplet patterns are consistent across all 12 subjects for both NAA and NAAG as edited by HERMES. c) Fitting of the in vivo data (shown for one subject) was performed based on the simulations, in order to extract the NAA:NAAG concentration ratio.

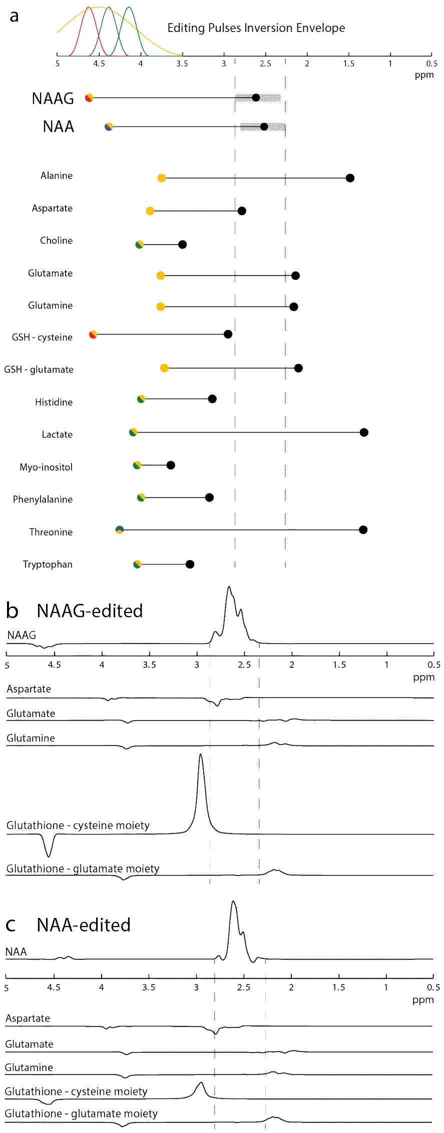

Figure 3.7. Coediting of other molecules in NAA/NAAG HERMES. a) Plot of coupled spin systems that may co-edit with NAA/NAAG. Spins that fall within the bandwidth of editing pulses applied in the HERMES experiment (shown by the colored Gaussian functions at the top) are color-coded accordingly. Species that are 'NAAG-like' (color-coded yellow-red) tend to appear in the NAAG-edited combination. Species that are only inverted by the yellow (ON,ON) inversion pulse will appear equally in NAA and NAAG edited spectra. Dotted vertical lines mark the range of the detected NAA and NAAG edited signals. b) Equimolar simulations of co-edited spectra in the NAAG HERMES reconstruction. The most efficiently co-edited species is the GSH-cysteine moiety, which appears in the NAAG-edited spectrum. Aspartate, Glutamine and GSH-Glu are co-edited to similar degrees in NAA- and NAAG-edited spectra, as they are only inverted by the yellow (ON, ON) pulse.

ratio based on these fits, an average value of 4.22:1 (standard deviation: ±0.66) was found. NAAG and NAA concentrations were calculated as 1.85 ± 0.33 mmol/dm^3 and 7.81 ± 0.79 mmol/dm^3 respectively (mean±standard deviation) , in good agreement with literature values (105, 111, 113).

Figure 3.7a shows the compounds potentially co-edited by the HERMES NAA/NAAG experiment. Glutamate, glutamine, glutathione (cysteine and glutamate moieties), and aspartate have multiplets close to the range of the detected NAA/NAAG peaks at ~2.6 ppm. In the HERMES NAA/NAAG simulations of these compounds (Figure 3.7b) however, only aspartate results in overlapping spectra in the detected range in both the NAA and NAAG reconstructions, at a level of about 5% of the signal achieved in an aspartate-targeted MEGA-PRESS experiment. Glutathione gives a peak at 2.95 ppm, co-editing in the NAAG-edited spectra at 78% (relative to a GSH-targeted MEGA-PRESS experiment) and in the NAA-edited spectra at 20%. This glutathione peak can also be seen in the NAAG reconstruction in vivo.

3.4.2 HERMES NAA/NAAG/Asp

In both simulations and phantom experiments, Asp shows significant TE-modulation of the observed peak at 2.6 ppm from TE = 70 ms to 210 ms, reaching a maximally negative signal at 140-160 ms, as shown in Figures 3.8a. Simulations and phantom experiments for Asp show good agreement for TEs up to about 170 ms, but start to diverge at longer echo times (Figure 3.8a). In both phantom experiments and simulations, the TE-modulation of Asp deviates significantly from that of NAA and NAAG over the same echo time range (Figure 3.8b). NAA and NAAG simulations also show maximal positive signal at TE 130 ms to TE 170 ms. This is also a range in which Asp obtains a maximal negative signal, thus a TE of 150 ms was chosen for HERMES editing of Asp, NAA, and NAAG.

Simulated HERMES NAA/NAAG/Asp sub-spectra are shown in Figure 3.9. NAA and NAAG show the expected positive refocused signal in the ON cases (A and B for NAA, A and C

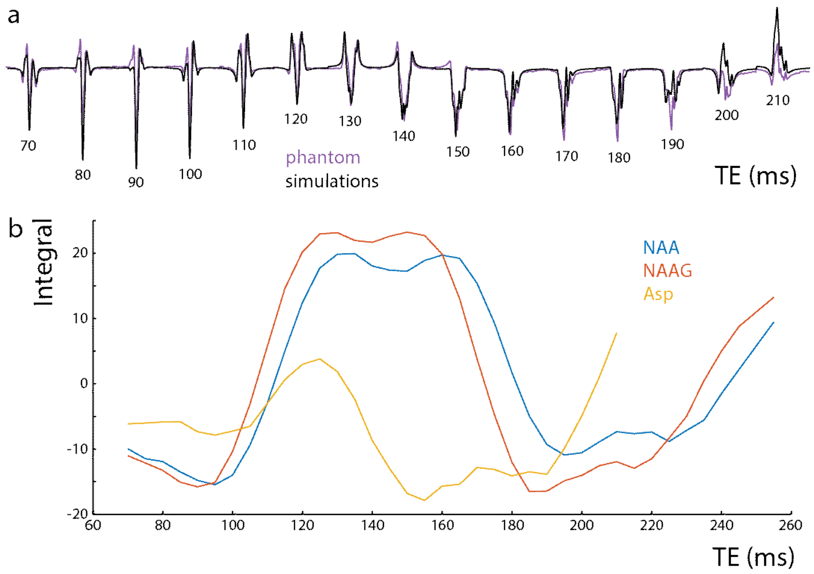

Figure 3.8. Simulations of MEGA-PRESS difference spectra of Asp, NAA, and NAAG at a range of echo times. (a) Simulations (black) and phantom (purple) MEGA-PRESS experiments of the Asp peak (~2.7 ppm) at echo times varying from 70 to 210 ms. (b) Simulations of the peak areas of MEGA-PRESS difference spectra for Asp, NAA, and NAAG peaks at ~2.6-2.7 ppm ppm as a function of echo time (70 to 260 ms).

for NAAG) and the expected negative signal in the OFF cases (C and D for NAA, B and D for NAAG). For Asp, however, signals are negative in the ON cases (A and D) and positive in the OFF cases (B and C). Hadamard combinations of these subspectra are shown in Figure 3.10. It can be seen that reconstructed spectra for each metabolite are well segregated with little crosstalk between them (mean RMS 4.5%).

There is good agreement between phantom data (Asp, NAA) and simulations of the HERMES reconstructions of individual metabolites, as shown in Figure 3.10, although the phantom multiplet patterns of NAA more closely agree with simulations than those of Asp. Phantom crosstalk values averaged to 6.3% RMS.

Figure 3.11a shows the Hadamard-reconstructed NAA, NAAG, and Asp spectra in all 9 subjects. The *in vivo* multiplet patterns and relative signal intensity of the three metabolites are

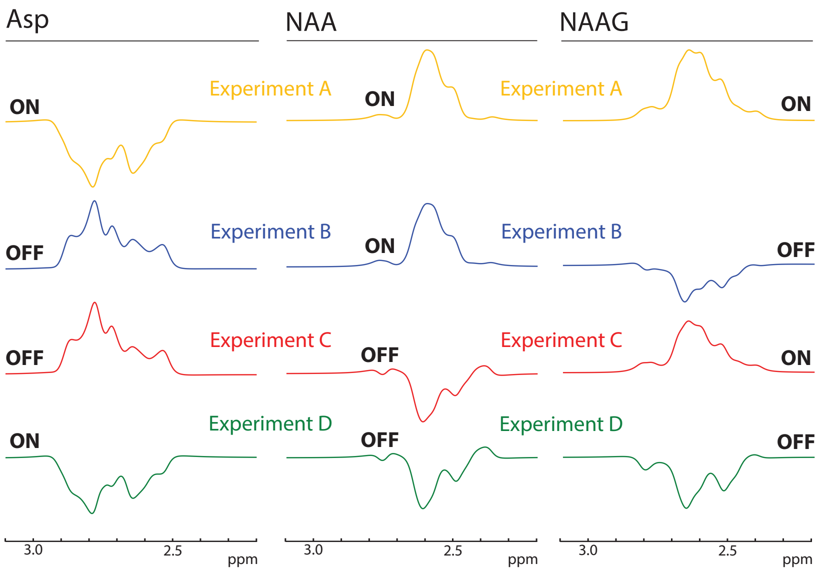

Figure 3.9. The simulated subspectra for Asp, NAA, and NAAG for each of the HERMES steps. Each row corresponds to the outcome of a single sub-experiment (A, B, C, D), as simulated for a different metabolite. The editing pulses that are used for each case are shown (with the same color coding) in Figure 3.2, bottom left. For NAA and NAAG, a positive refocused signal can be seen in the ONs for each metabolite and an inverted peak can be seen in the OFFs for each metabolite as expected. Relative to NAA and NAAG, the phase of the Asp peak in the ONs and OFFs is inverted, showing a negative signal in the ONs and a positive signal in the OFFs.

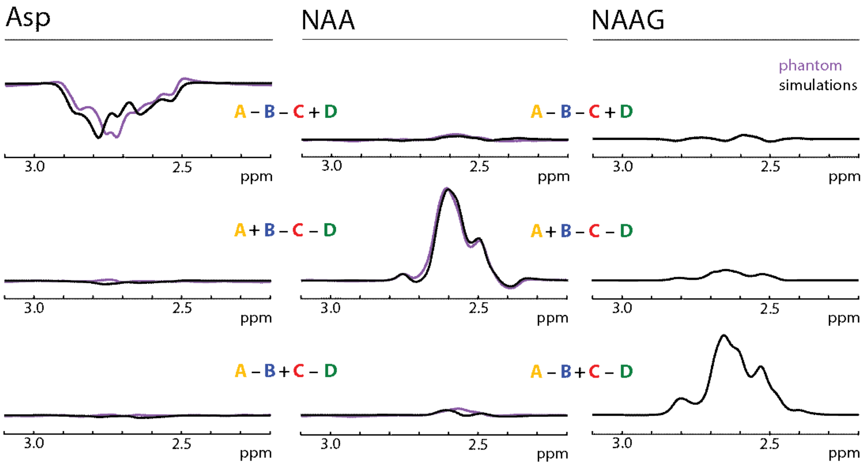

Figure 3.10. Simulations (purple) and phantom spectra (black) of Hadamard reconstructions of Asp (left), NAA (middle) and NAAG (right) for the editing scheme of Figure 2. The multiplet patterns are in good agreement between simulations and phantom experiments and all metabolites show good segregation into their intended reconstruction with little crosstalk between the Hadamard combinations.

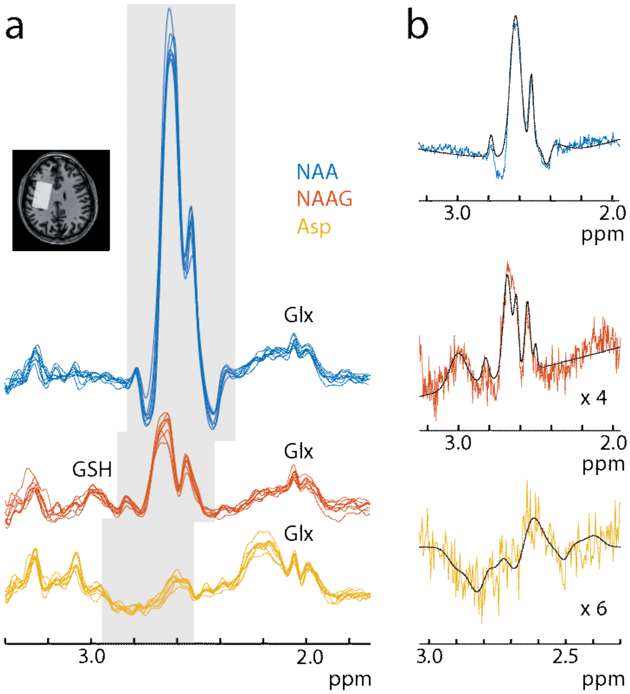

Figure 3.11. (a) Simultaneous, separable in vivo HERMES editing of NAA (blue), NAAG (orange), and Asp (yellow) in all 9 subjects. The β-aspartyl resonances are highlighted in grey. The reconstructed spectra show consistent multiplet patterns and relative signal intensities between subjects. b) Representative fits of the in vivo data in one subject for NAA, NAAG and Asp.

consistent across all subjects. Representative fits to the data (shown in Figure 3.11b) demonstrate that the simulated model fits the data well for NAA, NAAG and Asp, yielding the following concentrations: NAA 8.03 ± 0.69 mM, and NAAG 2.16 ± 0.34 mM and Asp 0.88 ± 0.17 mM, in good agreement with literature values of about 7.8 mM for NAA, 1.9 mM for NAAG, and 1 – 1.4 mM for Asp. (13, 111, 117).

Simulations of co-edited metabolites are shown in Figure 3.12. All of the metabolites considered (except taurine) have resonances in the vicinity of the detected region of Asp, NAA, and NAAG, however actual resonance overlap is minimal (Figure 3.12a). When in vivo concentrations of co-edited metabolites are considered, this overlap is more significant but still relatively small (Figure 3.12b). Glutamate, glutamine, and the glutamate moiety of GSH (Glx) are co-edited to a greater degree in the Asp Hadamard combination than in either the NAA or

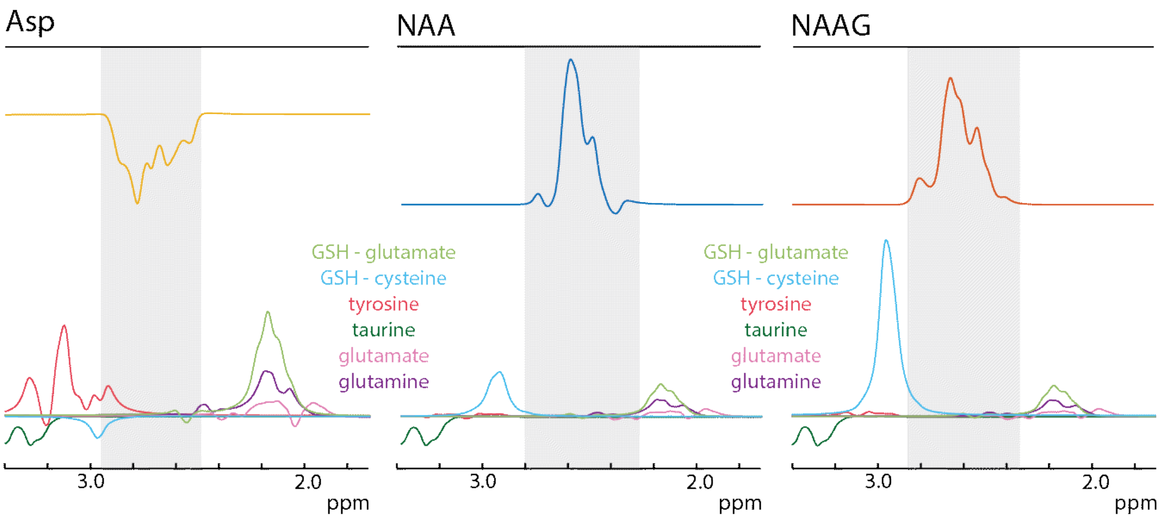

Figure 3.12. Simulations of co-edited metabolites in each Hadamard combination for the HERMES scheme given in Figure 3.3 (a) assuming equimolar concentrations and (b) weighted according to in vivo concentration values in literature. Grey denotes the detected β-aspartyl region of Asp, NAA, or NAAG in the reconstructed spectra. The cysteine moiety of glutathione is most predominantly edited in the NAAG spectrum and partially overlaps with the detected region of NAAG. Glutamate, glutamine, and the glutamate moiety of glutathione are co-edited to a greater degree in the Asp Hadamard combination but do not overlap significantly with the detected region.

NAAG reconstructed spectra. The predicted co-editing of glutamate, glutamine, and the glutamate moiety of GSH between the three Hadamard combinations agrees well with the spectra recorded *in vivo* (Figure 3.11a); the signal intensity of these peaks ~2.1-2.2 ppm is similar in the NAA and NAAG reconstructed spectra, but is greater in the Asp reconstructed spectra. The cysteine moiety of glutathione at 2.95 ppm is larger in the NAAG Hadamard combination than in the Asp or NAA Hadamayord combinations and partially overlaps with the detected region of NAAG. This glutathione peak can also be seen in vivo (Figure 3.11a). Thus, a Gaussian function centered on 2.95 ppm for the GSH-cysteine moiety was included in the fitting of the NAAG spectrum (Figure 3.11b). Tyrosine is co-edited more in the Asp combination but was not included in the fit due to its low concentration and consequently low signal contribution in the resulting Asp combination (Figure 3.12b)

3.5 Discussion

In this chapter, it is demonstrated that the simultaneous detection of more than one molecule is possible using HERMES. For the examples given here for NAA/NAAG and for NAA/NAAG/Asp, HERMES gives minimal cross-talk in the reconstruction of two or three otherwise overlapping molecules. HERMES editing represents a two-fold or three-fold reduction of scan time compared to sequential editing of each compound individually using MEGA-PRESS. Although it is only demonstrated here for editing two or three molecules simultaneously, as a Hadamard-based method, HERMES can in principle be applied to larger numbers of editing targets (or other pairs of compounds, such as GABA and overlapping co-edited macromolecules). Hadamard 'editing' methods have long been applied in high-resolution NMR to accelerate the acquisition multiple one-dimensional experiments (118).

Simultaneous edited detection of multiple metabolites carries a temporal SNR advantage over consecutive measurements of $\sqrt{n}$, where n is the number of molecules simultaneously detected (so long as the SNR of the combined measurement is not compromised). In the case of time-resolved measurements of a dynamic system, such as pharmacological or functional (119) studies, simultaneous measurements are scientifically preferable and increase the available temporal resolution by a factor of n.

The spin systems of NAA, NAAG, and Asp are amenable to detection by HERMES as their editing target spins are sufficiently resolved that they can be separately inverted using highly selective (long-duration) editing pulses in experiments B and C. This is aided by the similar echo-time-dependence of all three molecules with near-maximal signal intensity at a relatively long optimal TE, within which long-duration editing pulses with sufficient frequency selectivity needed to separate NAA, NAAG, and Asp with minimal crosstalk can be accommodated. These data also demonstrate that Asp can be edited *in vivo*.

Additional work is needed to further reduce the spillover of metabolites into their non-intended Hadamard reconstruction. More sophisticated fitting techniques using basis sets of individual molecules, e.g. LCModel (72) or Tarquin (120), may also lessen the effects of co-editing on the accuracy of measuring NAA, NAAG, and Asp. To extend this technique for use in chemical shift imaging, good B_0 homogeneity and stability would be needed. It is worth noting that the long editing pulses used here have narrow bandwidth, and are therefore very susceptible to B_0 field instabilities (104, 112). For this reason, it was necessary to apply prospective field-frequency correction during the experiment, based on voxel-localized B_0 offset measurements.

In HERMES editing of NAA and NAAG, the long editing pulses in experiment B and C, which are ideally fully ON for one molecule and fully OFF for the other, in fact do not perfectly invert just NAA, or just NAAG. Bloch equation simulations of the pulses (as shown in Figure 3.3a) indicate a partial inversion of NAA in the NAAG-only experiment (1%) and vice versa. This will lead to 'cross-talk' between the two experiments. Therefore in experiment D of HERMES NAA/NAAG, the editing pulse is placed at 4.14 ppm, symmetrically about the 4.38 ppm NAA resonance relative to the experiment C. Thus, NAA spins are partially inverted to the same degree in C and D, which are subtracted for the NAAG spectrum, reducing the NAA contribution to the NAAG-edited spectrum by a quarter. Cross-talk of NAAG into the NAA spectrum is a lesser concern, since NAA is the more highly concentrated of the two molecules. Although this scheme results in a slight reduction of NAA signal intensity in the NAA-edited spectra, this is also acceptable from an SNR viewpoint due to its higher concentration.

One potential consequence of the 4.14 ppm editing pulse in experiment D, however, is the co-editing of additional compounds. It can be seen in Figure 3.7a that this pulse (as well as the less selective editing pulse used in experiment A) partially inverts aspartate at 3.89 ppm, which is coupled to aspartate signals at 2.65 and 2.8 ppm, within the detected NAA/NAAG frequency range. Since the inversion of this aspartate spin is slight, and only affects one of the four spectra used to form the final reconstruction, its contribution to the final NAA and NAAG reconstructions are minimal as shown in Figure 3.7b.

Of the other potentially co-edited compounds in HERMES editing of NAA/NAAG as shown in Figure 3.7a, glutamate and glutamine, as well as the glutathione cysteine and glutamate moieties have coupled spins whose spectra appears in or near to the detected NAA/NAAG region. The cysteine moiety of glutathione at 2.95 ppm strongly co-edits in the NAAG reconstruction, but not the NAA reconstruction. The substantial representation of the cysteine moiety in the NAAG reconstruction is due to the inversion of glutathione spins at 4.56 ppm from both the editing pulse at 4.5 ppm (ON both NAA and NAAG) from experiment A and the editing pulse at 4.62 ppm (NAAG) in experiment C. The glutathione cysteine moiety co-edits less in the NAA reconstruction since the editing pulse at 4.38 ppm (NAA) inverts the 4.56 glutathione spins to a much smaller degree. This glutathione peak can be seen in the in vivo NAAG reconstruction as shown in Figure 3.6, but since it is resolved from the observed NAAG peaks has relatively little influence on quantitation of the NAAG spectra. Glutamate, glutamine, and the glutamate moiety of glutathione minimally co-edit on both the reconstructed NAA and NAAG spectra, since their corresponding target resonances are only partially inverted (16% for glutamate and glutamine and 18% for glutamate moiety of glutathione) by one of the four editing pulses.

It is interesting to consider the full 4x4 Hadamard reconstruction matrix. In addition to the NAA- and NAAG-edited difference spectra discussed for HERMES NAA/NAAG, it is also possible to calculate the A+B+C+D and A-B-C+D combinations. The A+B+C+D sum spectrum contains those signals that are not affected by the editing pulses at full SNR, which may be useful for quantification of the non-edited spectral resonances. The A-B-C+D subtraction spectrum should not contain any signal from either edited or non-edited compounds; it may potentially be useful either as an empty spectrum from which to quantify subtraction artifacts. The Hadamard editing encoding is scalable to detect a large number of molecules, with four-to-seven molecules detectable with eight editing pulse combinations. The two-molecule approach demonstrated here may also be applicable to other pairs of molecules, e.g. GABA and macromolecular signals at 3 ppm. Co-editing of non-overlapping signals will occur as with MEGA-PRESS, and will further increase the number of metabolites that can be quantified with these experiments.

The edited Asp signal is optimally edited in the same TE range as NAA and NAAG (at TE = 150 ms), but with opposite polarity. This unexpected result is likely due to its larger geminal **β -β** ($J_{33'}$) coupling (-17.43 Hz, compared to the -15.92 Hz and -15.91 Hz of NAA and NAAG respectively), which is not refocused by the editing pulses. Although the Asp TE-modulation is in good agreement between simulations and phantom experiments up to about TE ~160 ms, the multiplet form diverges significantly at longer TE; the reason for this is unclear, but may either be due to inaccuracies in the spin system parameters used for the simulations, or other factors such as spatially inhomogeneous coupling evolution which was not considered in the simulations (17, 45).

In this implementation of HERMES NAA/NAAG/Asp, both NAA and NAAG are edited reliably with concentrations and metabolite patterns similar to those found in HERMES NAA/NAAG and in phantom experiments and simulations. This suggests that the implementation of the triple-aspartyl HERMES presented here does not bias the metabolite concentration measurements relative to double editing of NAA and NAAG with HERMES. It is also shown that, despite its low concentration, Asp can be quantified reliably using J-difference editing. HERMES detection of all three metabolites is aided by the high-bandwidth editing pulse in experiment A that has a more rectangular inversion åprofile (compared to the conventional (sinc-Gaussian editing pulses) that can fully invert the full frequency range of targeted spins (0.72 ppm) of NAA, NAAG, and Asp. The editing pulses in experiments B, C, and D are also sufficiently selective so that NAA and NAAG are well separated from other edited metabolites. Quantification of Asp with HERMES can be improved upon, however, by reducing the contamination from NAA and NAAG in the Asp Hadamard combination with a fuller optimization of the frequency offsets and durations of the applied editing pulses. It is a limitation that the quantification presented here relies on assumptions about the relaxation behavior of the different aspartyl spin systems. Indeed, HERMES experiments like this, performed with variable TR (and possibly TE) might provide a feasible route to measuring relaxation parameters in vivo.

Comparing the co-editing simulations performed for HERMES NAA/NAAG/Asp to those in HERMES NAA/NAAG, this implementation of HERMES does not significantly co-edit any additional metabolites. The cysteine moiety of glutathione remains the most significantly co-edited metabolite within the detected NAAG frequency range and was included in the fitting of the spectra. Considering the dissimilarity between the Asp multiplet pattern ~2.6 ppm in phantom experiments and in vivo, residual NAA and NAAG were included in the final fit to the Aspartate spectrum which resulted in a good fit of the simulated model to the Asp spectrum.

In conclusion, the HERMES method has been developed to allow the simultaneous and separable editing of two or more overlapping molecules with near maximal sensitivity, and illustrated in detail for the examples of NAA/NAAG and NAA/NAAG/Asp. The method has the advantage of increased SNR compared to sequential measurements of individual molecules in the same total amount of scan time. In healthy subjects, the method is shown to be reliable both in terms of the multiplet pattern of the spectra, as well as the absolute and relative concentrations of the two molecules, indicating minimal molecule crossover between the two reconstructed spectra. HERMES can be applied to other overlapping edited species, and extended to more than two compounds by appropriate experimental design and Hadamard reconstruction.

Chapter 4 - Spatial Hadamard encoding of J-edited spectroscopy using slice-selective editing pulses

4.1 Introduction

One difficulty with in vivo ^{1}H MRS is the relatively low concentrations of metabolites studied, which require long acquisitions for sufficient signal-to-noise ratio (SNR). It is often desirable to measure spectra from multiple brain regions, but sequential collection of SV data quickly becomes time-prohibitive, and is also inefficient, in that only a fraction of the total scan time is used to collect signal from any one region. Consequently, strategies for the simultaneous acquisition of MRS data in multiple locations have been developed, most notably MR spectroscopic imaging (MRSI) using phase-encoding and other techniques (30, 121). While MRSI can offer full brain coverage and relatively high spatial resolution (122), it does also place increased demand on scanner stability, difficulties in simultaneously optimizing field homogeneity over all regions, and is more artifact prone than SV-MRS, particularly with regard to head motion.

Therefore there has been interest in the development of techniques that simultaneously excite a limited number of voxels, and use a variety of methods to reconstruct the spectra from individual regions (123-125). These methods can be viewed as hybrid methods that have some of the advantages of both SV-MRS (i.e. good quality, less artifact-prone, easy to process and display) and MRSI (all voxels acquired simultaneously). The limitations of SV-MRS and MRSI are particularly relevant for the detection of editable metabolites such as γ-aminobutyric acid (GABA), lactate (Lac), and glutathione (GSH) (17, 35, 47). J-difference editing techniques are traditionally tailored to only detect one metabolite at a time in one region at a time which leads to a substantial loss in metabolite information relative to conventional MRS.

In this chapter, a new approach is described that extends the detection of edited spectra from single-voxel to multiple voxels simultaneously to increase the efficiency of data collection. The method, dubbed ‘Spatial Hadamard Editing and Reconstruction for Parallel Acquisition’ (SHERPA), allows for J-difference editing to be performed simultaneously in multiple voxels by the use of dual- or multi-slice RF pulses, and the application of a field gradient during the editing pulses to encode location-dependent editing. The editing pulses are applied according to a spatial Hadamard editing scheme, allowing difference-edited spectra from the two or more voxels to be separately reconstructed. A scheme to edit one metabolite in two voxels simultaneously and two metabolites in two voxels simultaneously is introduced and demonstrated for the example editing GABA and dual-editing of GSH and Lac respectively in simulations, phantom, and in vivo experiments. Performing multi-metabolite, multi-region editing with SHERPA has the potential to condense a series of time-intensive scans into a single acquisition while maintaining the same SNR level.

4.2 Theory

In Chapter 3, it has been shown that a Hadamard-encoded editing scheme allows the simultaneous acquisition of two or more metabolites in the edited spectrum of a single brain region (56). SHERPA also uses a Hadamard encoding scheme, the purpose of which is to simultaneously acquire edited signals from two voxels.

The method is initially illustrated for the case of one metabolite. The first step is to replace the slice-selective excitation pulse of the MEGA-PRESS sequence (76) with a dual-band excitation pulse, exciting two voxels simultaneously (as shown in Figure 4.1a). The editing pulses are then applied during a field gradient, which allows independent control of the editing-on frequencies in the two locations (as shown in Figure 4.1b). Four experiments are performed with the editing pulses either on-resonance (ON) or off-resonance (OFF) with respect to the editing

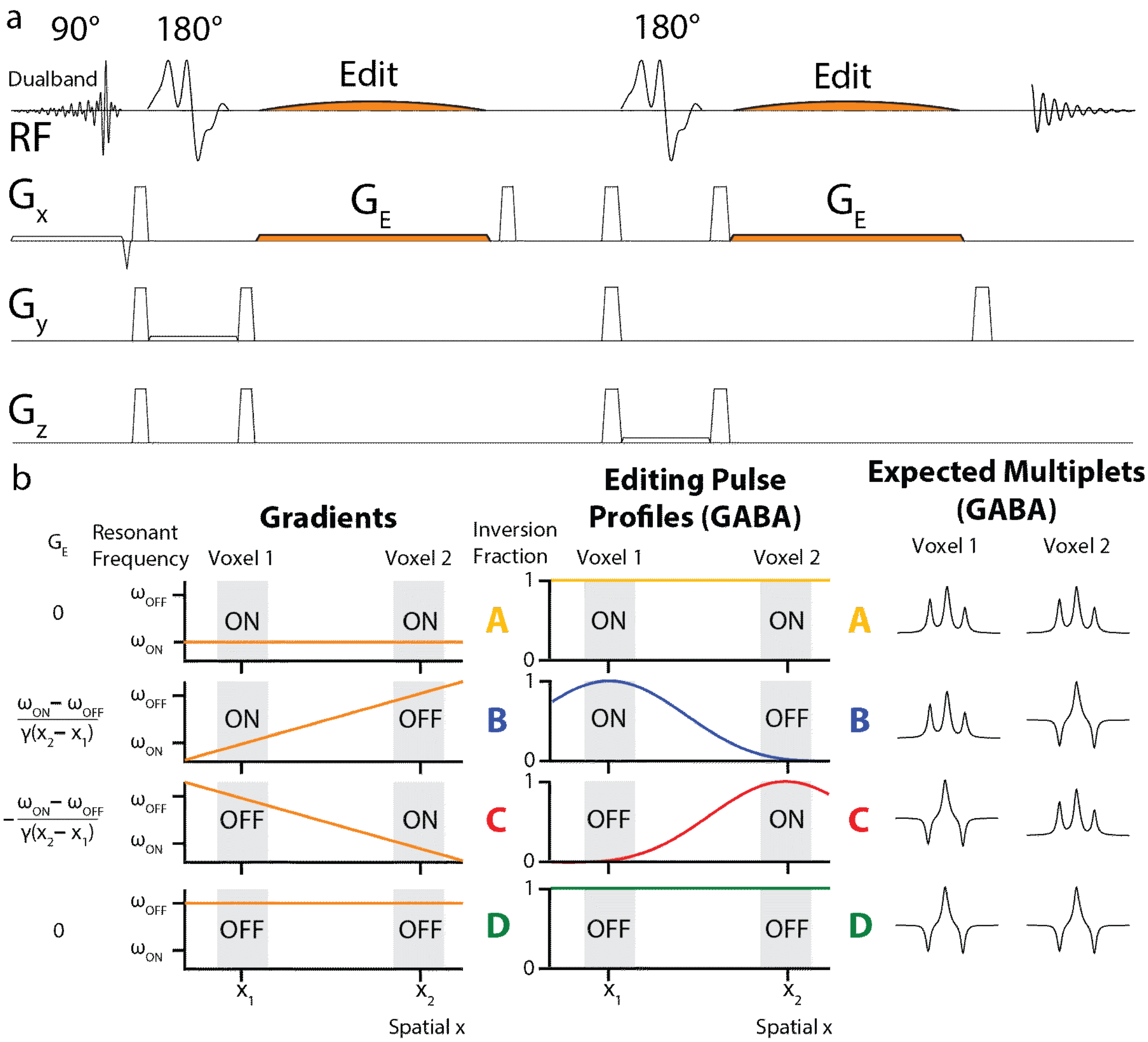

Figure 4.1. SHERPA schematic. (a) Pulse sequence based on MEGA-PRESS with dualband excitation pulses and field gradients applied during the editing pulses. The editing pulses and their associated field gradients are highlighted in orange. (b) Spatially dependent editing pulses can be applied to separate the difference spectra of two voxels (denoted Voxel 1 and Voxel 2). The gray shading denotes the dualband slice-selective range of the voxels. SHERPA consists of four sub-experiments A-D. The editing encoding (ON/OFF) is spatially dependent in experiments B and C through the introduction of a gradient G_E. ω_{ON} and ω_{OFF} correspond to the 'ON' and 'OFF' editing pulse frequencies respectively. The middle column shows the expected editing pulse inversion profiles in each of the sub-experiments for the example of GABA-editing. The right-hand column shows spectral simulations of the expected spectra for each experiment in response to the spatially selective editing pulses, in this case for editing of the GABA molecule.

|target: (ON_{vox1}, ON_{vox2}); (ON_{vox1}, OFF_{vox2}); (OFF_{vox1}, ON_{vox2}); and (OFF_{vox1}, OFF_{vox2}), denoted Experiments A-D in Figure 4.1b. Experiments A and D, (ON_{vox1}, ON_{vox2}) and (OFF_{vox1}, OFF_{vox2}), require the same editing frequency in both voxels, and thus have the editing gradient set to zero. Experiments B and C, (ON_{vox1}, OFF_{vox2}) and (OFF_{vox1}, ON_{vox2}), require different editing pulse frequencies in the two voxels, and thus have the editing gradient on with opposite polarity in each. The predicted outcome of these four experiments is schematically illustrated in Figure 4.1 for the example of GABA editing, with editing pulses applied at 1.9 ppm in ON scans (ω_{ON}), at some other frequency off-resonance in the OFF scans (ω_{OFF}) and TE ~ 1/2J (68 msec).

Combining the experiments (A+B-C-D) gives the J-difference-edited spectrum for Voxel 1, with signal from Voxel 2 suppressed. The combination (A-B+C-D) gives the J-difference-edited spectrum for Voxel 2, with signal from Voxel 1 suppressed. The function of the editing gradient G_E is to ensure that the editing pulse is experienced at the ON frequency in one voxel while at the OFF frequency in the other. Assuming the positions of the two voxels are x_1 and x_2 respectively, the strength of the editing gradient is therefore given by:

$$G_E = (\omega_{ON} - \omega_{OFF})/\gamma(x_1 - x_2).$$

(4.1)

Assuming that the gradient field is zero at x = 0, the frequency at which the editing pulse should be applied for experiment B is given by:

$$\omega_B = \omega_{ON} + \gamma G_E x_1.$$

(4.2)

and for Experiment C:

$$\omega_C = \omega_{OFF} - \gamma G_E x_1.$$

(4.3)

Note that the orientation of the editing gradient is the same as that of the gradient used for slice-selective excitation. Often in spectral editing, the choice of the OFF editing pulse frequency can be relatively arbitrary. In the case of the SHERPA experiment, the OFF pulse frequency directly influences the editing gradient strength, and should be carefully considered; too small a difference between ON and OFF results in a weak gradient and difficulty in separating the 2 voxels, while the choice of a large difference may result in suboptimal editing within each voxel.

Finally, SHERPA also offers the possibility of editing two molecules (double editing, as in the 'DEW' experiment (78)) by placing the 'OFF' editing pulse at the target editing frequency of a second molecule. DEW-SHERPA allows two molecules to be simultaneously edited from two different voxel locations.

4.3 Methods

4.3.1 Simulations

SHERPA spectral simulations were performed for GABA, Lac and GSH. Density-matrix simulations were performed for a B_0 field strength of 3T using 'FID-A' (21), with GABA chemical shifts and coupling constants taken from reference (93), and those for GSH and Lac taken from reference (13). Simulations were spatially resolved in the excitation direction to include the effects of the editing pulse field gradient across the voxel. For the simulations and experiments, single-lobed sinc-Gaussian editing pulses (35) and conventional amplitude-modulated slice-selective refocusing pulses were used (88, 89). To determine the frequency variation of the editing pulse across the voxels in Experiments B and C, Bloch simulations were performed for the editing pulses in the GABA SHERPA and DEW SHERPA experiments examined in this study and the frequency offset at each voxel-edge was calculated. These same Bloch simulations were also performed for GABA SHERPA with a smaller distance (5 cm) between the two voxels, using two different editing pulse gradient strengths (0.041 mT/m and 0.054 mT/m). Density-matrix simulations were also performed.

Spatially Resolved GABA-edited SHERPA Simulations

GABA-edited SHERPA was simulated for two voxels of 30 mm thickness and 66 mm spacing (center-to-center). Ideal dualband slice-selective excitation was assumed, i.e. that the GABA spins are fully excited within the voxel slice width and not excited outside. A one-dimensional array of 16 spectra at a spatial resolution of 1.9 mm was calculated for each voxel. The pulse sequence shown in Figure 4.1A was simulated with echo time of 80 ms and 14-ms editing pulses with a 90 Hz bandwidth, applied at 1.9 ppm for ON and 1.0 ppm for OFF acquisitions. Experiments A and D were simulated with the editing gradient set to zero. In Experiment B (ON_{vox1}, OFF_{vox2}) the gradient strength was set to 0.041 mT/m, so that the editing pulse was close-to-resonance for 1.9-ppm GABA spins in Voxel 1, and off-resonance in Voxel 2, as described above. For Experiment C (OFF_{vox1}, ON_{vox2}), the gradient was applied with opposite polarity. The editing pulse in Experiment D (OFF_{vox1}, OFF_{vox2}) was applied at 1.0 ppm.

The Hadamard combinations (A + B – C – D) and (A – B + C – D) were calculated for all spatial locations. Spectra from locations within each voxel were then added together. The imperfection in separation of signals from the two voxels was quantified by calculating the signal from Voxel 1 that appears in the Voxel 2 Hadamard combination (expressed as a percentage of the signal from Voxel 1 that appears in the Voxel 1 Hadamard combination). This quantity is referred to as ‘crosstalk’ in this chapter. The SHERPA efficiency for each voxel was also calculated by dividing the simulated SHERPA signal by the signal simulated from an equivalent MEGA-PRESS experiment.

Spatially Resolved Simulations of GSH- and Lac-edited DEW-SHERPA

To demonstrate the feasibility of SHERPA for editing two metabolites at a time, the double-editing With (DEW) method (78) was adapted to simultaneously edit GSH and Lac for both voxels. Spatially resolved spectral simulations were performed in a similar manner to above, but with 9 spectra per voxel, a TE of 140 ms and 30 ms editing pulses with a bandwidth of 40 Hz, which had sufficient selectivity to ensure separation between the ON GSH (4.56 ppm) and the

ON Lac (4.1 ppm) editing pulses. Experiment A was simulated with no editing gradients and editing pulses applied at 4.56 ppm. Thus for GSH, this serves as the (ON_{vox1}, ON_{vox2}) experiment, while for Lac, this is the (OFF_{vox1}, OFF_{vox2}). Conversely Experiment D was simulated with no editing gradients and editing pulses applied at 4.1 ppm, to serve as (OFF_{vox1}, OFF_{vox2}) for GSH and (ON_{vox1}, ON_{vox2}) for Lac. Experiment B was simulated with a 0.021 mT/m editing gradient, so that the editing pulse is on-resonance at 4.56 ppm in Voxel 1 and at 4.1 ppm in Voxel 2, to serve as (ON_{vox1}, OFF_{vox2}) for GSH and (OFF_{vox1}, ON_{vox2}) for Lac. Similarly, Experiment C was simulated with a -0.021 mT/m editing gradient, so that the editing pulse is on-resonance at 4.1 ppm in Voxel 1 and at 4.56 ppm in Voxel 2, to serve as (OFF_{vox1}, ON_{vox2}) for GSH and (ON_{vox1}, OFF_{vox2}) for Lac.

As with GABA-edited SHERPA above, Hadamard combinations of the experiments were calculated, and crosstalk and SHERPA efficiency quantified for both GSH and Lac. Co-editing of different compounds (aspartate (Asp)), creatine (Cr), GABA, N-acetyl aspartate (NAA), N-acetyl aspartyl glutamate (NAAG), glycerophosphocholine (GPC), phosphocholine (PC), glucose (Glc) and ascorbate (Asc) was also simulated in the DEW-SHERPA experiments assuming equimolar concentrations and with chemical shifts and coupling constants taken from reference 13 (for all metabolites except GABA).

4.3.2 Phantom SHERPA experiments

All experiments were performed on a Philips Achieva 3T scanner using a 32-channel phased-array head coil for receive and a body coil for transmit (B_{1max} = 13.5 μT). To demonstrate the capability of SHERPA to accurately distinguish concentration differences between the two voxels, SHERPA experiments were performed in a 1L agarose gel phantom (pH 7.2) with different concentrations of GABA in the top half (10 mM) and bottom half (16 mM) of the phantom. Acquisition parameters were the same as the simulations described above, with the following additional parameters: chemical-shift-selective water suppression; two outer-volume

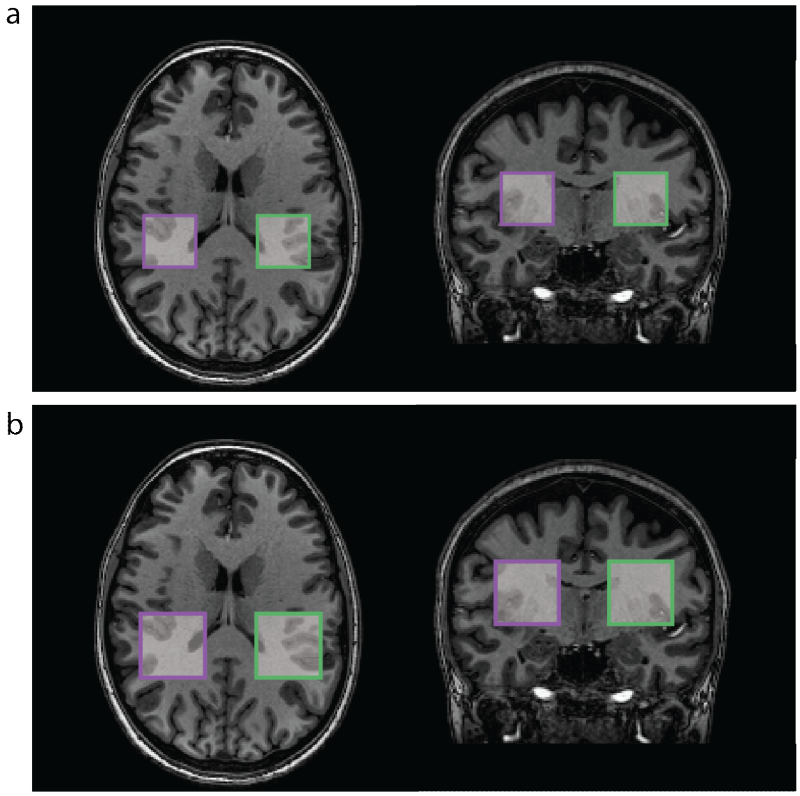

Figure 4.2. Voxel placements of in vivo SHERPA experiments overlaid on a T1-weighted axial image (left) and coronal image (right). The voxels are placed symmetrically about the midline in the right (purple, Voxel 1) and the left (green, Voxel 2) frontoparietal lobes. (a) 3 x 3 x 3 cm^3 GABA-edited SHERPA and (b) 3.6 x 3.6 x 3.6 cm^3 lactate and glutathione DEW SHERPA.

suppression bands to saturate signal in the phantom cap and base; TR 2 s; 2.7 x 2.7 x 2.7 cm^3 voxels; and 64 signal averages (i.e. 16 averages for each sub-experiment A-D). Spectra were line-broadened using a 5-Hz exponential filter and Hadamard-reconstructed to give difference-edited spectra for both voxels. SHERPA experiments were acquired with dualband excitation of the two voxels. RF excitation pulses were calculated by summing two individual single band excitation RF pulses (126) and reducing the B_1 amplitude and lengthening the duration of the pulse to maintain the correct flip angle (as described in reference 3). For comparison, SHERPA experiments with only Voxel 1 or Voxel 2 excited, were also acquired using conventional single-band slice-selective excitation pulses (126), and MEGA-PRESS acquisitions for each voxel excited separately were also collected. In these MEGA-PRESS acquisitions, 14 ms sinc-Gaussian editing pulses with a bandwidth of 90 Hz were placed at 1.9 ppm in the ON case and at 7 ppm in the OFF case.

One challenge with SHERPA is how to acquire matched non-water-suppressed data for each voxel for quantification, or other, purposes (such as phased-array coil combination). The approach taken here was to use the saturating effect of MEGA pulses applied on-resonance (i.e. when the editing pulses is applied at the water frequency, the water signal is effectively dephased (76)), repeating the SHERPA sequence with editing pulses applied to the water resonance in a Hadamard fashion. This allows for the separation of water signals from each voxel. Thus, the same four-part pulse sequence was performed with 10 ms editing pulses with a bandwidth of 122 Hz applied at 4.68 ppm and 5.25 ppm (and no water suppression). These SHERPA water signals were compared to the unsuppressed water scans from each voxel obtained during the MEGA-PRESS acquisition.

4.3.3 In vivo experiments

SHERPA GABA editing was performed in 10 healthy adults (3 female, 7 male; age 25 ± 3 years) in 3 x 3 x 3 cm^3 voxels located symmetrically in the left and right frontoparietal lobes (as shown in Figure 4.2a). DEW-SHERPA experiments for Lac and GSH were also performed in one healthy subject (1 male, age 22) in 3.6 x 3.6 x 3.6 cm^3 voxels centered on the same locations (Figure 4.2b). An outer-volume suppression pulse was applied to the scalp adjacent to Voxel 1 (right hemisphere) to suppress lipid signal from the scalp. Water suppression was achieved using the VAPOR sequence (54), and shimming performed up to second order. Non-water-suppressed SHERPA scans were also acquired with 16 averages, in order to obtain water references for both the SHERPA and DEW-SHERPA experiments. GABA MEGA-PRESS acquisitions of each voxel separately were also taken in another subject (1 male, age 28) for comparison to the SHERPA data.

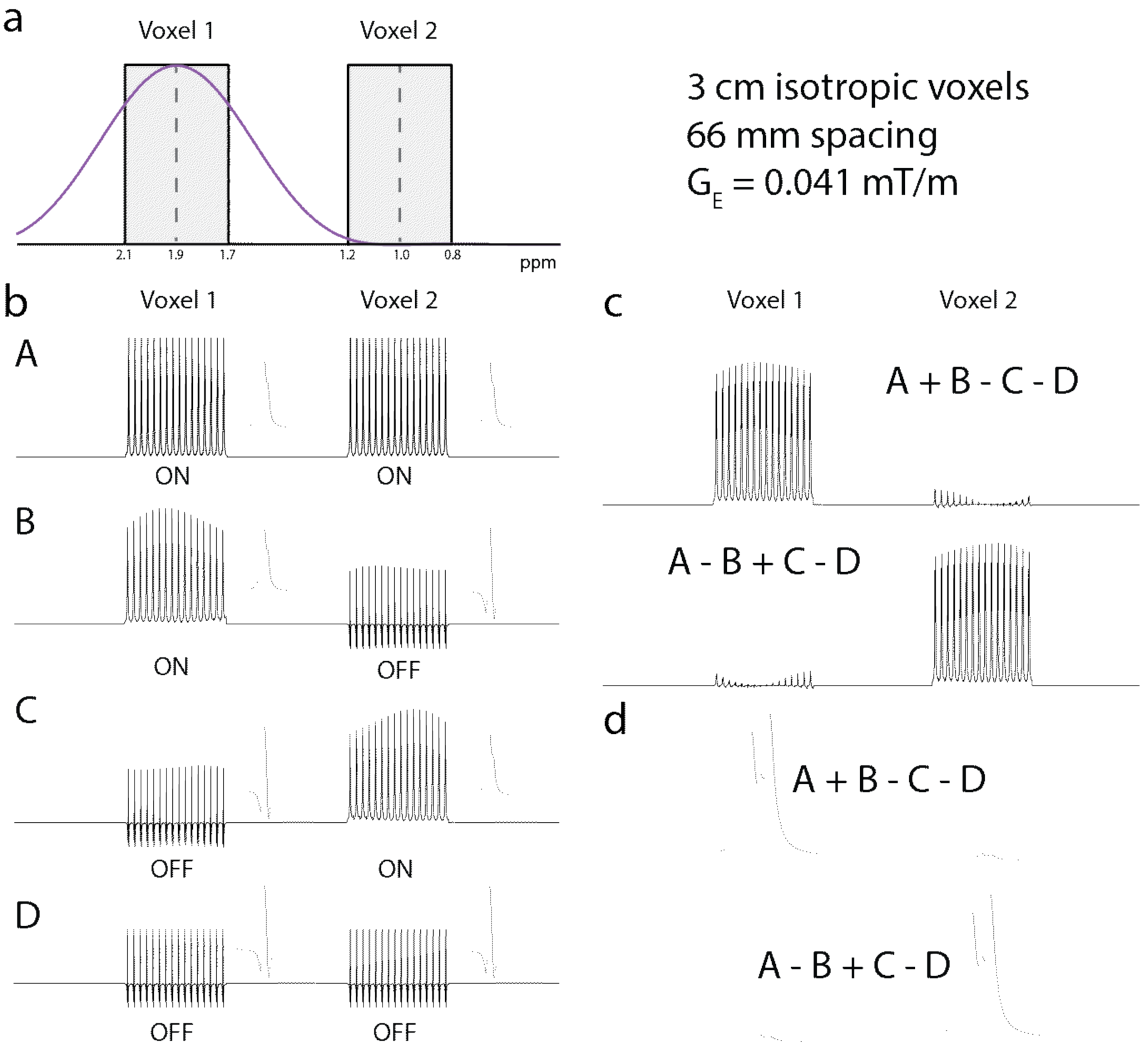

Figure 4.3. Spatially resolved simulations of SHERPA GABA-editing. (a) Editing pulse profile overlaid on the two excited voxels. The effective editing offset is marked for the voxel centers and edges. (b) The four sub-experiments A-D were simulated for a 1-D spatial arrays within Voxel 1 and Voxel 2. Only the 3-ppm GABA signal is shown. The voxel-average spectrum is also shown in each case to the right of the 1D array. (c) Hadamard combinations of the four experiments shown in (b). (d) Voxel average spectra corresponding to (c) demonstrate minimal crosstalk between the two voxels.

Acquisition parameters were the same as for the phantom GABA experiments, except 320 averages were acquired. DEW-SHERPA editing of GSH and Lac was performed as in the simulations, with 512 averages and TR 2s.

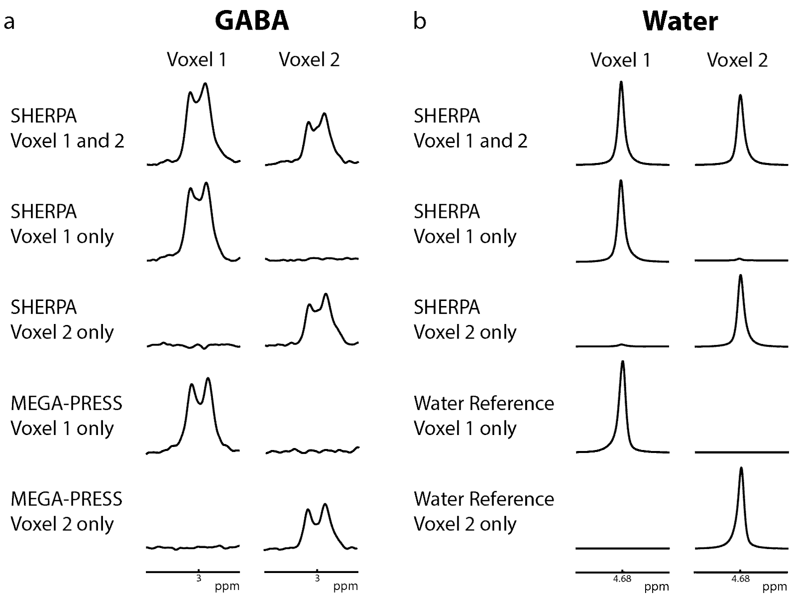

Figure 4.4. SHERPA and MEGA-PRESS spectra in a two compartment phantom containing GABA in a ratio of 1.6:1.0 (voxel 1: voxel 2). (a) GABA-edited spectra from Voxel 1 (left) and Voxel 2 (right) are shown, acquired with SHERPA (dual and single-voxel excitations) and MEGA-PRESS (single-voxel excitations). There is good qualitative and quantitative agreement in both voxels between the SHERPA and MEGA-PRESS GABA spectra. (b) SHERPA and MEGA-PRESS spectra of the unsuppressed water signal are also consistent between methods.

Prospective frequency correction for B_0 field drift during the scan was performed for DEW-SHERPA editing based on the water frequency of interleaved water-unsuppressed scans from the localized voxels that were acquired every 32 averages (39).

4.3.4 Reconstruction Software and Data Analysis

Prior to SHERPA reconstruction, individual transients of the GABA SHERPA experiment were phase-and-frequency corrected based on the residual water frequency (44). To reconstruct the spectra from each voxel, in-house software was used to combine the signals from the different channels. The spectra from each coil were first separated into the two voxels using the Hadamard combinations, as described above. Then, data from each coil were phased by the first point of the

FID of the unsuppressed water signal from each voxel, and then combined. This separation into the voxel-specific spectra before coil combination addresses coil-dependent phase differences between signals from the two voxels. After combining the data from the different channels, the data were zero-filled and the GABA peak at 3.0 ppm was fit using a Gaussian lineshape model. The resulting GABA peak area and the area of the water reference peak were then used to estimate GABA concentrations (in institutional units, ‘i.u.’) using the Gannet program (98). The SHERPA water reference area was multiplied by a factor of two to account for the water signal being saturated in two of the four Hadamard experiments. To compare the spectra from the SHERPA acquisitions to the MEGA-PRESS acquisitions from the same voxels, the signal-to-noise ratio was calculated for each spectrum by finding the maximum value of the fitted GABA peak and dividing by twice the standard deviation of the noise.

4.4 Results

Bloch simulations of the frequency variation of the editing pulse across the voxel in the GABA SHERPA experiments shown in Figure 4.3a indicate a slight frequency variation (±0.2 ppm) of the editing pulse across the voxel. Spatially resolved simulations of GABA-edited SHERPA, shown in Figure 4.3b, demonstrate that spatially dependent manipulation of the coupling evolution occurs as intended. GABA sub-spectra for each spatial location across the two voxels, and the voxel-sum spectra show the expected modulations, with positive outer lobes in ON spectra and negative outer lobes in OFF spectra. It can be seen that in Experiments B and C, the peak heights of the sub-spectra vary within the ‘ON’ voxel as the editing frequency shifts slightly from 1.9 ppm along the applied gradient. Hadamard combinations of the sub-experiments, shown in Figure 4.3c and 4.3d, demonstrate good separation of the GABA signal from each voxel. The SHERPA efficiency within each voxel was 97.8% (of that of MEGA-PRESS) and the crosstalk was 2.2%.

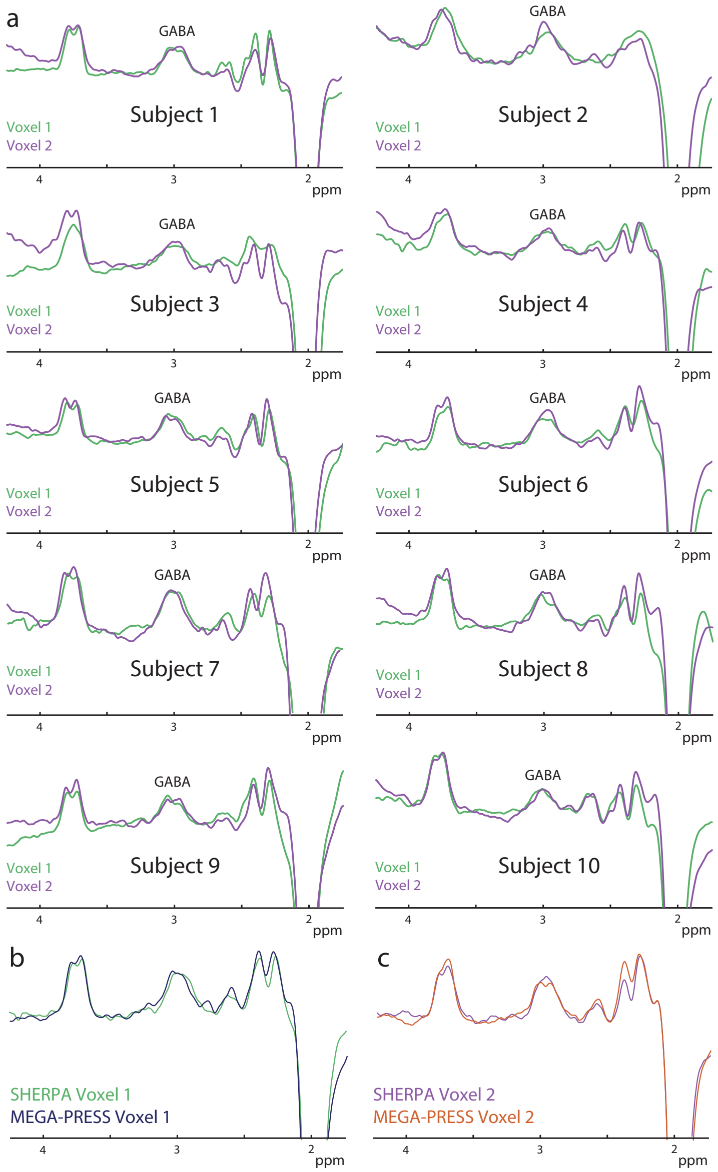

Figure 4.5. (a) Comparison of the in vivo GABA-edited SHERPA spectra between two equally sized voxels placed symmetrically about the midline in all 10 subjects. The edited spectra are consistent between subjects and between voxels of the same subject, demonstrating equal editing efficiency in both voxels as well as good repeatability of the experiment between subjects. Spectra are colored by location, as shown in Figure 4.2a with voxel 1 located left of subjects' midline and voxel 2 located right of the subjects' midline. (b) In vivo comparison between GABA-edited SHERPA and MEGA-PRESS acquisitions for one subject. The GABA-edited spectra at 3.0 ppm are consistent, demonstrating that the editing efficiency and quality of the SHERPA experiments is comparable to that of two conventional MEGA-PRESS editing experiments of twice the total duration.

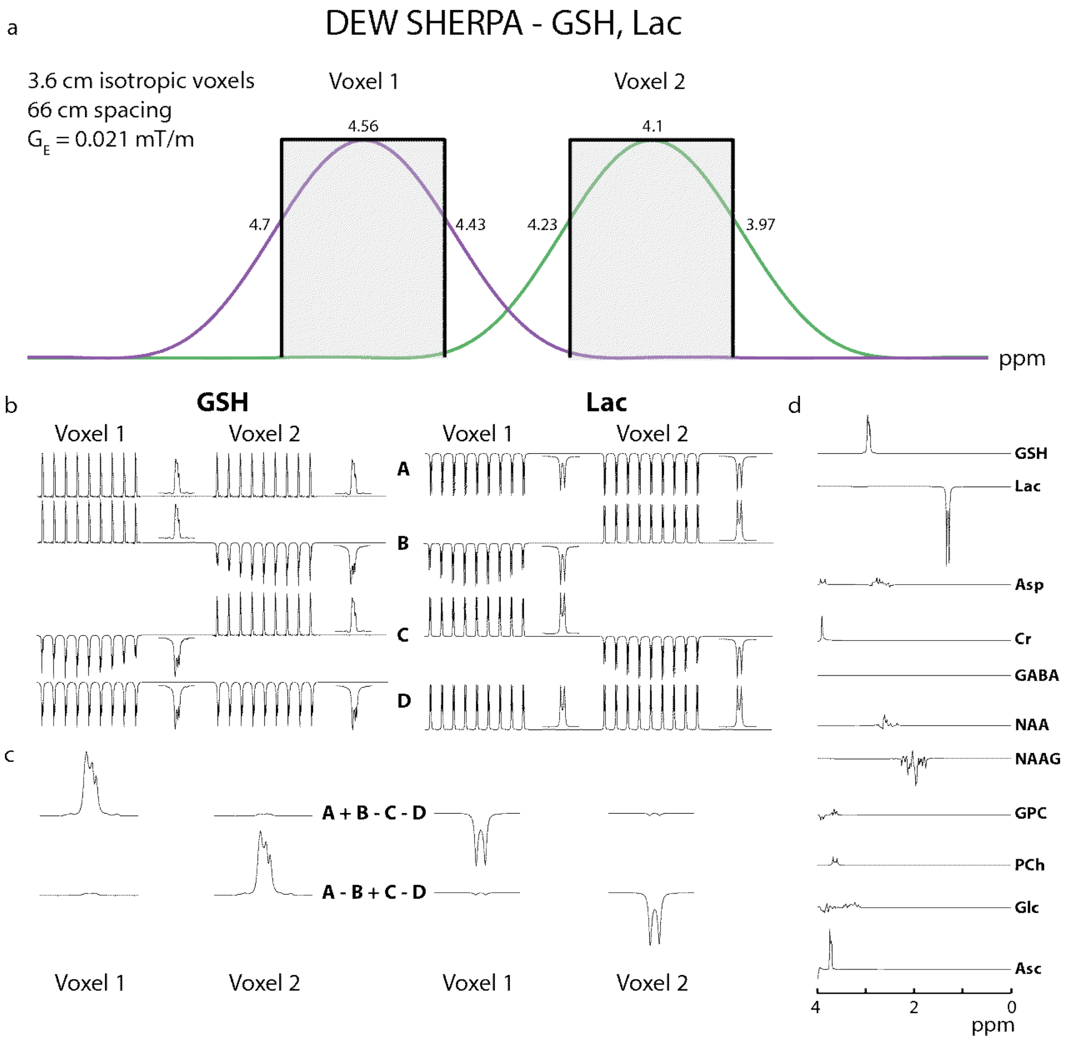

Figure 4.6. Spatially resolved simulations of DEW-SHERPA editing of GSH and Lac. (a) Editing pulse profile overlaid on the two excited voxels. The effective editing offset is marked for the voxel centers and edges. (b) The four sub-experiments A-D were simulated for 1-D spatial arrays within Voxels 1 and 2. The 2.95-ppm GSH signal (left) and the 1.3 ppm Lac signal (right) are shown for each experiment. The voxel-average spectrum is also shown in each case, demonstrating inverted signals in OFF experiments and positive signal in ON experiments. (c) Hadamard combinations of the four experiments show minimal crosstalk between the voxels. and positive GSH and negative Lac signals as expected. (d) Simulations of metabolites that may potentially co-edited in the DEW-SHERPA experiment, plotted between 4 ppm and 0 ppm. The GSH (2.95 ppm) and Lac (1.32 ppm) resonances are resolved from other co-edited signals. Abbreviations: Asp aspartate; Cr creatine; NAA N-acetylaspartate; NAAG N-acetylaspartylglutamate; GPC glycerophosphocholine; PCh phosphorylcholine; Glc D-glucose; Asc ascorbate.

GABA-edited SHERPA spectra from the phantom are shown in Figure 4.4a. Good agreement can be seen between the SHERPA reconstructions with either dual-voxel or single-voxel excitations, and in comparison to conventional single-voxel MEGA-PRESS spectra from each voxel. In addition, there is minimal crosstalk between the two voxels, as demonstrated in the SHERPA reconstructions of data collected when only one voxel is excited at a time. The ratio (voxel 1/voxel 2) of estimated GABA concentrations was found be 1.61:1 for SHERPA, which agreed well with the ratio 1.68:1 for SHERPA reconstructions of single voxel excitation data, and also ratio of 1.67:1 found for the MEGA-PRESS data. All these concentration ratios are close to the actual concentration ratio of 1.6:1. Figure 4.4b shows the reconstructed water spectra from the corresponding SHERPA and MEGA-PRESS acquisitions, which are again consistent between the different experiments.

Figure 4.5a shows GABA-edited brain spectra from both voxels of all ten subjects. Prior to plotting, spectra were normalized to the water signal. As expected, the GABA peak at 3.0 ppm is comparable between the two voxels for each subject, and also between subjects. This is verified in the GABA concentrations, which are also comparable between the voxels and are calculated as 3.25 ± 0.44 I.U. for voxel 1 and 3.05 ± 0.54 I.U. for voxel 2. Figure 4.5b shows that the GABA-edited SHERPA spectra are very similar to those from a standard MEGA-PRESS acquisition of

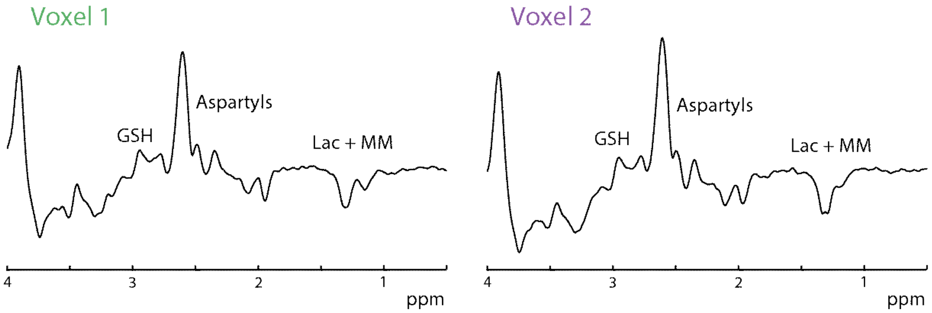

Figure 4.7. In vivo DEW SHERPA-editing of GSH and Lac in one subject. GSH-edited and Lac-edited spectra were acquired in two locations simultaneously, demonstrating the feasibility of fourfold editing acceleration with DEW-SHERPA. In addition to GSH and lactate, signals also co-edit from aspartyl resonances and macromolecules (MM).

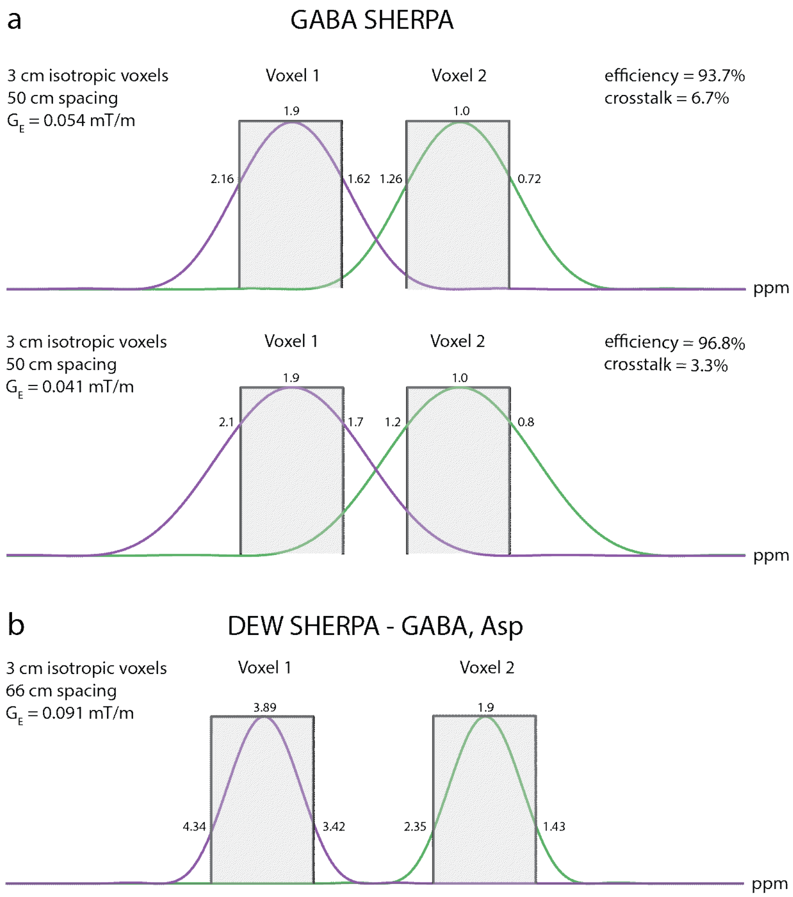

Figure 4.8. Further SHERPA implementations. Reducing the voxel spacing from 66 mm to 50 mm, it is possible either to scale up the editing gradient to 0.054 mT/m, sacrificing signal within the voxel (upper) or to maintain the same gradient strength and accept partial editing in the OFF voxel (lower). The latter option gives more signal in the intended voxel and, unexpectedly, less crosstalk signal.

the two voxels acquired separately. This is reflected in their respective signal-noise-ratios of 13 and 12 for voxel 1 and voxel 2 respectively with SHERPA and 10 and 12 respectively with MEGA-PRESS.

Bloch simulations of the editing pulses used in the DEW-SHERPA experiment show a small frequency variation of the editing pulse across the voxel (±0.13 ppm) as illustrated in Figure 4.6a. Spatially-resolved DEW-SHERPA simulations demonstrate feasibility to simultaneously detect GSH and Lac in both voxels with minimal crosstalk between the voxels (Figure 4.6b and 4.6c). Figure 4.6d shows that Asp, Cr, NAA, NAAG, GPC, PCh, and Glc are co-edited in the GSH-Lac-edited spectra, but no overlap with the resonances of interest (GSH at 2.95 ppm and Lac at 1.32 ppm) is observed. Figure 4.7 shows the results of a DEW SHERPA experiment performed in the brain of one subject (normalized by the water signal prior to plotting) where the GSH peak at 2.95 ppm and the lactate and co-editing macromolecule peaks at ~1.32 ppm can be seen.

When the voxels are placed closer together in the GABA SHERPA experiment (Figure 4.8), keeping the editing pulses gradients at 0.041 mT/m results in a higher editing efficiency and a smaller percent crosstalk (96.8% and 3.3% respectively) than increasing the editing pulse gradients to 0.054 mT/m (93.7% and 6.7% respectively).

4.5 Discussion

In this chapter, it is demonstrated that spectral editing of two different brain regions can be performed simultaneously using spatially dependent spectral editing pulses in SHERPA. For the examples given here, detecting either GABA, or GSH and Lac simultaneously, there is little crosstalk between the two voxels and minimal loss of signal compared to conventional MEGA-PRESS scans. SHERPA should also be applicable to any other J-coupled molecules that can be edited with MEGA-PRESS (such as NAAG and 2-hydroxyglutarate (56, 107), for instance) and can be applied to other combinations of brain regions.

One issue that has to be carefully considered with SHERPA is minimization of inhomogeneous editing within-voxel. In deciding the appropriate strength of editing gradients (intrinsically linked to the editing-off frequency and the distance between the voxels), a compromise must be met between achieving full inversion across the ON voxel and no inversion in the OFF voxel. Failing on either count will result in incomplete separation of signal from the two voxels, while incomplete within-voxel inversion also results in a loss of editing efficiency. For the implementations shown here, the loss in editing efficiency and crosstalk are both small

(~2% for both). This becomes more difficult to achieve when the voxels become closer together, and stronger editing gradients may be needed. However, depending on the voxel separation and the spin system, a weaker editing gradient strength may still result in high editing efficiency and low crosstalk, as seen for GABA here. For DEW-SHERPA, the frequency difference between the two edited metabolites fixes the editing gradient strength. A larger frequency difference requires a stronger editing gradient, which leads to a greater frequency variation within each voxel, which may lead to a lower overall editing efficiency of both metabolites. Another downside to this method is that the degrees of freedom of voxel placement is limited due to parallel excitation of the voxels. Namely, each voxel cannot be rotated relative to one another since both voxels are excited along the same plane. This limits the region combinations that can be measured from with this method. Region combinations that would be amenable to dual-voxel measurement with SHERPA are contralateral regions and the ACC and PCC. However, bilateral regions such as the thalami are too close together to be reliably detected.

An advantage of the SHERPA method over parallel-reconstruction methods such as PRIAM (123) is that SHERPA can be performed on a single-channel receive coil and is not reliant upon phased-array coil geometry. However, SHERPA can be performed with phased-array receive coils, providing care is taken in reconstructing the spectra from each voxel after acquisition. The relative phase of the MR signal in each coil of the phased-array differs between the two voxels. Therefore, the Hadamard transform of the FIDs from each coil was taken before coil combination, so as to separate the signal from each voxel for each coil, before combining the channels using a phase-sensitive average across all coils.

The demonstration of GSH and Lac editing with the DEW method (originally proposed for GSH and ascorbate (78), but adapted for GSH and Lac) shows the capability of SHERPA to simultaneously edit two metabolites from two voxels, a four-fold acceleration compared to

sequential MEGA-PRESS acquisitions. This dual editing with SHERPA (DEW-SHERPA) is possible for spin systems where both the spins targeted by the editing pulses and the observed spins of each molecule are sufficiently resolved from another. This presentation of DEW-SHERPA is preliminary, and intended as a demonstration of principle, rather than a mature technology. In order to convert simultaneous detection of GSH and Lac into simultaneous quantification, further refinements of the acquisition parameters will be required, in addition to more refined post-processing and frequency-domain modeling using simulated basis functions. In theory, SHERPA can also be adapted to edit more than one metabolite where the spectra from the observed spins overlap, by integrating it with a HERMES editing scheme (56).

One challenge when acquiring edited data from two voxels simultaneously is the need to shim both voxels at once. In the data presented, this was achieved by performing a projection-based shim of a cuboid including both voxels. This approach was adopted pragmatically, but may not result in optimal shimming of the voxels, and more advanced shimming methods such as 'shimtool' that only consider the tissue within the two voxels for optimization of field homogeneity would be expected to perform better (123). There was some evidence of a frequency shift between some pairs of voxels, which, if large enough, would result in imperfect editing and separation of signals, so dual-voxel shimming should include a further constraint to not only maximize homogeneity but also to minimize differences in the center frequency (Ω_0) between the two voxels.

One area that has received much attention recently in edited MRS, is the robustness of measurements in the presence of B_0 field instability (39, 104). Although it is possible to achieve little crosstalk between the two SHERPA voxels, this is unlikely to hold in the presence of significant frequency drift. In this case, the editing pulse of one voxel may start to impinge on the other voxel resulting in a loss of separation, in addition to the usual issues of subtraction artifacts (39, 104) and losses of editing efficiency. These issues can be reduced by applying prospective field-frequency correction during the acquisition (39).

When extending this method to clinical applications, it is likely that SHERPA will have greater motion sensitivity than MEGA-PRESS, since four sub-spectra are now needed instead of two. This would affect the quality of both spatial localization and editing, similar to MEGA-SPECIAL, which also acquires four subspectra for localization and editing (127).

In conclusion, the SHERPA method has been developed to acquire J-difference-edited spectra from multiple voxels simultaneously, using spatially dependent editing pulses. SHERPA was demonstrated to detect either one metabolite (GABA) or two metabolites (GSH and Lac) per experiment, providing two- and four-fold acceleration, respectively, over sequential MEGA-PRESS measurements.

Chapter 5 - Simultaneous editing of GABA and GSH with Hadamard-encoded MR spectroscopic imaging

5.1 Introduction

As mentioned previously, in vivo proton (^{1}H) MR spectroscopy (MRS) can readily detect signals from a variety of molecules within the human brain, such as N-acetylaspartate, creatine, choline, myo-inositol and glutamate. However, relatively lower-concentration compounds such as gamma-aminobutyric acid (GABA) or glutathione (GSH) are difficult to quantify in conventional MRS at field strengths of 1.5 or 3T, because their resonances extensively overlap with the signals from the other, more abundant compounds. Therefore, for low-concentration compounds such as GABA+ and GSH, spectral editing techniques have been developed which selectively detect individual compounds, while suppressing overlapping signals from more concentrated compounds. A variety of editing methods have been proposed, including those based on multiple-quantum filtering (128-130) and J-difference editing (128, 129, 131). Spectral editing methods are usually implemented in combination with single-voxel (SV) spatial localization, but have also sometimes been used in combination with MRSI (8, 10, 82, 132-134). In particular, GABA has been a of interest for metabolite mapping using edited MRSI (8, 132-134).

Typically, spectral editing methods have been typically designed to selectively detect a single compound. As shown in previous chapters, however, it has been shown that it is possible to simultaneously edit multiple compounds using a Hadamard-encoded approach known as HERMES ('Hadamard Encoding and Reconstruction of MEGA-Edited Spectroscopy'). HERMES has been demonstrated for two (GSH and GABA, or N-acetyl aspartate (NAA) and N-acetyl aspartyl glutamate (NAAG) (56, 135)) or three metabolites (such NAA, NAAG, and aspartate (Asp) (57)). In principle, depending on the size of the Hadamard encoding matrix, there is no upper limit on the number of metabolites (n) that can be simultaneously edited. Relative to separate MEGA acquisitions of n metabolites, HERMES offers scan-time savings of at least 1/n while maintaining signal-to-noise ratios (SNR) of the individually edited metabolites. Thus for a two metabolite acquisition, HERMES reduces the total scan time two-fold. HERMES can be thought of as performing two MEGA-PRESS scans simultaneously, and thus has the same SNR as the sequential acquisition of each metabolite separately.

This report describes the implementation of HERMES in combination with MRSI for simultaneous editing of GABA and GSH from multiple regions of interest. The feasibility of performing HERMES editing of GABA and GSH with a PRESS-localized spectroscopic imaging sequence was examined using both phantoms and in vivo experiments, and compared to results from conventional MEGA-encoded MRSI scans.

5.2 Methods

All experiments were performed on a Philips Achieva 3T scanner with a 32-channel head coil. The edited spectroscopic imaging sequence was based on the MEGA-PRESS pulse sequence with additional phase encoding gradients in two directions. A frequency-modulated 90° excitation pulse with a bandwidth of 4.3 kHz and a duration of 8.65 ms and amplitude-modulated 180° refocusing pulses with a bandwidth of 1.3 kHz and durations of 6.91 ms were used as described previously (97). TE_1 was 18 ms, TE_2 was 62 ms, and the editing pulses were 40 ms apart (TE/2). For both HERMES and MEGA-PRESS acquisitions, 20 ms sinc-Gaussian editing pulses with a bandwidth of 62 Hz were used. Additional scan parameters common to all experiments were: TE = 80 ms (previously shown to be a reasonable compromise value that allows editing of both GABA and GSH (5)); TR = 1.5s; and elliptical k-space sampling. For all edited MRSI acquisitions, four excitations were averaged for each phase-encoding step: all four sub-acquisitions for HERMES or two edit-ONs and two edit-OFFs for MEGA. Prior to data acquisition, B_0 field homogeneity was optimized using a field-map-based 2nd-order shimming routine (136). In addition to the edited experiments, separate water-unsuppressed references were acquired for coil combination and phasing purposes. Water data were acquired with one average and with the same field-of-view and resolution as the edited MRSI scans.

5.2.1 Phantom Experiments

HERMES and MEGA MRSI experiments with PRESS localization were performed in three 1L phantoms: one containing 10 mM GABA and 10 mM GSH (pH 7.0), one containing 10 mM GABA only (pH 7.2), and one containing 10 mM GSH (pH 7.0) only. For the GABA MEGA-PRESS acquisition, the edit-ON pulse was applied at 1.9 ppm and the edit-OFF pulse at 7.5 ppm. In the GSH MEGA-PRESS acquisition, the edit-ON pulse was applied at 4.56 ppm and the edit-OFF pulse at 7.5 ppm. For the HERMES acquisition (135), the editing pulse frequencies were applied as described in reference (135)

Spectra were recorded from a 2-cm slice with a field of view of 10 x 10 cm^2 and PRESS voxel dimensions of 5×5 cm^2. Data were acquired with a 10×10 phase encoding matrix resulting in a nominal in-plane resolution of 1×1 cm^2 and 2 cm^3 nominal voxel volume. MRSI data were subsequently interpolated to 20×20. Water suppression was achieved using the 'VAPOR' sequence (54). In the HERMES acquisition, the ability to separate the signals of GABA and GSH (' crosstalk'), was quantified as previously described (56, 135) across all the voxels in the PRESS volume of interest.

5.2.2 In Vivo Experiments

Edited MRSI experiments were performed in 3 healthy adults (1 male; age 26 ± 0.6 years). A single 2-cm transverse slice placed immediately above the level of the lateral ventricles was recorded with a field of view of 18×21 cm^2 (LR x AP) and a PRESS excitation volume of 8×10

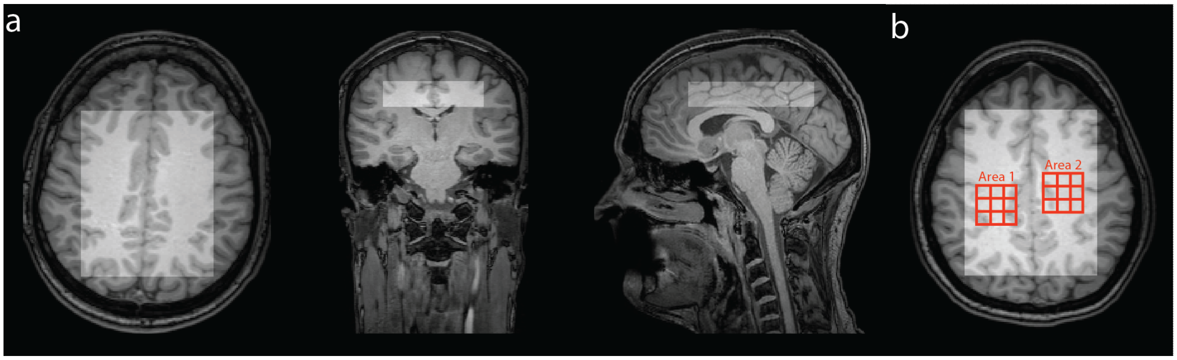

Figure 5.1. (a) PRESS excitation volume placements of in vivo HERMES and MEGA experiments overlaid on triplanar T1-weighted images. (b) Two 3 × 3 voxel areas overlaid on an axial T1-weighted image from which inter-region and inter-subject CVs were calculated.

cm^2. The anterior edge of the PRESS excitation volume was placed just anterior to the genu of the corpus callosum (Figure 5.1a). The chemical shift displacement effect on the spins to which editing pulses are applied, relative to the detected 3 ppm spins, in the refocusing directions of the PRESS volume was 11% of the VOI dimension for GABA and 16% for GSH. Slice excitation was performed in the left-right direction while the first refocusing pulse was played out in the anterior-posterior direction and the second refocusing pulse was played out in the superior-inferior direction. Hypergeometric dual band (HGDB), a dual-band water and lipid suppression sequence, was used for simultaneous water and lipid suppression (137). Data were acquired with a 12 × 14 phase encoding matrix which resulted in a nominal in-plane resolution of 1.5 × 1.5 cm^2 and nominal voxel size of 4.5 cm^3. MRSI data were subsequently interpolated to 24 × 28. Each scan had a total duration of 13 minutes.

GSH MEGA-PRESS acquisitions were performed with the same editing pulse frequency offsets as in the phantom experiments, but in the GABA+ MEGA-PRESS acquisition, the ‘OFF’ editing pulse was moved from 7.5 ppm to 0.7 ppm, so that the ‘ON’ and ‘OFF’ GABA+ editing pulses were symmetric about the 1.3 ppm lipid signal. This procedure has been previously found to reduce the amount of lipid contamination in the resulting GABA+ edited difference spectra (8). The HERMES sequence was also modified to include 0.7 ppm editing pulses in the GABA+ OFF

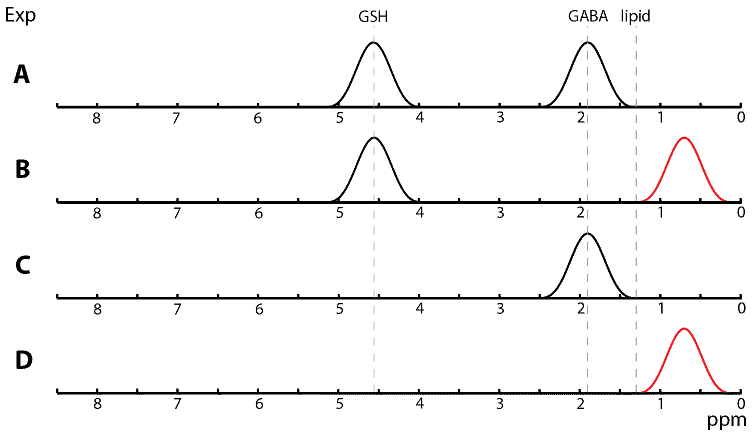

Figure 5.2. Frequencies and inversion envelope of the editing pulses for HERMES editing of GABA+ and GSH in vivo with symmetrical lipid suppression lobes applied in GABA-OFF scans. These lobes (indicated in red) are placed at 0.7 ppm in sub-acquisitions B and D so as to be symmetrical about the 1.3 ppm lipid resonance relative to the 1.9 ppm GABA 'ON' editing pulse.

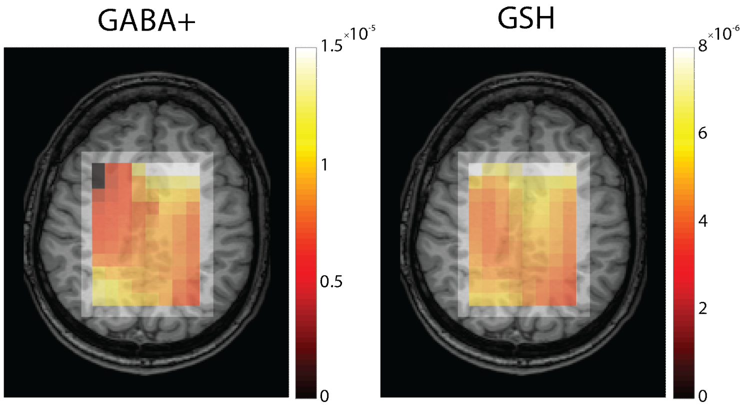

Figure 5.3. GABA+ and GSH maps overlaid on a T1-weighted axial image in one subject demonstrating the distribution of the metabolites over the voxels used for analysis in this current study.

sub-acquisitions (B and D) as shown in Figure 5.2. Spectra were also compared to HERMES and MEGA acquisitions with the OFF GABA+ editing pulse placed at 7.5 ppm. Note that the GABA editing pulses used for all experiments partially invert the 1.7 ppm macromolecule (MM) peak (19, 34, 140) and the 1.9 ppm homocarnosine peak (43, 141), so that the 3 ppm signal detected in the *in vivo* experiments contains components from MM and homocarnosine in addition to GABA, and is referred to as 'GABA+'.

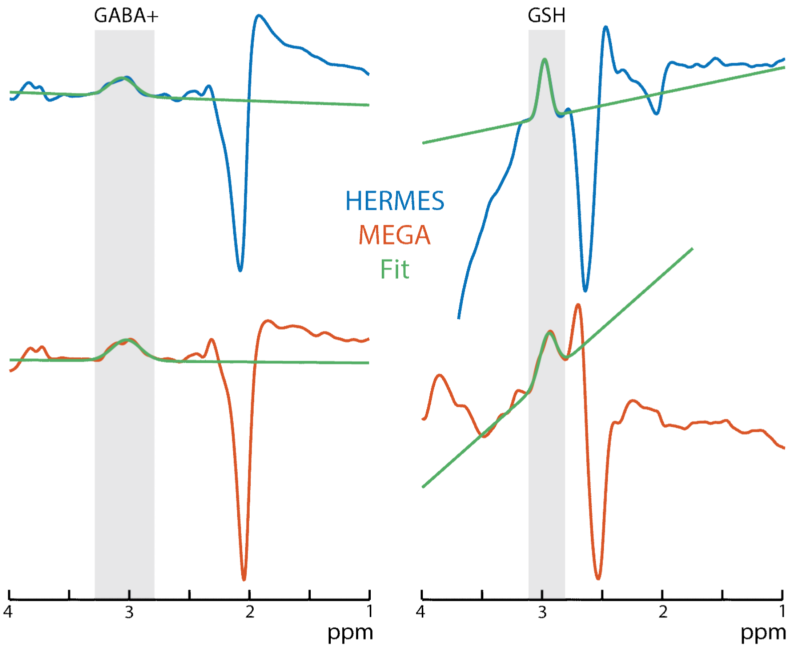

Figure 5.4. Representative GABA+ and GSH modeling in one subject from both HERMES- and MEGA-encoded experiments.

T_1-weighted 3D MPRAGE scans with 1 mm isotropic resolution were also acquired to plan the PRESS MRSI scan volume of interest and used in data processing to estimate gray matter (GM), white matter (WM) and cerebrospinal fluid (CSF) content of each voxel by segmenting these images using SPM12.

All MRSI scans were reconstructed using a 3DFFT, and multi-channel combination and phase-correction using data from the non-suppressed water acquisitions. Water was further filtered with an HLSVD algorithm (138). In the GABA+ and GSH spectra, the 3.0 ppm and 2.95 ppm peaks, respectively, were fitted with a single Gaussian model and a linear baseline to estimate GABA+ and GSH peak areas in voxels located at the center of the VOI (figure 5.3) (98). GABA+ was fit from 2.75 ppm to 3.4 ppm while GSH was fit from 2.78 ppm to 3.15 ppm (figure 5.4). To compare the performance of HERMES to the individual-metabolite MEGA acquisitions, the ratio of GABA+ and GSH peak areas between HERMES and MEGA was calculated for each voxel. The closeness of this ratio to 1 (the value which would indicate no measurement bias in HERMES- compared to MEGA-encoded scans) was assessed for all subjects.

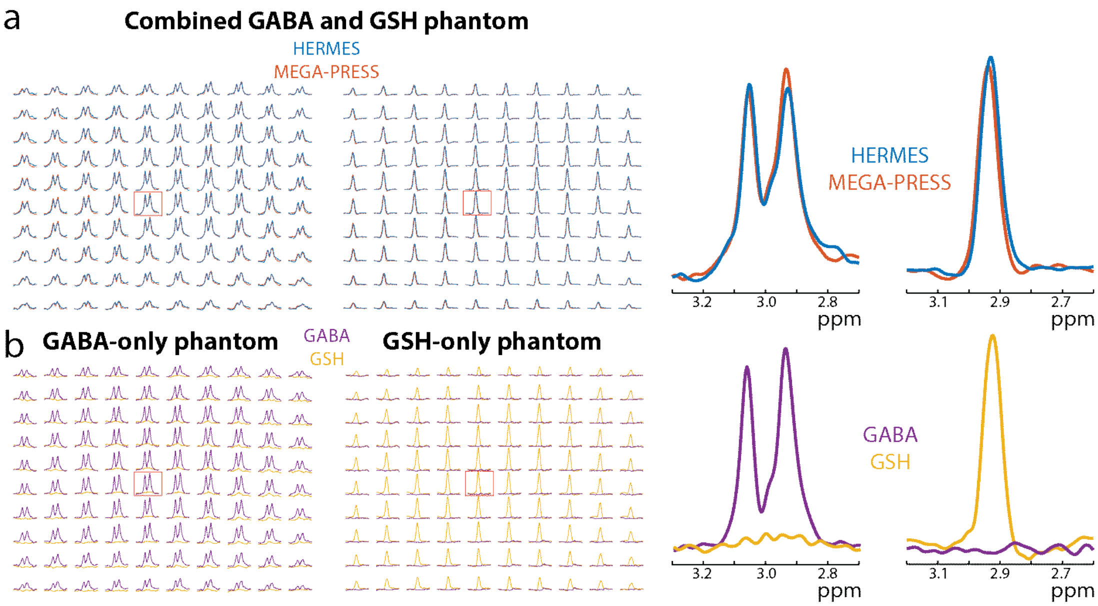

Figure 5.5. GABA and GSH multiplets from HERMES phantom experiments. (a) The first row shows the results from the combined GABA-GSH phantom. HERMES and MEGA-PRESS have equivalent GABA and GSH signal intensities and multiplets across the entire volume of interest. (b) In the GABA-only and GSH-only phantoms (second row) GSH and GABA are segregated into their respective reconstructions with minimal metabolite crossover across the volume of interest.

To estimate differences in GABA+ and GSH between GM and WM, the edited MRSI data (GABA+/H_2O and GSH/H_2O ratios) were examined for correlations with tissue composition (GM fraction). Tissue composition (GM fraction) for each nominal MRSI voxel within the PRESS-excited volume (without correction for point-spread function) was linearly regressed versus the GABA+/H_2O and GSH/H_2O ratios for all subjects, excluding voxels with a CSF percentage over 3%. The GM tissue fraction was calculated as $^{f_{GM}}/_{f_{GM} + f_{WM}}$ where f_{GM} is the GM volume fraction and f_{WM} is the WM volume fraction (to account for CSF).

To compare the reliability of HERMES and MEGA, the coefficient of variation (CV) of the water-normalized GABA+ and GSH peak areas across two 3 × 3 voxel regions in the left and right hemispheres (Area 1 and Area 2 respectively) within the PRESS volume of interest (Figure 5.1b) in each subject was calculated. These regions of interest are relatively homogeneous in tissue content and therefore reduce variance in the data due to different tissue composition. CVs of the water-normalized GABA+ and GSH peak areas between subjects were also calculated in those two regions.

5.3 Results

Results from the HERMES and MEGA-encoded MRSI scans from the GABA and GSH phantom are shown in Figure 5.5a; arrays of 10 × 10 spectra are plotted over the PRESS excitation volume. The HERMES-encoded reconstructions of GABA and GSH are plotted in blue, while the separate MEGA-PRESS scans of each metabolite are plotted in red. It can be visually observed that there is a very high degree of concordance between the HERMES and MEGA-PRESS reconstructions, in terms of multiplet shape (the edited phantom GABA signal is a 'pseudo-doublet', whereas the GSH peak appears as a singlet due to line broadening), intensities, and signal-to-noise ratio (SNR). The multiplet patterns are also in very good agreement with those previously reported in edited single voxel acquisitions of GSH and GABA phantoms (17, 135) at the same echo time.

Results from the HERMES acquisitions performed in the phantoms containing either GSH or GABA only are shown in Figure 5.5b. It can be seen that the GABA and GSH signals are well separated with only a small amount of crosstalk across the VOI (median (interquartile range) 8.2% (6.7%) GSH crosstalk into the GABA combination in the GSH-only phantom, 11.7% (8.7%) GABA crosstalk into the GSH combination in the GABA-only phantom).

Representative HERMES and MEGA GABA+ and GSH spectra taken from a 13 × 10 voxel array in subject 2 are shown in Figure 5.6 and Figure 5.7 respectively. As in the phantom experiments, the GABA+ and GSH spectra are in good visual agreement between MEGA and HERMES acquisitions, although the GSH spectra are superimposed on somewhat different baselines, likely due to different levels of residual water signal.

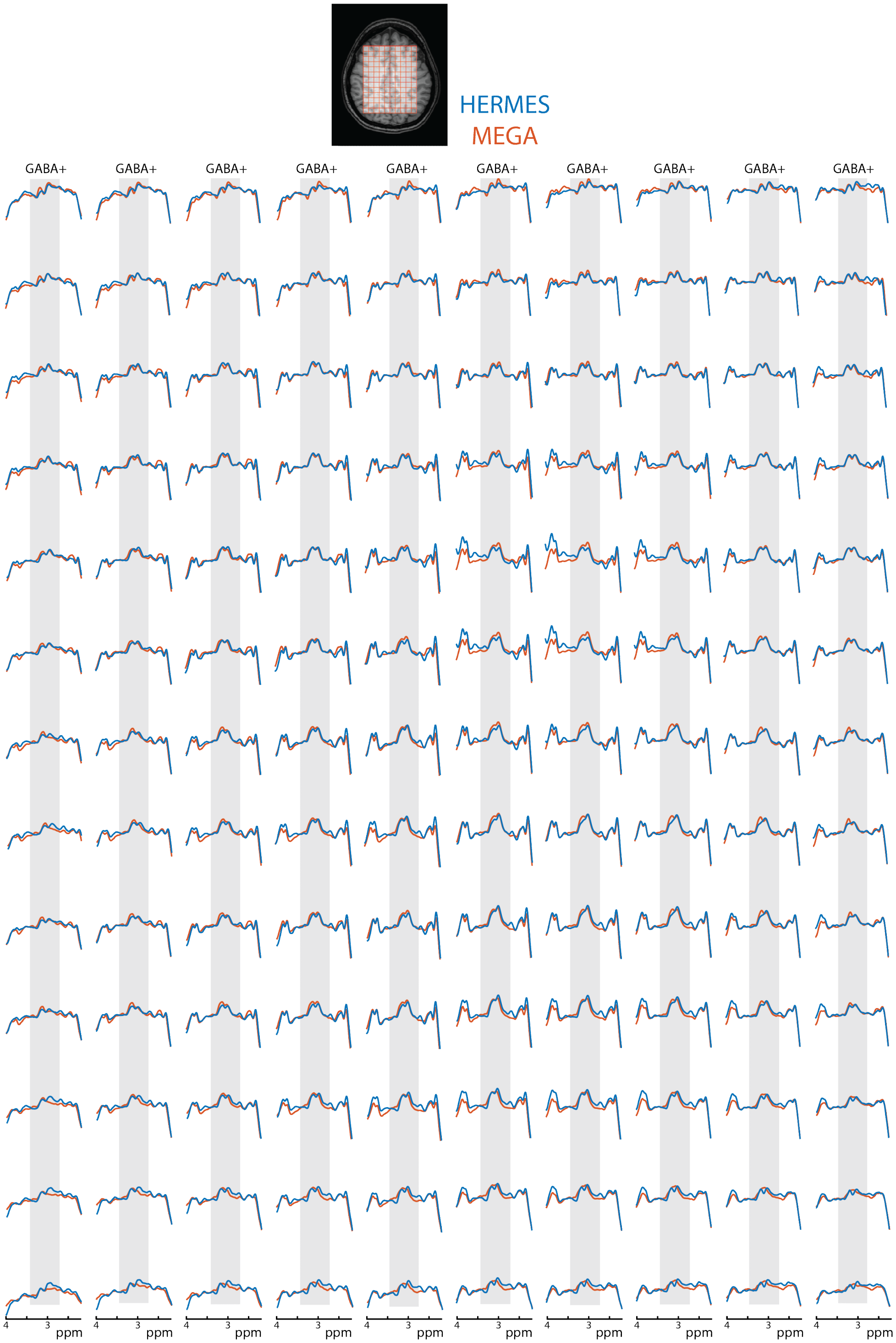

Figure 5.6. PRESS excitation volume overlaid on an axial T1-weighted image (top). Representative MEGA- and HERMES-encoded GABA+ spectra plotted from 2.2 to 4 ppm across the entire volume of interest shown top from subject 2. The MEGA- and HERMES-encoded GABA+ spectra are in good agreement between methods.

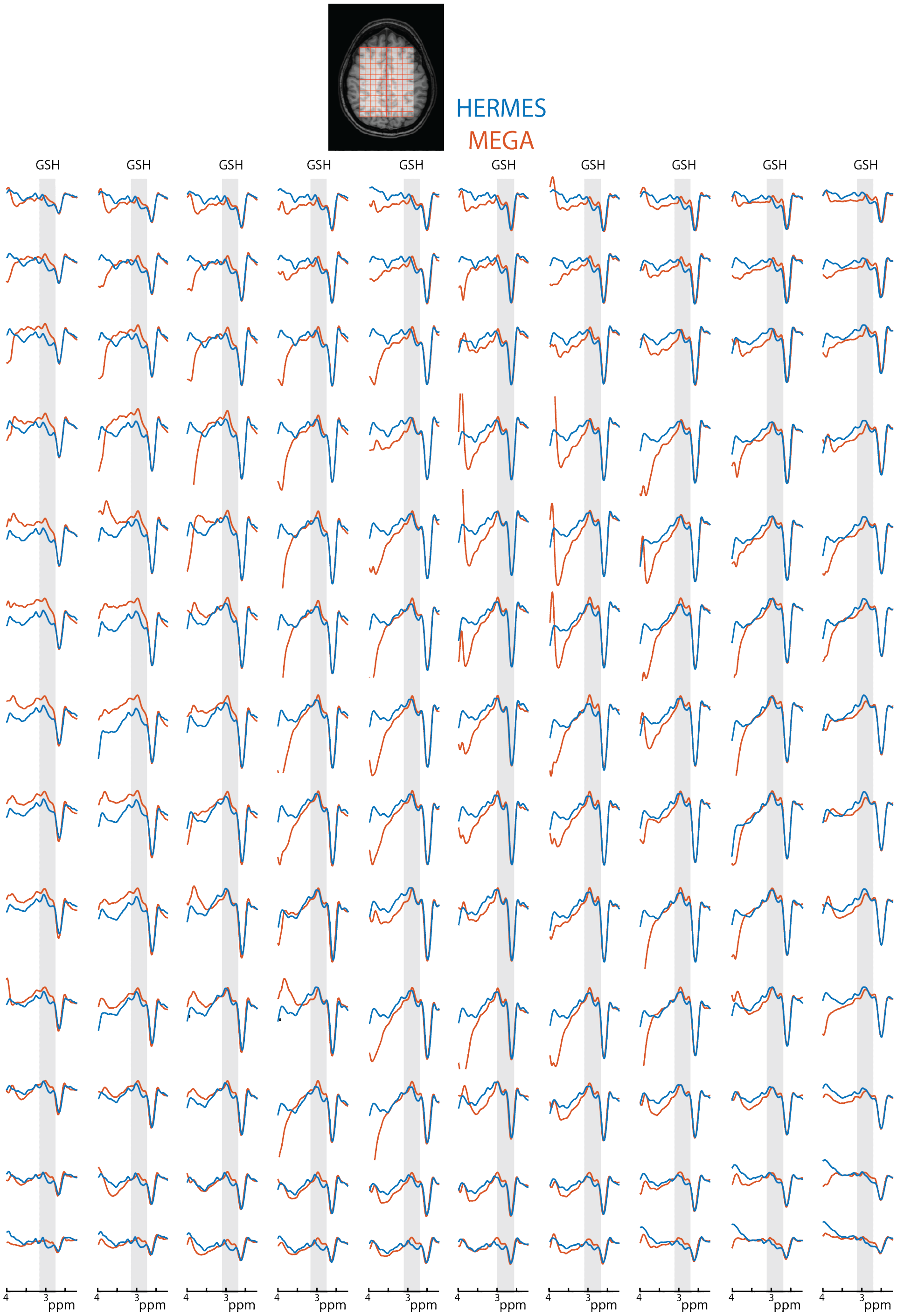

Figure 5.7. PRESS excitation volume overlaid on an axial T1-weighted image (top). Representative MEGA- and HERMES-encoded GSH spectra plotted from 2.2 to 4 ppm across the entire volume of interest shown top from subject 2. The MEGA- and HERMES-encoded GSH spectra are in good agreement between methods.

Scattergrams overlaid on box plots of the GABA+ and GSH peak ratios (HERMES/MEGA) for all 3 subjects are shown in Figure 5.8. The HERMES/MEGA ratio is close to 1 in all subjects, demonstrating that HERMES and the individual MEGA-PRESS acquisitions give similar quantification of both GABA+ and GSH without any systematic bias (HERMES/MEGA GABA+ = 1.05 ± 0.1, GSH = 1.06 ± 0.03, over all subjects). Although both the median GABA+ and GSH peak area ratios are close to 1, the interquartile ranges are slightly larger for GSH, indicating that the GSH estimates have greater variability than those of GABA+.

The inter-regional GABA CV ranges were comparable between HERMES and MEGA at 6 – 15% and 5 – 13% respectively (Table 5.1). The inter-regional GSH CV ranges were also comparable between HERMES and MEGA at 3 – 15% and 5 – 17% for MEGA (Table 5.1). The average inter-subject GSH CVs were higher for HERMES than for MEGA at 14.8% and 7% respectively. However, both of these values are comparable to, or lower than, previously reported inter-subject CVs from single-voxel acquisitions of about 15 - 17% for GSH (80, 139, 140). The

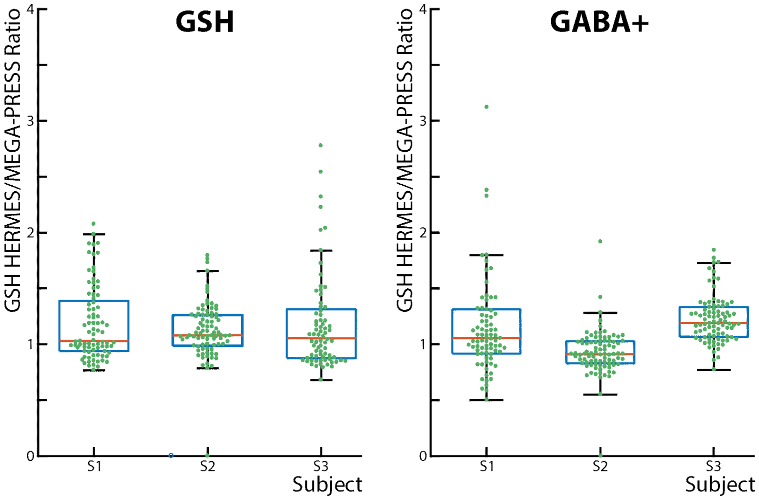

Figure 5.8. Scattergrams plotted on top of box plots of the voxel-by-voxel GSH and GABA+ peak area ratios (HERMES/MEGA) for each subject. The number of voxels included for each subject ranged from 85 to 88 voxels and were located at the center of the VOI (excluding voxels at the edges). Median ratio values for both GABA+ and GSH were close to one, indicating that HERMES and MEGA give comparable results.

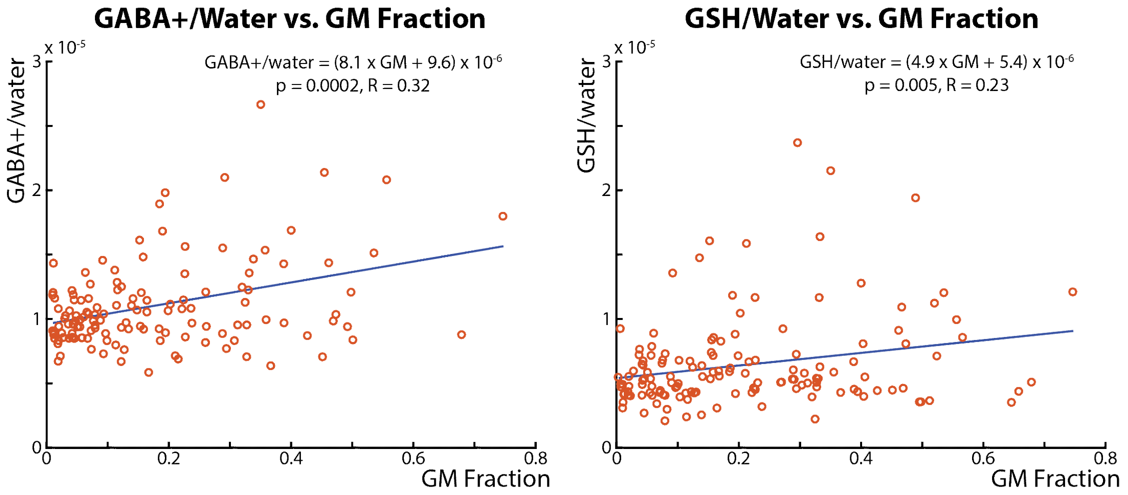

Figure 5.9. Scattergrams plotted on top of box plots of the voxel-by-voxel GSH and GABA+ peak area ratios (HERMES/MEGA) for each subject. The number of voxels included for each subject ranged from 85 to 88 voxels and were located at the center of the VOI (excluding voxels at the edges). Median ratio values for both GABA+ and GSH were close to one, indicating that HERMES and MEGA give comparable results.

average inter-subject GABA+ CVs were comparable between HERMES and MEGA at 10.8% and 8.7% respectively and are consistent with previously reported inter-subject CVs from single-voxel acquisitions of 8-18% for GABA (98, 141-144). In addition, the average water linewidths across all subjects was 8 Hz, which is comparable to that obtained with single-voxel acquisitions (145, 146) while the average NAA linewidth in the GABA-edited spectra across all subjects was 7 Hz.

Area 1 had more gray matter than Area 2 (0.37 ± 0.01% for Area 2 versus 0.16 ± 0.03%) with comparable levels of CSF (0.05 ± 0.02% for Area 1 versus 0.02 ± 0.01% CSF for Area 2). As expected, Area 1 also had higher levels of GABA+/H_2O and GSH/H_2O of $9.94 \pm 0.94 \times 10^{-6}$ and $4.87 \pm 0.51 \times 10^{-6}$ respectively versus that of Area 2 which had GABA+/H_2O and GSH/H_2O levels of $9.52 \pm 1.07 \times 10^{-6}$ and $4.11 \pm 0.79 \times 10^{-6}$ respectively. This is consistent with previous literature reports which indicate higher GABA+ and GSH levels in gray matter (10, 144, 147-149).

Figure 5.9a shows the linear regression results for HERMES GABA+/H_2O versus GM tissue fraction in all three subjects. Regression analysis indicates 1.84 times greater GABA+/H_2O in pure GM compared to WM (GABA+/H_2O = $(8.1 \text{ x GM} + 9.6) \times 10^{-6}$, p = 0.0002 and R = 0.32). This GM/WM ratio is within the range of literature ratios reported previously: 2.18, 2.0, 1.74, and 1.52 (144, 147-149). The linear regression results for HERMES GSH/H_2O versus GM fraction is shown in Figure 5.9b. Regression analysis of the tissue dependence of GSH shows a correlation with 1.91 times greater GSH/ H_2O in GM than in WM (GABA+/H_2O = $(4.9 \text{ x GM} + 5.4) \times 10^{-6}$, p = 0.005 and R = 0.23). This value is consistent with a previously reported value of 1.57 times greater GSH in GM than in WM (10).

5.4 Discussion

The data presented in this chapter show that edited MRSI with HERMES encoding allows for the simultaneous mapping of GABA+ and GSH in the human brain at 3T. HERMES reduces the total measurement time relative to sequential measurements of each metabolite without any penalty in editing efficiency or signal-to-noise ratio (56, 135). In the current example, there was a two-fold scan time reduction from 26 to 13 minutes. HERMES experiments in phantoms demonstrated minimal crosstalk between the two metabolite reconstructions across the volume of interest. It is expected that HERMES-MRSI can be applied to other combinations of metabolites as well, as previously demonstrated using single-voxel localization, e.g. NAA and NAAG (56), or NAA, NAAG and aspartate (57).

Compared to editing methods based on single-voxel localization, edited MRSI (including HERMES-MRSI) presents a number of additional challenges; these include obtaining sufficient B_0 field homogeneity over the volume of interest, minimizing lipid contamination from peri-cranial fat, minimizing the effects of B_0 field drift over the duration of the scan, and minimizing subtraction artifacts due to head motion or other instabilities.

In the current study, excitation of peri-cranial lipids was largely avoided by using PRESS localization confined to the brain, and residual lipids were further suppressed in GABA+ edited scans by placing the 'OFF' editing pulse at 0.7 ppm, symmetric about the 1.3 ppm lipid resonance. A limitation of this approach, however, is that the addition of these editing pulses precludes symmetrical macromolecule suppression where additional editing pulses in the GABA+-OFF acquisitions at 1.5 ppm are typically needed (34, 35, 150). This symmetrical suppression scheme enables the reduction of the macromolecule signal that can make up to 60% of the GABA+ signal (32). The HGDB dualband suppression pulse was also used to suppress the lipid signals at 1.3 ppm; however, this lipid suppression pulse also partially suppresses the NAA signal, leading to a reduced NAA peak at 2.0 ppm. In this study, a simple Gaussian model was used to fit both the GABA and GSH peaks. Although both metabolites have been shown to have more complicated multiplet patterns in both simulations and phantom experiments, these are less apparent here in vivo due to the shorter T_2 relaxation times and exponential line-broadening to improve the SNR. Because of this, it is unlikely that using different models will significantly alter the results presented here as shown previously for GABA (98).

In both phantom and in vivo experiments, the signal strengths vary across the VOI with the signals being stronger in the middle of the VOI and decreasing smoothly towards the edges. This reflects two effects: (1) the excitation profiles of the slice selective 180˚ pulses of the PRESS sequence (2) the filtering used in the reconstruction. It should be noted that reference signals (here, water) recorded with the same sequence will have the same sensitivity profile, so that ratios of GABA or GSH to water should not be affected.

Table 5.1 Coefficients of variation of the GABA+ and GSH peak areas across the voxels in each subject for both HERMES and MEGA-PRESS acquisitions. The average coefficients of variation are also listed and are equivalent between methods for GABA+ and are close for GSH.

Inter-regional CVs

GABA+

	Area 1		Area 2	
Subject	HERMES	MEGA	HERMES	MEGA
1	5.8%	9.3%	6.2%	8.2%
2	5.9%	5.2%	14.8%	5.4%
3	7.0%	13.2%	10.2%	8.3%
average	6.2%	9.2%	10.4%	7.3%

GSH

	Area 1		Area 2	
Subject	HERMES	MEGA	HERMES	MEGA
1	7.1%	5.5%	3.5%	8.0 %
2	15.2%	16.9%	7.0%	5.0%
3	10.0%	9.8%	12.5%	8.6%
average	10.8%	10.7%	7.7%	7.2%

Inter-subject CVs

	Area 1		Area 2			
Subject	HERMES	MEGA	HERMES	MEGA	Average HERMES (both areas)	Average MEGA (both areas)
GABA+	9.5%	5.9%	12.0%	11.4%	10.8%	8.7%
GSH	10.5%	5.6%	19.2%	8.4%	14.8%	7.0%

Since the duration of the first spin echo is kept short, it is estimated that signal loss due to chemical shift displacement in the direction of the first refocusing pulse (anterior-posterior direction) is minimal, as previously shown for single-voxel simulations for GSH editing (17) and GABA editing (45). In the direction of the excitation pulse (left-right), chemical shift displacement was kept to a minimum with the use of high-bandwidth pulses with an estimated shift of 8.4 mm and 5.9 mm (approximately a half-voxel shift) between the coupled spins of GSH and GABA that are used for editing, respectively. Full effects from the chemical shift displacement effect are registered in the second refocusing direction: the slice direction (foot-head). Since the slice thickness is relatively small at 20 mm, chemical shift displacement effects were also small with an estimated shift of 3.2 mm and 2.3 mm between the edited and detected spins for GABA and GSH respectively (resulting in ~10% loss of edited signal). Although relatively small, these shifts have an effect on the SNR at the edge voxels of the VOI and were not considered for further analysis.

In this study, no specific efforts were made to monitor or correct for frequency drift or head motion; scans were performed in compliant healthy volunteers under stable conditions. B_0 field drift was largely avoided by not performing MRSI after other studies which involve gradient heating, known to be the most common cause of field drift (44, 104). Subject motion may be more of an issue in clinical and/or less-compliant subject populations who may move more (for instance pediatric subjects). Motion during MRSI scans result in artifacts such as line-broadening, reduced spatial resolution and concomitant increased lipid contamination (151). It has previously been shown that the robustness of edited MRSI scans to compensate for subject motion can be improved by including MR volume navigators for real-time motion and shim correction (151, 152). However, such an approach requires software for real-time updating of scan control parameters that is not currently widely available. It should be noted that relative to MEGA-encoding, HERMES may have increased subject motion sensitivity since four sub-spectra are acquired, compared to two MEGA. In single-voxel-localized MEGA or HERMES, it is possible to use post-acquisition phase- and frequency-correction of individual transients in order to improve SNR and reduce subtraction artifacts (44, 153); note that because of the use of phase-encoding gradients, in MRSI there is no simple way to perform such a correction. The phase of the FID at each point of k-space is different (and unknown) due to the presence of the phase-encoding gradient. In addition, due to the presence of the editing pulses, phase-correction methods (for instance, those based on the spectral-registration routine) comparing the 4 Hadamard acquisitions will also typically fail (154); therefore there is currently no simple way to perform phase correction with this type of acquisition. This is a challenge which makes edited MRSI experiments (either with MEGA or HERMES-encoding) very sensitive to head motion, since subtraction artifacts on a small number of phase-encoding steps will propagate throughout the dataset once Fourier-transformed into the spatial domain.

Although edited MRSI acquisitions were performed in compliant healthy volunteers, it is likely that subtle movements during acquisition were present and are a source of the variance and outliers seen in the voxel-by-voxel metabolite area ratios between HERMES and MEGA. Another potential source of error is the reduced SNR in some of the transition voxels located near the edge of the PRESS box. This may result in compromised fitting of the metabolite peaks and consequently inaccurate metabolite ratios. This may be improved upon in the future with the use of improved localization techniques such as semi-LASER, which provides better slice profiles.

Linear regression analysis of the HERMES GABA+/H_2O peak areas showed ~1.84 times higher GABA+/H_2O in gray matter than in white matter, as similar to previous reports which indicate higher GABA+ concentrations in gray matter (144, 147-149). Although no consensus on the tissue-dependence of GSH exists in literature, linear regression analysis of the HERMES GSH/H_2O showed a correlation with ~1.91 times higher GSH/H_2O in gray matter than in white matter which is consistent with a previous literature report (10). This analysis did not account for the MRSI point-spread-function, so it is likely to underestimate the difference between tissue types. For both 3 × 3 voxel areas, the inter-region GABA+ and GSH CVs were comparable between HERMES- and MEGA- encoded MRSI indicating that both methods were equally reliable in editing GABA+ and GSH within a similar anatomical location. Between subjects, HERMES- and MEGA-encoded MRSI sequences edited GABA+ equally reliably. However, the average inter-subject CV for the HERMES GSH measurement is ~7% higher than that of the MEGA measurement of GSH. This is possibly due to the more difficult curve-fitting of the HERMES GSH spectra due to the complicated baseline near the 2.95 ppm GSH resonance.

Recently (155) it has been shown that simultaneous measurement of glutamate, glutamine, GABA, and glutathione is possible at 7T using by spectral editing without subtraction in combination with single voxel localization. Such methods in the future may also be possible in combination with MRSI in order to map the distributions of these compounds.

In summary, HERMES-encoded MRSI was shown to be feasible for simultaneous editing of GABA+ and GSH using a PRESS-localized sequence at 3T. Scan time was reduced by a factor of 2 compared to sequential MEGA-encoded MRSI scans, but without any reduction in SNR or increase in measurement variability. HERMES-encoded MRSI is a practical method for mapping the distribution of multiple, low-concentration brain metabolites.

Chapter 6 - Retrospective motion compensation for edited MR spectroscopic imaging

6.1 Introduction

Edited proton MR spectroscopy (MRS) of the human brain at 3T is increasingly being used to detect lower-concentration compounds such as gamma-aminobutyric acid (GABA) or glutathione (GSH). As said earlier, GABA is the principle inhibitory neurotransmitter (128) and GSH is the brain's main antioxidant (60, 61). Both metabolites have also been implicated in a large range of neurological disorders and neuropsychiatric disorders (14, 84, 131, 156-159) and have been of interest in basic neuroscience (7, 160, 161). As described earlier, a variety of spectral editing techniques have been proposed based on either multiple-quantum filtering (73, 74) or J-difference editing (47, 63, 75). Of these two techniques, J-difference editing is the more widely used, most often in conjunction with single-voxel localization. However, in many cases it is desirable to detect spectra from multiple regions of interest, in order to map out spatial variations in metabolite levels. J-difference editing has been used in combination with MR spectroscopic imaging (MRSI) for multi-voxel localization and has previously been shown to be capable of mapping both GABA (8, 9) and GSH (10).

Since J-difference editing involves the subtraction of two scans with and without editing pulses applied, it is very sensitive to head motion or other instabilities which cause subtraction artifacts (41, 152). In single-voxel spectral editing, various post-processing schemes are available to identify and correct shot-to-shot phase and frequency variations (42-44). These have been shown to remove subtraction artifacts and improve spectral quality. However, in edited MRSI, the presence of phase-encoding gradients has generally precluded application of such routines. Motion-related corruption of even just a few points in k-space then leads to subtraction artifacts which propagate throughout the entire MRSI dataset after spatial fast Fourier transformation (FFT).

In this paper, a retrospective motion compensation method for edited MR spectroscopic imaging is presented. This sequence compares residual water and lipid peaks between different transients acquired at the same point in k-space, and either phase corrects, replaces or removes those that do not share the same properties as the others. After correction in k-space, data are processed as normal by spatial FFT. The performance of the method was evaluated for both GABA- and GSH-edited spin echo MRSI data (8). The algorithm is designed to work with datasets that contain only a limited amount of motion, i.e. the majority of the data being of good quality with only occasional head motion followed by a return to the original position. The method is not designed to compensate for larger or more continuous motion, in which case only prospective motion correction schemes (e.g. (9)) would be expected to be successful.

6.2 Methods

6.2.1 Retrospective Motion Compensation Scheme

In MRSI, the phase of the signal changes from one point in k-space to the next, so correction schemes developed for SV MRS will not work as applied to the whole dataset. However, if more than one transient is acquired for each point in k-space, then different transients at the same point in k-space can be compared for similarity. The pulse sequence used in this study (see below) gives quite strong residual water and lipid signals, which can be used to estimate motion-related phase, frequency or amplitude changes. It may also be possible to compare k-space spectra between acquisitions with the editing pulse either ON and OFF; for instance, in editing for GABA, the water peak will usually be the same in both the ON and OFF spectra, so can also be compared for similarity, whereas the lipid peaks are usually affected by the 1.9 ppm ON GABA editing, so cannot be compared.

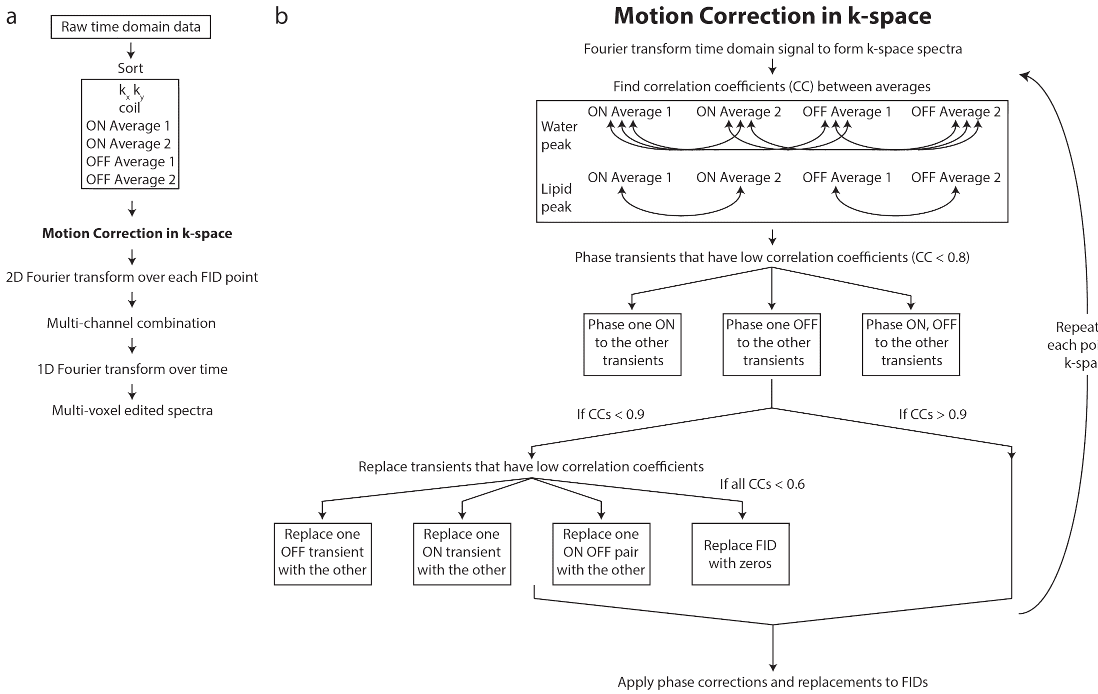

Figure 6.1. (a) General schematic diagram of the edited MR spectroscopic imaging data processing pipeline including the retrospective motion compensation algorithm in k-space. After coil-combination and Fourier transformation with respect to time to form spectra in k-space. (b) Motion-affected transients are identified depending on their correlation coefficients with the spectra at the same k-space point and are either phased to match the other transients, replaced with an unaffected average of the same type of sub-acquisition, or replaced by zeroes.

Figure 6.1a shows the general schematic of the entire data processing pipeline including the added motion compensation in k-space before 2D spatial FFT. Figure 6.1b shows the schematic of the motion compensation algorithm in k-space. To determine similarity between transients at the same k-space point, Pearson's correlation coefficients (CC) were calculated for the real parts of the water peaks (4.4 ppm to 5.2 ppm) and lipid peaks (0 ppm to 2.5 ppm) between all four transients to generate six CCs per point in k-space: $CC_{ON1,ON2}$, $CC_{ON1,OFF1}$, $CC_{ON1,OFF2}$, $CC_{ON2,OFF1}$, $CC_{ON2,OFF2}$, and $CC_{OFF1,OFF2}$. Since the lipid peaks differed between the ON and the OFF spectra, the lipid CC was only calculated between transients of the same sub-acquisition.

After calculating the CCs between transients, the algorithm then determines which averages are affected by motion by determining which of the six CCs have values below a threshold of 0.8. Depending on the combination of CCs have values below this threshold, the motion affected average(s) can be surmised. For example if $CC_{ON1,ON2}$, $CC_{ON1,OFF1,}$ $CC_{ON1,OFF2}$ are all below 0.8, it can be inferred that ON average 1 is the motion-affected average as that average is shared between the CCs with values below the thresholds. At times, however, ambiguity can exist as to which of the average(s) are motion affected. For those cases, the general rules apply:

1. If there is ambiguity over which of two transients is motion affected, the algorithm sums the CCs for each average separately and finds which of the two averages has the higher (lower) sum CC. The transient with the lowest sum CC is deemed the motion-affected average. For example, if only $CC_{ON1,OFF2}$ is below the threshold, it is unclear as to whether OFF transient 1 or OFF transient 2 is the motion-affected average. Thus, non-motion affected average can be found with the equation:

$$\arg\max(CC_{\mathrm{ON1,OFF1}} + CC_{\mathrm{ON2,OFF1}} \ , CC_{\mathrm{ON1,OFF2}} \ + CC_{\mathrm{ON2,OFF2}})$$

   If this equation is equal to 1, then it can be surmised that OFF transient 2 is the motion-affected average. Conversely, if the equation is equal 2, then OFF transient 1 is the motion-affected average.

2. Ambiguity can also arise when trying to identify ON/OFF pairs spared from motion-related phase changes. In these instances, the algorithm identifies the CC between different ON/OFF combinations with the highest value and considers the other two ON/OFF transients to be motion-affected. For example, if $CC_{ON1,ON2}$, $CC_{ON2,OFF1,}$ and $CC_{OFF1,\ OFF2}$ are all below threshold, it is difficult to determine which ON/OFF is motion-affected. This can be narrowed down with the following equation:

$$\arg\max(CC_{\mathrm{ON1,OFF1}} , CC_{\mathrm{ON2,OFF1}} , CC_{\mathrm{ON2,OFF2}})$$

   If this equation is equal to 1, 2, or 3 then it can be surmised that ON transient 2 and OFF transient 2, ON transient 1 and OFF transient 2, or ON transient 1 and OFF transient 1 respectively are the motion-affected averages.

After identifying motion-affected transients, a decision was made as to what to do with these motion-affected averages. If all six CCs were below a threshold of 0.6, the k-space point was replaced with zeros. If not, however, an attempt was made at phasing the motion-affected transients so that the phase of the water peaks matched that of other transients as closely as possible. If a CC of 0.9 and above was obtained between the water peaks of the phased motion-affected spectra and the motion-unaffected spectra, the phase that was used to correct the spectra was saved for later use. If it was not possible to obtain a CC of 0.9 and above by phasing the motion-affected spectra, the transient was marked for replacement by a transient of the same sub-acquisition type (e.g. replacing OFF average 1 with OFF average 2).

After corrections are determined for the motion-affected transients at each point in k-space, these corrections are applied to the FIDs in k-space after which, the conventional post-processing steps can be performed to create multi-voxel spectra.

6.2.2 In Vivo Data

All experiments were performed on an Achieva 3T scanner (Philips, Best, The Netherlands) equipped with a 32-channel head coil. Data were acquired in 8 healthy adults (6 male, age: 30 ± 7 years) using an edited, spin-echo MRSI sequence with hyper-geometric dual-band (HGDB) water and lipid suppression, and outer-volume lipid suppression, as described previously (8, 137). A single 20 mm thick axial slice placed just above the level of the ventricles was acquired with 2D phase encoding, field-of-view of 180 mm x 210 mm, an 12 x 14 phase encoding matrix, and elliptical k-space sampling, resulting in a nominal in-plane resolution of 1.5 cm x 1.5 cm and voxel size of 4.5 cm^3. TR was 2s and TE 80 ms. Two transients for each of the ON and OFF sub-acquisitions were acquired at each phase-encoding step. A frequency-modulated 90° excitation pulse with a bandwidth of 4.3 kHz and an amplitude-modulated 180° refocusing pulse with a bandwidth of 1.3 kHz were used as previously described (97). 20 ms sinc-gaussian editing pulses were used with a bandwidth of 62 Hz. For GABA-editing, these editing pulses were placed at 1.9 and 0.7 ppm in the ON and OFF acquisitions respectively.

GSH-edited data were also acquired in 1 healthy adult (male, age 26) with the same acquisition parameters, including TR and TE, as the GABA-edited acquisition. In this acquisition, however, the edit-ON pulse was placed at 4.56 ppm and the edit-OFF pulse was placed at 7.58 ppm.

B_0 field homogeneity was optimized using a field-map based 2nd-order shimming routine (136). Separate water unsuppressed references were also acquired with one average and at the same field-of-view and resolution as the edited-MRSI scans for coil combination and phasing purposes.

Data were processed with and without the use of the retrospective motion compensation algorithm (Figure 6.1). For GABA-editing, in the absence of any motion, there should be no residual signal at 3.2 ppm, i.e. the choline (Cho) peak should be completely removed. A measure of the subtraction artifact intensity can therefore be quantified by measuring the Cho signal in the difference spectra. Cho and GABA peaks were therefore fit using lineshape models as described previously (98). To evaluate the goodness of the fits, the coefficient of determination was calculated between the fitted model values and spectra. Voxels that the algorithm was unable to fit or had a coefficient of determination (R^2) of less than 0.85 were not included in further analyses. In addition, voxels that were better fit by a single Gaussian model from 2.75 ppm to 3.4 ppm to the GABA than the Cho + Cr/GABA model were considered to contain no Cho subtraction artifacts. The fitted Cho artifact areas from the DIFF spectra were normalized against the fitted Cho artifact areas from the OFF. Outliers were calculated as elements greater than 3 scaled median absolute deviations away from the median and were removed from further analyses.

For one subject, the GABA+ peak in the uncorrected and the corrected spectra were fit with a

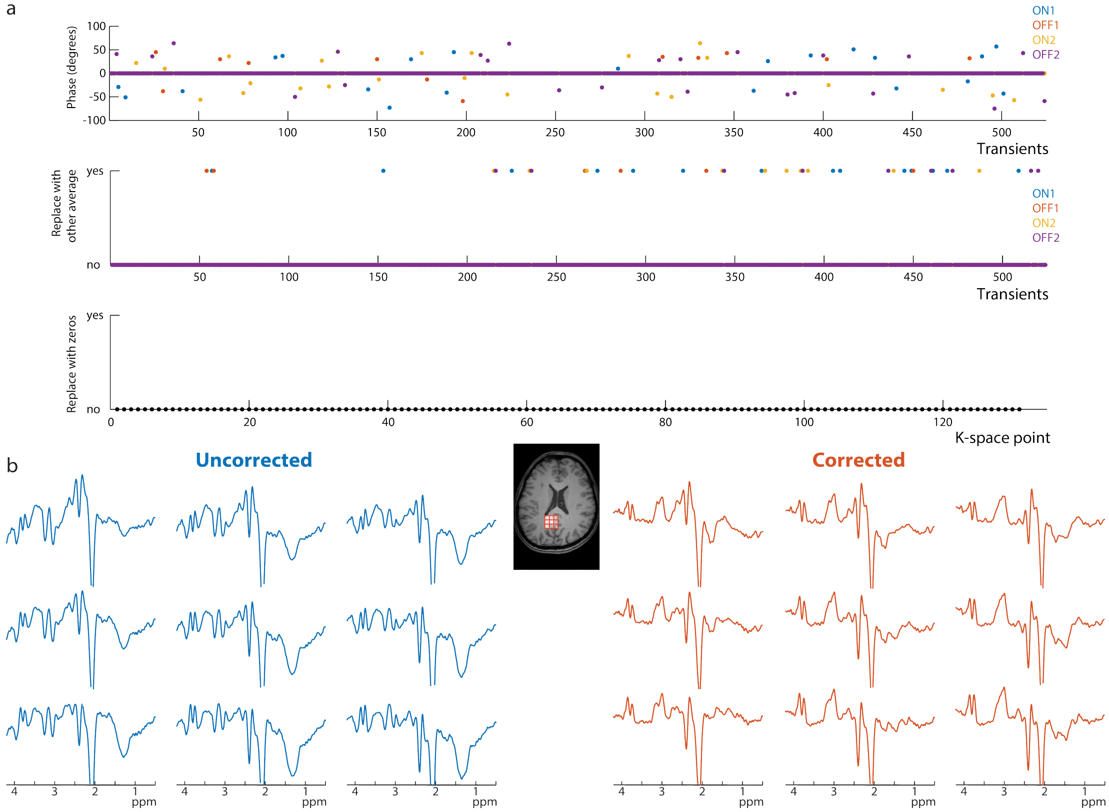

Figure 6.2. Slice location for the edited MRSI acquisitions on an axial T1-weighted image (left). Representative uncorrected and corrected difference spectra from a 3 x 3 voxel area within this slice location are shown on the right plotted from 0.5 – 4.2 ppm. Negative Cho and Cr subtraction artifacts can be seen in the uncorrected data; these artifacts are removed after compensation and clear GABA and Glx peaks at 3.0 ppm and 3.75 ppm can be visualized in the corrected spectra.

single Gaussian peak and their integrals relative to water were calculated in each voxel to form a GABA+ map. This was also done for the GSH peak in the uncorrected and the corrected spectra for another subject.

6.3 Results

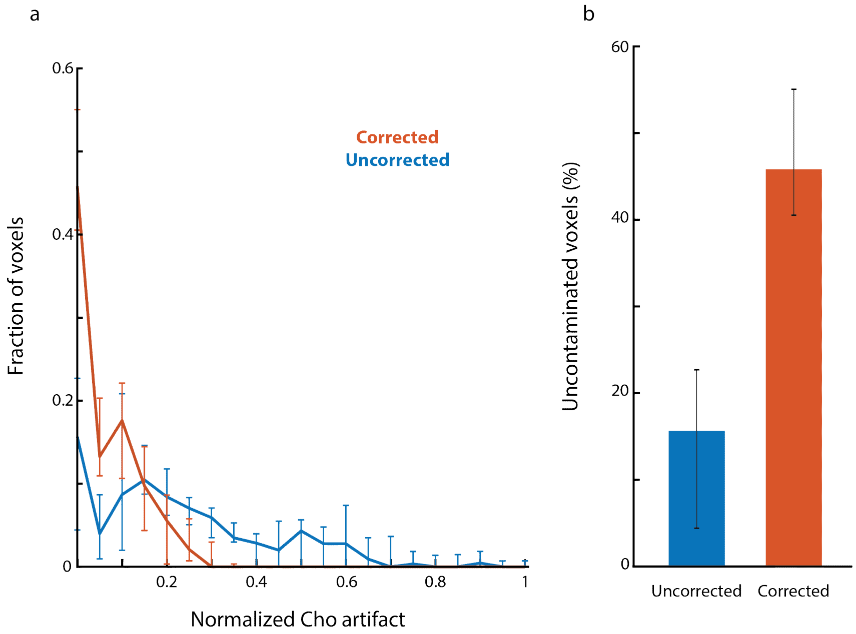

Figure 6.3. Cho subtraction artifacts resulting from fits to the GABA-edited data (a) Median distribution and interquartile range of the Cho subtraction artifacts across all subjects. The distribution of the Cho subtraction artifacts for the corrected spectra is skewed towards lower values versus that of the uncorrected spectra. In addition, there are significantly more voxels with no Cho artifacts in the corrected spectra than in uncorrected spectra (b).

Figure 6.2a shows the phase corrections and transient replacements made for a GABA-edited acquisition taken from one subject. Figure 6.2b shows representative spectra taken from a 3 x 3 voxel area in one subject with and without the corrections depicted in Figure 6.2a. It can be seen that there are significant artifacts, in this case manifest predominantly negative Cho and Cr signals resulting from the magnitude of the OFF sub-acquisition being significantly greater than that of the ON sub-acquisition. With motion compensation, however, these subtraction artifacts are significantly reduced and clean GABA and glutamate+glutamine (Glx) peaks can be visualized at 3.0 and 3.7 ppm respectively. There is also less lipid contamination in the corrected spectra.

Figure 6.3a shows the median distribution and interquartile range of the Cho artifacts across all 8 subjects represented as a fraction of the voxels fit inside the brain (average ± standard deviation of 128 ± 23 voxels). It can be seen that the Cho artifact distribution is skewed towards lower values in the corrected spectra versus the uncorrected spectra. This is also reflected in their median Cho artifact areas with a median (interquartile range) of 0.055 (0.053) for the corrected spectra versus 0.2 (0.32) for the uncorrected spectra. This amounted to about 3.6 times as much Cho subtraction artifacts in the uncorrected versus the corrected spectra. In addition, the Cho subtraction artifacts are smaller in the corrected spectra than the uncorrected spectra in the majority of the voxels affected by the motion compensation algorithm (~84%), and the corrected data sets have a significantly larger fraction of voxels with no Cho subtraction artifacts (figure 6.3b).

For the GSH-edited MRSI acquisition, a replacement-only motion compensation strategy was used since the water peak is saturated by the 4.56 ppm editing pulse which makes the peak more unreliable for phasing purposes. Figure 6.4 shows representative uncorrected and corrected GSH spectra taken from a 3 x 3 voxel area region in one subject. Significant subtraction artifacts are apparent in the uncorrected spectra, but these are largely removed by the compensation algorithm allowing a clean GSH peak at 2.95 ppm to be visualized.

Figure 6.5 shows represented GABA+ and GSH maps with and without motion compensation. Both the GABA+ map and the GSH maps become smoother after the motion compensation algorithm is applied, especially at the central regions of the brain. In particular, it can be seen that in the uncorrected GABA+ and GSH maps, a significant amount of signal relative to the rest of the brain can be seen at the center of the brain where the lateral ventricles are located at. This is largely, removed, however with the use of the motion compensation algorithm and we can see a dip in the GABA+ and GSH signal at the ventricles, as expected.

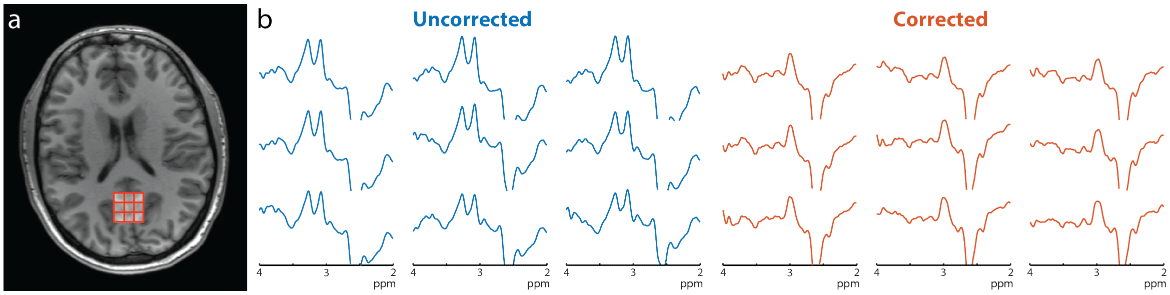

Figure 6.4. Representative GSH uncorrected and corrected spectra from a 3 x 3 voxel area (left) within this slice location is shown on the right plotted from 2 – 4 ppm. Large Cho and Cr subtraction artifacts can be seen in the uncorrected spectra, which are removed after compensation allowing visualization of the GSH peak at 2.95 ppm.

6.4 Discussion

The sensitivity of edited MR spectroscopic imaging to head motion necessitates the availability of accessible motion compensation methods to improve the accuracy and reliability of measurements. This chapter presents a retrospective motion compensation algorithm for edited MRSI. This compensation does not require any additional hardware or acquisitions, and only requires additional data post-processing. In addition, this technique is data-based and does not rely on any assumptions about the data which could potentially lead to the introduction of

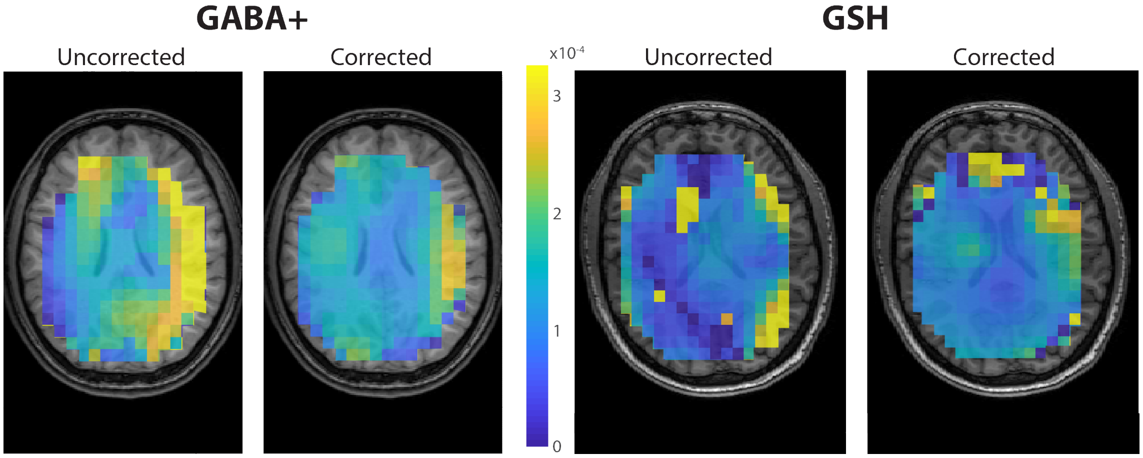

Figure 6.5. Representative GABA+ and GSH maps with and without motion compensation. Motion compensation removes much of the artifacts present in the metabolic maps and results in smoother GABA+ and GSH maps across the brain.

artifacts upon compensation. The technique presented here is shown here to be effective in reducing subtraction artifacts by about two-thirds in GABA-edited MRSI acquisitions and to have potential in correcting for motion in GSH-edited MRSI acquisitions. Although shown here to be effective in correcting edited MRSI acquisitions with Cartesian-based k-space sampling, this method can also be extended to other edited MRSI acquisitions with different k-space sampling techniques such as spiral-based trajectories or zig-zag transversal of k-space with echo planar spectroscopic imaging provided that at least 2 transients exist for each sub-acquisition type (at least 2 ONs and 2 OFFs).

Retrospective motion compensation in this study is made possible by the acquisition of multiple transients of the same type of sub-acquisition with the same phase-encoding gradient. For accurate phase compensation at a particular k-space point, at least 2 of the averages must be similar for the algorithm to phase the other averages to. If the program is unable to phase the averages and must replace a motion-corrupted average, one of those two averages must be of the same sub-type. Thus, for a 4-average acquisition, the two similar averages must be of different subtypes. However, the program preferentially chooses to preserve as many averages as possible with phase-correcting rather than replacing averages to reduce the amount of SNR loss resulting from replacing averages which results in an increase in the noise level relative to the signal level. However, it is possible that this SNR loss will be increased in acquisitions where more averages are removed with more severe head movements. Replacing all averages with zeros at certain k-space points was avoided as much as possible as removing too many k-space points would increase the effective point spread function.

For effective retrospective motion compensation, a reliably large residual water peak was necessary for identifying and correcting motion-affected averages. In this study, the HGDB dual water and lipid suppression sequence not only provided good enough water suppression to allow for the detection of the metabolite spectra, but also provided a reliably large residual water peak for retrospective motion compensation. This is likely to be possible as well with other weaker water suppression techniques such as CHESS (52) or with water-cycling (162) provided that the sequence isn’t optimized to remove all residual water. However, even with good suppression there is enough residual water signal for motion compensation as it originates from the entire slice. This is essential especially for GSH-edited acquisitions where the water peak at 4.68 ppm is saturated even further by the ON-editing pulse at 4.56 ppm, thus making the residual water in the ON-acquisition less reliable for phasing. However, the saturated residual water peak proved to be sufficient for identifying movement-affected averages. Because of this, a replacement-only approach was taken for the GSH-edited data which can result in an even greater reduction of the SNR. This approach could be improved upon to include phase correction with the use of a weaker water suppression method which would provide a more reliable water peak even in the presence of an editing pulse on resonance for GSH.

Although effective, the thresholds for motion compensation used in this study were chosen after preliminary exploratory investigations aimed at minimizing the corrected Cho subtraction artifacts and retaining SNR. These thresholds could be further improved upon by fuller optimization of the thresholds over a larger search space of thresholds aimed at reducing SNR loss and Cho subtraction artifacts. Additionally, this compensation technique can be extended to also incorporate phase and frequency compensation resulting from B_0 drift during the scan and some rarely used decisions made by the algorithm can be improved upon or combined for a more streamlined approach.

In this study, a repetition time of 1.5 - 2s was sufficiently long enough so that moderate motion would not affect sequential averages at the same k-space point. As the repetition time decreases, however, it is possible that some movements would affect more than 2 of the 4 averages at the same k-space point which would make it difficult to find a motion-uncorrected average. This can be mitigated by interleaving k-space averages to reduce the number of averages at the same k-space point corrupted by motion.

As noted above, methods exist for prospective motion correction for edited-MRSI acquisitions by acquiring a volumetric navigator each TR and performing real-time shim and motion compensation (9, 152). These techniques however do require software (and also hardware, if optical detection of motion is performed) that at the current time is not widely available in the MR community. In addition, the time to perform the volume navigator acquisition and online processing is long (~760 ms) and may put a restriction on the minimum repetition time for fast MRSI sequences such as multislice acquisitions.

In summary, a retrospective motion compensation for edited MR spectroscopic imaging was proposed and evaluated. The method requires no additional hardware or additional scan time making it suitable for implementation with any J-difference MR spectroscopic imaging sequence which acquires more than one transient per point in k-space. The method is expected to work best when there are small subject movements, and is not intended for use when motion is more frequent and/or larger amplitude; in these cases, full prospective motion correction will be needed (9).

Chapter 7 - Water suppression in the human brain with hypergeometric RF pulses for single- and multi- voxel MR spectroscopy

7.1 Introduction

In vivo ^{1}H magnetic resonance spectroscopy (MRS) and spectroscopic imaging (MRSI) allow for the non-invasive detection of a variety of neurochemicals within the brain. These endogenous compounds, however, are present in significantly lower concentrations than water, making their detection and quantification difficult without the use of pulse sequences that suppress the water signal. A number of techniques have been developed to separate the metabolite signals from the more abundant water signal, using either specialized acquisition techniques such as metabolite cycling (1), water suppression (52-54) and/or post-processing techniques to filter out the water signal (164). The most commonly used method is the inclusion of a water suppression module to saturate the water signal before spectral acquisition (52-54).

Most suppression techniques are based on the difference in chemical shift between the water and metabolite signals. One of the simplest and earliest water suppression methods, CHESS (52), used a single, frequency selective, saturation pulse applied to water prior to excitation and acquisition of the free induction decay. Another type of water suppression, referred to as MEGA (76) or BASING (49), uses selective spin-echo dephasing to remove the water signal by applying a selective refocusing pulse in conjunction with bipolar crusher gradients to dephase the water signal while rephrasing the metabolites. Other methods use either saturation or inversion pulses, where the delay after the RF pulse is optimized to minimize the longitudinal magnetization of water based on its T_1 relaxation time (51). Methods such as the WET (53) or VAPOR (54) sequences apply frequency-selective pre-saturation pulses in conjunction with crusher gradients to dephase and consequently suppress the water signal while leaving the magnetization of the metabolites untouched. An important component of these sequences is compensation for variations in the transmitter B_1 field (and/or miscalibrations of the RF flip angle) and a range of water T_1s, by applying multiple pre-saturation pulses and optimizing their delays and flip angles. The VAPOR sequence (54, 165) uses either seven or eight RF pulses of variable flip angles to make the sequence B_1 and T_1 insensitive. This results in highly effective water suppression and is currently the most commonly used water suppression sequence in single voxel (SV) MRS. A disadvantage of VAPOR, however, is that it has a long duration of ~750 ms which prohibits its use in short TR sequences, for instance fast MRSI (167).

In this article, a new water suppression sequence with one third of the duration of VAPOR is described. This sequence applies five frequency-selective hypergeometric saturation pulses, RF pulses with an asymmetric amplitude waveform that are closely related to the widely used hyperbolic secant pulses, (137, 167-170) at variable flip angles and delays that were optimized to minimize the residual water signal through iterative, numerical simulations over a range of B_1 variations and water T_1 values. The performance of hypergeometric water suppression (HGWS) was compared to VAPOR in vivo for both single voxel and multi-voxel acquisitions.

7.2 Methods

7.2.1 Pulse Sequence Design

The HGWS sequence was designed with consideration to both the longitudinal relaxation (T_1) of water, which varies depending on the tissue type (including possible lesions, and cerebrospinal fluid (CSF)), and the inhomogeneity in the RF field which is influenced by both transmit RF coil geometry and loading. To account for the tissue dependence of the water longitudinal relaxation, the sequence must null the longitudinal magnetization of a large range of

T_1 values. In the human brain at 3T, these values range from 800 ms in white matter to 4100 ms in CSF (24, 26, 171). In addition, the sequence must be insensitive to RF field variations to avoid flip angle variations which can affect the effectiveness of water suppression sequence.

Amplitude- and frequency-modulated hypergeometric (HG) RF pulses were chosen as the frequency selective pulses (137, 167-170). Hypergeometric RF pulses can be designed with an asymmetric frequency profile that contains one edge with a transition width significantly narrower than the other edge. Since most of the resonances of interest in the proton spectrum are upfield from water, the pulse can be designed with a sharp cutoff upfield and a broader transition band on the downfield side.

These hypergeometric RF pulses were created using the following pulse modulation functions for the effective field vector components in Eqn. 1 in Rosenfeld et al. (168):

$$\omega_x = \omega_1 = \Omega_0 \frac{\sqrt{z(1-z)}}{az+b}$$

$$\omega_y = 0$$

$$\omega_z = \omega - \omega_0 = \frac{cz+d}{az+b} - \omega_0$$

(7.1)

$$t = ln\left(\frac{z^b}{(1-z)^{a+b}}\right)$$

$$z \epsilon [0,1], t \epsilon [-\infty, \infty]$$

where ω_x and ω_y is in rad/s. To create a 30 ms hypergeometric pulse with a sufficiently small transition bandwidth (37 Hz) so that no metabolite spins downfield of 4.1 ppm would be affected, the following parameters were used: a = 4, b = 0.5, c = -4, d = 3.5, and $\Omega_0 = 8$ (ω_{1max} = 0.2 kHz) and the waveform was sampled to 1172 points with evenly spaced time points. The pulse was truncated at .1% of the peak amplitude to the left of the peak amplitude and at 7.9 x 10^{-6} % to the right of the peak amplitude.

Hypergeometric pulses were previously used to create a dual-band water and lipid suppression sequence for MR spectroscopic imaging (HGDB) (137). The sequence developed here differs in that it uses single band HG pulses only for water suppression, and does not include a 100 ms delay which was previously used for 8 outer-volume suppression (OVS) pulses. The pulse amplitudes and delays of the new HGWS sequence were optimized using the water suppression portion of the HGDB sequence (2) as starting values. These starting amplitudes and delays were 1.08 μT/50 ms, 2.54 μT/35 ms, 1.09 μT/100 ms, 1.24 μT/35 ms, and 3.08 μT/18.5 ms. The optimization searched for the combination of delays and pulse amplitudes that best

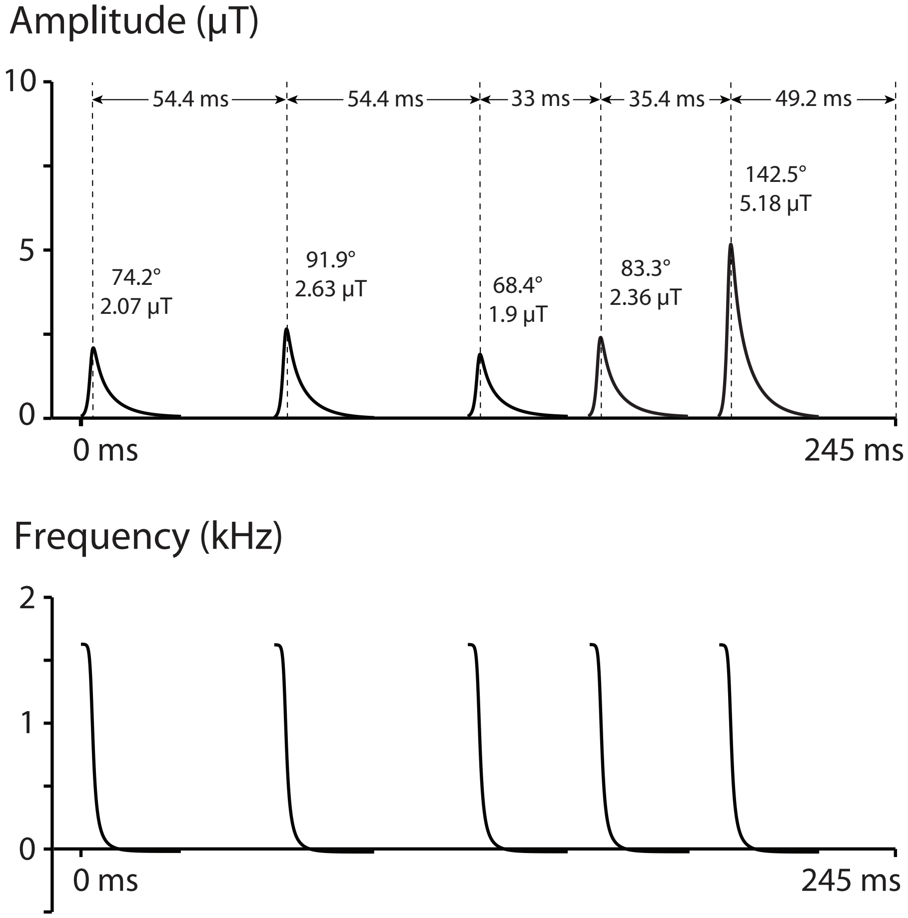

Figure 7.1. (a) Amplitude and frequency modulation functions for the HG pulses, (b) schematic diagram of the full HGWS sequence showing the delays (ms) and amplitudes (T) of each RF pulse. The total duration of the HGWS water suppression sequence is 245 ms which is significantly shorter than the total duration of 750 ms for VAPOR (not shown).

suppressed the water signal over a range of T_1 and B_1 variations. Both the amplitudes and delays of the new HGWS sequence were optimized using simulated annealing in two dimensions in MATLAB (172) using an analytical predictor of the adiabatic pulse response (167) rather than a full pulse simulation. This optimization covered a range of T_1 values from 500 ms to 3000 ms and a max B_1 range of 200 Hz to 300 Hz ($\approx$ 4.7 to 7.0 μT) . The performance of the optimized sequence was then simulated over a range of T_1 values from 500 ms to 5000 ms and a B_1 variance of -25% to 25% of the nominal B_1 strength of 5.18 μT (.22 kHz, the point of zero B1+ variance) and compared to a VAPOR water suppression sequence with sinc-Gaussian pulses that had the following flip angles and delays: 90°, 150 ms; 90°, 100 ms; 160.2°, 122 ms; 90°, 105 ms; 160.2°, 102 ms; 90°, 61 ms; 160.2°, 67 ms; and 160.2°, 28.5 ms. The total duration of the VAPOR sequence was 750 ms. Crusher gradients after each RF pulse were also simulated and assumed to perfectly suppress all transverse magnetization. MATLAB was used to perform all computations.

7.2.2 In Vivo Experiments

All experiments were performed on a Philips Achieva 3T scanner using a body coil for transmit and a 32-channel head coil for receive. All subjects underwent a 3D T_1-weighted MPRAGE scans with 1 mm isotropic resolution which was used to plan MRS scan voxel locations and also in data processing to estimate gray matter (GM), white matter (WM) and CSF content of each voxel by segmenting these images using SPM. Prior to MRS, field homogeneity was adjusted up to 2nd order. No optimization of RF pulses flip angles was performed for the water suppression pulses. HGWS and VAPOR water suppression sequences were added as prepulses to the PRESS sequence and compared in both single voxel experiments and multi voxel experiments. For the VAPOR sequence, crusher gradients with a 10 ms duration were applied after RF pulse 1 – 7 and a crusher gradient with a 5 ms duration was added after the last pulse. These gradients had the following strengths (mT/m) in the x, y, and z direction: (10,0,0), (0,10,0), (0,0,10), (9,0,0), (0,8,0), (0,0,7), (8,0,0), (0,10,10). Crusher gradients with a 3 ms duration were added after each RF pulse in the HGWS sequence with gradient strengths (mT/m) in the x, y, and z direction: (10,0,0), (0,10,0), (0,0,10), (9,0,0), (0,8,0).

Single voxel experiments were performed 7 healthy adults (3 female; age 27 ± 2 years) in (3 cm)^3 voxels in the centrum semiovale (CSO), midline parietal region, and insula with 80 signal averages. An additional single voxel experiment was performed in a (4.5 cm)^3 midline parietal region with 40 signal averages. Additional scan parameters included an echo time of 35 ms, a repetition time of 2 s, a spectral bandwidth of 2 kHz, and 2048 points. Water un-suppressed references were also collected with 8 signal averages and water suppression factors were calculated as the peak height of the residual water peak divided by the peak height of the unsuppressed water signal. To test for differences in water suppression effectiveness between the two methods, two-tailed paired t-tests were performed with statistical significance defined as $p < 0.05$.

Multi voxel experiments were performed in 6 healthy adults (3 female; age 27 ± 2 years) at an echo time of 41 ms and a repetition time of 1.5 s for a total scan time of 14 min and 52 sec. The PRESS sequence used frequency modulated excitation pulses with a peak B_1 of 13.5 μT and a bandwidth of 4.26 kHz. One 20 mm thick slice was recorded with a field of view of 180 x 210 mm and a volume of interest of 80 x 100 mm sampled with a matrix size of 18 x 21. This resulted in a nominal in-plane resolution of 10 x 10 mm and a voxel size of 2 cm^3. Corresponding water-unsuppressed reference MRSI scans were also acquired with the same scan parameters for calculation of water suppression factors. To suppress unwanted signals outside the VOI in the MRSI experiments, four OVS pulses were also applied.

7.3 Results

7.3.1 Simulation Results

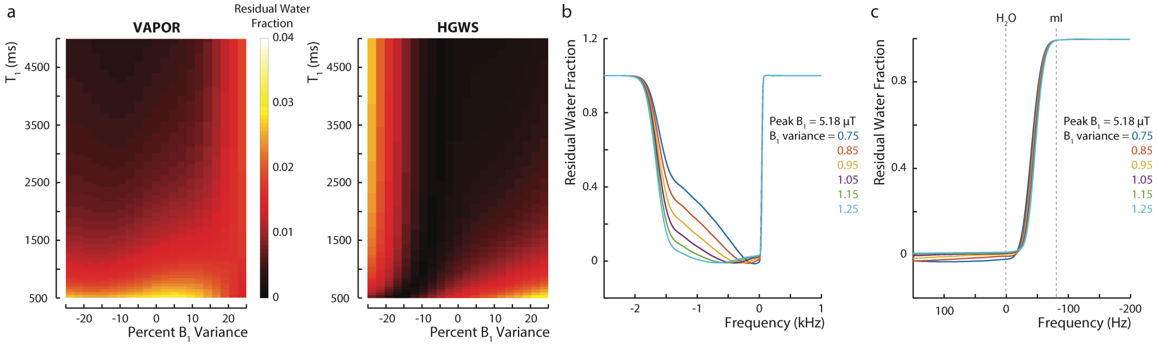

Figure 7.2. (a) Simulated residual water magnetization fraction (see color bar for scale) as a function of T1 and B1 for VAPOR (left) and HGWS (right). (b) Calculated residual Z-magnetization as a function of frequency offset using a fixed T1 value of 1150 ms for a range of B1 values between + and – 25% deviation from the nominal B1. (c) Close-up of the residual Z-magnetization as a function of frequency offset from (b) about the transition region. The spectral positions of water and myo-inositol (mI) at 3T are indicated in the figure.

Table 1. Tissue composition of the four single voxel locations (mean ± SD)

	WM (%)	GM (%)	CSF(%)
Parietal - small	35.3 ± 3.5	54.1 ± 3.0	10.7 ± 4.0
Parietal - large	50.3 ± 3.5	37.9 ± 2.0	11.8 ± 4.3
CSO	73.4 ± 2.9	21.4 ± 3.0	5.2 ± 1.8
Insula	33.5 ± 4.4	59.2 ± 1.7	7.3 ± 3.9

Table 7.1. Tissue composition of all four single voxel regions showing the percentage of white matter (WM), gray matter (GM), and cerebral spinal fluid (CSF) in each voxel. The CSF volume makes up a small fraction of the voxels and do not vary significantly between regions. The small parietal region and insula region have significantly more gray matter and less white matter than the centrum semiovale and large parietal region.

The optimized sequence with a total duration of 245 ms is shown in Figure 7.1. This sequence had the following amplitudes and delays: 2.07 μT/58.2 ms, 2.63 μT/58.2 ms, 1.9 μT/36.8 ms, 2.36 μT/39.1 ms, 5.18 μT/49.2 ms. Figure 7.2a shows the simulated absolute residual magnetization as a function of T_1 and B_1 for both the HGWS sequence and the VAPOR sequence. In both sequences, the residual Z-magnetization does not vary substantially as a function T_1 or B_1 except at low T_1 values and large B_1 variations. Consequently, the standard deviation of the residual longitudinal magnetization is similar for both VAPOR and HGWS at 0.0057 and 0.0066 respectively. However, HGWS has better overall water suppression factors than VAPOR over the range of T_1s and B_1 values simulated; the average residual water suppression fraction is 0.0043 for HGWS and 0.0078 for VAPOR. Figure 7.2b plots the frequency profile of the HGWS sequence as a function of B_1 and Figure 7.2c shows a close-up of the frequency profile ~200 Hz about the water frequency (0 Hz); it can be seen that the shape of the transition band changes slightly with B_1 (with increasing bandwidth as B_1 increases), however, even at the highest B_1 value, metabolite resonances such as the *myo*-inositol peak at 4.06 ppm will remain unaffected by the HGWS sequence.

The specific absorption rate (SAR) of the PRESS sequence with VAPOR and HGWS prepulses were comparable at 0.20 W/kg and 0.23 W/kg respectively.

7.3.2 Single Voxel Experimental Results

The four brain regions measured contained different amounts of gray and white matter (table 1). HGWS showed significantly better water suppression factors than VAPOR in all four regions ($p < 0.001$) for all subjects (figure 7.3). The improvement ranged from 2.7-fold better water suppression in the insula to 5.6-fold better water suppression in the large parietal region. Taking tissue composition into consideration (table 1), the HGWS sequence performed best in the regions with more white matter. HGWS performed better for the large parietal voxel and CSO, which have more white matter than the for small parietal region with more gray matter ($p < 0.05$). In addition, the HGWS residual water signal was greater in the gray matter-rich insula than in the large parietal region with $p < 0.01$. These differences in water suppression can be seen qualitatively in the representative water peak from one subject in each of the regions (figure 7.4).

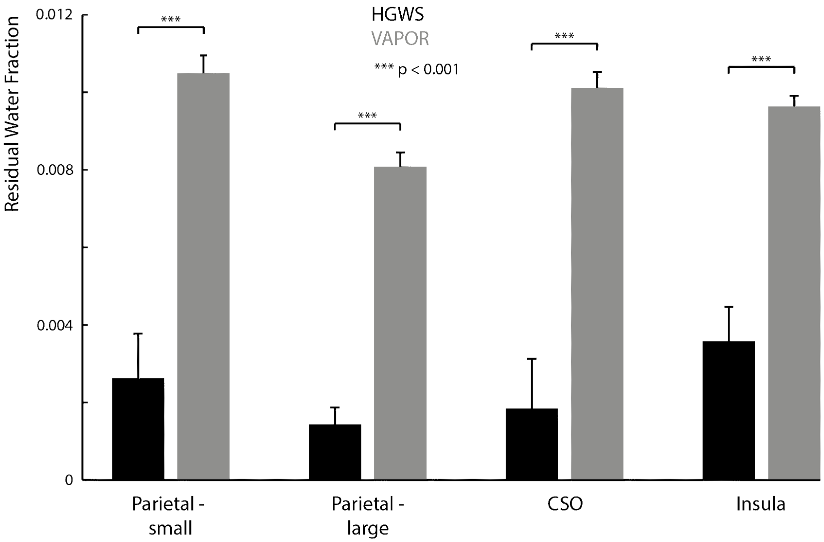

Figure 7.3. In vivo single voxel water suppression factors (residual water fraction) calculated as the peak height of the residual water over that of the unsuppressed water averaged across subjects. In all four brain regions (large and small parietal voxels, centrum semiovale (CSO) white matter, and insular cortex), the HGWS sequence gave a significantly ($p < 0.001$) lower residual water fraction than VAPOR.

As can be seen in the rightmost panel in figure 7.4, the different water suppression methods lead to differences in the baseline of the acquired spectra. However, the metabolite peak intensities are equivalent between the two methods, thus demonstrating that the HGWS sequence does not lead to a loss in signal of other compounds upfield from the 4.68 ppm water peak. In particular, it can be seen that the signal intensity of the *myo*-inositol peak at 4.06 ppm which is close to the water peak at 4.68 ppm is preserved, demonstrating that the transition bandwidth of the hypergeometric pulses is sufficiently small.

7.3.3 Multi Voxel Experimental Results

Figure 7.5a, shows the PRESS volume of interest, an overlay of a map of the residual water for both the HGWS and VAPOR sequence as well as the HGWS/VAPOR residual water ratio in each voxel. The blue, green, and orange box indicate 3x3 voxel areas with nine example spectra where the mean HGWS/VAPOR residual water ratio is 0.83, 0.41, and 0.068 respectively. It can

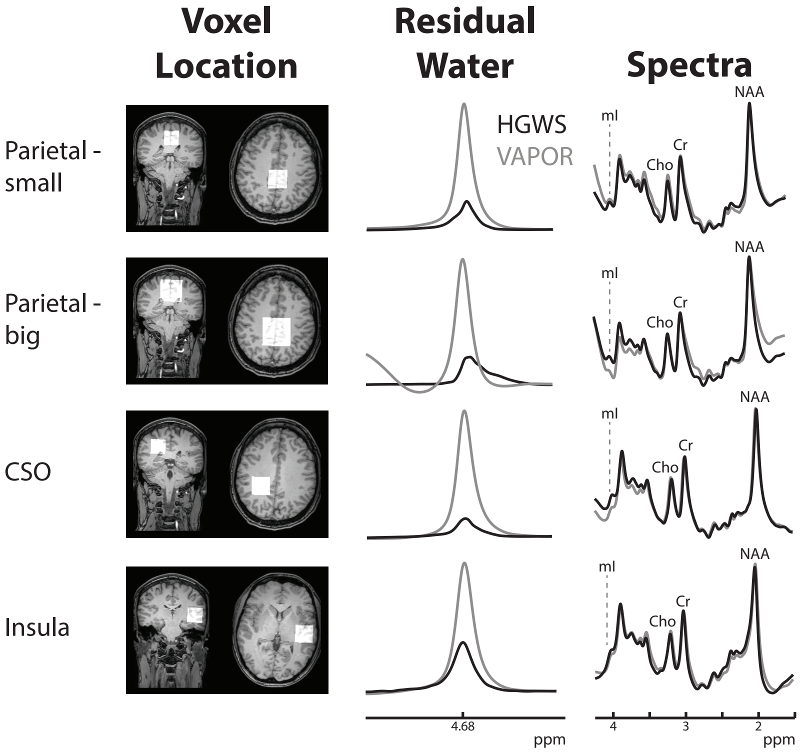

Figure 7.4. Voxel placements of in vivo single voxel acquisitions in all four regions overlaid on T1-weighted axial and coronal images as well as representative water peaks, and spectra from each location for both HGWS and VAPOR sequences. The residual water from the VAPOR sequence has a visibly higher peak than HGWS while the metabolite spectra are qualitatively equivalent between the two methods, although differences in spectral baselines can be observed, most notably for the large parietal voxel. The residual water peaks are plotted with a vertical scale 10 times that of the metabolite spectra.

be seen that across the volume of interest, the residual water peak is lower in the HGWS sequence than in the VAPOR sequence. This is reflected in the HGWS/VAPOR residual water ratio map where most of the ratios were below 0.8. Figure 7.5b shows the residual water peaks and spectra from the regions of interest in figure 7.5a. It can be seen that the spectra have equivalent signal intensity indicating that the HGWS sequence does not lead to metabolite signal loss relative to VAPOR, similar to the single voxel experiments. Figure 7.6a shows a histogram of the HGWS/VAPOR residual water fraction as well as the mean values across the six subjects. It can be seen that the distribution of the residual water fractions for HGWS is skewed towards lower values with the mean residual water fraction 2.3 times lower when using HGWS versus VAPOR. The mean residual water fraction over all the voxels for each subject was 0.0044 for HGWS and 0.0099 for VAPOR and are in agreement with simulation values of 0.0043 and 0.0078 respectively. It can also seen in figure 7.6b that across subjects, the HGWS/VAPOR residual water ratio is less than one in 98.9% of the voxels, indicating that the HGWS sequence performs better than the VAPOR sequence in most voxels across subjects. In addition, 80% of the voxels have a HGWS/VAPOR residual water ratio of 0.6 or less. The B_0 inhomogeneity, as calculated by the deviation of the residual water peak frequency from 4.68 ppm, was 4.7 Hz (average) ± 2.9 Hz (standard deviation).

7.4 Discussion

Sufficient water suppression is crucial for both single voxel and multi voxel spectroscopic acquisitions as sub-optimal water suppression can lead to errors in metabolite quantification. In this chapter, HGWS, a new method for water suppression, is introduced, and compared to VAPOR, which is currently a very widely used (the ‘gold standard’) water suppression sequence for in vivo brain spectroscopy. This current study extends on our previous work on dual water and lipid suppression with hypergeometric pulses (HGDB) in the following ways: (a) it builds a new basic RF pulse with a sharper transition bandwidth that does not affect the metabolite spins (b) it removes the lipid suppression portion of the sequence, and re-optimizes it for water suppression only. A limitation of the HGDB sequence is that the inclusion of frequency-selective lipid suppression prepulses can impede detection of compounds with resonances around the frequency of the lipid prepulses such as lactate, alanine, and leucine. In addition, the inclusion of a 100 ms delay within the sequence for the inclusion of lipid OVS pulses limits the sequence from being completely optimized for water suppression. Thus, a sequence optimized for more

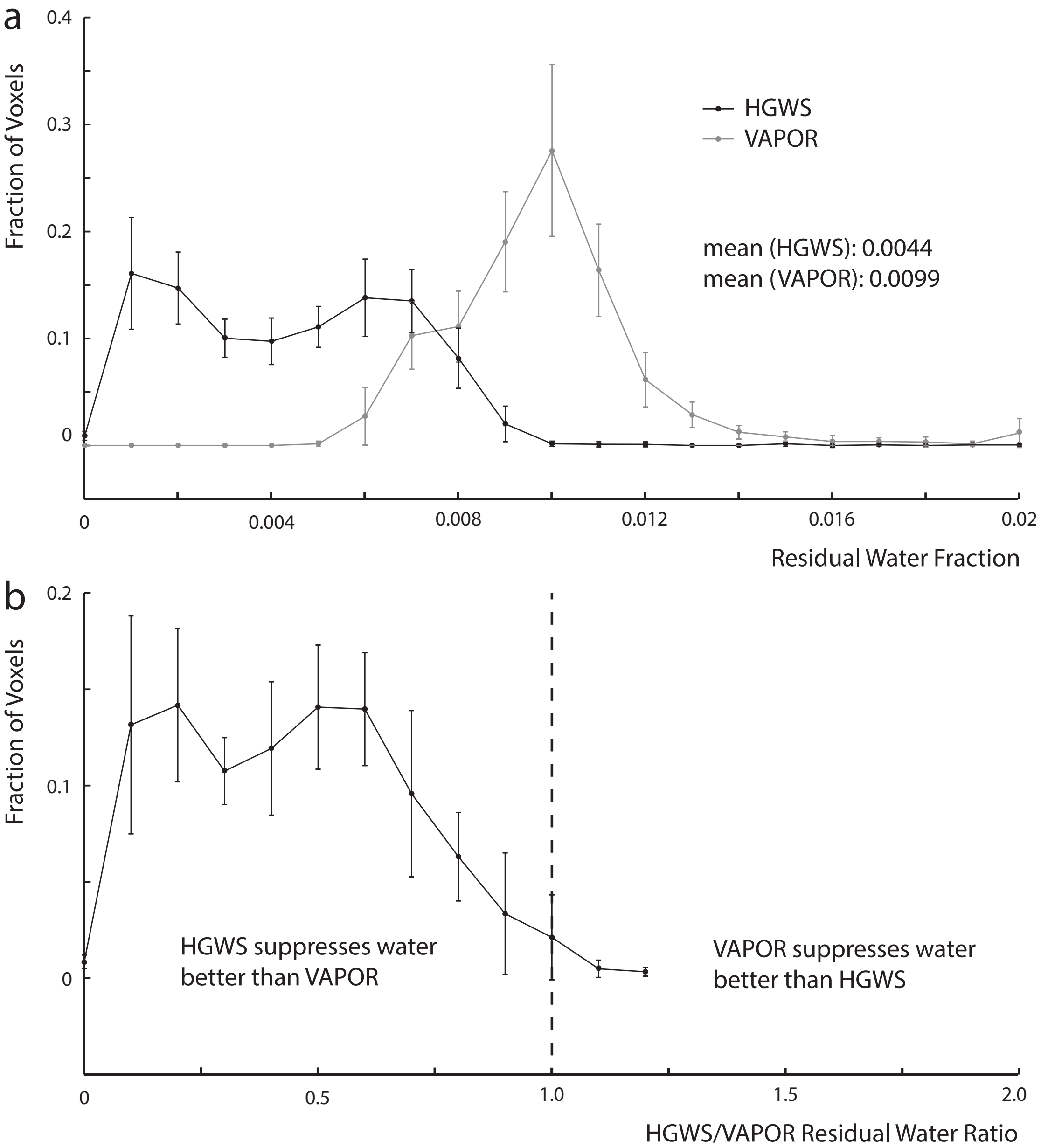

Figure 7.6. (a) Distribution of the residual water fractions in the MRSI acquisitions for both HGWS and VAPOR across subjects. The average residual water fraction for HGWS is 0.0044 which less than half of the average residual water fraction of 0.0099 for VAPOR. (b) The residual water ratio of HGWS to VAPOR across subjects. Ratios less than one are voxels in which the HGWS sequence performs better than VAPOR. HGWS performs better than VAPOR in 98.9 percent of the voxels.

effective water suppression only is especially useful for single voxel and PRESS-MRSI acquisitions where the region of interest is far from the lipid-rich peri-cranial regions.

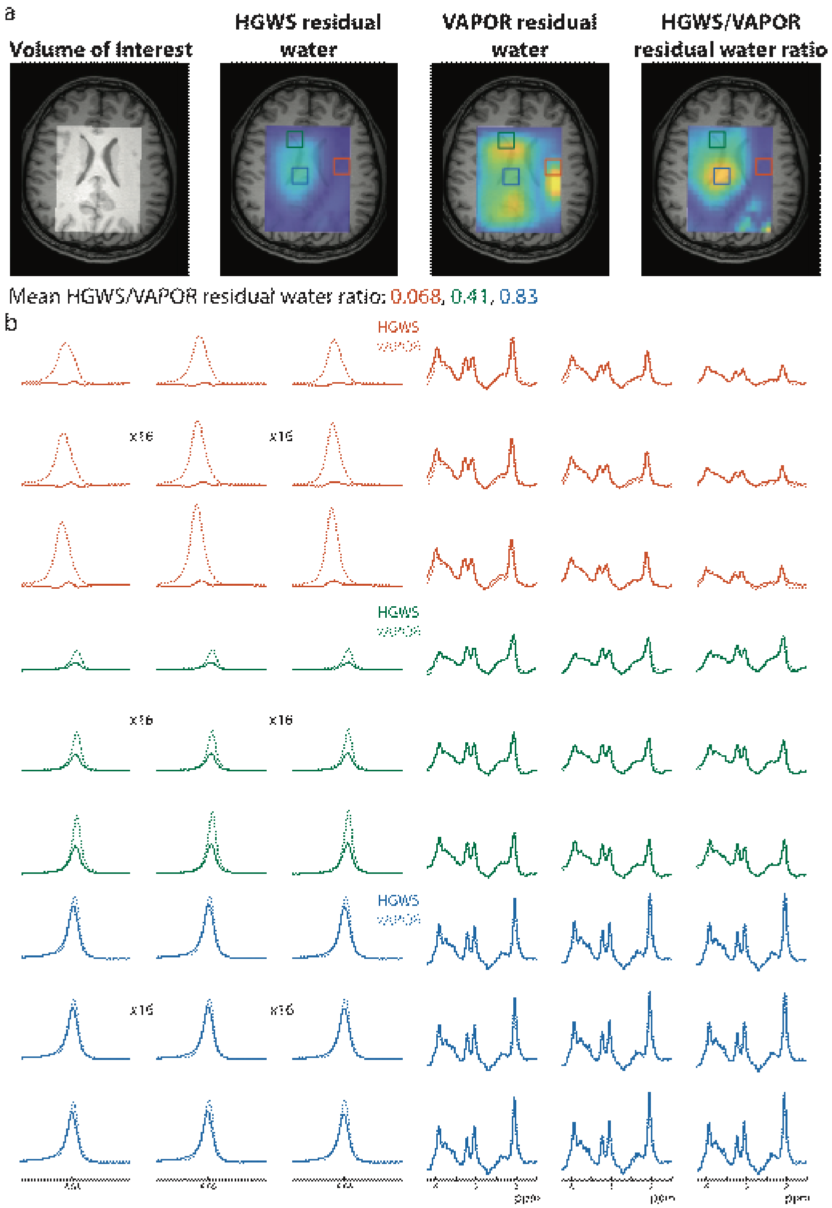

Figure 7.5. (a) Volume of interest of the in vivo MRSI acquisitions, representative residual water fraction maps, and a representative residual water peak ratio map of HGWS to VAPOR overlaid on a T1-weighted axial image. The colored boxes represent 3x3 voxel areas of low (orange), medium (green), and high (blue) HGWS to VAPOR ratios. The average residual water ratios for these areas are below the T1-weighted images and are 0.068, 0.41, and 0.83 respectively. (b) The residual water peaks (left three columns) and metabolite spectra (right three columns) for the regions of interest shown in figure 7.5. The residual water peaks are plotted with a vertical scale 16 times that of the metabolite spectra. Although the relative HGWS to VAPOR residual water ratio varies significantly, across the volume of interest, the metabolite spectra between the two water suppression methods are qualitatively equivalent.

Overall, this optimized sequence is robust, of relatively short duration, and performs better than the VAPOR sequence, despite having fewer RF pulses. Simulations demonstrate that the sequence is relatively insensitive across the range of T_1 and B_1 variations likely to be found in vivo in the human brain at 3T. This was confirmed in experiments in vivo for both single-voxel and multi-voxel measurements. In addition, this sequence is only 245 ms long, a considerably shorter duration than VAPOR which has eight RF pulses and delays resulting in duration of over 700 ms long. This water suppression effectiveness and reduced duration relative to VAPOR makes the sequence especially suited for fast MRSI sequences where insensitivity to B_1 inhomogeneity and minimization of the presaturation sequence duration is necessary. For example, a shorter presaturation sequence would allow for more slices to be incorporated into a pulse repetition time of a multislice MRSI acquisition (137).

Considering the small region from which measurements were acquired, differences in the HGWS water suppression factors in single voxel acquisitions is not likely to be driven by either B_0 or B_1 inhomogeneity, but T_1 differences arising from different tissue types with HGWS performing better in areas with higher ratios of white to gray matter. Unlike single voxel acquisitions, however, differences in residual water fractions in MRSI acquisitions appear to be tissue-independent. In the multi-voxel acquisitions, areas with low and high water suppression effectiveness have a large heterogeneity of different tissue types. Thus, the differences in water suppression effectiveness is likely driven by RF field inhomogeneity. Even with this additional confounding factor, however, HGWS performs better than VAPOR in most voxels across subjects. In the presence of significant B_0 inhomogeneity, HGWS is also expected to perform better than VAPOR. This is due to the flat inversion profile of the HGWS sequence upfield from the resonant frequency of water (4.68 ppm) relative to the VAPOR sequence which uses more selective sinc-Gaussian editing pulses. This would lead to better water suppression in locations with B_0 inhomogeneities that shift water towards higher frequencies.

In this work, the basic water suppression sequence for VAPOR and HGWS were compared without a separate prospective flip angle optimization for the water suppression sequence prior to acquisition. As commonly performed on many scanners, such optimizations result in a scaling of all water suppression pulses by a single correction factor. In principle, this procedure should not be necessary as flip angle calibration on clinical 3T scanners is usually very accurate, however water suppression factors may be improved by 'tuning' the flip angles to minimize the water signal according to the tissue/CSF composition of individual voxels. It is likely that the experimental performance of both sequences compared here could have been improved by such an empirical optimization. However, performing this optimization is often very time-consuming, so sequences that give adequate suppression without optimization are preferable.

In summary, a novel water suppression method using five hypergeometric RF pulses and delays is proposed and evaluated. The sequence is significantly shorter than the VAPOR water suppression sequence making it especially suitable for use in fast MRSI sequences, and performs significantly better in vivo for both single voxel and multi voxel acquisitions.

Chapter 8 – General Discussion and Conclusions

Since its conception, J-difference editing has been a promising technique for probing low concentration metabolites with applications in both clinical and basic neuroscience research. Some challenges that prohibit its more widespread use, however, is its inherently low signal-to-noise and sensitivity to motion and field instabilities. In addition, the technique takes a targeted approach which limits both the spatial and spectral information that can be acquire within a single scan. Thus, the ultimate goal of this thesis was two part: one, to develop methods to improve the reliability of edited MRS/MRSI scans and two, to increase efficiency of edited-MRS/MRSI data acquisition by either decreasing the sequence duration or multiplexing scans to increase the amount of information acquired within a scan session. The development of these methods has broader implications for increasing both the reproducibility and scope of applied studies.

When this thesis was started, J-difference editing was already being used to edit a range of J-coupled metabolites including GSH (10, 14, 16) and Lac (6, 47, 67). Most applications, however, focused solely on GABA and its role in the pathophysiology of neurological and psychiatric disorders (1, 2, 7, 33) despite the existence of other editable metabolites. Thus, despite the role of GSH as the brain's main antioxidant, its function has been studied less extensively. Consequently, a range of optimal echo times from 68 – 131 ms to edit GSH have been reported. Here, a complete study of the optimal echo time to edit GSH is presented and an echo time of 120 ms in vivo is found. Since both GSH and Lac have been implicated in the same brain pathologies and share similar optimal echo times (120 ms and 144 ms respectively) and edited resonant chemical shifts, it was possible to simultaneously edit both metabolites simultaneously. It was also realized in this study that although the longer echo time of 120 ms was optimal for editing GSH, it only provided a marginal benefit (~15% higher SNR) relative to the shorter echo time of 68 ms. This resulted in part from the relatively short GSH T_2 relaxation constant which skewed the optimal echo time towards lower values. This insight became important when implementing an approach to dual-editing of GABA which has an optimal echo time from 68 ms – 80 ms (135) and GSH as it was realized that both metabolites can be edited simultaneously with a compromise echo time of 80 ms (135) without too much loss in GSH SNR. Chapter 2 also evaluated two approaches to edit GSH and Lac simultaneously: sinc-MEGA with less selective editing pulses that encompasses both edited frequencies and DEW which was first introduced in reference 78 for the example of dual-editing of Asc and GSH with more selective editing pulses. In this implementation, the editing pulses alternated between being ON for GSH and ON for Lac. Subtracting the two sub-acquisitions from one another resulted in a spectrum with both GSH and Lac peaks but with opposite polarities. Both methods are shown to be similar with a high overall editing efficiency of GSH and Lac comparable with separate acquisitions of each metabolite using conventional MEGA-PRESS. However, both methods co-edit Cr with the Lac editing pulse which overlaps with the GSH peak and can make quantification of GSH more difficult. In the assessment of the two methods presented in chapter 2, this did not appear to pose a problem to the data acquired from healthy adults in a region located near the back of the brain. In the presence of significant motion and/or linewidth increases due to poor shimming in regions such as the frontal lobe, the distinction between these two overlapping peaks can diminish and complicate quantification of GSH.

From this study, we found that editing two metabolites simultaneously is feasible if both their edited and observed frequencies are sufficiently resolved from one another. If the observed spins share the same chemical shift, however, the approaches presented in chapter 2 will not suffice. This lead us to the development of a novel technique called HERMES that can edit two metabolites simultaneously even if the detected signals overlap one another. This was done using a Hadamard-based encoding of combinations of editing pulse frequencies which can be reconstructed to give the edited spectrum of each metabolite separately. We also showed that HERMES is capable of editing both NAA and NAAG simultaneously which provides an acceleration factor of two-fold relative to acquiring the edited spectrum of each metabolite separately. From this study, however, we quickly realized that HERMES can be extended to edit three overlapping metabolites simultaneously using the same number of sub-acquisitions. Thus, a HERMES scheme to edit Asp in addition to NAA and NAAG with the same number of sub-acquisitions was also developed and assessed. Editing all three metabolites simultaneously provided an acceleration factor of three-fold relative to acquiring the edited spectrum of each metabolite separately. In particular, such an acquisition would be advantageous in examining the metabolic pathway formed by Asp, NAA and NAAG. This early work on HERMES laid the groundwork for other implementations with different combinations of J-coupled metabolites such as GABA+ and GSH (135), MM-suppressed GABA and GSH (150), and HERCULES (173). This method can also be applied to other combinations of compounds such as GSH and Lac which would also remove the overlap of co-edited Cr introduced by dual editing techniques in chapter 2 by keeping the reconstruction of compounds affected by the Lac and GSH editing pulses separate. In addition, this work has gone on to be used in several different applied studies such as evaluating the role of GABA and GSH in decision making or in depression (174).

Although, the spectral content of edited acquisitions can be increased by multiplexing our acquisitions, J-difference editing is typically used in conjunction with single-voxel localization which limits the amount of spatial content that can be acquired within a single scan session. With the development of HERMES, we realized that the Hadamard-based approach can used to separate edited spectra from two voxels. This lead to the development of SHERPA which is demonstrated in chapter 4 to be capable of editing GABA in two voxels simultaneously. This technique is also demonstrated here to be promising in editing two metabolites in two voxels simultaneously for the example of GSH and Lac with DEW for multi-metabolite, multi-region editing. This particular method, however, is not without drawbacks. Relative to separate MEGA-PRESS acquisitions of each voxel separately, SHERPA some degree of freedom in voxel placement as the two voxels cannot be rotated independently relative to one another. In addition, the voxels cannot be placed together as the editing pulse loses efficiency at the edge of the voxels when they are placed closer together which leads to a reduction in SNR.

Although SHERPA provides an improvement in spatial coverage over conventional single-voxel localization, there are often times where fuller spatial coverage is desired such as instances when the region of interest is unknown. This can be done using spectroscopic imaging localization. Thus, we decided to extend our HERMES-editing technique for use with spectroscopic imaging localization for multi-voxel editing and evaluated the feasibility of performing HERMES-editing of GABA and GSH with PRESS-MRSI. This allowed for multi-metabolite, multi-region editing. It was found that HERMES-MRSI of GABA and GSH was equivalent to separate MEGA-MRSI acquisitions of each metabolite separately and was capable of detecting GABA and GSH concentration differences between grey matter and white matter. However, when extending HERMES-MRSI to clinical applications, it is likely that HERMES-MRSI will have greater motion sensitivity than MEGA-MRSI, since four sub-spectra are now needed instead of two. This would affect the quality of both spatial localization and editing.

While we found that edited-MRSI is feasible at 3T, performance of the technique was variable due to the sensitivity of both the MRSI-sequence and J-difference editing scheme to head motion or other instabilities which cause subtraction artifacts. In single-voxel spectral editing, post-processing schemes to identify and correct variations in phase and frequency between averages are available. For edited-MRSI, however, the presence of phase-encoding gradients prohibits the direct application of such techniques. Thus, our next goal was to develop a retrospective motion compensation method that provides similar post-processing corrections to individual transients. Consequently, this lead to the development of the method presented in chapter 6 where individual transients were either phase-corrected or replaced with an average of the same sub-acquisition type at each point in k-space. In vivo, this technique was shown to be capable of reducing subtraction artifacts by a factor of three when using GABA-edited spin echo MRSI sequence. In addition, a replacement-only version of the method showed promise in reducing subtraction artifacts in GSH-edited spin echo MRSI acquisitions. With the reliance of the method on the magnitude and phase of the residual water peak, it is also likely that the performance of the motion compensation method will improve with the use of techniques that provide less effective water suppression such as CHESS or WET (52, 53). It may also be beneficial to use non-water suppressed acquisitions such as metabolite cycling (163) to retain the full intensity of the water signal in each average. Although this work focused mostly edited MRSI acquisitions, this method can be extended for use with conventional MRSI acquisitions. Direct application of the technique, however, is difficult as conventional MRSI acquisition only acquires at one k-space point. This can be accounted for by increasing the number of averages acquired and using parallel reconstruction methods such as a SENSitivity Encoding (SENSE) (175) to accelerate acquisition so that the scan duration remains the same. Unfortunately, the replacement portion of this method cannot be directly applied to HERMES-MRSI acquisitions as HERMES requires four independent sub-acquisitions. And although shown here to be effective in reducing subtracting artifacts in healthy adults, this method is not designed to compensate for larger or more continuous motion such as instances where clinical populations or children who are more uncomfortable with the MR setting are being examined. For such cases, only prospective motion correction schemes (e.g. (151)) would be expected to be successful.

From these spectroscopic imaging acquisitions, it was found that while the PRESS-MRSI and spin-echo sequences increased the spatial coverage of edited sequences significantly, data from many important cortical areas were not being acquired as both methods were limited to data within a single slice (spin-echo) or within a specific region of a single slice (PRESS-MRSI). In order in to further increase spatial coverage, slices from different locations can be interleaved within a TR. To do so, however, the duration of OVS or water/lipid suppression prepulses needs to be reduced in order to maximize the number of slices that can be acquired at a time. However, VAPOR, the gold standard water suppression technique, has a long sequence duration of ~750 ms which places a significant limit the amount of slices that can be included in a multi-slice acquisition. Thus, we created a new water suppression technique called HGWS with a much shorter duration of ~250 ms. In addition, we demonstrated that this technique suppresses water better than Philips' implementation of VAPOR in both simulations and in vivo single-voxel and multi-voxel acquisitions. Future work will focus on implementing this water suppression technique in conjunction with edited multi-slice acquisitions. Combined with the use of the retrospective motion compensation technique introduced in chapter 6, it is anticipated that edited multi-slice MRSI will be feasible at 3T. Although not nearly as common as 3T, high field MR (7T and above) has been of especial interest recently due to benefits such as an increase in SNR, larger frequency dispersion, and a reduction in the J-coupling of strongly coupled spin systems (176). Thus, it might be desirable for future work to adapt this technique for use at higher magnetic field strengths by re-optimizing the sequence for a range of different conditions. In particular, the sequence can be designed to have less pulses so that the SAR values are reduced to meet the lower limit at higher field strengths due to faster tissue heating (176). In addition, due to the greater inhomogeneity of the B_1 field and altered T_1 relaxation rates, the sequence must also be optimized for a larger range of B_1 values and different water T_1 relaxation rates.

With the interest in measuring low concentration metabolites such as GABA and GSH, and the role they play in the pathophysiology of a large range of diseases, J-difference editing has the potential for widespread use. However, it is also apparent in this thesis that much progress must still be made to address longstanding methodological issues of edited measurements with single-voxel and multi-voxel localization. Thus, it is hopeful that methods such as the ones introduced in this thesis will have the potential of facilitating future clinical and research studies and further increasing their scope by allowing the inclusion of more spatial and spectral content within a single scan session. With further advances in editing techniques, it is hopeful that the J-difference methodology will be increasingly adopted across sites.

References

1. Horder J, Petrinovic MM, Mendez MA, Bruns A, Takumi T, Spooren W, Barker GJ, Künnecke B, Murphy DG. Glutamate and GABA in autism spectrum disorder — a translational magnetic resonance spectroscopy study in man and rodent models. Transl. Psychiatry 2018;8:106.
2. Chattopadhyaya B, Cristo G Di. GABAergic circuit dysfunctions in neurodevelopmental disorders. Front. Psychiatry 2012;3:51.
3. Alger JR, Frank JA, Bizzi A, et al. Metabolism of human gliomas: assessment with H-1 MR spectroscopy and F-18 fluorodeoxy- glucose PET. Radiology. 1990;177:633-641.
4. Horska A, Barker PB. Imaging of Brain Tumors: MR Spectroscopy and Metabolic Imaging. 2010;20:293–310.
5. Port JD, Agarwal N. MR Spectroscopy in Schizophrenia. 2011;1261:1251–1261.
6. Rowland LM, Pradhan S, Korenic S, Wijtenburg SA, Hong LE, Edden RA, Barker PB. Elevated brain lactate in schizophrenia: a 7 T magnetic resonance spectroscopy study. 2016;6:e967-7.
7. Dharmadhikari S, Ma R, Yeh C, Stock A, Snyder S, Zauber SE, Dydak U, Beste C. NeuroImage Striatal and thalamic GABA level concentrations play differential roles for the modulation of response selection processes by proprioceptive information. Neuroimage 2015;120:36–42.
8. Zhu H, Edden RAE, Ouwerkerk R, Barker PB. High resolution spectroscopic imaging of GABA at 3 Tesla. Magn. Reson. Med. 2011;65:603–609.
9. Bogner W, Gagoski B, Hess AT, et al. 3D GABA imaging with real-time motion correction, shim update and reacquisition of adiabatic spiral MRSI. Neuroimage 2014;103:290–302.

10. Srinivasan R, Ratiney H, Hammond-Rosenbluth KE, Pelletier D, Nelson SJ. MR spectroscopic imaging of glutathione in the white and gray matter at 7 T with an application to multiple sclerosis. Magn. Reson. Imaging 2010;28:163–170.
11. de Graaf RA. In Vivo NMR Spectroscopy: Principles and Techniques (2nd ed.), Wiley-Interscience; 2007
12. Barker PB, Bizzi A, De Stefano N, Gullapalli RP, Lin DDM. Clinical MR Spectroscopy: Techniques and Applications. Cambridge University Press: Cambridge; 2010.
13. Govindaraju V, Young K, Maudsley AA. Proton NMR chemical shifts and coupling constants for brain metabolites. NMR Biomed 2000;13: 129–153.
14. Wood SJ, Berger GE, Wellard RM, Proffitt T-M, McConchie M, Berk M, McGorry PD, Pantelis C. Medial temporal lobe glutathione concentration in first episode psychosis: a 1H-MRS investigation. Neurobiol Dis 2009;33:354–357.
15. Cooper AJ, Kristal BS. Multiple roles of glutathione in the central nervous system. Biol Chem 1997;378:793–802.
16. Sofic E, Lange KW, Jellinger K, Riederer P. Reduced and oxidized glutathione in the substantia nigra of patients with Parkinson's disease. Neurosci Lett 1992;142:128–130.
17. Chan KL, Puts NAJ, Snoussi K, Harris AD, Barker PB, Edden RAE. Echo time optimization for J-difference editing of glutathione at 3T. Magn. Reson. Med. 2017;77:498–504.
18. Chan KL, Snoussi K, Edden RAE, Barker PB. Simultaneous detection of glutathione and lactate using spectral editing at 3T. NMR Biomed 2017;30:e3800
19. Behar KL, Rothman DL, Spencer DD, Petroff OAC. Analysis of macromolecule resonances in1H NMR spectra of human brain. Magn Reson Med 1994;32:294–302.
20. Nishimura DG. Principles of magnetic resonance imaging. Stanford, CA: Stanford University Press. 2010.

21. Simpson R, Devenyi GA, Jezzard P, Hennessy TJ, Near J. Advanced processing and simulation of MRS data using the FID appliance (FID-A)-An open source, MATLAB-based toolkit. Magn. Reson. Med. 2015;33:23–33.
22. Terpstra, M., Gruetter, R., 2004. 1H NMR detection of vitamin C in human brain in vivo. Magn. Reson. Med. 51, 225–229. Terpstra,
23. Haacke EM, Brwon RW, Thonpson MR, Venkatesan R: Magnetic Resonance Imaging: Physical Principles and Sequence Design. 1999, John Wiley and Sons.
24. Wansapura JP, Holland SK, Dunn RS, Ball WS. NMR relaxation times in the human brain at 3.0 Tesla. J. Magn. Reson. Imaging 1999;9:531–538.
25. Gold GE, Han E, Stainsby J, Wright G, Brittain J, Beaulieu C. Musculoskeletal MRI at 3.0 T: Relaxation Times and Image Contrast. Am. J. Roentgenol. 2004;183:343–351.
26. Lu H, Nagae-Poetscher LM, Golay X, Lin D, Pomper M, Van Zijl PCM. Routine clinical brain MRI sequences for use at 3.0 tesla. J. Magn. Reson. Imaging 2005;22:13–22.
27. Piechnik SK, Evans J, Bary LH, Wise RG, Jezzard P. Functional Changes in CSF Volume Estimated Using Measurement of Water T2 Relaxation. Magn. Reson. Med. 2009;586:579–586.
28. Rakow-penner R, Daniel B, Yu H, Sawyer-glover A, Glover GH. Relaxation Times of Breast Tissue at 1.5T and 3T Measured Using IDEAL. J. Magn. Reson. Imaging 2006;91:87–91.
29. Bernstein MA, King KF, Zhou XJ. Handbook of MRI Pulse Sequences. Amsterdam: Academic Press. 2004.
30. Barker PB, Lin DDM, Purcell C, Gill M, Press CP. In vivo proton MR spectroscopy of the human brain. Prog. Nucl. Magn. Reson. Spectrosc. 2006;49:99–128.
31. Keeler J Understanding NMR Spectroscopy. Wiley: Chichester. 2010.
32. Rothman DL, Petroff O a, Behar KL, Mattson RH. Localized 1H NMR measurements of gamma-aminobutyric acid in human brain in vivo. Proc. Natl. Acad. Sci. U. S. A. 1993;90:5662–5666.

33. Shungu DC, Mao X, Gonzales R, Soones TN, Dyke JP, Willem J, Veen V Der, Kegeles LS. Brain γ-aminobutyric acid (GABA) detection in vivo with the J-editing 1 H MRS technique: a comprehensive methodological evaluation of sensitivity enhancement, macromolecule contamination and test – retest reliability. NMR Biomed. 2016;29:932–942.
34. Henry PG, Dautry C, Hantraye P, Bloch G. Brain GABA editing without macromolecule contamination. Magn Reson Med 2001;45: 517–520.
35. Edden RAE, Puts NAJ, Barker PB. Macromolecule-suppressed GABA-edited magnetic resonance spectroscopy at 3T. Magn. Reson. Med. 2012;68:657–661.
36. Snoussi K, Gillen JS, Horska A, Puts NAJ, Pradhan S, Edden RAE, Barker PB. Comparison of Brain Gray and White Matter Macromolecule Resonances at 3 and 7 Tesla. 2015;613:607–613.
37. Harris AD, Puts NAJ, Barker PB, Edden RAE. Spectral-editing measurements of GABA in the human brain with and without macromolecule suppression. Magn. Reson. Med. 2015;74:1523–1529.
38. Marjanska M, Deelchand DK, Hodges JS, Mccarten JR, Hemmy LS, Grant A, Terpstra M. Altered macromolecular pattern and content in the aging human brain. NMR Biomed. 2017:e3865.
39. Edden RAE, Oeltzschner G, Harris AD, Puts NAJ, Chan KL, Boer VO, Schär M, Barker PB. Prospective frequency correction for macromolecule-suppressed GABA editing at 3T. J. Magn. Reson. Imaging 2016;44:1474–1482.
40. Bhattacharyya PK, Lowe MJ, Phillips MD. Spectral Quality Control in Motion-Corrupted Single- Voxel J-Difference Editing Scans : An Interleaved Navigator Approach. Magn. Reson. Med. 2007;812:808–812.
41. Evans CJ, Puts NAJ, Robson SE, Boy F, Mcgonigle DJ, Sumner P, Singh KD, Edden RAE. Subtraction Artifacts and Frequency (Mis-) Alignment in J -Difference GABA Editing. 2013;975:970–975.

42. Mullins PG, Mcgonigle DJ, Gorman RLO, Puts NAJ, Vidyasagar R, Evans CJ, Symposium C, Edden RAE. NeuroImage Current practice in the use of MEGA-PRESS spectroscopy for the detection of GABA. Neuroimage 2014;86:43–52.
43. Waddell KW, Avison MJ, Joers JM, Gore JC. A practical guide to robust detection of GABA in human brain by J -difference spectroscopy at 3 T using a standard volume coil. 2007;25:1032–1038.
44. Near J, Edden R, Evans CJ, Harris A, Jezzard P. Frequency and Phase Drift Correction of Magnetic Resonance Spectroscopy Data by Spectral Registration in the Time Domain. Magn. Reson. Med. 2015;50:44–50.
45. Near J, Evans CJ, Puts NAJ, Barker PB, Edden RAE. J -Difference Editing of Gamma-Aminobutyric Acid (GABA): Simulated and Experimental Multiplet Patterns. 2013;1191:1183–1191.
46. Kaiser LG, Young K, Matson GB. Elimination of Spatial Interference in PRESS-Localized Editing Spectroscopy. 2007;818:813–818.
47. Edden RAE, Schär M, Hillis AE, Barker PB. Optimized detection of lactate at high fields using inner volume saturation. Magn. Reson. Med. 2006;56:912–917.
48. Barker PB, Soher BJ, Blackband SJ, Chatham JC, Mathews VP, Bryan RN. Quantitation of Proton NMR Spectra of the Human Brain Using Tissue Water as an Internal Concentration Reference. 1993;6:89–94.
49. Males RG, Vigneron DB, Star-lack J, Falbo SC, Nelson SJ, Hricak H, Kurhanewicz J. Clinical Application of BASING and Spectral / Spatial Water and Lipid Suppression Pulses for Prostate Cancer Staging and Localization by In Vivo 3D 1 H Magnetic Resonance Spectroscopic Imaging. Magn. Reson. Med. 2000;22:17–22.
50. Ebel A, Govindaraju V, Maudsley AA. Comparison of Inversion Recovery Preparation Schemes for Lipid Suppression in 1 H MRSI of Human Brain. Magn. Reson. Med. 2003;908:903–908.

51. Bydder GM, Young IR. MR imaging: clinical use of the inversion re- covery sequence. J Comput Assist Tomogr 1985;9:659–675.
52. Haase A, Frahm J, Hanicke W, Matthaei D. 1H NMR chemical shift selective (CHESS) imaging. Phys Med Biol 1985;30:341–344.
53. Ogg RJ, Kingsley RB, Taylor JS. WET, a T1- and B1-Insensitive Water-Suppression Method for in Vivo Localized 1H NMR Spectroscopy. J. Magn. Reson. Ser. B 1994;104:1–10.
54. Tkac I, Starc Z, Choi I, Gruetter R. In Vivo 1 H NMR Spectroscopy of Rat Brain at 1 ms Echo Time. Magn. Reson. Med. 1999;41:649–656.
55. Chan KL, Ouwerkerk R, Barker PB. Water suppression in the human brain with hypergeometric RF pulses for single-voxel and multi-voxel MR spectroscopy. Magn. Reson. Med. 2018;80:1298–1306.
56. Chan KL, Puts NAJ, Schär M, Barker PB, Edden RAE. HERMES: Hadamard encoding and reconstruction of MEGA-edited spectroscopy. Magn. Reson. Med. 2016;76:11–19.
57. Chan KL, Saleh MG, Oeltzschner G, Barker PB, Edden RAE. Simultaneous measurement of Aspartate, NAA, and NAAG using HERMES spectral editing at 3 Tesla. Neuroimage 2017;155:587–593.
58. Chan KL, Oeltzschner G, Schär M, Barker PB, Edden RAE. Spatial Hadamard encoding of J - edited spectroscopy using slice-selective editing pulses. NMR Biomed 2017:e3688.
59. Chan KL, Oeltzschner G, Saleh MG, Edden RAE, Barker PB. Simultaneous editing of GABA and GSH with Hadamard-encoded MR spectroscopic imaging. Magn. Reson. Med.
60. Mytilineou C, Kramer BC, Yabut JA. Glutathione depletion and oxidative stress. Parkinsonism Relat Disord 2002;8:385–387.
61. Schulz JB, Lindenau J, Seyfried J, Dichgans J. Glutathione, oxidative stress and neurodegeneration. Eur J Biochem 2000;267:4904–4911

62. Lin DDM, Crawford TO, Barker PB. Proton magnetic resonance spectroscopy in the diagnostic evaluation of suspected mitochondrial disease. AJNR Am J Neuroradiol 2003;24:33–41.
63. Matsuzawa D, Obata T, Shirayama Y et al. Negative correlation between brain glutathione level and negative symptoms in schizophrenia: a 3T 1H-MRS study. PLoS One 2008;3:e1944
64. Beasley CL, Dwork AJ, Rosoklija G et al. Metabolic abnormalities in fronto-striatal-thalamic white matter tracts in schizophrenia. 2009;109:159–166.
65. Das Neves Duarte JM, Kulak A, Gholam-Razaee MM, Cuenod M, Gruetter R, Do KQ. N-acetylcysteine normalizes neurochemical changes in the glutathione-deficient schizophrenia mouse model during development. Biol Psychiatry 2012;71:1006–1014.
66. Dager SR, Friedman SD, Parow A et al. Brain metabolic alterations in medication-free patients with bipolar disorder. Arch Gen Psychiatry 2004;61:450–458.
67. Soeiro-de-Souza MG, Pastorello BF, Leite C da C, Henning A, Moreno RA, Otaduy MCG. Dorsal Anterior Cingulate Lactate and Glutathione Levels in Euthymic Bipolar I Disorder: 1H-MRS Study. Int J Neuropsychopharmacol 2016;19:pyw032.
68. Rosa AR, Singh N, Whitaker E et al. Altered plasma glutathione levels in bipolar disorder indicates higher oxidative stress; a possible risk factor for illness onset despite normal brain-derived neurotrophic factor (BDNF) levels. Psychol Med 2014;44:2409–2418.
69. Chu W-J, Delbello MP, Jarvis KB et al. Magnetic resonance spectroscopy imaging of lactate in patients with bipolar disorder. 2013;213:230–234.
70. Mintzopoulos D, Gillis TE, Robertson HR, Dalia T, Feng G, Rauch SL, Kaufman MJ. Striatal Magnetic Resonance Spectroscopy Abnormalities in Young Adult Sapap3 Knockout Mice. Biol Psychiatry Cogn Neurosci Neuroimaging 2016;1:39–48.
71. Shungu DC, Weiduschat N, Murrough JW et al. Increased ventricular lactate in chronic fatigue syndrome. III. Relationships to cortical glutathione and clinical symptoms implicate oxidative stress in disorder pathophysiology. NMR Biomed 2012;25:1073–1087.

72. Provencher SW. Automatic quantitation of localized in vivo 1H spectra with LCModel. NMR Biomed. 2001; 14: 260–264.

73. Choi C, Zhao C, Dimitrov I, Douglas D, Coupland NJ, Kalra S, Hawesa H, Davis J. Measurement of glutathione in human brain at 3T using an improved double quantum filter in vivo. J Magn Reson 2009 ;198:160–166.

74. Trabesinger A, Weber O, Duc C, Boesiger P. Detection of glutathione in the human brain in vivo by means of double quantum coherence filtering. Magn Reson Med 1999;42(2):283–9.

75. Harris AD, Saleh MG, Edden RAE. Edited 1 H magnetic resonance spectroscopy in vivo: Methods and metabolites. 2017;1389:1377–1389.

76. Mescher M, Merkle H, Kirsch J, Garwood M, Gruetter R. Simultaneous in vivo spectral editing and water suppression. NMR Biomed 1998;11:266–272.

77. Snoussi K, Pradhan S, Harris AD, Edden RAE, Barker PB. Optimization of MEGA-PRESS for the simultaneous detection of Glutamate and Glutamine, and GABA In Proceedings of the 23rd Annual Meeting of ISMRM, Toronto, Ontario, Canada, 2015. Abstract 4694.

78. Terpstra M, Marjanska M, Henry PG, Tkáč I, Gruetter R. Detection of an antioxidant profile in the human brain in vivo via double editing with MEGA-PRESS. Magn Reson Med 2006;56:1192–1199.

79. Smith MA, Koutcher JA, Zakian KL. J-difference lactate editing at 3.0 Tesla in the presence of strong lipids. J Magn Reson Imaging 2008;28:1492–1498.

80. Terpstra M, Henry P-G, Gruetter R. Measurement of reduced glutathione (GSH) in human brain using LCModel analysis of difference-edited spectra. Magn Reson Med 2003;50:19–23.

81. Kaiser LG, Marjańska M, Matson GB, Iltis I, Bush SD et al. (2010) H MRS detection of glycine residue of reduced glutathione in vivo 1. J Magn Reson 2010;202:259-266.

82. Bogner W, Strasser B, Povazan M, Hangel G, Gagoski B, Gruber S, Rosen B, Trattnig S, Andronesi O. 3D mapping of Glutathione in the human brain via real-time motion corrected

MEGA-LASER MRSI. In: Proceedings of the 23rd Annual Meeting of ISMRM, Toronto, Ontario, Canada, 2015 (Abstract 0988).

83. Sailasuta N, Iwata Y, Nakajima S, Chavez S, Caravaggio F, Plitman E, De Luca V, Chung JK, Gerretsen P, Remington G. Lower Glutathione Levels in the Anterior Cingulate Cortex of Patients with Schizophrenia: A preliminary 3T 1H-MRS Study In: Proceedings of the 23rd Annual Meeting of ISMRM, Toronto, Ontario, Canada, 2015 (Abstract 3562).
84. Weiduschat N, Mao X, Hupf J, Armstrong N, Kang G, Lange DJ, Mitsumoto H, Shungu DC. Motor cortex glutathione deficit in ALS measured in vivo with the J-editing technique. Neuroscience Letters 2014;570:102–107.
85. Satoh T, Yoshioka Y. Contribution of reduced and oxidized glutathione to signals detected by magnetic resonance spectroscopy as indicators of local brain redox state. Neuroscience Res 2006;55:34–9.
86. An L, Zhang Y, Thomasson DM, Latour LL, Baker EH, Shen J, Warach S. Measurement of glutathione in normal volunteers and stroke patients at 3T using J-difference spectroscopy with minimized subtraction errors. J Magn Reson Imaging 2009;30:263–70.
87. Nehzad FS, Anton A, Deakin B, Williams S. Glutathione cannot be quantified reliably from short echo PRESS spectra. In: Proceedings of the 23rd Annual Meeting of ISMRM, Toronto, Ontario, Canada, 2015 (Abstract 1952).
88. Edden RAE, Barker PB. If J doesn’t evolve, it won't J-resolve: J-PRESS with bandwidth-limited refocusing pulses. Magn Reson Med 2011;65:1509–1514.
89. Murdoch JB, Lent AH, Kritzer MR. Computer-optimized narrowband pulses for multislice imaging. 1987;74(2):226–263.
90. Yablonskiy DA, Neil JJ, Raichle ME, Ackerman JJ. Homonuclear J coupling effects in volume localized NMR spectroscopy: pitfalls and solutions. Magn Reson Med 1998;39:169–78.

91. Thompson RB, Allen PS. Sources of variability in the response of coupled spins to the PRESS sequence and their potential impact on metabolite quantification. Magn Reson Med 1999;41:1162–9.

92. Yahya A, Mädler B, Fallone BG. Exploiting the chemical shift displacement effect in the detection of glutamate and glutamine (Glx) with PRESS. J Magn Reson 2008;191:120–127.

93. Kaiser LG, Young K, Meyerhoff DJ, Mueller SG, Matson GB. A detailed analysis of localized J-difference GABA editing: theoretical and experimental study at 4 T. NMR Biomed 2008; 21:22-32.

94. Edden RAE, Barker PB. Spatial effects in the detection of gamma-aminobutyric acid: improved sensitivity at high fields using inner volume saturation. Magn Reson Med 2007;58:1276–82.

95. Emir UE, Deelchand D, Henry P-G, Terpstra M. Noninvasive quantification of T2 and concentrations of ascorbate and glutathione in the human brain from the same double-edited spectra. NMR Biomed 2011;24:263–9.

96. Edden RAE, Intrapiromkul J, Zhu H, Cheng Y, Barker PB. Measuring T2 in vivo with J-difference editing: application to GABA at 3 Tesla. J Magn Reson Imaging 2012;35:229–234.

97. Henning A, Fuchs A, Murdoch JB, Boesiger P. Slice-selective FID acquisition, localized by outer volume suppression (FIDLOVS) for 1H-MRSI of the human brain at 7 T with minimal signal loss. 2009;22(7):683–696.

98. Edden RAE, Puts NAJ, Harris AD, Barker PB, Evans CJ. Gannet: A batch-processing tool for the quantitative analysis of gamma-aminobutyric acid-edited MR spectroscopy spectra. J Magn Reson Imaging 2014;1452:1445–1452.

99. Soher BJ, Hurd RE, Sailasuta N, Barker PB. Quantitation of automated single-voxel proton MRS using cerebral water as an internal reference. Magn Reson Med 1996;36:335–339.

100. Shen J, Novotny EJ, Rothman DL. In Vivo Lactate and B-Hydroxybutyrate Editing Using a Pure-Phase Refocusing Pulse Train. Magn Reson Med 1998;40:783-8.

101. Thomas MA, Yue K, Binesh N et al. Localized two-dimensional shift correlated MR spectroscopy of human brain. Magn Reson Med 2001;46:58–67.

102. Chan KL, Edden RAE, Barker PB. J-difference editing of Creatine in the human brain. In Proceedings of the 25th Annual Meeting of ISMRM, Honolulu, Hawai'i, USA, 2017. Abstract 5473.

103. Terpstra M, Vaughan TJ, Ugurbil K, Lim KO, Schulz SC, Gruetter R. Validation of glutathione quantitation from STEAM spectra against edited 1H NMR spectroscopy at 4T: application to schizophrenia. MAGMA 2005;18:276–282

104. Harris AD, Glaubitz B, Near J et al. Impact of frequency drift on gamma-aminobutyric acid-edited MR spectroscopy. Magn Reson Med 2014;72:941–948.

105. Edden RAE, Pomper MG, Barker PB. In vivo differentiation of N-acetyl aspartyl glutamate from N-acetyl aspartate at 3 Tesla. Magn Reson Med 2007;57: 977-982.

106. Star-Lack J, Spielman D, Adalsteinsson E, Kurhanewicz J, Terris DJ, et al. In vivo lactate editing with simultaneous detection of choline, creatine, NAA, and lipid singlets at 1.5 T using PRESS excitation with applications to the study of brain and head and neck tumors. J Magn Reson 1998;133: 243-254.

107. Choi C, Ganji SK, DeBerardinis RJ, Hatanpaa KJ, Rakheja D, Kovacs Z, Yang XL, Mashimo T, Raisanen JM, Marin-Valencia I, Pascual JM, Madden CJ, Mickey BE, Malloy CR, Bachoo RM, Maher EA. 2-hydroxyglutarate detection by magnetic resonance spectroscopy in IDH-mutated patients with gliomas. Nat Med 2012;18: 624-629.

108. Rae CD. A guide to the metabolic pathways and function of metabolites observed in human brain 1H magnetic resonance spectra. Neurochem Res 2014;39: 1-36.

109. Coyle JT. The nagging question of the function of N-acetylaspartylglutamate. Neurobiol Dis 1997;4: 231-238.

110. Hadamard J. Résolution d'une Question Relative aux Déterminants. Bull Sci Math 1893;17: 240-248.

111. Pouwels PJ, Frahm J. Differential distribution of NAA and NAAG in human brain as determined by quantitative localized proton MRS. NMR Biomed 1997;10: 73-78.
112. El-Sharkawy AM, Schar M, Bottomley PA, Atalar E. Monitoring and correcting spatio-temporal variations of the MR scanner's static magnetic field. Magn Reson Mater Phy 2006;19: 223-236.
113. Choi C, Ghose S, Uh J, Patel A, Dimitrov IE, Lu H, Douglas D, Ganji S. Measurement of N-acetylaspartylglutamate in the human frontal brain by 1H-MRS at 7 T. Magn Reson Med 2010;64: 1247–1251.
114. Haase A, Frahm J, Hänicke W, Matthaei D. 1H NMR chemical shift selective (CHESS) imaging. Phys. Med. Biol. 1985;30:341–4.
115. Harris AD, Puts NAJ, Edden RAE. Tissue correction for GABA-edited MRS: Considerations of voxel composition, tissue segmentation, and tissue relaxations. J Magn Reson Imaging 2015;42:1431–1440.
116. Träber F, Block W, Lamerichs R, Gieseke J, Schild HH. 1H Metabolite Relaxation Times at 3.0 Tesla: Measurements of T1 and T2 Values in Normal Brain and Determination of Regional Differences in Transverse Relaxation. J Magn Reson Imaging 2004;19:537–545.
117. Ljungberg M, Nilsson MKL, Melin K, Jönsson L, Carlsson A, Carlsson Å, Forssell-Aronsson E, Ivarsson T, Carlsson M, Starck G. 1H magnetic resonance spectroscopy evidence for occipital involvement in treatment-naive paediatric obsessive–compulsive disorder. Acta Neuropsychiatr 2016; 1–12.
118. Kupče Ē, Nishida T, Freeman R. Hadamard NMR spectroscopy. Prog NMR Spectrosc 2003;42: 95-122.
119. Landim RCG, Edden RAE, Foerster B, Li LM, Covolan RJM, Castellano G. Investigation of NAA and NAAG dynamics underlying visual stimulation using MEGA-PRESS in a functional MRS experiment. Magn Reson Imaging 2015;34(3):239–245.

120. Wilson M, Reynolds G, Kauppinen RA, Arvanitis TN, Peet AC. A constrained least-squares approach to the automated quantitation of in vivo (1)H magnetic resonance spectroscopy data. Magn Reson Med 2011;65: 1-12.

121. Posse S, Otazo R, Dager SR, Alger J. MR Spectroscopic Imaging : Principles and Recent Advances. J Magn Reson Imaging 2013;37:1301–1325.

122. Sabati M, Sheriff S, Gu M, Wei J, Zhu H, Barker PB, Spielman DM, Alger JR, Maudsley AA. Multivendor implementation and comparison of volumetric whole-brain echo-planar MR spectroscopic imaging. Magn Res Med 2015;74:1209–1220.

123. Boer VO, Klomp DWJ, Laterra J, Barker PB. Parallel reconstruction in accelerated multivoxel MR spectroscopy. Magn Reson Med 2015;74:599–606.

124. Bolinger L, Leigh JS. Hadamard. Spectroscopic imaging (HSI) for multivolume localization. J Magn Reson 1969;80:162–167.

125. Lemke C, Hess A, Clare S, Bachtiar V, Stagg C, Jezzard P, Emir U. Two-voxel spectroscopy with dynamic B_0 shimming and flip angle adjustment at 7 T in the human motor cortex. NMR in Biomed 2015;852–860.

126. Schär M, Vonken EJ, Stuber M. Simultaneous B0- and B1+-map acquisition for fast localized shim, frequency, and RF power determination in the heart at 3 T. Magn Reson Med 2010; 63:419–426.

127. Near J, Simpson R, Cowen P, Jezzard P. Efficient gamma-aminobutyric acid editing at 3T without macromolecule contamination: MEGA-SPECIAL. NMR Biomed 2011;24:1277–1285.

128. Puts NAJ, Edden RAE. In vivo magnetic resonance spectroscopy of GABA: A methodological review. Prog. Nucl. Magn. Reson. Spectrosc. 2012;60:29–41.

129. Bogner W, Hangel G, Esmaeili M, Andronesi OC. 1D-spectral editing and 2D multispectral in vivo 1H-MRS and 1H-MRSI - Methods and applications. Anal. Biochem. 2017;529:48–64.

130.Payne GS, Harris LM, Cairns GS, Messiou C, deSouza NM, Macdonald A, Saran F, Leach MO. Validating a robust double-quantum-filtered 1H MRS lactate measurement method in high-grade brain tumours. NMR Biomed. 2016;29:1420–1426.

131.Mao X, Jiang CS, Kang G, Milrad S, Mcewen BS, Krieger AC, Shungu DC. Dorsolateral prefrontal cortex GABA deficit in older adults with sleep-disordered breathing. Proc. Natl. Acad. Sci. 2017;114:E9424–E9424.

132.Shen J, Shungu DC, Rothman DL. In vivo chemical shift imaging of gamma-aminobutyric acid in the human brain. Magn. Reson. Med. 1999;41:35–42.

133.Dydak U, Xu JS, Marjanska M, Posse S. 3D GABA Spectroscopic Imaging using MEGA-PEPSI. In Proceedings of the 19th Annual Meeting of ISMRM, Montreal, Quebec, Canada, 2011. Abstract 1428.

134.Bogner W, Gagoski B, Hess AT, Bhat H, Tisdall MD, van der Kouwe AJ, Strasser B, Marjańska M, Trattnig S, Grant E, Rosen B, Andronesi OC. 3D GABA imaging with real-time motion correction, shim update and reacquisition of adiabatic spiral MRSI. Neuroimage 2014;103:290–302.

135.Saleh MG, Oeltzschner G, Chan KL, Puts NAJ, Mikkelsen M, Schär M, Harris AD, Edden RAE. Simultaneous edited MRS of GABA and glutathione. NeuroImage 2016;142:576-582.

136.Gruetter R. Automatic, localized in Vivo adjustment of all first- and second-order shim coils. Magn. Reson. Med. 1993;29:804–811.

137.Zhu H, Ouwerkerk R, Barker PB. Dual-band water and lipid suppression for MR spectroscopic imaging at 3 tesla. Magn. Reson. Med. 2010;63:1486–1492.

138.H. Barkhuysen, R. de Beer, and D. van Ormondt. Improved algorithm for noniterative time-domain model function to exponentially damped magnetic resonance signals. J. Magn. Reson. 1987;73:553–557.

139. Raschke F, Noeske R, Auer DP, Rob D. Measuring Glutathione using 1H MR spectroscopy at 3T: MEGA-PRESS vs. STEAM. In Proceedings of the 23rd Annual Meeting of ISMRM, Toronto, Ontario, Canada, 2011. Abstract 1951.
140. Da Silva T, Hafizi S, Andreazza AC, et al. Glutathione –the major redox regulator- in the prefrontal cortex of individuals at clinical high risk for psychosis. Int. J. Neuropsychopharmacol. 2017;0:1–8.
141. Evans CJ, McGonigle DJ, Edden RAE. Diurnal stability of gamma-aminobutyric acid concentration in visual and sensorimotor cortex. J. Magn. Reson. Imaging 2010;31:204–209.
142. Larsen R, Gagoski B, Drottar M, Francel T, Matos A, Carruthers C, Vu C, Litt J, Sutton B, Grant E. GABA Concentration Measurements in Infants Without Sedation. In Proceedings of the 23rd Annual Meeting of ISMRM, Toronto, Ontario, Canada, 2011. Abstract 2975.
143. Bogner W, Gruber S, Doelken M, et al. In vivo quantification of intracerebral GABA by single-voxel 1H-MRS—How reproducible are the results? Eur J Radiol. 2010;73:526-531.
144. Geramita M, van der Veen JW, Barnett AS, Savostyanova AA, Shen J, Weinberger DR, Marenco S. Reproducibility of prefrontal gamma-aminobutyric acid measurements with J-edited spectroscopy. NMR Biomed. 2011;24:1089–1098.
145. Tkác I, Oz G, Adriany G, Uğurbil K, Gruetter R. In vivo 1H NMR spectroscopy of the human brain at high magnetic fields: metabolite quantification at 4T vs. 7T. Magn. Reson. Med. 2009;62:868–79.
146. Graaf RA De, Brown PB, Mcintyre S, Nixon TW, Behar KL, Rothman DL. High Magnetic Field Water and Metabolite Proton T 1 and T 2 Relaxation in Rat Brain In Vivo. 2006;394:386–394.
147. Jensen JE, de B. Frederick B, Renshaw PF. Grey and white matter GABA level differences in the human brain using two-dimensional, J-resolved spectroscopic imaging. NMR Biomed. 2005;18:570–576.

148. Mikkelsen M, Singh KD, Brealy JA, Linden DEJ, Evans CJ. Quantification of gamma-aminobutyric acid (GABA) in 1H MRS volumes composed heterogeneously of grey and white matter. NMR Biomed. 2016;29:1644–1655.

149. Chen M, Li G, Zhang Z, Chen L, Pei M, Yan X, Li J. The anterior cingulate cortex GABA levels with varied tissue composition measured by in vivo single voxel MRS. In Proceedings of the 24th Annual Meeting of ISMRM, Suntec City, Singapore, 2016. Abstract 4005.

150. Oeltzschner G, Chan KL, Saleh MG, Mikkelsen M, Puts NA, Edden RAE. Hadamard editing of glutathione and macromolecule-suppressed GABA. NMR Biomed. 2018;31:e3844.

151. Hess AT, Andronesi OC, Dylan Tisdall M, Gregory Sorensen A, van der Kouwe AJW, Meintjes EM. Real-time motion and B0 correction for localized adiabatic selective refocusing (LASER) MRSI using echo planar imaging volumetric navigators. NMR Biomed. 2012;25:347–358.

152. Bogner W, Hess AT, Gagoski B, Tisdall MD, van der Kouwe AJW, Trattnig S, Rosen B, Andronesi OC. Real-time motion- and B0-correction for LASER-localized spiral-accelerated 3D-MRSI of the brain at 3T. NeuroImage 2014;88:22–31.

153. Helms G, Piringer A. Restoration of motion-related signal loss and line-shape deterioration of proton MR spectra using the residual water as intrinsic reference. Magn Reson Med 2001;46:395–400.

154. Mikkelsen M, Saleh MG, Near J, et al. Frequency and Phase Correction for Multiplexed Edited MRS of GABA and Glutathione. Magn Reson Med 2018;28:21–28.

155. An L, Ferraris M, Christopher A, Shen J. Simultaneous measurement of glutamate, glutamine, GABA, and glutathione by spectral editing without subtraction. Magn. Reson. Med. 2018;80:1776–1786.

156. Petroff OAC. GABA and Glutamate in the Human Brain. 2002:562–573.

157. Shetty AK, Bates A. Potential of GABA-ergic cell therapy for schizophrenia , neuropathic pain , and Alzheimer ' s and Parkinson ' s diseases. Brain Res. 2016;1638:74–87.

158. Do KQ, Cuenod M, Hensch TK. Targeting Oxidative Stress and Aberrant Critical Period Plasticity in the Developmental Trajectory to Schizophrenia. 2018;41:835–846.
159. Chang L, Cloak CC, Ernst T. Magnetic resonance spectroscopy studies of GABA in neuropsychiatric disorders. J Clin Psychiatry. 2003;64:7–14.
160. Jocham G, Hunt LT, Near J, Behrens TEJ. A mechanism for value- guided choice based on the excitation-inhibition balance in prefrontal cortex. Nat. Neurosci. 2012;15:960–961.
161. Isaacson JS, Scanziani M. How inhibition shapes cortical activity. Neuron 2011;72:231–243.
162. Ernst, T., Li, J., 2011. A novel phase and frequency navigator for proton magnetic reso- nance spectroscopy using water-suppression cycling. Magn. Reson. Med. 65, 13–17.
163. Dreher W, Leibfritz D. New Method for the Simultaneous Detection of Metabolites and Water in Localized in vivo 1 H Nuclear Magnetic Resonance Spectroscopy. Magn. Reson. Med. 2005;195:190–195.
164. Pijnappel WWF, van den Boogaart A, de Beer R, van Ormondt D. SVD-based quantification of magnetic resonance signals. J. Magn. Reson. 1992;97:122–134.
165. Tkáć I, Gruetter R. Methodology of 1 H NMR Spectroscopy of the Human Brain at Very High Magnetic Fields. Appl. Magn. Reson. 2005;29:139–157.
166. Hangel G, Strasser B, Považan M, Heckova E, Hingerl L, Boubela R, Gruber S, Trattnig S, Bogner W. Ultra-high resolution brain metabolite mapping at 7 T by short-TR Hadamard-encoded FID-MRSI. Neuroimage 2016.
167. Ouwerkerk R. Fast Sequence Optimization for Superior Signal Suppression with Multiple Hyperbolic Secant Pulses. Proc. Fifteenth Meet. Int. Soc. Magn. Reson. Med. 2007;15:1674.
168. Rosenfeld D, Panfil SL, Zur Y. Design of adiabatic pulses for fat-suppression using analytic solutions of the Bloch equation. Magn. Reson. Med. 1997;37:793–801.
169. Rosenfeld D. Analytic solutions of the Bloch equation involving asymmetric amplitude and frequency modulations. Phys Rev A 1996; 54i:2439–2443.
170. de Graaf RA, Nicolay K. Adiabatic water suppression using frequency selective excitation.

Magn Reson Med 1998;40:690–696.

171. Chen L, Bernstein M. Measurements of T1 relaxation times at 3.0 T: implications for clinical MRA. Proc. 9th Meet. Int. Soc. Magn. Reson. Med. 2001; Abstract 1391.

172. Kirkpatrick S, Gelatt CD, Vecchi MP. Optimization by Simulated Annealing. Science 1983;220:671-680.

173. Oeltzschner G, Saleh MG, Rimbault D, Mikkelsen M, Chan KL, Puts NAJ, Edden RAE. Advanced Hadamard-encoded editing of seven low-concentration brain metabolites: Principles of HERCULES. Neuroimage 2019;185:181–190.

174. Flores-Ramos M, Alcauter S, López-Titla M, Bernal-Santamaría N, Calva-Coraza E, Edden RAE. Testosterone is related to GABA+ levels in the posterior-cingulate in unmedicated depressed women during reproductive life. J. Affect. Disord. [Internet] 2019;242:143–149.

175. Pruessmann KP, Weiger M, Scheidegger MB, Boesiger P. SENSE : Sensitivity Encoding for Fast MRI. Magn. Reson. Med. 1999;42:952–962.

176. Henning A. Proton and multinuclear magnetic resonance spectroscopy in the human brain at ultra-high field strength: A review. Neuroimage 2018;168:181–198.

Curriculum Vitae

Kimberly Chan was born in Mountain View, California on August 16th, 1991. She received a B.S. degree in Bioengineering from the University of California, Berkeley in 2013. After graduating, she worked as a research assistant at NASA Ames Research Center and Stanford University where she worked with Dr. Brian Wandell on evaluating white matter models of diffusion MRI data in the human brain. She came to Johns Hopkins in 2014 and completed her Ph.D. in Biomedical Engineering under the guidance of Drs. Peter Barker and Richard Edden where she worked on developing techniques for MR spectroscopy and spectroscopic imaging. Her work has been published in NMR in Biomedicine, Magnetic Resonance in Medicine, and NeuroImage. Her future work includes continuing to develop new MR spectroscopy methods at the University of Texas, Southwestern.